

**Understanding hydrodynamics in
Membrane Bioreactor systems for
wastewater treatment:
Two-phase empirical and numerical
modelling and experimental validation**

Nicolás Ratkovich



M.Sc. Nicolás Ratkovich

**Understanding hydrodynamics in Membrane
Bioreactor systems for wastewater treatment:
Two-phase empirical and numerical modelling
and experimental validation**

Thesis submitted in fulfilment of the requirements
for the degree of Doctor (PhD) in Applied Biological Science

Dutch translation of the title:

Verwerven van inzicht in de hydrodynamica van membraanbioreactorsystemen voor afvalwaterzuivering: Twee-fase empirische en numerieke modellering en experimentele validatie

Please refer to this work as follows:

Ratkovich, N. (2010) Understanding hydrodynamics in Membrane Bioreactor systems for wastewater treatment: Two-phase empirical and numerical modelling and experimental validation. PhD Thesis, Ghent University, Belgium, pp 223

ISBN-number: 978-90-5989-372-6

The author and the promoter give the authorisation to consult and copy parts of this work for personal use only. Every other use is subject to copyright laws. Permission to reproduce any material contained in this work must be obtained from the author.

For Niki
And
Nikola-Ivan

Members of the Examination Committee

Prof. Dr. P.Eng. Pierre Bérubé	University of British Columbia, Canada
Prof. Dr. -Ing. Anja Drews	HTW Berlin, Germany
Prof. Dr. ir. Jan Pieters	Ghent University, Belgium
Prof. Dr. ir. Paul Van der Meeren	Ghent University, Belgium
Prof. Dr. Ir. Willy Verstraete (Chair)	Ghent University, Belgium
Prof. Dr. -Ing. Thomas Wintgens	Fachhochschule Nordwestschweiz, Switzerland

Promotor: Prof. Dr. ir. Ingmar Nopens
Department of Applied Mathematics, Biometrics and Process Control
Research group BIOMATH - Model-based analysis and optimisation of
bioprocesses
Faculty of Bioscience Engineering
Ghent University

Dean: Prof. Dr. ir. Guido Van Huylenbroeck

Rector: Prof. Dr. Paul Van Cauwenberge

Acknowledgments

He aprendido que todo el mundo	I have learned that everybody wants
quiere vivir en la cima de la montaña,	to live at the top of the mountain
sin saber que la verdadera felicidad	without realizing that true happiness
está en la forma de subir la escarpada.	lies in the way we climb the slope.

Taken from *La Marioneta / The Puppet* by Gabriel García Márquez

After so much work for accomplishing this thesis, I can hardly believe the time to write a few words of acknowledgment have arrived. I would like to thank every person that directly or indirectly contributed to the realisation of this work.

First, I would like to thank deeply my supervisor, Prof. Ingmar Nopens, not only for choosing me to do this research work on the MBR-TRAIN project but mainly for the help, orientation and unconditional support during these three years.

Prof. Pierre Bérubé, from the University of British Columbia, for his encouragement throughout this research and the excellent accompaniment of the experimental work performed in Vancouver (Canada),

Dr. Michaela Hunze, from FlowConcept, for giving me the opportunity to do my secondment at her company, learn so much about CFD and to have the chance to live in Hannover (Germany)

Rita Hochstrat, from RWTH, for her support in all the administrative and bureaucratic stuff and of course for been comprehensive about my status in Miles & More going to conferences during this three years in: Aachen (DE), Algarve (PT), Antwerp (BE), Atlanta (US), Berlin (DE), Bialystok (PL), Bonn (DE), Brno (CZ), Cranfield (GB), Chicago (US), Delft (NL), Harrogate (GB), Krakow (PL), Milan (IT), Montpellier (FR), Québec City (CA), Toulouse (FR) and Vancouver (CA).

To the MBR-TRAIN fellows: (in alphabetical order with the country of origin and the country where they worked to show how international was the project): Luca (IT-BE), Loïc (FR-DE), Helene (FR-IT), Marina (ES-DE), Alessio (IT-BE), Antinea (EC-BE), Jose (ES-NL), Jozef (SK-DE), Pawel (PL-NL), Ramona (DE-IT), Nacho (ES-UK), Zuzana (SK-CZ), Adrien (FR-NL), Johanna (FR-DE), Evelyne (FR-DE), Petra (SK-CZ), Tina (SK-CZ), Jan (CZ-DE), Teresa (ES-DE) and Bart (BE-GB), for the great experiences in conferences, summer schools, project meetings, social networking, etc during these three years of the EU project.

To the graduate students at UBC that made my stay in Vancouver really enjoyable: Colleen, Blair, Thomas, Sepideh, Isabel and Zaki.

To the people that I worked with at FlowConcept: Jan, Arthur, Oliver and Thorsten for making my stay in Hannover likeable.

To the people that I talked about MBR-CFD modelling and N-S equations: Charlotte, Lutz, Matthew, Steffen, Anja, Christelle, Boris, Laure, Helmut, Mark and Sreepriya.

To some of the people that I met in conferences: Elif, Linda, Luis, Joel, Hector, Lene, Eugenio, Kristy, Güçlü, Igor, Simon, Ricardo, Robert, Meritxell, Samuel, Marlène, Peter, Runi, among others.

To people that belong(ed) to the BIOMATH research unit: Andres, Luca (again), Lorenzo, Tinne, Thomas, Salvatore, Viv, Ramiro, Stefania, Phuong, Karel and Sreepriya.

To the friends that I meet in my stay in Ghent: Bibiana, Teresa, Abhi, Franciska, Mariangiola and Armando.

A mis amigos de Colombia, Juan Pablo, Ana Maria, Ivan Andres, Carlos Andres, Jorge Mario (El Paisa) y Camilo.

A mi mama por su apoyo incondicional durante mi estancia en Gante. Mi tío Iván y mis primos Iván y Juan David por su soporte.

Y por último a mi esposa, Niki, por darme el regalo más bello... Nikola-Ivan.

List of symbols and abbreviations

Abbreviations

CAS	Conventional Activated Sludge
CMC	CarboxyMethyl Cellulose
DFCm	Delft Filtration Characterization method
MBR	Membrane BioReactor
SADm	Specific Aeration Demand to membrane area ($\text{m}\cdot\text{h}^{-1}$)
SADp	Specific Aeration Demand to permeate volume ($\text{m}^3\cdot\text{m}^{-3}$)
SRT	Solids Retention Time (d)
<i>SSE</i>	sum of square errors (-)
<i>TMP</i>	TransMembrane Pressure (Pa)
<i>TSS</i>	Total Suspended Solids ($\text{g}\cdot\text{L}^{-1}$)
WWTP	WasteWater Treatment Plant

Symbols

c	concentration ($\text{g}\cdot\text{L}^{-1}$)
C	slope in gas slug rising velocity (-)
C_0	distribution parameter (-)
c_b	solute concentration in the bulk ($\text{g}\cdot\text{L}^{-1}$)
c_m	solute concentration at the membrane surface ($\text{g}\cdot\text{L}^{-1}$)
C_o	bulk concentration of ferricyanide (= $3 \text{ mol}\cdot\text{m}^{-3}$)
c_p	specific heat ($\text{kJ}\cdot\text{kg}^{-1}\cdot\text{K}^{-1}$)
c_{per}	permeate concentration ($\text{g}\cdot\text{L}^{-1}$)
d	tube diameter (m)
d_e	probe diameter (m)
d_{eqv}	equivalent hydraulic diameter (m)
D_f	diffusion coefficient ($\text{m}^2\cdot\text{s}^{-1}$)
DF	degrees of freedom (-)
d_{mem}	membrane diameter (m)
d_p	particle diameter (-)
E_a	activation energy ($\text{J}\cdot\text{mol}^{-1}$)
e_{blower}	blower efficiency (-)
E_{blower}	blower power (W)
E_{mix}	energy for mixing (W)
$E\ddot{o}$	Eötvös number (-)
e_{pump}	pump efficiency (-)
E_{pump}	pump power (W)

E_{total}	total power (W)
f	Darcy friction factor (-)
F	Faraday constant (= 96 500 C·mol ⁻¹)
f_{lam}	Darcy friction factor for laminar regime (-)
F_p	flow pattern factor (-)
Fr	Froude number (-)
Fr'	mixture Froude number (-)
F_s	shape factor (-)
f_{tp}	two-phase friction factor (-)
f_{tur}	Darcy friction factor for turbulent regime (-)
g	gravity acceleration (= 9.81 m·s ⁻²)
G	amplifier gain (= 1000)
h	heat transfer coefficient (W·m ⁻² ·K ⁻¹)
h_L	heat transfer coefficient for liquid (W·m ⁻² ·K ⁻¹)
h_{tp}	two-phase heat transfer coefficient (W·m ⁻² ·K ⁻¹)
I^*	inclination factor (-)
I_L	electrical current (A)
J	permeate flux (lmh or m·s ⁻¹)
k	flow consistency index (Pa·s ⁿ)
k_c	thermal conductivity (W·m ⁻¹ ·K ⁻¹)
$k_{c,G}$	thermal conductivity of gas (W·m ⁻¹ ·K ⁻¹)
$k_{c,L}$	thermal conductivity of liquid (W·m ⁻¹ ·K ⁻¹)
$k_{c,tp}$	two-phase thermal conductivity (W·m ⁻¹ ·K ⁻¹)
k_m	mass transfer coefficient (m·s ⁻¹)
$k_{m,ff}$	mass transfer coefficient for falling film zone (m·s ⁻¹)
$k_{m,ls}$	mass transfer coefficient for liquid slug zone (m·s ⁻¹)
$k_{m,probe}$	mass transfer coefficient for the probe (m·s ⁻¹)
$k_{m,w}$	mass transfer coefficient for wake zone (m·s ⁻¹)
k_{TB}	intercept in gas slug rising velocity (m·s ⁻¹)
L	tube length (m)
Le	Lewis number (-)
L_{LS}	length of the liquid slug (m)
L_{mem}	membrane length (m)
l_{ref}	reference lines (m)
L_{TB}	length of the gas slug (m)
\dot{m}_G	momentum flux for gas (kg·m ⁻² ·s ⁻¹)
\dot{m}_L	momentum flux for liquid (kg·m ⁻² ·s ⁻¹)
\dot{m}_{total}	total momentum flux (kg·m ⁻² ·s ⁻¹)
n	flow behaviour index (-)
n'	exponent (-)
N_{LP}	liquid property group (-)

Nu	Nusselt number (-)
Nu_{N-N}	non-Newtonian Nusselt number (-)
Nu_{tp}	two-phase Nusselt number (-)
P_{atm}	atmospheric pressure (=101 325 Pa)
Pr	Prandtl number (-)
Pr_L	liquid Prandtl number (-)
Pr_{tp}	two-phase Prandtl number (-)
R	resistance (Ω)
R_{air}	specific gas constant for air (= 286.88 J·kg ⁻¹ ·K ⁻¹)
R_c	cake resistance (m ⁻¹)
Re	Reynolds number (-)
Re_{ff}	falling film Reynolds number (-)
Re_G	gas Reynolds number (-)
Re_h	homogeneous Reynolds number (-)
Re_{int}	intermediate Reynolds number (= 2720)
Re_L	liquid Reynolds number (-)
Re_m	mixture Reynolds number (-)
Re_{MR}	Metzner and Reed Reynolds number (-)
$Re_{MR,c}$	critical Reynolds number (-)
Re_{sf}	slug flow Reynolds number (-)
Re_{SG}	superficial gas Reynolds number (-)
Re_{tp}	two-phase Reynolds number (-)
R_f	fouling resistance (m ⁻¹)
R_{gas}	universal gas constant (= 8.3145 J·K ⁻¹ ·mol ⁻¹)
R_m	intrinsic membrane resistance (m ⁻¹)
R_T	total membrane resistance (m ⁻¹)
\bar{S}	wall velocity gradient (or shear rate) (s ⁻¹)
Sc	Schmidt number (-)
Sh	Sherwood number (-)
Sh_{N-N}	Non-Newtonian Sherwood number (-)
St	Stanton number (-)
St_m	mass Stanton number (-)
t	time (s)
T	absolute temperature (K)
T_{in}	inlet temperature (K)
t_x	thickness of the membrane (m)
u	velocity (m·s ⁻¹)
u_0	gas slug rising velocity in stagnant liquid (m·s ⁻¹)
u_{axial}	axial velocity component (m)
u_{ff}	falling film velocity (m·s ⁻¹)

u_G	gas velocity (m·s ⁻¹)
u_{GLS}	velocity of gas in a liquid slug (m·s ⁻¹)
u_{GM}	drift velocity (m·s ⁻¹)
u_L	liquid velocity (m·s ⁻¹)
u_m	mixture velocity (m·s ⁻¹)
u_{mem}	liquid cross-flow velocity (m·s ⁻¹)
u_{SG}	superficial velocity of gas (m·s ⁻¹)
u_{SL}	superficial velocity of liquid (m·s ⁻¹)
u_{TB}	gas slug (Taylor bubble) rising velocity (m·s ⁻¹)
$u_{TB,exp}$	experimental gas slug rising velocity (m·s ⁻¹)
V	electrical potential (V)
ν_e	number of electrons involved in the reaction (= 1)
V_{tan}	tank volume (m ³)
$w_{1,2}$	fitting parameters (width peak) (-)
We	Weber number (-)
x	vapor quality (-)
z	vertical height (m)

Greek symbols

α_l	void fraction of the liquid (-)
α_{ip}	two-phase void fraction (-)
α_{TB}	void fraction of the slug flow (-)
α_V	void fraction for a vertical tube (-)
β	ratio of the gas slug to the sum of the gas and liquid slug (-)
$\dot{\gamma}$	shear rate (s ⁻¹)
$\dot{\gamma}_w$	shear rate at the wall surface (s ⁻¹)
δ	thickness of the boundary layer (m)
δ_L	thickness of the falling liquid film (m)
ΔL	section length (m)
Δp	pressure drop (Pa)
ΔP_{frict}	frictional pressure drop (Pa)
ΔP_{mea}	measured pressure drop (Pa)
ΔP_{mem}	pressure drop along the membrane (Pa)
ΔP_{mom}	momentum pressure drop (Pa)
ΔP_{static}	static pressure drop (Pa)
ΔP_{total}	total pressure drop (Pa)
ΔZ	height difference (m)
κ	Boltzmann's constant (= 1.38·10 ⁻²³ J·K ⁻¹)
μ	viscosity (Pa·s)
μ_{app}	apparent viscosity (Pa·s)

μ_B	viscosity of the bulk (Pa·s)
μ_G	viscosity of gas (Pa·s)
μ_L	viscosity of liquid (Pa·s)
μ_{water}	viscosity of water ($\text{kg}\cdot\text{m}^{-3}$)
μ_W	viscosity at the wall (Pa·s)
ξ_{gs}	correction factor for gas slug (-)
ξ_{ls}	correction factor for liquid slug (-)
ρ	density ($\text{kg}\cdot\text{m}^{-3}$)
ρ_G	density of gas ($\text{kg}\cdot\text{m}^{-3}$)
ρ_L	density of liquid ($\text{kg}\cdot\text{m}^{-3}$)
ρ_{sludge}	density of activated sludge ($\text{kg}\cdot\text{m}^{-3}$)
ρ_{ip}	two-phase density ($\text{kg}\cdot\text{m}^{-3}$)
ρ_{ips}	two-phase density for the static pressure component ($\text{kg}\cdot\text{m}^{-3}$)
ρ_{water}	density of water ($\text{kg}\cdot\text{m}^{-3}$)
σ	surface tension ($\text{N}\cdot\text{m}^{-1}$)
τ	shear stress (Pa)
τ_0	yield stress (Pa)
τ_w	shear stress at the wall (Pa)
$\tau_{w,gs}$	gas slug shear stress (Pa)
$\tau_{w,ls}$	liquid slug shear stress (Pa)
ϕ	inclination angle (degrees)
φ	weighting factor (-)

Table of contents

Acknowledgments	v
List of symbols and abbreviations	vii
Table of contents	xiii
Chapter 1. Literature Review	1
Introduction.....	1
1.1 Membrane Bioreactors (MBR)	2
1.1.1 MBR technology.....	2
1.1.2 Types of Membrane Bioreactors	2
1.1.3 MBR economics.....	5
1.2 Thermo-physical properties of fluids	7
1.2.1 Density.....	7
1.2.2 Surface tension.....	8
1.2.3 Viscosity	8
1.3 Hydrodynamics of single-phase flow.....	12
1.3.1 Laminar versus turbulent flow	12
1.3.2 Pressure drop and shear stress	13
1.4 Hydrodynamics of two-phase slug flow	18
1.4.1 Flow patterns	19
1.4.2 Two-phase flow in pipes.....	22
1.4.2.1 Slug flow	23
1.4.2.2 Pressure drop	27
1.4.2.2.1 Static pressure drop.....	27
1.4.2.2.2 Frictional pressure drop	28
1.4.3 Energy consumption	30
1.5 Air sparging	31
1.6 Filtration modelling.....	32
1.6.1 Cake layer.....	33
1.7 Mass transfer coefficient.....	36
1.7.1 Determination of the mass transfer for single phase flow	36
1.7.2 Determination of the mass transfer for two-phase flow.....	38
1.8 Heat transfer.....	41
1.8.1 Determination of the heat transfer for single phase flow.....	41
1.8.2 Determination of the heat transfer for two-phase flow	42
1.8.3 Heat-and-mass transfer analogy	45
1.8.3.1 Reynolds analogy.....	46
1.8.3.2 Chilton-Colburn analogy.....	47
1.9 Numerical modelling	48
1.9.1 Multiphase flow modelling	48
1.9.1.1 Mixture model	50
1.9.1.2 Eulerian model	51
1.9.1.3 Volume of Fluid (VOF).....	52
1.9.2 Turbulence modelling of two-phase flow	54
1.9.3 MBR-CFD modelling.....	55
1.10 Experimental techniques for CFD model validation.....	55
1.10.1 Local shear measurement using electrochemical shear probes	56
1.10.2 Flow field velocity by Particle Image Velocimetry (PIV)	56
1.11 Objectives of this work.....	56
1.12 Outline	57
Chapter 2. Gas slug rising velocity in vertical tubes	59
Abstract	59

Introduction.....	60
2.1 Setup description.....	60
2.2 Properties of the fluids.....	62
2.3 Gas slug rising velocity.....	63
2.4 Qualitative behaviour of gas slugs.....	68
2.5 Conclusions.....	70
Chapter 3. Shear stress quantification and relationship with energy consumption in a slug flow	71
Abstract.....	71
Introduction.....	72
3.1 Surface shear stress measurements.....	73
3.2 Shear stress histograms.....	77
3.3 Development of a bi-modal model for shear stress histograms (SSH).....	79
3.4 Optimizing energy consumption.....	84
3.5 Conclusions.....	86
Chapter 4. CFD modelling of a slug flow	89
Abstract.....	89
Introduction.....	90
4.1 Description of the CFD model.....	90
4.2 Grid dependency and surface monitors.....	91
4.3 Slug flow rising velocity.....	96
4.4 Modelled shear stresses near the membrane wall.....	98
4.5 Conclusions.....	101
Chapter 5. CFD modelling of an airlift MBR module.....	103
Abstract.....	103
Introduction.....	104
5.1 Airlift MBR.....	105
5.2 CFD modelling of the bundle of tubes.....	105
5.2.1 Modelling of the porous zone (membrane).....	107
5.2.2 Extrapolation to a membrane module.....	112
5.3 CFD modelling of the air diffusers.....	114
5.3.1 Simulation of the disk aerator.....	117
5.3.2 Simulation of the ring aerator.....	119
5.3.3 Comparison of the air diffusers.....	120
5.4 CFD modelling of the membrane module + air diffusers.....	121
5.5 Conclusions.....	125
Chapter 6. MBR Sludge Rheology.....	127
Abstract.....	127
Introduction.....	128
6.1 Plant description.....	128
6.2 Delft Filtration Characterization method (DFCm).....	129
6.3 Description of different rheometer principles.....	130
6.4 Apparent viscosity calculation.....	131
6.5 Impact of apparent viscosity on pumping.....	139
6.6 Conclusions.....	140
Chapter 7. Heat-and-mass transfer analogy.....	143
Abstract.....	143
Introduction.....	144
7.1 Shear profiles in single phase flow.....	146
7.2 Shear profiles in two-phase flow.....	149
7.3 Practical use of the heat-and-mass transfer analogy: an example.....	154
7.4 Conclusions.....	156
Chapter 8. Hydrodynamic CFD model of a hollow fiber MBR validated with experimental shear stress measurements.....	157

Introduction.....	158
8.1 Description of the setup	158
8.2 Operational conditions	161
8.3 Electrochemical shear measurements	162
8.4 CFD model specification	163
8.4.1 System geometry	164
8.4.2 Boundary and operational conditions	165
8.4.3 Numerical specifications of the CFD model.....	166
8.5 Surface shear measurements.....	167
8.6 Numerical simulations.....	169
8.6.1 Preliminary CFD comparison	172
8.7 Conclusions	174
Chapter 9. Conclusions	175
Introduction.....	175
9.1 Slug flow	175
9.1.1 Gas slug rising velocity	175
9.1.2 Coalescence	176
9.1.3 Shear Stress Histograms (SSH).....	176
9.1.4 CFD model of slug flow	177
9.2 Side-stream (airlift) MBR.....	177
9.2.1 Membrane module	177
9.2.2 Air diffusers.....	178
9.2.3 Combined CFD model.....	178
9.3 MBR sludge rheology	178
9.4 Heat-and-mass transfer analogy	179
9.5 Submerged MBR	180
9.6 Perspectives and future work.....	180
Summary	183
Samenvatting	187
Bibliography.....	191
Curriculum Vitae.....	203

Chapter 1. Literature Review

Introduction

In recent years a number of factors have put conventional wastewater treatment technologies under pressure. A very important factor is the high effluent quality standards imposed by the EU Water Framework Directive (EU-WFD) regarding discharge of pollutants to the water environment. Another factor is an increasing wish that all receiving waters have high water quality, which poses demands on the hygienic quality of effluent water from wastewater treatment plants (WWTP). A third factor is an increasing focus on reuse of treated wastewater in an attempt to close the water cycle. Regarding reuse of treated effluents, the potential benefit is of course highest in countries with serious water scarcity and internationally there are already examples of reuse of treated wastewater for purposes such as irrigation, recreative use (fountains, channels, lakes in parks, etc) and even drinking water. All these drivers have resulted in a strong incentive for the development of new technologies that produce improved effluent quality and at the same time are more cost effective. Membrane bioreactor (MBR) technology appears to be a treatment technology having the potential to fulfil requirements.

An MBR treatment plant is an activated sludge plant where the separation of the activated sludge and the treated effluent is accomplished through a membrane filter instead of sedimentation tank as in Conventional Activated Sludge (CAS) treatment plants. An MBR plant is characterised by an extremely low content of suspended solids in the effluent, as the membrane constitutes an efficient barrier to particles larger than the membrane pore size including pathogens. At the same time, it is possible to operate the process tanks with concentrations of Total Suspended Solids (TSS) which are 3 to 4 times higher compared to those in CAS plants resulting in plants with a smaller footprint. MBR plants are also less sensitive to washing out of microorganisms that are not liable to be incorporated in settleable sludge flocs. Consequently, if MBR plants are operated with very long sludge ages, there will be potential to ensure the presence of microorganisms that can degrade toxic pollutants, that are otherwise non degradable in conventional activated sludge plants.

There are, however, a number of technical process barriers which must be overcome in order for the MBR technology to reach a position as a competitive or even dominating technology for wastewater treatment. One of the most important barriers is the fouling of the membrane, i.e. the accumulation of unwanted material onto the membrane, resulting in a reduction of the membrane area and increase of the TransMembrane Pressure (TMP). Another technical barrier is the relatively high energy consumption of most types of MBR plants, caused by the need of having a constant cross flow of air bubbles along the membrane's surface to avoid build-up of a sludge cake layer on the membrane surface. These barriers still make the MBR technology relatively expensive compared to CAS

resulting mainly in applications in niche areas or in cases where no other alternatives are possible (e.g. space limitation).

The purpose of this work is to develop tools for design and optimization of the current hydrodynamic conditions in MBR systems bearing in mind energy efficiency. A more profound outline of the thesis is given at the end of this chapter.

1.1 Membrane Bioreactors (MBR)

1.1.1 MBR technology

Membrane activated sludge technology is a relative new technology (Judd, 2006), already implemented worldwide on a large scale to treat industrial wastewater, and is considered a key technology to achieve advanced municipal wastewater purification in the future.

The MBR process involves a suspended growth activated sludge system and permits bioreactor operation with higher mixed liquor solids concentrations, typically in the range of 8 to 12 g·L⁻¹. This elevated biomass concentration allows compact design, typically reducing the required footprint of the plant by up to 50%, and allows for highly effective removal of organic compounds and nutrients (carbon, ammonium, phosphorus) in the waste stream (Judd, 2006). The micro-porous membranes act as a barrier for a complete retention of suspended solid particles and pathogens, therefore also achieving disinfection. The problems associated with poor settling of sludge in conventional activated sludge processes are hereby overcome.

The MBR technology is particularly useful for areas with specific reduced space availability, highly concentrated influent, local water scarcity (water reuse application), stringent legislation affecting effluent discharge, area prone to important seasonal variation (touristic zone) and stable effluent quality.

To achieve a successful and sustainable performance, some critical points with regard to MBR operation need to be addressed, such as: adapted pre-treatment (fine screening to remove fibrous material such as hair, grease treatment...), fouling control (back-flushing and periodical chemical cleaning), adapted and sufficient membrane scouring (through aeration) and flow variation control (buffer tank), among others.

1.1.2 Types of Membrane Bioreactors

In waste water treatment processes (WWTP), there are two main steps: the biological removal of organic substances and nutrients and the sludge-water separation. The first step occurs in the bioreactor and for the last step two types of technologies exist: 1) CAS systems

where the separation is brought about by gravity (Figure 1.1a) and 2) MBR systems where the separation is achieved through filtration (Figure 1.1b and c). The latter one has proven to be a good alternative to achieve high effluent quality compared to CAS. There are two types of membrane bioreactors. A first one has the membrane inside the bioreactor and sucks the permeate outside-in, and is commonly known as immersed or submerged membrane bioreactor (iMBR) (Figure 1.1b). The other has the membrane outside the bioreactor and pushes the permeate inside-out, and is termed side-stream membrane bioreactor (sMBR) (Figure 1.1c).

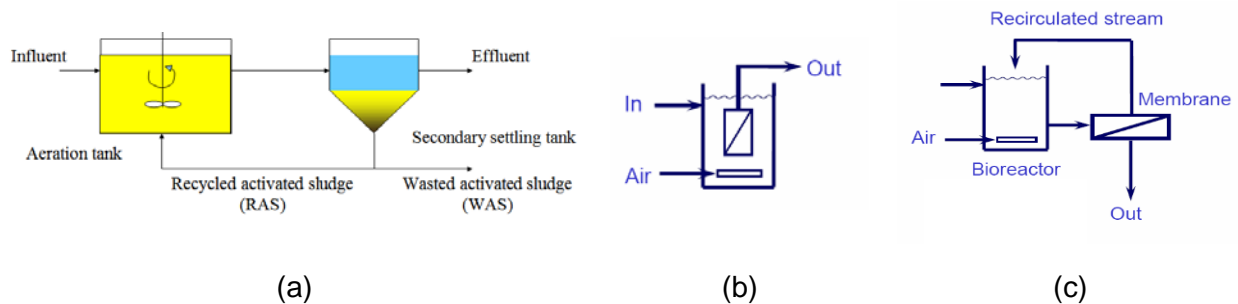


Figure 1.1 Process configurations of (a) a CAS system (Tchobanoglous et al., 2003), (b) an immersed MBR and (c) a side-stream MBR (Judd, 2006)

Side-stream MBR: This type of MBR already has a long application history in industrial applications other than wastewater. Here, membrane modules are located outside the bioreactor and the mixed liquor is pumped into the membrane module. In order to reduce deposition of suspended solids near the membrane surface, a high cross flow velocity is supplied by means of the circulation pump and insertion of air. Although this type of membrane bioreactor is simple, stable and easy to use, it consumes significant amounts of energy due to the use of the circulation pump and insertion of compressed air. Moreover, the excessive shear stress generated by the circulation force and air might lower the activity of the micro-organisms due to stress. The membrane configuration commonly used in this system is the tubular/multitube (MT) membrane. The operational principle is inside-out, which means that the influent goes inside the tube and the permeate (or effluent) flows through the walls (Judd, 2006; Le-Clech et al., 2003).

Immersed MBR: Here, membrane modules are located inside a bioreactor and filtration is obtained by means of a suction pump. A cross flow stream over the membrane surface produced by air bubbling induces a moderate shear stress which generates the back transport of deposited sludge particles from the membrane surface. It is more compact and energy saving because of the low TransMembrane Pressure (TMP) applied and disuse of the circulation pump. This type of membrane bioreactor, therefore, has attracted great attention in the research and application field for wastewater treatment in recent years. The membrane configurations commonly used in this system are hollow fiber (HF) and flat sheet (FS). The operational principle is outside-in, which means that the influent is located outside

(in the bioreactor) and the permeate flows inside the membrane (Judd, 2006; Le-Clech et al., 2003).

The two main advantages of the MBR systems are: 1) excellent and stable effluent quality, including disinfection (Krauth and Staab, 1993) and 2) high solid concentration. This leads to compact design and low sludge production. Due to this, MBRs have received considerable attention in the treatment of municipal wastewater (Judd, 2006).

In MBRs, the aeration is one of the most important parameters in the design and operation, since it is required for bio-treatment, agitation and membrane module scouring (Germain et al., 2007; Judd, 2004; Marrot et al., 2005). However, the effective distribution of the air over the whole module cross-section and length becomes a particular challenge since energy consumption related to membrane aeration represents an important part of the total energy consumption (around 30 – 40 %) (Judd, 2006; Laborie et al., 1998). The design of the aeration system becomes an industrial issue and any reduction of the operational cost is highly sought (Bellara et al., 1996; Cui and Wright, 1996).

As was mentioned before, the main drawback of MBR systems is the membrane fouling, which is caused by the attachment of particles and soluble substances onto the membrane surface. To decrease fouling, MBRs are generally run at lower fluxes (decreasing fouling propensity) and adequate cleaning methods and frequencies (operation and maintenance protocols). This has led to sustainable operating conditions (Brepols et al., 2008; Verrecht et al., 2008). Moreover, to improve the membrane rejection characteristics, the hydrodynamics within the system play an important role for reducing sludge deposition on the membrane surface and prolonging the operating period. Another important factor to consider in the hydrodynamics of the MBRs is the thermo-physical properties of the fluid which also affect the energy consumption, pressure drop, etc (Garcia et al., 2007; Gomez et al., 2000b).

Depending on the application and the desired effluent quality, different competitive technologies exist. The main competing technology is the CAS. If the effluent regulations are not too stringent, usually a CAS system will be economically beneficial as it does not require energy for membrane air scouring. However, one of the main benefits of MBR is its very good and consistent effluent quality (due to membrane separation, which may make it the preferred option for water reclamation or in case of stringent effluent regulations). For a CAS system to reach the same effluent quality, generally tertiary filtration (TF) is required, which adds a significant cost (Cote et al., 2005). Also, aeration demand has come down considerably over the past decade due to improvements in module design. Hence, MBR technology has certainly gained ground in terms of competitiveness compared to CAS. Some other technologies that have been explored to cure restrictions of CAS are:

- The Moving Bed Biofilm Reactor (MBBR): this technology is based on aerobic biofilm growth on carrier elements. These latter provide a large protected surface area for the biofilm to grow. The biofilm that is created around each carrier element protects the bacterial cultures from operating conditions (shear) making the system very robust. Also, the carrier provides a more stable home for the bacteria to grow. Essentially nutrient levels and DO levels are the only control points for the system. These MBBRs are designed also allow nutrient removal (Hem et al., 1994; Lee et al., 2006; Luostarinen et al., 2006; Salvetti et al., 2006).
- Integrated Fixed-film Activated Sludge (IFAS): this technology is based on a fixed film system (different from the MBBR) where the biomass grows. Making the biomass resistant to shock loads and is possible to meet more stringent effluent parameters as is also the case in MBR (Kim et al., 2010; Randall and Sen, 1996).
- Reverse osmosis (RO): this technology is commonly use in drinking water purification from seawater, removing the salt and other substances from the water molecules (Cote et al., 2005).

The two first technologies are comparable to MBR as they produce high effluent quality effluent. However, they do not use coarse bubble aeration (scouring) like in the MBRs. Nevertheless, the main drawbacks are (1) the growth control (homogeneous) over the fixed/moving carrier and (2) the homogeneous air distribution in the carriers to carry out the biological processes. RO is not possible to directly compare with MBR as it serves a very different goal in terms of effluent quality (for drinking water), and obviously that results in a penalty in terms of capital and operation expenditure (capex and opex) (Verrecht et al., 2008).

1.1.3 MBR economics

The costs of MBR and CAS nowadays are rather similar (Chang et al., 2002; Cote et al., 2005) (Figure 1.2c and d). This has been achieved over the years by use of new equipment, designs, membrane types, processes and expertise in MBR technology. The latter is available commercially for a wide range of MBR applications, reducing unit costs up to 30-fold since 1990 (Judd, 2006). Further cost reduction is expected due to technical improvements and the growing demand for production of membranes. A clear decreasing trend in membrane cost (Figure 1.2a) and the overall MBR process cost (Figure 1.2b) could be observed during the last decade. These reductions are due to improvements in process design, improved operation and maintenance and a greater membrane life expectancy.

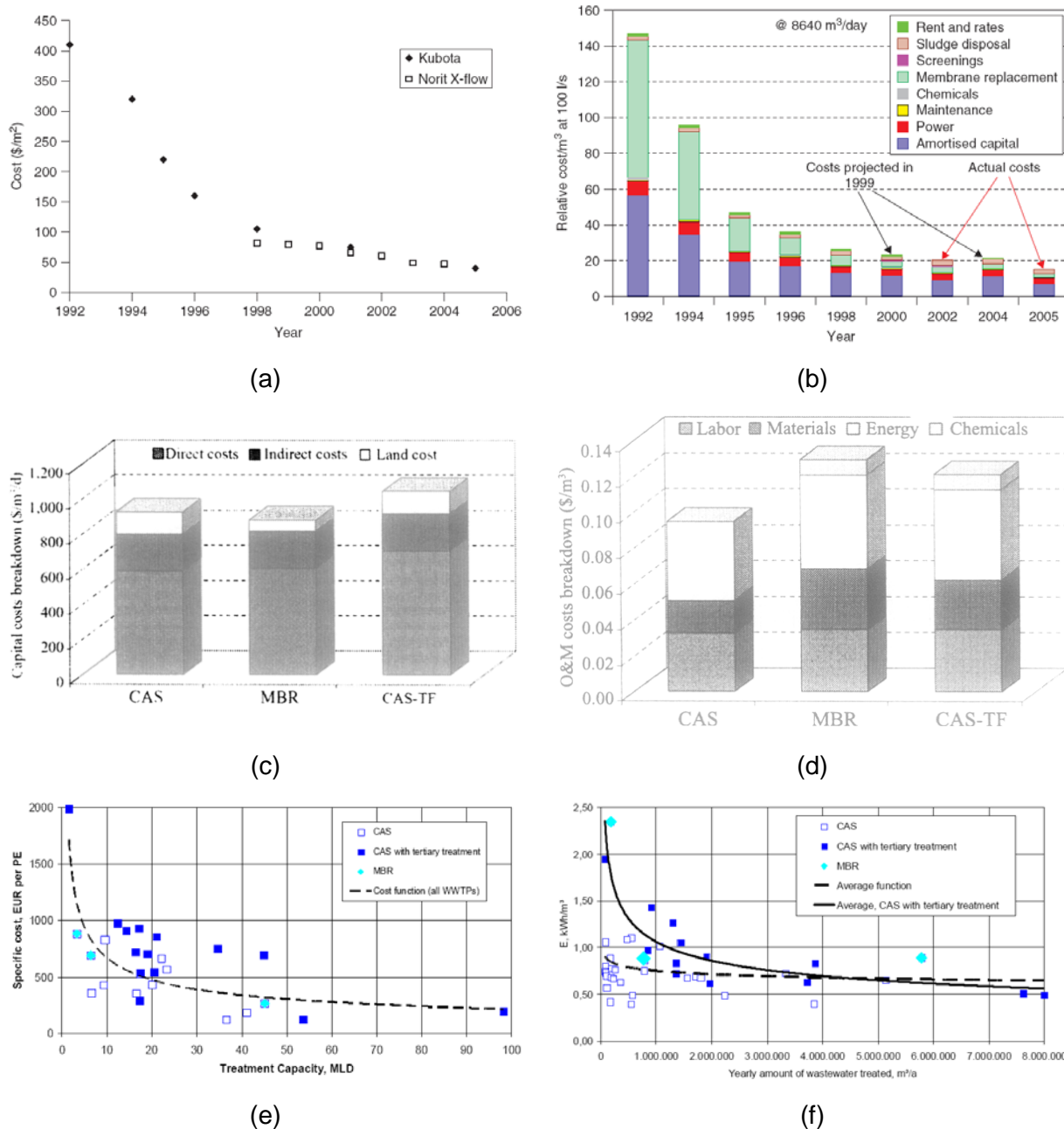


Figure 1.2. (a) Microfiltration membrane replacement costs in US\$ as a function of time, from information provided by 2 membrane manufacturers (Kubota and Norit X-Flow), (b) MBR process costs (Kubota) vs. time (Judd, 2006), comparison of (c) capital and b) operational and maintenance cost for CAS, MBR and CSA-TF (Cote et al., 2005) and comparison of the (e) Investment cost and (f) energy consumption of CAS, MBR and CAS-TF (Brepols, 2009)

Figure 1.2a reveals that the replacement cost of membranes has decreased considerably over the last decade. Figure 1.2b shows how the cost of membrane material have decreases. However, the power fraction (aeration) has remained almost constant and, hence, has become relatively more important. This is why energy optimization forms the next challenge in MBR systems and research in optimizing the gas sparging is a must. Figure 1.2c compares capital costs of MBR, CAS and CAS with tertiary filtration (CAS/TF). Cost are

similar are comparable and, when a similar effluent quality is pursued, the CAS systems requires an additional TF step, which makes the system more expensive. In terms of operational cost (Figure 1.2d), energy consumption is still greater in MBR compared to CAS and even CAS-TF, although differences are not that large. In Figure 1.2e, it is possible to observe a trend that the investment cost in any of the three technologies decreases at higher treatment capacities. However, at low treatment capacities the investment cost of CAS and MBR are similar and the CAS-TF is more expensive. Similarly, looking at Figure 1.2f, there is a decrease in the power consumption at high treated water flows. At low treated water flows, the power consumption is higher for MBR and CAS-TF and lower for CAS, but increasing the treated water, CAS and MBR power consumption is similar and the CAS-TF requires more energy. Hence, this surplus in energy consumption is the incentive of this work to investigate its possible reduction.

1.2 Thermo-physical properties of fluids

The thermo-physical properties of liquids, such as viscosity, density and surface tension, play an important role in the behaviour of bubbles. More precisely, they will affect bubble shape, bubble length, the coalescence of bubbles, bubble rising velocity and pressure drop along a tube in which they are transported (Viana et al., 2003).

1.2.1 Density

The density of water (ρ_{water} , $\text{kg}\cdot\text{m}^{-3}$) is correlated with temperature through (Linstrom et al., 2009):

$$\rho_{water} = 1855.8979 - 1.5664T - \frac{116862.3}{T} \quad (1.1)$$

where T is the absolute temperature (K) and the previous relation is valid for a range from 0 to 100°C (273-373 K).

The density of activated sludge (ρ_{sludge}) is estimated using equation (1.2), as presented in Tchobanoglous et al. (2003).

$$\rho_{sludge} = \rho_{water} + 0.2TSS \quad (1.2)$$

where TSS is the Total Suspended Solids ($\text{g}\cdot\text{L}^{-1}$).

1.2.2 Surface tension

The surface tension (σ , N·m⁻¹) of water-air is correlated with temperature through (Linstrom et al., 2009):

$$\sigma = 0.0950 - 2.5959 \cdot 10^{-7} T^2 \quad (1.3)$$

The previous relation is valid for a range from 0 to 100°C (273-373 K).

1.2.3 Viscosity

Viscosity (μ , Pa·s) is a property that influences the hydraulic regime and transport phenomena. It is defined by the ratio between shear stress (τ , Pa) and shear rate ($\dot{\gamma}$, s⁻¹), as follows:

$$\mu = \frac{\tau}{\dot{\gamma}} \quad (1.4)$$

The viscosity of Newtonian liquids (e.g. water) exhibits a linear shear stress-rate relationship and, hence, a constant viscosity. A temperature dependent relation for the viscosity of water is given by an exponential Arrhenius type relation (Linstrom et al., 2009; Yang et al., 2009):

$$\mu_{water} = 1.2182 \cdot 10^{-6} \exp\left(\frac{16440.4488}{R_{gas} T}\right) \quad (1.5)$$

where R_{gas} is the universal gas constant (= 8.3145 J·K⁻¹·mol⁻¹) and the previous relation is valid for a range from 0 to 100°C (273-373 K).

Activated sludge exhibits complex flow behaviour and is called a non-Newtonian liquid. The rheological properties related with non-Newtonian liquids are complex and they have a substantial importance in industrial applications relating to handling, transportation and processing. Also, it allows designing equipment for mixing, dispersing, pumping, etc, and therefore, a characterization of this liquid property is important. This characterization is based on the measurement of the absolute viscosity which depends on the deformation (shear) rate and more specifically the relation between the shear stress and shear rate. For non-Newtonian fluids several power-law relationships (Figure 1.3) between shear stress and shear rate have been proposed. They are summarized in Table 1.1.

Table 1.1. Different widely used non-Newtonian shear stress-rate relationships.

Fluid	Relationship shear stress-rate
Shear-thinning (pseudoplastic) ($n < 1$) Shear-thickening (dilatant) ($n > 1$)	$\tau = k\dot{\gamma}^n$
Herschel – Bulkley ($0 < n < \infty$)	$\tau = \tau_0 + k\dot{\gamma}^n$
Bingham plastic ($n = 1$)	$\tau = \tau_0 + k\dot{\gamma}$

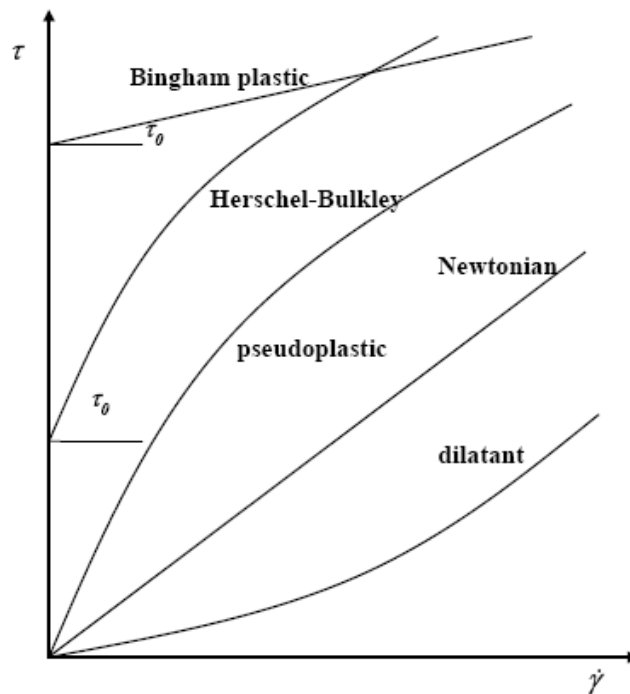


Figure 1.3. Non-Newtonian rheological models (De Clercq, 2003).

In Table 1.1, τ_0 is the yield stress (Pa), n is the flow behaviour index (-) and k is the flow consistency index (Pa·s ^{n}).

Activated sludge exhibits a pseudoplastic (non-Newtonian) behaviour and obeys a power-law relationship (Laera et al., 2007; Pollice et al., 2007; Rosenberger et al., 2006), where the shear stress is defined by:

$$\tau = k\dot{\gamma}^n \quad (1.6)$$

Replacing equation (1.6) in (1.4) results in an apparent viscosity (μ_{app}) which depends on the shear rate:

$$\mu_{app} = k\dot{\gamma}^{n-1} \quad (1.7)$$

For MBR activated sludge Rosenberger *et al.* (2006) and Pollice *et al.* (2007) proposed empirical models for k and n as a functions of TSS :

$$k = a_1 \exp(a_2 TSS^{a_3}) \quad (1.8)$$

$$n = 1 - a_4 TSS^{a_5} \quad (1.9)$$

where a_1 , a_2 , a_3 , a_4 and a_5 are fitting parameters. Reported values are summarized in Table 1.2.

Table 1.2. Parameters for equations (1.8) and (1.9) reported in literature

Parameters	Rosenberger <i>et al.</i> (2006)	Pollice <i>et al.</i> (2007)
a_1 (Pa s)	0.001	0.001
a_2 (-)	2.000	0.882
a_3 (-)	0.410	0.494
a_4 (-)	0.230	0.050
a_5 (-)	0.370	0.631

From Table 1.2, it is possible to observed that the coefficients are different, which means that heterogeneity of sludge, particle size (Petersen *et al.*, 2008), etc may play an important role in sludge rheology besides the TSS . However, since the model is over-parameterized, also the calibration procedure followed can have a significant impact.

Other studies have looked into using surrogates for activated sludge that behave in a similar fashion, or at least, exhibit the same rheological behaviour (pseudoplastic). Popular compounds are xanthan gum and carboxymethyl cellulose (CMC) (Buetehorn *et al.*, 2010; Rosenberger *et al.*, 2001). In Figure 1.4 a comparison of viscosity between xanthan gum (Buetehorn *et al.*, 2010), CMC (Benchabane and Bekkour, 2008) and the activated sludge model of Rosenberger *et al.* (2006) is shown.

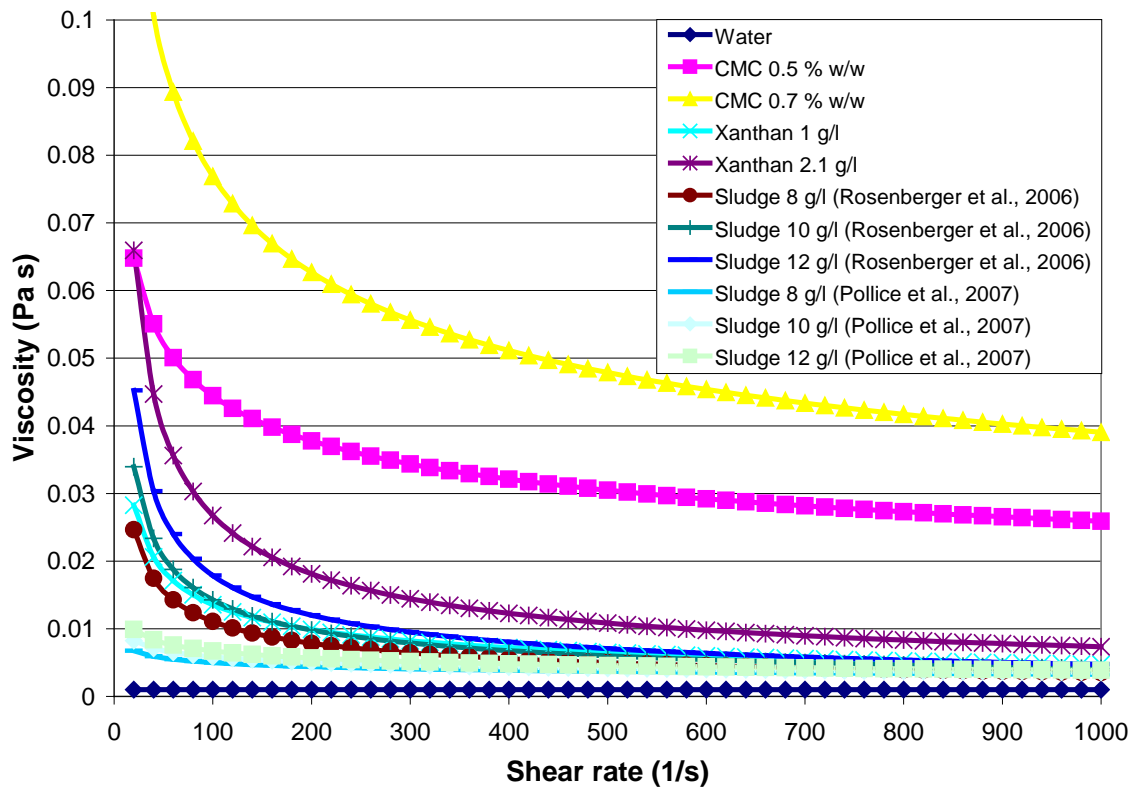


Figure 1.4. Viscosities of water, xanthan, CMC and activated sludge

The rheological properties of each compound are summarized in Table 1.4.

Table 1.4. Rheological properties of activated sludge and two popular surrogates

	CMC*		Xanthan gum**		Activated sludge***		
	0.5 % w/w	0.7 % w/w	1 g·L ⁻¹	2.1 g·L ⁻¹	8	10	12
TSS (g·L ⁻¹)					8	10	12
k (Pa s)	0.131	0.298	0.111	0.354	0.109	0.171	0.255
n	0.766	0.706	0.544	0.439	0.504	0.461	0.423

* (Benchabane and Bekkour, 2008)

** (Buetehorn et al., 2010)

*** (Rosenberger et al., 2006)

From Figure 1.4 and Table 1.4, it is possible to observe that three compounds (CMC, xanthan gum and activated sludge) have a pseudoplastic behaviour. Looking closely at the xanthan gum, it provides a better match to the rheological behaviour of activated sludge rather than CMC. However, CMC has been extensively used in research PIV (Particle Image Velocimetry) systems (Sousa et al., 2005; Sousa et al., 2007) and with shear probes

(Dumont et al., 2002) unlike Xanthan. The resemblance of CMC as a surrogate for sludge for validation is a huge assumption that needs to be borne in mind when interpreting the behaviour, as can be seen from the qualitative behaviour of rising bubbles. In terms of rheological properties, xanthan gum seems to be more similar to sludge (Buetehorn et al., 2008). However, this compound was not yet used with PIV and shear probes measurements.

1.3 Hydrodynamics of single-phase flow

The transport of a fluid (liquid or gas) in tubes or pipes with a circular cross section (or duct if it is not round) is extremely important in our daily lives. E.g. in our body, the veins and arteries that carry blood and air; in our homes, the water pipes that deliver water from the city well to the house; in our vehicles and machines, hoses and pipes carry hydraulic fluid or other fluids to various components. The air quality within our buildings is maintained at comfortable levels by the distribution of conditioned air (heated, cooled, humidified, etc) through pipes and ducts, etc. Although all of these systems are different, the fluid-mechanical principles governing the fluid motion are common. There are two types of flow: pipe flow and open-channel flow. For the flows involved in this section, it is assumed that the pipe is completely filled with the fluid being transported (pipe flow). Therefore, open-channel flow is not considered further in this study.

1.3.1 Laminar versus turbulent flow

The flow regime of a fluid in a pipe may be either laminar, transitional or turbulent. The regime depends on the Reynolds number (Re), which is a dimensionless number. For pipe flow, this is the most important dimensionless parameter. It is the ratio of the inertial to viscous effects in the flow. This number is defined as follows (White, 2002):

$$Re = \frac{\rho u d}{\mu} \quad (1.10)$$

where u is the average velocity ($\text{m}\cdot\text{s}^{-1}$) and d is the hydraulic diameter (m), which for pipe flow is the same as the tube diameter. The Re ranges for which laminar, transitional, or turbulent pipe flows are obtained cannot be precisely given. The actual transition from laminar to turbulent flow may take place at different Reynolds numbers, depending on how much the flow is disturbed by vibrations of the pipe, roughness of the entrance region, etc. For design purposes the following values are typically used. The flow is laminar if the Reynolds number is less than 2100 and turbulent if the Reynolds number is larger than approximately 4000. For Reynolds numbers between these two limits, the flow may switch between laminar and turbulent conditions and is defined as the transition regime (Travis and Mays, 2007; White, 2002).

1.3.2 Pressure drop and shear stress

Fully developed steady flow in a constant diameter pipe may be driven by pressure forces and/or gravity, depending on the inclination of the pipe. For horizontal pipe flow, gravity has no effect except for a hydrostatic pressure variation across the pipe, which is usually negligible. The pressure difference between two sections of the horizontal pipe forces the fluid flow through the pipe. Viscous effects provide the restraining force that exactly balances the pressure force, thereby allowing the fluid to flow through the pipe with no acceleration. If viscous effects were absent in such flows, the pressure would be constant throughout the pipe, except for the hydrostatic variation. In non-fully developed flow regions, such as the entrance region of a pipe, the fluid accelerates or decelerates as it flows.

The nature of the pipe flow is strongly dependent on whether the flow is laminar or turbulent. This is a direct consequence of the differences in the nature of the shear stress in laminar and turbulent flows. The shear stress in laminar flow is a direct result of momentum transfer among the randomly moving molecules (a microscopic phenomenon). The shear stress in turbulent flow is largely a result of momentum transfer among the randomly moving, finite-sized bundles of fluid particles (a macroscopic phenomenon). The net result is that the physical properties of the shear stress are quite different for laminar flow compared to turbulent flow. Figure 1.5 shows a control volume for an inclined pipe section.

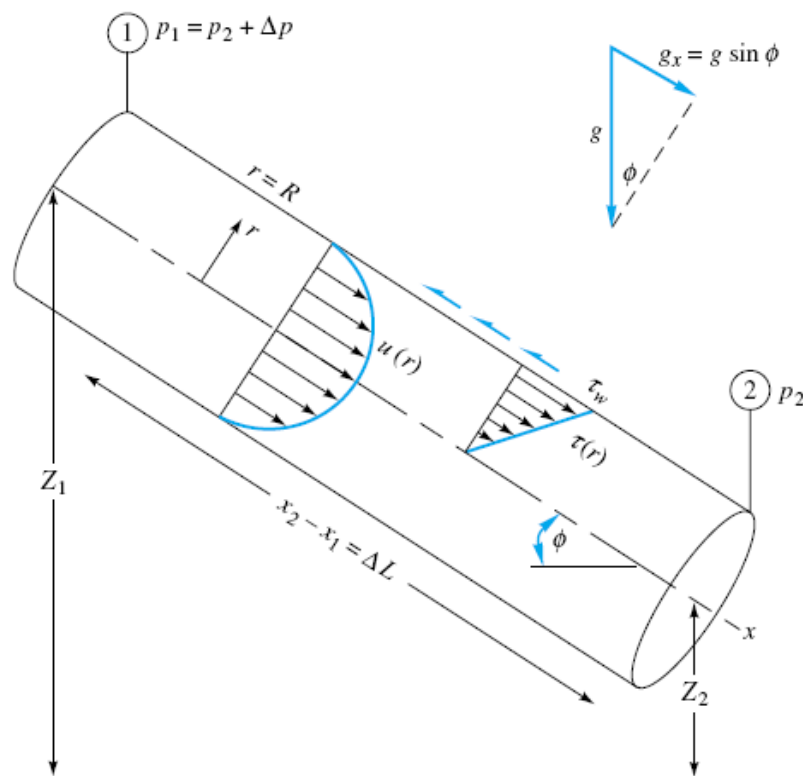


Figure 1.5. Control volume of steady, fully developed flow between two sections in an inclined pipe (White, 2002).

The pressure drop (Δp , Pa) in Figure 1.5 is defined by:

$$\Delta Z \rho g + \Delta p = \frac{4 \tau_w \Delta L}{d} = f \frac{\Delta L \rho u^2}{d} \quad (1.11)$$

where ΔZ is the height (m) difference ($Z_1 - Z_2 = \Delta L \sin \phi$), ΔL is the section length (m), ϕ is the inclination angle (degrees), g is the gravity acceleration ($= 9.81 \text{ m}\cdot\text{s}^{-2}$), τ_w is the shear stress at the wall (Pa) and f is the Darcy friction factor (dimensionless) (Darcy friction factor is 4 times larger than the Fanning friction factor). Rewriting equation (1.11) in terms of length results in:

$$\Delta Z + \frac{\Delta p}{\rho g} = \frac{4 \tau_w \Delta L}{\rho g d} = f \frac{\Delta L u^2}{d 2 g} \quad (1.12)$$

The friction factor expresses the linear relationship between mean flow velocity and pressure gradient, as follows:

$$f = \frac{2 d \Delta p}{\Delta L \rho u^2} = \frac{8 \tau_w}{\rho u^2} \quad (1.13)$$

The friction factor for a fluid flowing in a tube is defined as a function of the Reynolds number and the tube roughness (ε , dimensionless). It can be calculated from the Moody diagram (Figure 1.6).

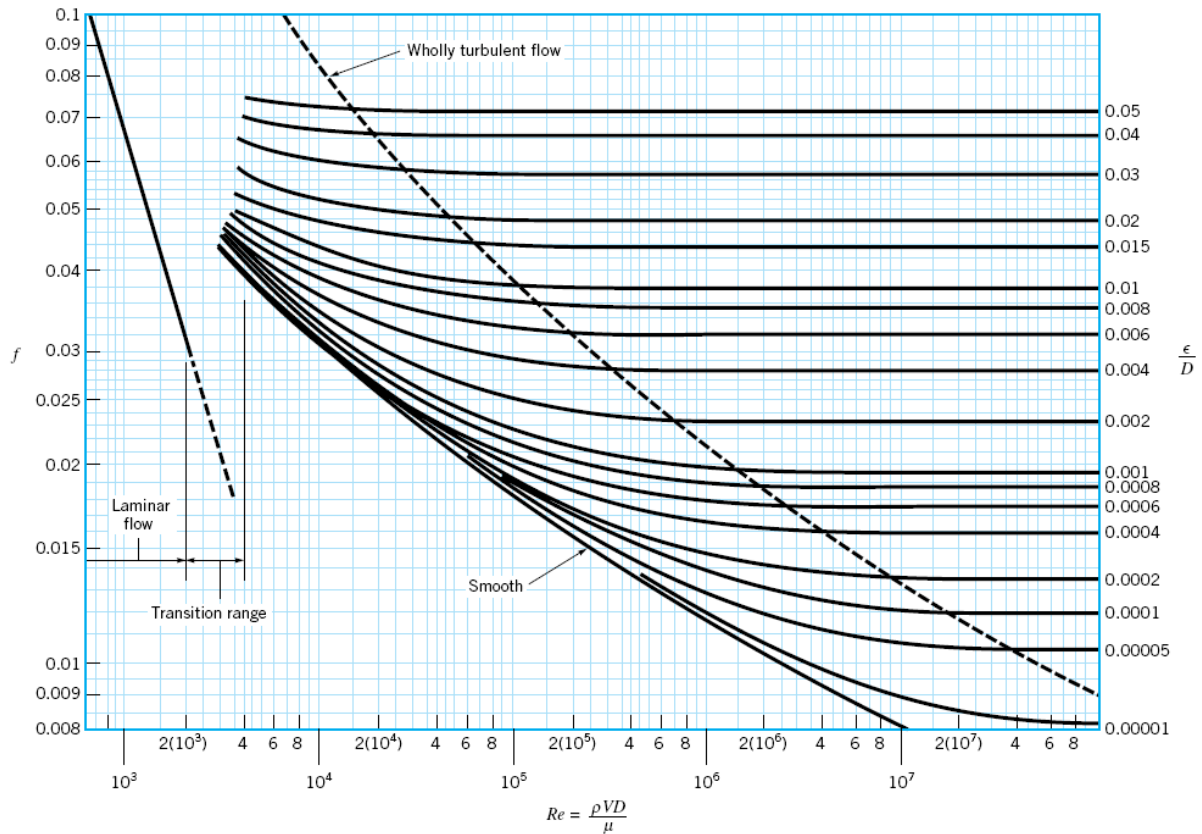


Figure 1.6. Moody diagram (White, 2002)

Analytical equations for the Moody diagram exist and depend on the fluid flow regime. According to the flow regime, the friction factor is defined by:

$$\text{Laminar (Re} < 2000\text{):} \quad f_{lam} = 64 Re^{-1} \quad (1.14)$$

$$\text{Turbulent (Re} > 4000\text{):} \quad f_{tur} = \frac{0.25}{\left[\log_{10} \left(\frac{\varepsilon}{3.7d} + \frac{5.74}{Re^{0.9}} \right) \right]^2} \quad (1.15)$$

The friction factor is not defined in the transition zone ($2100 < Re < 4000$) as it oscillates between laminar and turbulent regime. Therefore, a weighted function can be developed (Cheng, 2008; Yen, 2002). First, it can be assumed that in the transition between laminar and turbulent flows, the variation of the friction factor is composed of a laminar and a turbulent component. Therefore, it is suggested that the friction factor is given by:

$$f = f_{lam}^{\varphi} f_{tur}^{1-\varphi} \quad (1.16)$$

where φ is the weighting factor. Yen et al. (2002) developed a probability conjecture, where φ can be considered the probability of the effect of the laminar component on the friction, and $1-\varphi$ the probability of the contribution of the turbulent component. Evidently, the flow remains in the laminar regime at $\varphi=1$ and switches to turbulent regime at $\varphi=0$. As a result, φ is somehow related to the mechanism of intermittency and depends on the Reynolds number. This weighted factor can be defined as:

$$\varphi = \frac{1}{1 + \left(\frac{Re}{Re_{int}}\right)^m} \quad (1.17)$$

where Re_{int} is an intermediate Reynolds number for the weighting factor and m is an exponent. The values for Re_{int} and m are 2720 and 9 respectively (Cheng, 2008). A comparison between the friction factors of equations (1.14) and (1.15) with (1.16) is presented in Figure 1.7.

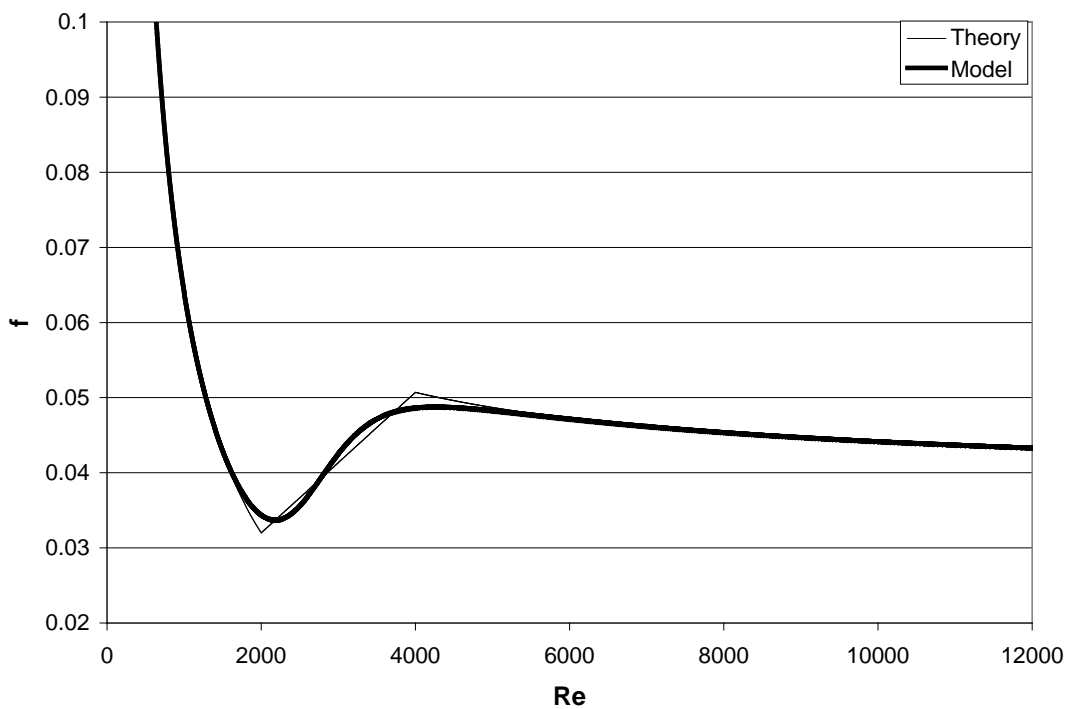


Figure 1.7. Reynolds numbers vs friction factor using the theoretical equation (equations 1.14) and (1.15)) and the model proposed by Cheng (2008) in equation (1.16)

The previous analysis is only valid for Newtonian fluids. As mentioned before activated sludge exhibits non-Newtonian behaviour. Therefore, some modifications are needed regarding the viscosity. The shear rate at the wall surface ($\dot{\gamma}_w$) for a liquid flowing in a pipe can be calculated using equation (1.18) (Coulson and Richardson, 2002).

$$\dot{\gamma}_w = \left(\frac{3n+1}{4n} \right) \left(\frac{8u}{d} \right) \quad (1.18)$$

Substituting equation (1.18) in (1.7), the apparent viscosity near the wall becomes:

$$\mu_{app} = k \left(\frac{3n+1}{4n} \right)^{n-1} \left(\frac{8u}{d} \right)^{n-1} \quad (1.19)$$

The non-Newtonian Reynolds number, also known as Reynolds number of Metzner and Reed (Re_{MR}) (Coulson and Richardson, 2002) is defined as:

$$Re_{MR} = \frac{\rho u d}{\mu_{app}} \quad (1.20)$$

The friction factor for non-Newtonian liquids is defined by:

$$\text{Laminar } (Re_{MR} \leq Re_{MR,c}): \quad f_{lam} = 64 Re_{MR}^{-1} \quad (1.21)$$

$$\text{Turbulent } (Re_{MR} \geq Re_{MR,c}): \quad f_{tur} = 0.3168 n^{0.675} Re_{MR}^{-0.25} \quad (1.22)$$

And the critical Reynolds number ($Re_{MR,c}$) is defined by:

$$Re_{MR,c} = \frac{6464 n (2+n)^{\frac{2+n}{1+n}}}{(3n+1)^2} \quad (1.23)$$

When n is equal to 1, the critical Reynolds number is 2100, as for the transition from laminar to turbulent for Newtonian fluids.

1.4 Hydrodynamics of two-phase slug flow

Multiphase flow is the simultaneous flow consisting of more than one phase or component, like gas, liquid or solid in any combination. The multiphase flow regime groups in five types: gas-liquid, liquid-liquid, liquid-solid, gas-solid and three phases flow mostly. This work focuses on gas-liquid flow. These types of flows are important in industrial applications: oil-gas, chemical, civil and nuclear industries, food manufacturing, waste water treatment among others. Since different phases distribute and affect each other in very complicated ways, it is very tough to predict the behaviour of multiphase flow. Common problems include: (1) the calculation of the pressure loss and liquid holdup in the pipeline in tubing, gathering and separation system design, (2) sizing of gas lines, (3) heat exchanger design, and (4) condensate line design (Takeshima et al., 2002).

Multiphase flows are common in nature but the understanding is still rather limited resulting in increased research nowadays. There are two types of topologies in multiphase flow: 1) disperse flow, when bubbles, drops or particles spread out on a continuous phase and 2) separate flows, when two or more continuous fluids are separated by defined interfaces. The way to approach these type of flows can be threefold: 1) experimentally, which can only be done in a lab-scale under specific conditions to produce specific results; however, scale-up is not completely reliable and measurement techniques that are currently available, but are expensive, could be limiting 2) theoretically, based on equations and correlation from experimental work and 3) computationally, which links to the theoretical approach and allows to solve numerically a set of partial differential equations that describe the multiphase flow. These three approaches can be linked to have a successful modelling and simulation based on experimental data.

The most unique characteristic of multiphase flow is phase distribution, which is very difficult to be characterized and predicted due to the existence of moving interphases-boundaries and turbulence. Almost all current models are based on the concept of flow regimes. For a specific system, the flow regime needs to be predicted by flow maps or flow regime transition theory. Then different flow models are used for the prediction of pressure drop and other parameters. The disadvantage of these models is that they create discontinuities and may induce divergence problems across the transition regions as the result of switching from one flow model to another. To avoid this problem, the interpolation technique or some special criteria can be used (Gomez et al., 2000a).

The current methodology of multiphase flow modelling falls into three categories: empirical correlations, mechanistic models and numerical models. Empirical correlations develop simplified relations between important parameters which must be evaluated by experimental data. The empirical correlations do not address any physical phenomena and behave like a black box. They can yield excellent results but their application is limited to the conditions that were used in the experiments that were used to derive them. Mechanistic models approximate the physical phenomenon by taking into consideration the most important processes and neglecting other less important effects that can complicate the problem but

do not add accuracy considerably. Numerical models introduce multi-dimensional Navier-Stokes (NS) equations for multiphase flow. More detailed information can be obtained from numerical models such as distribution of phases, dynamic flow regime transition and turbulent effects. On the other hand, both the empirical, mechanistic and numerical models have to utilize some inputs based on correlations due to the limitations of the current knowledge.

Another important phenomenon making up the complexity of multiphase flow is that the gas phase tends to flow faster than liquid phase which is called slippage. The slippage effect makes the mixing fluid properties dependent on flowing conditions, fluid properties and pipe geometry. Therefore, there is no way to obtain the fluid properties for the mixture of liquid and gas using simple methods.

It is important to consider some characteristics of the flow before developing a two-phase model: 1) The flow patterns; 2) flow rates (velocities); 3) geometry (length, inclination, diameter and roughness of the pipe); 4) the hold-up of each phase and their relative velocity; 5) pressure drop along the tube and 6) thermo-physical properties of the phases (viscosity, surface tension, density for liquid and gas) (Fabre and Line, 1992).

1.4.1 Flow patterns

The flow patterns depend on the flowing conditions, fluid properties and pipe geometries. However, flow patterns are a subjective and qualitative concept. There is no way to incorporate it into mathematical equations as a parameter. The predicted results usually show some discontinuity between different patterns which in reality are smooth and continuous. For co-current upflow of gas and liquid in a vertical tube, the liquid and gas distribute themselves in specific flow structure. These are known as flow patterns and they can be classified in four flow regimes: bubbly flow, slug flow, churn flow and annular flow. Figure 1.8 illustrates these types of flow patterns for both Newtonian and non-Newtonian liquids.

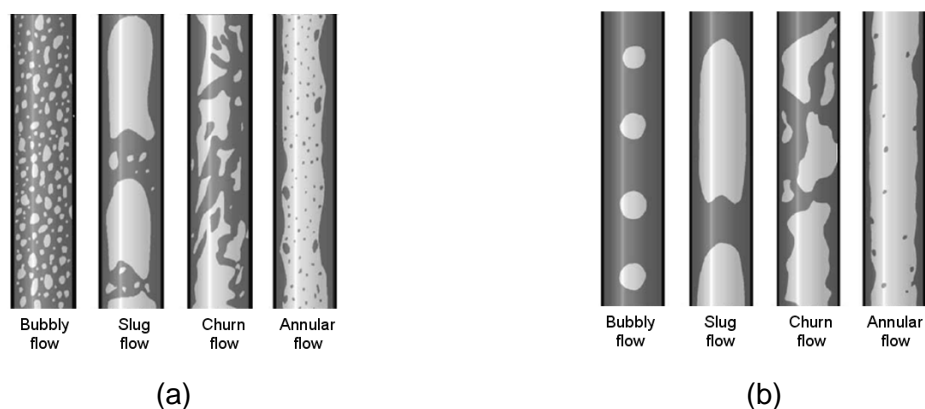


Figure 1.8. Vertical two-phase flow patterns: bubbly, slug, churn and annular flow for (a) Newtonian and (b) non-Newtonian liquids (Dziubinski et al., 2004).

A brief description of the flow patterns is presented below (Cheng et al., 2009). The order is that of increasing gas flow rate.

Bubbly flow: In this flow pattern, the gas is dispersed in the form of discrete bubbles in the continuous liquid phase. The bubbles vary in size and shape and they are much smaller than the tube diameter.

Slug flow: In this flow pattern, there is an increase in the gas void fraction (high gas flow rate), which reduces the distance between the bubbles and promotes coalescence to form large bubbles, which are similar in dimension to the tube diameter. These bubbles have a shape similar to a bullet with a hemispherical nose and a blunt tail, and are also referred to as Taylor bubbles (or gas slugs). The gas slugs are separated from one another by a liquid slug and from the tube wall by a thin liquid film which flows downward; even if the flow is going upward.

Churn flow: In this flow pattern, due to the high liquid and gas velocity, the structure of the flow becomes unstable with the flow travelling up and down in an oscillatory way but with the net upward flow. This instability is due to the gravity and shear forces acting in opposite direction on the thin liquid film of the gas slugs.

Annular flow: In this flow pattern, once the interfacial shear of the high velocity gas on the liquid film becomes dominant over the gravity, the liquid is expelled from the center of the tube to the wall, and it flows as a thin film on the wall forming an annular ring of liquid, while the gas flows as a continuous phase in the middle of the tube.

The models for bubbly flow and annular flow are more developed than those for slug flow and churn flow, because in the last two patterns, a highly irregular interface with a strong unsteady nature is apparent. However, slug flow appears in a very wide range of flowing conditions and is very common (e.g. wellbores). The pseudo-periodical character of slug flow has attracted so many researchers to study it using various methods including correlations, one-dimensional mechanistic methods (Barnea and Taitel, 1993; Fernandes et al., 1983) to multi-dimensional exact solution of continuum equations and momentum equations (Anglart and Podowski, 2002; Clarke and Issa, 1997; Kawaji et al., 1997; Mao and Dukler, 1989). This work tries to elucidate the application of this specific flow pattern for WWTP.

Vertical two-phase flow pattern maps have been developed in literature for water-air as a function of the superficial momentum fluxes for liquid (G_L) and gas (G_G) which are defined as follows:

$$G_L = \rho_L u_{SL}^2 \quad (1.24)$$

$$G_G = \rho_G u_{SG}^2 \quad (1.25)$$

where u_{SL} and u_{SG} are the liquid and gas superficial velocities respectively and the subscripts L and G stand for liquid and gas, respectively. Figure 1.9a shows the flow pattern as a function of the superficial momentum fluxes.

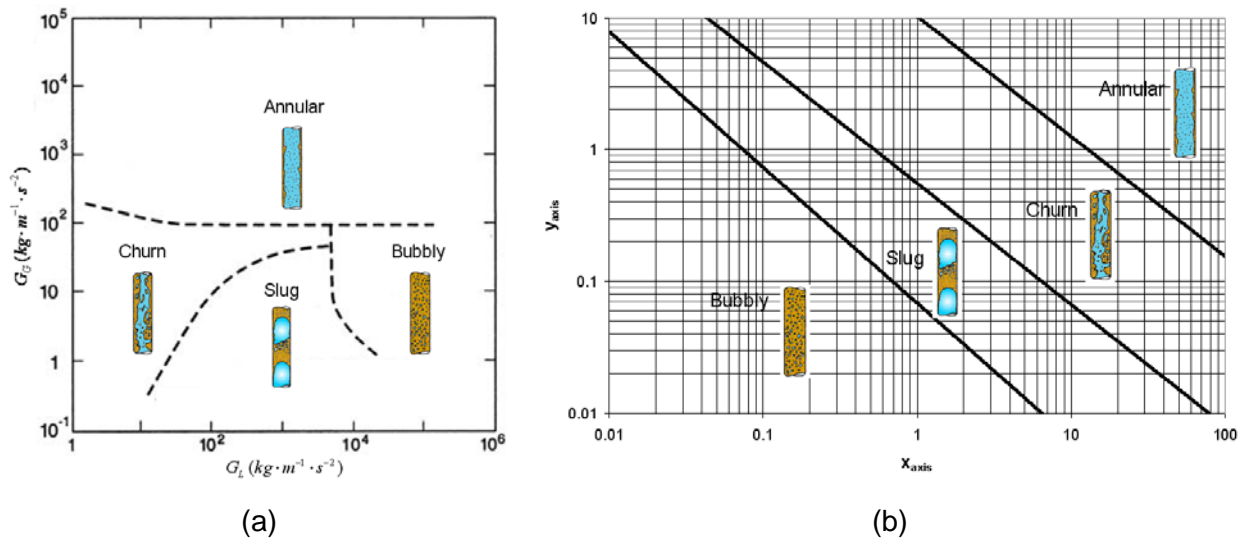


Figure 1.9. Flow pattern map for vertical pipes for (a) Newtonian (Cheng et al., 2009) and (b) non-Newtonian (Dziubinski et al., 2004) liquids.

The flow patterns map for non-Newtonian liquids have not received a lot of attention and only maps for horizontal tubes with non-Newtonian liquids have been developed (Chhabra and Richardson, 1984). Nevertheless, the importance to determine the flow pattern in a specific combination of gas and non-Newtonian liquid is rising nowadays. Dziubinski et al. (2004) proposed the following set of equations to determine the flow pattern map for non-Newtonian liquids in vertical pipes (Figure 1.9b):

The x- and y-axis are defined by:

$$x_{axis} = \frac{u_{SG}}{u_{SL}} \left(\frac{\rho_G \rho_{water}}{\rho_{air} \rho_L} \right)^{0.5} \quad (1.26)$$

$$y_{axis} = u_{SL} \left(\frac{\rho_L}{\rho_{water}} \right)^{0.5} \quad (1.27)$$

The boundaries are defined as:

- Between bubbly and slug flow:

$$y_{axis} = 0.0685 x_{axis}^{-1.03} \quad (1.28)$$

- Between slug and churn flow:

$$y_{axis} = 0.556 x_{axis}^{-0.92} \quad (1.29)$$

- Between churn and annular:

$$y_{axis} = 10.25 x_{axis}^{-0.91} \quad (1.30)$$

Dziubinski et al. (2004) found that: 1) during the two-phase flow of non-Newtonian liquids, the same flow patterns exist; 2) solid particles (<18 % wt.) had no significant effect on the type of flow pattern; 3) The non-Newtonian features of liquids had a negligible effect on the type of the two-phase flow structure. The most important appeared to be the superficial velocities of liquid and gas flow; 4) liquid apparent viscosities higher than 0.001 Pa·s had an effect on the behaviour of the flow pattern.

1.4.2 Two-phase flow in pipes

The science of multiphase flow has undergone significant changes, especially in recent years with the advancement of experimental facilities and numerical calculations (Barnea and Taitel, 1993). Empirical and mechanistic models are available for the prediction of pressure drop and liquid holdup of multiphase flow (Barnea and Taitel, 1993; Fernandes et al., 1983; Gomez et al., 2000; Mao and Dukler, 1985; Thome, 2008). To date, more and more models have been introduced for the modification of prediction accuracy. It is generally believed that mechanistic models performed well against experimental data (Thome, 2008). In this section, the modelling of various mechanisms is reviewed according to flow regimes.

1.4.2.1 Slug flow

This study focuses on the slug flow pattern. In the latter, three distinctive zones can be distinguished (Figure 1.10): 1) the falling film zone, where the bubble is passing, 2) the wake zone, which is just behind the bubble (here, mixing between the liquid and the gas takes place) and 3) the liquid slug zone (Ghosh and Cui, 1999).

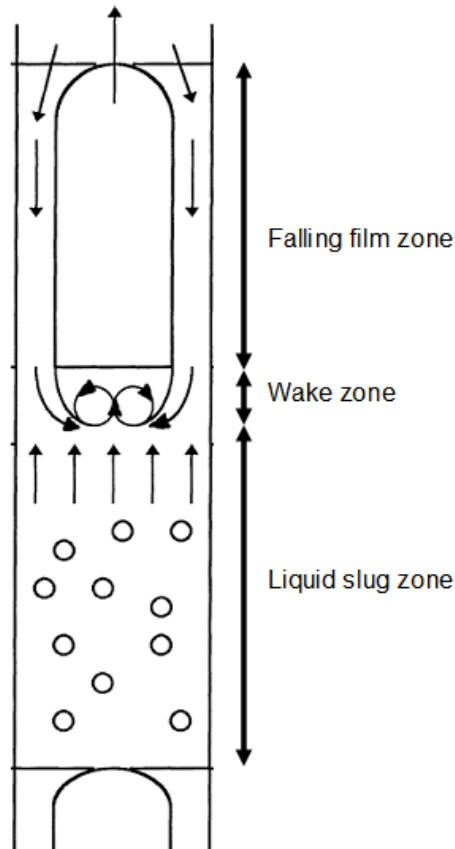


Figure 1.10. Illustration of the different zones in a slug flow (Ghosh and Cui, 1999)

An important factor to consider is the gas slug flow rising velocity. This rising velocity is important because it affects the velocity field due to the slippage of the phases and pressure drop. A great deal of research has been performed to determine this parameter (Bugg and Saad, 2002; Collins et al., 1978; Dziubinski et al., 2003; Nogueira et al., 2006a; Nogueira et al., 2006b; Pinto et al., 1998; Pinto et al., 2001; Sousa et al., 2005; Sousa et al., 2007). There seems to be consensus on the validity of equation (1.31) to estimate the velocity (u_{TB}) of rising gas slugs (Polonsky et al., 1999; van Hout et al., 2002).

$$u_{TB} = C u_m + u_0 \quad (1.31)$$

where the first term on the right hand side is related to the bubble rising in a moving liquid and the second term (u_0) is related to the bubble rising in a stagnant liquid. For the first

term, u_m is the mixture velocity ($u_{SL} + u_{SG}$) and the parameter C depends on the velocity profile of the liquid upstream of the rising bubble.

The value of C has been reported to be 2 for laminar ($Re_m < 2100$) and 1.2 for turbulent flow ($Re_m > 4000$) conditions (Frechou, 1986). In the transition zone, Frechou (1986) reported that the value of C can be estimated using equation (1.32).

$$C = 1 + \frac{0.80}{1 + 10^{-8} Re_m^{2.55}} \quad (1.32)$$

where Re_m is the mixture Reynolds number defined by:

$$Re_m = \frac{\rho_L u_m d}{\mu_L} \quad (1.33)$$

where μ_L is the liquid viscosity (or μ_{app} is the apparent viscosity for non-Newtonian liquids). The value of u_0 can be estimated using equation (1.34) (Viana et al., 2003).

$$u_0 = k_{TB} \left(g d \frac{(\rho_L - \rho_G)}{\rho_G} \right)^{0.5} \quad (1.34)$$

where k_{TB} is a constant function of the Froude number (Fr).

$$Fr = \frac{u_0}{(g d)^2} \quad (1.35)$$

The value for k_{TB} has been reported to be between 0.33 and 0.36 (Clift et al., 2005; Funada et al., 2005; Viana et al., 2003). A value of 0.345 for k is commonly used (Omebere-Iyari and Azzopardi, 2007).

For non-Newtonian fluids, the value of C is modified as a function of the flow behaviour index (Fidos et al., 2008) as follows:

$$C = \frac{3n+1}{1+n} \quad (1.36)$$

Therefore, when $n = 1$ in the case of Newtonian fluids, C is 2 which corresponds to laminar regime. Normally non-Newtonian processes are operating under laminar flow.

The hydrodynamic model of slug flow has already been reported in literature (Chang and Fane, 2000; Fabre and Line, 1992; Fernandes et al., 1983; Mao and Dukler, 1985). The model assumes that the slug flow is axisymmetric, one-dimensional and steady (Figure 1.11). It is based on closure of mass balances and liquid-gas velocities described next (Chang and Fane, 2000).

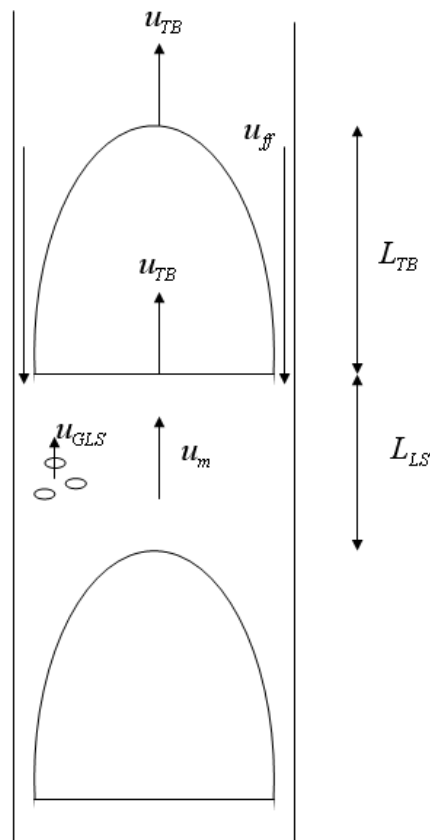


Figure 1.11. Velocities in a slug flow unit.

The velocity of gas in a liquid slug (u_{GLS}) is a function of the mixture velocity and is defined by:

$$u_{GLS} = u_m + 1.53 \left[\frac{\sigma(\rho_L - \rho_G)}{\rho_L^2} \right]^{0.25} \quad (1.37)$$

The velocity of the falling film (u_{ff}), assuming that it contains no gas and the gas slug has a cylindrical shape, is defined by:

$$u_{ff} = 9.916 \left[g d (1 - \alpha_{TB}^{0.5}) \right]^{0.5} \quad (1.38)$$

where α_{TB} is the void fraction of the slug flow. The gas/liquid volume entering the system in unit time is equal to the sum of gas/liquid volume being carried by the slug unit as is defined by (mass balance):

$$\frac{u_{SG}}{u_m} = \beta \alpha_{TB} \quad (1.39)$$

where β is in the ratio of the gas slug to the sum of the gas and liquid slug:

$$\beta = \frac{L_{TB}}{L_{TB} + L_{LS}} \quad (1.40)$$

where L_{TB} and L_{LS} are the length of the gas and liquid slug respectively.

For the liquid phase, the rate of liquid flow approaching the nose from the slug equals that being directed to the falling film:

$$\frac{u_{TB} - u_m}{u_{TB} + u_{ff}} = 1 - \alpha_{TB} \quad (1.41)$$

Hence, for a given slug flow, knowledge of the superficial liquid and gas velocities allows to determine all other velocities of the system (gas slug rising velocity, mixture velocity, falling film velocity, etc). Some other quantities can be defined:

- The thickness of the falling liquid film (δ_L) (Zheng and Che, 2007):

$$\delta_L = 0.5d(1 - \alpha_{TB}^{0.5}) \quad (1.42)$$

- The Reynolds number of the falling film (Re_{ff}):

$$Re_{ff} = \frac{\rho_L u_{ff} \delta_L}{\mu_L} \quad (1.43)$$

- The Reynolds number for slug flow (Re_{sf}):

$$Re_{sf} = \frac{\rho_L u_{TB} d}{\mu_L} \quad (1.44)$$

1.4.2.2 Pressure drop

The total pressure drop (ΔP_{total}) in two-phase flow can be estimated using the following equation (Thome, 2008) excluding phase change effects (e.g. boiling):

$$\Delta P_{total} = \Delta P_{static} + \Delta P_{frict} \quad (1.45)$$

where ΔP_{static} is the static pressure drop for a homogeneous two-phase flow and ΔP_{frict} is the frictional pressure drop.

1.4.2.2.1 Static pressure drop

The static pressure drop is defined by:

$$\Delta P_{static} = \rho_{tps} g z \quad (1.46)$$

where ρ_{tps} is the two-phase density for the static pressure component, and z is the vertical height, which in this particular case is the same as the length (L) of the tube. The homogeneous density is defined by:

$$\rho_{tps} = \rho_L (1 - \alpha_V) + \rho_G \alpha_V \quad (1.47)$$

where ρ_L and ρ_G are the densities of the liquid and gas, respectively, and α_V is the void fraction for a vertical tube, which is defined by (Thome, 2008):

$$\alpha_V = \frac{x}{\rho_G} \left[\left[1 + 0.2(1-x) \left(\frac{g d \rho_L^2}{\dot{m}_{total}^2} \right)^{0.25} \right] \left(\frac{x}{\rho_G} + \frac{1-x}{\rho_L} \right) + \frac{1.18(1-x)[g \sigma (\rho_L - \rho_G)]^{0.25}}{\dot{m}_{total} \rho_L^{0.5}} \right]^{-1} \quad (1.48)$$

where x is the quality, which is given by:

$$x = \frac{\dot{m}_G}{\dot{m}_{total}} \quad (1.49)$$

\dot{m}_{total} is the total mass velocity (\neq mass flow rate), which is defined by the sum of the liquid (\dot{m}_L) and gas (\dot{m}_G) mass velocities:

$$\dot{m}_{total} = \dot{m}_L + \dot{m}_G \quad (1.50)$$

The mass velocities for liquid and gas are defined by $\dot{m}_G = \rho_G u_{SG}$ and $\dot{m}_L = \rho_L u_{SL}$ respectively.

1.4.2.2.2 Frictional pressure drop

The frictional pressure drop is defined by (Shannak, 2008):

$$\Delta P_{frict} = f_{tp} \frac{L}{d} \frac{\dot{m}_{total}^2}{2 \rho_{tp}} \quad (1.51)$$

$$\rho_{tp} = \left[\frac{x}{\rho_G} + \frac{1-x}{\rho_L} \right]^{-1} \quad (1.52)$$

where ρ_{tp} is the two-phase density and f_{tp} is the two-phase friction factor which is function of the two-phase Reynolds number (Re_{tp}):

$$Re_{tp} = \frac{\dot{m}_{total} d \left[x^2 + (1-x)^2 \frac{\rho_G}{\rho_L} \right]}{\mu_G x + \mu_L (1-x) \frac{\rho_G}{\rho_L}} \quad (1.53)$$

For laminar or turbulent flow regime the friction factor is defined by:

$$\text{Laminar } (Re_{tp} \leq 11): \quad f_{tp} = 64 Re_{tp}^{-1} \quad (1.54)$$

$$\text{Turbulent } (Re_{tp} > 11): \quad f_{tp} = \left[-2 \log_{10} \left[\frac{1}{3.7065} \frac{\varepsilon}{d} - \frac{5.0452}{Re_{tp}} \log_{10} \left(\frac{1}{2.8257} \left(\frac{\varepsilon}{d} \right)^{1.1098} \right) + \frac{5.8506}{Re_{tp}^{0.8981}} \right] \right]^{-2} \quad (1.55)$$

For non-Newtonian liquid, the previous mechanistic model for the pressure drop (equation (1.45) to (1.55)) is no longer valid. Instead, to determine the frictional pressure drop for gas and non-Newtonian liquid two-phase flow (Biswas and Das, 2008; Das and Biswas, 1995) the following can be used:

$$\Delta P_{frict} = f_{tp} \frac{2 \rho_L L u_{SL}^2}{\left(1 + \frac{u_{SG}}{u_{SL}} \right) d} \quad (1.56)$$

where the friction factor for gas and non-Newtonian liquid two-phase flow is defined by (Das and Biswas, 1995):

$$f_{tp} = \frac{3.2231 Re_{SG}^{0.6102}}{Re_{MR}^{1.8291} N_{LP}^{0.3328}} \quad (1.57)$$

where Re_{SG} is determined using equation (1.10) using the properties of the gas and the superficial gas velocity. Re_{MR} is given by equation (1.20) and N_{LP} is the liquid property group, which is defined by:

$$N_{LP} = \frac{\mu_L^4 g}{\rho_L \sigma^3} \quad (1.58)$$

1.4.3 Energy consumption

The energy consumption in an MBR resides in air sparging, pumping and mixing (Delgado et al., 2008; Sanchez Perez et al., 2006). The energy for mixing (E_{mix}) is defined by:

$$E_{mix} = g \rho_L u_{SG} V_{tan} \quad (1.59)$$

where V_{tan} is the volume of the tank. The previous equation can be correlated to the shear rate (Sanchez Perez et al., 2006):

$$\dot{\gamma} = \left(\frac{g \rho_L u_{SG}}{k} \right)^{\frac{1}{n+1}} \quad (1.60)$$

The energy consumption for a pump is estimated by (Tchobanoglous et al., 2003):

$$E_{pump} = \frac{\Delta P u_{SL} \pi d^2}{4 e_{pump}} \quad (1.61)$$

The energy consumption for a blower is defined by (Tchobanoglous et al., 2003):

$$E_{blower} = \frac{\rho_G u_{SG} \pi d^2 R_{air} T_{in}}{4 \cdot 0.2857 e_{blower}} \left[\left(\frac{(P_{atm} + \Delta P)}{P_{atm}} \right)^{0.2857} - 1 \right] \quad (1.62)$$

where ΔP is the pressure drop, R_{air} is the specific gas constant for air ($= 286.88 \text{ J}\cdot\text{kg}^{-1}\cdot\text{K}^{-1}$) T_{in} is the inlet temperature (K), P_{atm} is the atmospheric pressure ($= 101\,325 \text{ Pa}$), e_i is the pump (usual range from 0.75 to 0.85) and blower (usual range from 0.60 to 0.70) efficiencies (Tchobanoglous et al., 2003). There are also other minor energy requirements (e.g. backwashing) but these are not considered here.

1.5 Air sparging

Membrane fouling caused by the attachment of suspended solids and soluble substances on the membrane surface is the major barrier for the widespread application of MBR technology. Different types of fouling can be identified (Judd, 2004; Liao et al., 2004):

- *Clogging* is a progressive accumulation of dry sludge in module volume, starting from “dead zones” in the reactor.
- *Sludging* refers to an accumulation of sludge at surface of membrane.
- *Fouling* represents all mechanisms of cake building, plus adsorption/blockage into membrane material.

In MBR, the hydrodynamics are of great importance for reducing sludge deposition on the membrane surface and prolonging the operating period below the critical TMP. Membrane performance measured in terms of membrane fouling has been observed to be enhanced by gas sparging and reports have shown improvements up to 63% when air is introduced (Bellara et al., 1996; Berube et al., 2006; Cui et al., 1997). Several mechanisms were identified, including bubble-induced secondary flow, physical displacement of the mass transfer boundary layer and pressure pulsing caused by slugs. Physical displacement and the reduction in fouling resistance are thought to be the main reasons for the observed enhancement in gas-sparged ultrafiltration with hollow fiber membrane systems (Cui et al., 2003). It has been found that bubbling can limit surface fouling (clogging and sludging), but not internal fouling (adsorption and pore blockage).

A comprehensive review of the effects of aeration on submerged hollow fibers reported that coarse, rather than fine bubbling, is the preferred mode to control fouling (Cui et al., 2003). Also, loose, rather than tight fibers are recommended to reduce fouling. Recent studies show that more movement of the fiber can be achieved using higher airflow rates, but amplitude and frequency both reach a plateau that depends on tightness, fibers diameter, liquid viscosity, etc (Wicaksana et al., 2005). The movement of a fiber within a bundle could have a number of effects including collisions between the fibers that loosen and erode the cake layer on the membrane surface. However, bubbling not only controls fouling by moving fibers because it is also effective with tight fibers. For example, Wicaksana et al. (2006) observed that a tight fiber had a fouling rate (suction pressure rise) of about 40 % larger than a loose fiber. Both fibers would experience bubble-induced shear stress and the difference could be attributed to fiber movement. A general observation is that larger airflow rates decrease the rate at which the pressure rises due to fouling, but that enhancement reaches a plateau as gas flow rate increases (Katsoufidou et al., 2005).

The benefits of bubbling appear to be most effective at low liquid velocities. At high liquid velocities, the performance becomes dominated by bulk liquid shear (Cui et al., 2003).

Studies on the aeration of submerged hollow fiber membranes tended to focus on the effect of overall gas flow rates. However, the effects of bubble size and frequency on the performance of hollow fibers in submerged systems were found important. For instance, for the same airflow rate, a smaller nozzle size provided a marginally lower fouling rate. Another study reported that bubbles of different size and frequency provided better fouling control (Yeo et al., 2006). When bubbling is applied to the filtration processes, it was found in some studies on flat sheet membranes that the fluctuation in shear stress affected the flux more than the absolute value of shear stresses induced by the bubbles. The peak of shear stresses induced by bubbling were up to 45% higher compared to when no bubbling was applied (Ducom et al., 2002). The experimental challenge in submerged hollow fiber systems with bubbly flow is to characterize the shear stress domain. Also, the shear stress is affected by the activated sludge composition and properties such as floc size and cake porosity (Wisniewski and Grasmick, 1998).

Similar observations were reported for the side-stream configuration. The studies report that the gas-sparging is more effective with a slug flow pattern. Slug flow increases the permeate flux, it increases the surface shear stress to remove foulants that are already attached (scouring effect) and it increases the mass transfer between the cake layer and the bulk region (Cui et al., 1997). However, the mechanism governing the mass transfer of foulants under two-phase flow conditions is poorly understood, and therefore, a trial-and-error approach is typically used to optimize the hydrodynamics of two-phase flow near a membrane surface.

The shear stress on surfaces can be measured with a variety of methods (e.g. hot film techniques, micro-electro-mechanical-system (MEMS), Laser Doppler anemometer (LDA)). The approach that was used in this study was using shear probes to measure the shear stresses on the wall surface with an electrolytic mixture of potassium chloride, potassium ferri- and ferro-cyanide (Berube et al., 2006; Chan et al., 2007; Cagnet et al., 1978; Pallares and Grau, 2008). Shear stress needed for the aeration to prevent membrane fouling may also have an impact on the flocculation state of the mixed liquor, which in turn influences the viscosity and filterability of the sludge.

1.6 Filtration modelling

There are several filtration models, like the back-transport model, which is based on the particle size, which is related to the transport of particles to and away from membrane surfaces (Sethi and Wiesner, 1997). The back-transport velocity can be related to the probability of deposition of particles leading to fouling. Due to the permeation of water through the membrane, there exists convective flux of particles normal to the membrane surface. The net particle velocity normal to the membrane surface arises from a combination of normal and tangential convection, along with the back-transport velocity associated with Brownian diffusion. The effect of tangential convection on the transport of a particle to a

membrane surface can be described by two processes: shear-induced diffusion and inertial lift, which act normal to and away from the membrane surface (Huisman et al., 1999; Huisman and Trägårdh, 1999).

Another model is the balance of forces models (Newton's first law of movement) (Broeckmann et al., 2006), which is based on the force balance of a spherical particle over the membrane taking into account different forces (e.g. tangential, normal, adhesion and friction forces) over the particle as a function of the flux.

Yet another model is the resistance in series model based on Darcy's law (Baker, 2004), which is the most common approach to model the flux (J) as a function of the TMP and total resistance (R_T) due to the membrane, cake polarization and irreversible fouling:

$$J = \frac{TMP}{\mu R_T} \quad (1.63)$$

The total resistance is defined by:

$$R_T = R_m + R_c + R_f \quad (1.64)$$

where μ is the viscosity of the permeate, R_m is the intrinsic membrane resistance, R_c is the cake resistance (reversible) and R_f is the fouling resistance (irreversible). Flux and TMP are used to calculate the resistances of equations (1.63) and (1.64). The determination of the values of the resistances is done experimentally. The R_m from a virgin or clean membrane is calculated based on filtration with pure water. $R_m + R_f$ is measured after removing the cake layer by washing the membrane with tap water after the operation followed by filtration of pure water. From these resistances, it is possible to determine the remaining parameters.

1.6.1 Cake layer

During the filtration process, the separation between the sludge and the suspended solids occurs at the membrane, resulting in an increase in the solute concentration near the membrane surface (Figure 1.12). This is called the concentration polarization (Mulder, 1998).

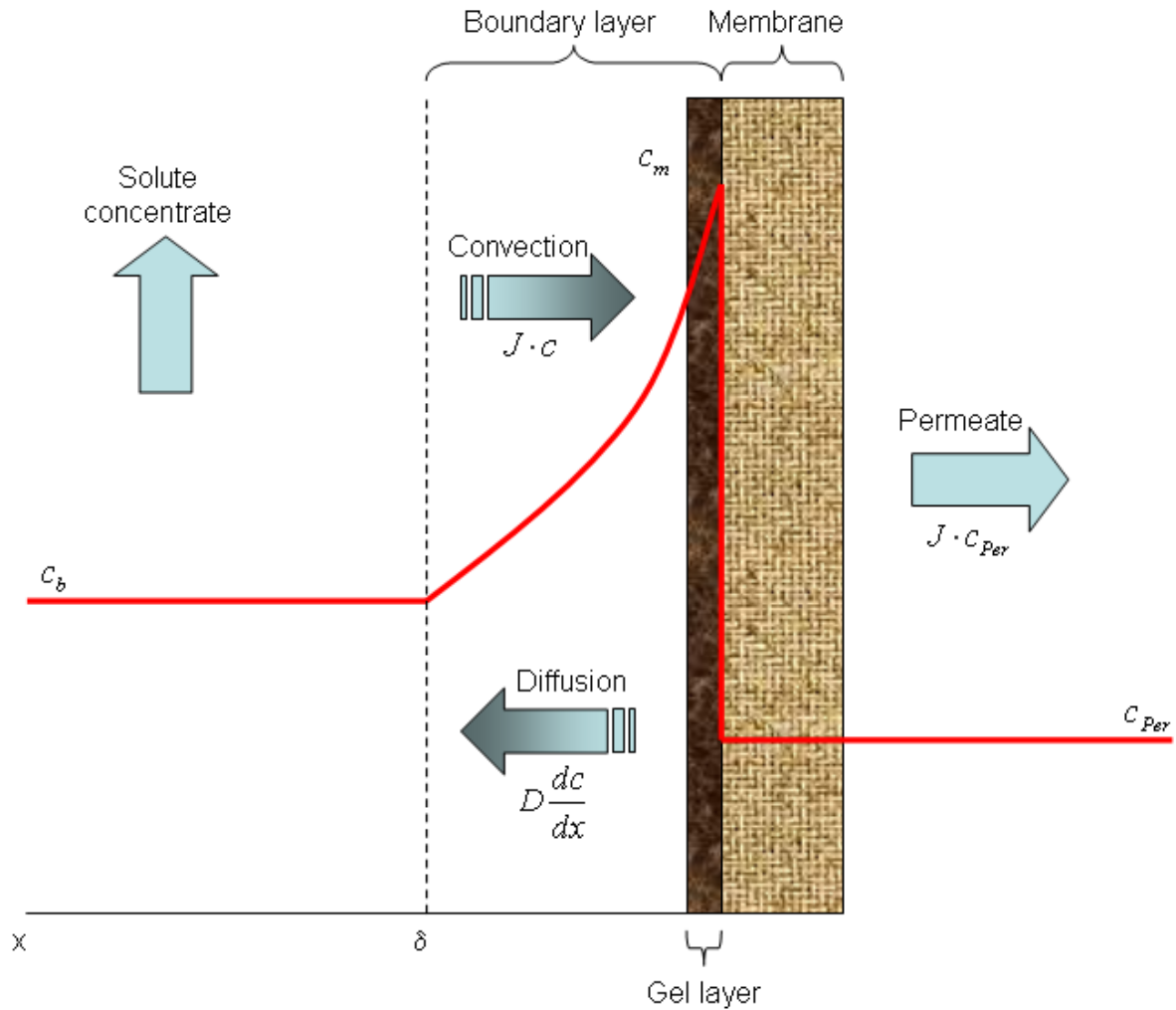


Figure 1.12. Concentration polarization

Closing the mass balance over the membrane:

$$\text{Convection} = \text{Diffusion} + \text{Permeate}$$

and based on the permeate flux (J) and diffusion coefficient (D_f), the following holds:

$$J c = -D_f \frac{dc}{dx} + J c_{per} \quad (1.65)$$

Boundary conditions for solving equation (1.65) are:

$$x = 0 \quad c = c_m$$

$$x = \delta \quad c = c_b$$

where c_m is the solute concentration at the membrane surface, c_b is the solute concentration in the bulk, c_{per} is the permeate concentration and δ is the thickness of the boundary layer. Integrating equation (1.65) using the mentioned boundary conditions resulting:

$$\frac{J \delta}{D_f} = \ln \left[\frac{c_m - c_{per}}{c_b - c_{per}} \right] \quad (1.66)$$

Moreover, from the film theory (Dieter and Stephan, 2006), the mass transfer coefficient (k_m) is:

$$k_m = \frac{D_f}{\delta} \quad (1.67)$$

Combining equation (1.66) and (1.67) yields:

$$J = k_m \ln \left[\frac{c_m - c_{per}}{c_b - c_{per}} \right] \quad (1.68)$$

Hence, the flux depends on the mass transfer coefficient and the concentrations in bulk, permeate and near membrane surface. Assuming that the membrane rejects all suspended solids ($c_{per} = 0$) the permeate flux is:

$$J = k_m \ln \left[\frac{c_m}{c_b} \right] \quad (1.69)$$

The mass transfer coefficient depends on the flow regime and whether single or two-phase flow is being used.

1.7 Mass transfer coefficient

1.7.1 Determination of the mass transfer for single phase flow

The mass transfer coefficient can be obtained by correlations using the Sherwood number (Sh). The Sherwood number is the ratio of convective to diffusive mass transport and is defined by:

$$Sh = \frac{k_m d}{D_f} \quad (1.70)$$

The Sherwood number for single phase flow in a tube depends on the fluid flow regime (De and Bhattacharya, 1997; De and Bhattacharya, 1999; Oliveira et al., 2001; Ranjan et al., 2004):

$$\text{Laminar } (Re \leq 2000) \quad Sh = 1.62 \left(Re Sc \frac{d}{L} \right)^{\frac{1}{3}} \quad (1.71)$$

$$\text{Turbulent } (Re > 4000) \quad Sh = 0.04 Re^{0.8} Sc^{\frac{1}{3}} \quad (1.72)$$

where Sc is the Schmidt number, which is defined as the dimensionless ratio of momentum and mass diffusivity:

$$Sc = \frac{\mu}{\rho D_f} \quad (1.73)$$

The constant and the exponent value of the Reynolds number for equations (1.71) and (1.72) are commonly modified to fit experimental data. The Sherwood number relations above are fairly simple, but they may give errors as large as 25 %. This error can be reduced considerably to less than 10 % by using more complex but accurate relations. Also it is important to mention that the correlations are for smooth tubes and they do not hold for transition flows ($2000 < Re < 4000$). However, the weighted factor introduced in equation (1.16) and (1.17) can be used here as well. However, the friction factor from equation (1.16) is replaced by the laminar and turbulent Sherwood number.

The previous equations do not consider filtration through the membrane. Therefore, another model was proposed for laminar regime (De and Bhattacharya, 1997; De and Bhattacharya, 1999):

$$Sh = 1.62 \left[Re Sc \frac{d}{L} \right]^{\frac{1}{3}} \lambda_2 \quad (1.74)$$

This equation needs to include the permeate flux and two correction parameters (λ_1 and λ_2) which are defined by:

$$\lambda_1 = \frac{J d}{D_f} \left[Re Sc \frac{d}{L} \right]^{\frac{1}{3}} \quad (1.75)$$

$$\lambda_2 = 1 + 0.37 \lambda_1 + 0.03 \lambda_1^2 - 1.05 \cdot 10^{-3} \lambda_1^3 \quad (1.76)$$

For non-Newtonian liquids some modifications are required (Ranjan et al., 2004a; Ranjan et al., 2004b; Ranjan et al., 2005):

$$Sh_{N-N} = 1.016 \left(\frac{3n+1}{n} \right)^{\frac{1}{3}} \left[Re_{MR} Sc \frac{d}{L} \right]^{\frac{1}{3}} \lambda_2 \quad (1.77)$$

It is possible to observe that when $n = 1$ (Newtonian fluids) equation (1.77) reduces to equation (1.71). In this case, the correction parameters for laminar regime are defined as:

$$\lambda_1 = \frac{J d}{D_f} \left[Re_{MR} Sc \frac{3n+1}{n} \frac{d}{L} \right]^{\frac{1}{3}} \quad (1.78)$$

$$\lambda_2 = 1 + 0.57 \lambda_1 + 0.08 \lambda_1^2 - 8.25 \cdot 10^{-3} \lambda_1^3 + 4.28 \cdot 10^{-4} \lambda_1^4 - 8.74 \cdot 10^{-6} \lambda_1^5 \quad (1.79)$$

For turbulent regime the correction parameters (λ_1 and λ_2) can be found in Ranjan et al., (2004b). Finally, it is complex to determine the diffusion parameter (D_f) due to the heterogeneity of the sludge. One equation that can be used is the Stokes-Einstein relationship for diluted solutions assuming that the particles are spherical:

$$D_f = \frac{\kappa T}{3\pi \mu d_p} \quad (1.80)$$

where d_p is the particle diameter (assuming spherical particles) and κ is the Boltzmann's constant ($= 1.38 \cdot 10^{-23} \text{ J}\cdot\text{K}^{-1}$).

1.7.2 Determination of the mass transfer for two-phase flow

Since slug flow is the core of this work, only this case is reviewed in this section. In the slug flow, there are three zones: the falling film zone (*ff*), the wake (or mixture) zone (*w*) and the liquid slug zone (*ls*) (Figure 1.13).

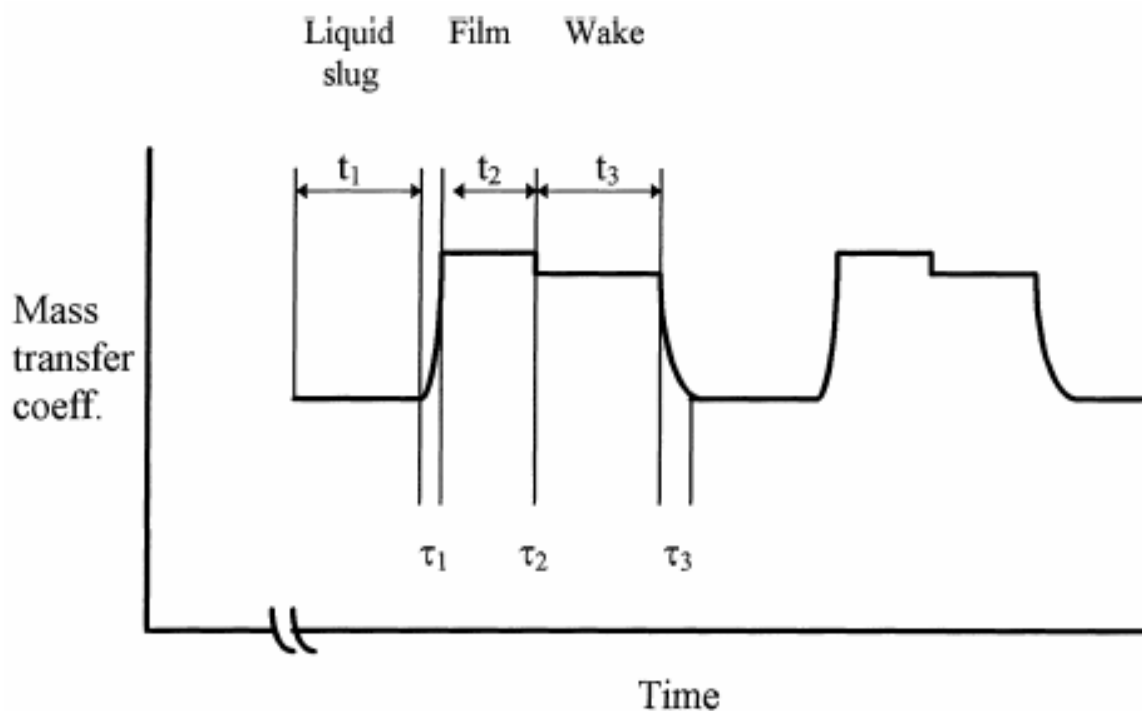


Figure 1.13 Mass transfer coefficients in different zones of the slug flow (Ghosh and Cui, 1999)

Each zone has its own mass transfer coefficient (Figure 1.13), which is defined by several authors as follows:

- *Ghosh and Cui (1999):*

- Falling film zone:

The mass transfer coefficient for the falling film zone ($k_{m,ff}$) is:

$$k_{m,ff} = 0.023 \left(\frac{u_{ff}^{0.8} D_f^{0.67} \mu_L^{0.47} \rho_L^{0.47}}{d_{eqv}^{0.2} \mu_L^{0.47}} \right) \quad (1.81)$$

where u_{ff} is the liquid film velocity and d_{eqv} is the equivalent hydraulic diameter or thickness of the boundary layer.

- Wake zone:

The mass transfer coefficient for the wake zone ($k_{m,w}$) is:

$$k_{m,w} = 0.023 \left(\frac{u_{axial}^{0.8} D_f^{0.67} \rho_L^{0.47}}{d^{0.2} \mu_L^{0.47}} \right) \quad (1.82)$$

where u_{axial} is the axial velocity component.

- Liquid slug zone:

The mass transfer coefficient for the liquid slug zone ($k_{m,ls}$) is:

$$\text{Laminar (} Re_h < 2000 \text{)} \quad k_{m,ls} = 1.62 Re_h^{\frac{1}{3}} Sc^{\frac{1}{3}} \left(\frac{d}{L} \right)^{\frac{1}{3}} \left(\frac{d}{D_f} \right) \quad (1.83)$$

$$\text{Turbulent (} Re_h > 4000 \text{)} \quad k_{m,ls} = 0.023 Re_h^{\frac{4}{5}} Sc^{\frac{1}{3}} \left(\frac{d}{D_f} \right) \quad (1.84)$$

where Re_h is the homogeneous Reynolds number. The definitions of these parameters can be found in the article of Ghosh and Cui (1999).

- *Zheng and Che (2008)*:

These authors define the mass transfer for turbulent regime as follows (Zheng et al., 2008):

$$k_{m,i} = 0.023 C' \left(\frac{\rho_i u_i d_i}{\mu_i} \right)^{0.8} \left(\frac{\mu_i}{\rho_i D_f} \right)^{0.33} \left(\frac{D_f}{d_i} \right) \quad (1.85)$$

where the subscript i refers to the different slug zones. Expressions for the different parameters to be used are summarized in Table 1.5, where α_l is the void fraction of the liquid. The definitions of these parameters can be found in Zheng and Che (2008).

Table 1.5. Summary of parameters to use in equation (1.85)

Parameter	k_{ff}	k_w	k_{ls}
u	$9.916 [g d (1-\alpha)^{0.5}]^{0.5}$	u_{axial}	$u_{SG} + u_{SL}$
d	$2d(1-\alpha^{0.5})$	d	d
ρ	ρ_L	$\rho_L(1-\alpha_l) + \rho_G \alpha_l$	$\rho_L(1-\alpha_l) + \rho_G \alpha_l$
μ	μ_L	$\mu_L(1-\alpha_l) + \mu_G \alpha_l$	$\mu_L(1-\alpha_l) + \mu_G \alpha_l$

The parameter C' is function of the mixture Froude number (Fr').

$$C' = 0.27 \left(1 + \frac{Fr'}{\beta} \right)^{0.5} \quad (1.86)$$

where

$$Fr' = \frac{u_{SG} + u_{SL}}{(g d)^2} \quad (1.87)$$

The work of Ghosh and Cui (1999) and Zheng and Che (2008) present mass transfer models for each zone. However, determining the parameters (e.g. thickness of the boundary layer, axial velocity, liquid void fraction, gas and liquid slug length, etc) requires dedicated experimental measurements, such as Particle Image Velocimetry (PIV) or Laser Doppler Anemometry (LDA). The latter require the medium to be transparent, which is not the case for activated sludge.

1.8 Heat transfer

1.8.1 Determination of the heat transfer for single phase flow

The heat transfer for single phase flow in a tube depends on the fluid regime (Ghajar, 2005; Kim et al., 1999):

$$\text{Laminar } (Re \leq 2000) \quad Nu = 1.86 \left(Re Pr \frac{d}{L} \right)^{\frac{1}{3}} \left(\frac{\mu_B}{\mu_W} \right)^{0.14} \quad (1.88)$$

$$\text{Turbulent } (Re > 4000) \quad Nu = 0.027 Re^{0.8} Pr^{\frac{1}{3}} \left(\frac{\mu_B}{\mu_W} \right)^{0.14} \quad (1.89)$$

where Nu and Pr are the Nusselt and Prandtl number, respectively. The Nusselt number is the ratio of convective to conductive heat transfer normal to the boundary and the Prandtl number is the ratio of the momentum diffusivity and the thermal diffusivity. They are defined as:

$$Nu = \frac{hd}{k_c} \quad (1.90)$$

and

$$Pr = \frac{c_p \mu}{k_c} \quad (1.91)$$

where h is the heat transfer coefficient ($W \cdot m^{-2} \cdot K^{-1}$), k_c is the thermal conductivity ($W \cdot m^{-1} \cdot K^{-1}$) and c_p is the specific heat ($kJ \cdot kg^{-1} \cdot K^{-1}$). For the transition regime the weighted function can be used as it was discussed in section 1.8.1. Comparing the heat (equations (1.88) and

(1.89)) and mass (equations (1.71) and (1.72)) transfer correlations for single phase flow, it is possible to observe that the equations have the same structure but the coefficients are slightly different.

For non-Newtonian liquids, a modification is required for equation (1.88) and (1.89) (Chhabra and Richardson, 2001):

$$\frac{Nu_{N-N}}{Nu} = \left(\frac{3n+1}{4n} \right)^{\frac{1}{3}} \quad (1.92)$$

1.8.2 Determination of the heat transfer for two-phase flow

The Nusselt number for two phase flow (Nu_{tp}) is defined as (Kim et al., 2000):

$$Nu_{tp} = \frac{h_{tp} d}{k_{c,tp}} \quad (1.93)$$

where h_{tp} is the heat transfer coefficient for two-phase flow and $k_{c,tp}$ is the thermal conductivity for two-phase flow, which is defined by:

$$k_{c,tp} = (1-x)k_{c,L} + xk_{c,G} \quad (1.94)$$

where $k_{c,L}$ and $k_{c,G}$ are the thermal conductivity of the liquid and the gas, respectively. The heat transfer coefficient for two-phase flow is defined by (Ghajar and Tang, 2010; Tang and Ghajar, 2007):

$$h_{tp} = F_p h_L \left[1 + 0.55 \left(\frac{x}{1-x} \right)^{0.1} \left(\frac{1-F_p}{F_p} \right)^{0.4} \left(\frac{Pr_G}{Pr_L} \right)^{0.25} \left(\frac{\mu_L}{\mu_G} \right)^{0.25} (I^*)^{0.25} \right] \quad (1.95)$$

where F_p is the flow pattern factor (dimensionless), h_L is the heat transfer coefficient for the liquid and I^* is the inclination factor (dimensionless). The flow pattern factor (F_p) is an effective wetted-perimeter as a function of the void fraction, it is used to capture the shape of the gas-liquid interface and is defined by:

$$F_p = (1 - \alpha_{tp}) + \alpha_{tp} F_s^2 \quad (1.96)$$

where α_{tp} is the general void fraction for two-phase flow and F_s is the shape factor (dimensionless), which is a modified and normalized Froude number. The void fraction (α_{tp}) is defined by:

$$\alpha_{tp} = \frac{u_{SG}}{C_0 (u_{SG} + u_{SL}) + u_{GM}} \quad (1.97)$$

where u_{SG} and u_{SL} are the superficial gas and liquid velocities, respectively, C_0 is the distribution parameter (dimensionless) and u_{GM} is the drift velocity ($\text{m}\cdot\text{s}^{-1}$) of gas, and they are respectively defined as:

$$C_0 = \frac{u_{SG}}{u_{SG} + u_{SL}} \left[1 + \left(\frac{u_{SL}}{u_{SG}} \right) \left(\frac{\rho_G}{\rho_L} \right)^{0.1} \right] \quad (1.98)$$

$$u_{GM} = 2.9 \left[\frac{g \sigma [\rho_L - \rho_G]}{\rho_L^2} \right]^{0.25} \quad (1.99)$$

The shape factor (F_s) is defined by:

$$F_s = \frac{2}{\pi} \tan^{-1} \left[\left(\frac{\rho_G (u_G - u_L)^2}{g d (\rho_L - \rho_G)} \right)^{0.5} \right] \quad (1.100)$$

where u_G and u_L are the gas and liquid velocities ($\text{m}\cdot\text{s}^{-1}$) and they are different to the superficial velocities, as follows:

$$u_G = \frac{u_{SG}}{\alpha_{tp}} \quad (1.101)$$

$$u_L = \frac{u_{SL}}{1 - \alpha_p} \quad (1.102)$$

The inclination factor (I^*) is defined by:

$$I^* = 1 + Eö |\sin \theta| \quad (1.103)$$

where $Eö$ is the Eötvös number (dimensionless) and θ is the inclination angle ($= 90^\circ$). The Eötvös number is defined as:

$$Eö = \frac{(\rho_L - \rho_G) g d^2}{\sigma} \quad (1.104)$$

The heat transfer coefficient for the liquid (h_L) in single phase flow, depends on the liquid flow regime:

$$\text{Laminar } (Re_L \leq 2000) \quad h_L = 1.86 \left(\frac{k_{c,L}}{d} \right) \left(Re_L Pr_L \frac{d}{L} \right)^{\frac{1}{3}} \left(\frac{\mu_B}{\mu_W} \right)^{0.14} \quad (1.105)$$

$$\text{Turbulent } (Re_L > 4000) \quad h_L = 0.027 \left(\frac{k_{c,L}}{d} \right) Re_L^{0.8} Pr_L^{\frac{1}{3}} \left(\frac{\mu_B}{\mu_W} \right)^{0.14} \quad (1.106)$$

where Re_L is the liquid Reynolds number and the subscripts B and W are for the bulk and wall respectively. Equation (1.105) and (1.106) are the same as (1.88) and (1.89) but now solved for the heat transfer coefficient. The liquid Reynolds number (Re_L) is defined by:

$$Re_L = \frac{\rho_L u_L d}{\mu_L} = \frac{\rho_L u_{SL} d}{(1 - \alpha_p) \mu_L} \quad (1.107)$$

The gas Reynolds number (Re_G) is defined by:

$$Re_G = \frac{\rho_G u_G d}{\mu_G} = \frac{\rho_L u_{SG} d}{\alpha \mu_L} \quad (1.108)$$

Equation (1.95) is valid for Re_L from 750 to $1.3 \cdot 10^5$ and Re_G from 14 to $2.1 \cdot 10^5$. Equation (1.95) was developed based on extensive literature review (Kim et al., 1999), including numerous heat transfer coefficient correlations that have been published over the past 50 years. This correlation was determined based on several experimental data sets for forced convective heat transfer during gas-liquid two-phase flow in vertical, horizontal and inclined pipes (524 data points). This correlation is robust and can be used for different flow patterns.

1.8.3 Heat-and-mass transfer analogy

In situations involving simultaneous heat and mass transfer by convection, the Lewis number (Le), which is the ratio of thermal diffusivity to mass diffusivity, can be used. It is defined by:

$$Le = \frac{Sc}{Pr} = \frac{k_c}{\rho c_p D_f} \quad (1.109)$$

The heat and mass transfer analogy can be written as:

$$\frac{Nu}{Pr^{n'}} = \frac{Sh}{Sc^{n'}} \quad (1.110)$$

Re-writing equation (1.110) yields:

$$\frac{h}{k_m} = \frac{k_c}{D_f Le^{n'}} = \rho c_p Le^{1-n'} \quad (1.111)$$

The previous relation can be used for laminar or turbulent regime and can be used to determine the heat or mass transfer given that respectively the mass or heat transfer coefficient are known. The exponent n' is $1/3$. Table 1.6 summarizes all the equations and links between wall shear stress, mass and heat transfer.

Table 1.6. Relationship among wall shear stress, mass and hear transfer for single phase flow.

	Mass transfer		Wall friction		Heat transfer	
	$Sh = function(d, Re, Sc)$		$f = function(d, Re)$		$Nu = function(d, Re, Pr)$	
Dimensionless numbers	$Sh = \frac{k_m d}{D_j}$	$Sc = \frac{\mu}{\rho D_j}$	$f = \frac{2 d \Delta p}{L \rho u^2} = \frac{8 \tau_w}{\rho u^2}$	$Re = \frac{\rho u d}{\mu}$	$Nu = \frac{h d}{k_c}$	$Pr = \frac{c_p \mu}{k_c}$
Laminar (Re<2000)	$Sh = 1.62 \left(Re Sc \frac{d}{L} \right)^{\frac{1}{3}}$		$f = \frac{64}{Re}$		$Nu = 1.86 \left(Re Pr \frac{d}{L} \right)^{\frac{1}{3}} \left(\frac{\mu_B}{\mu_W} \right)^{0.14}$	
Turbulent (Re>4000)	$Sh = 0.04 Re^{0.8} Sc^{\frac{1}{3}}$		$f = \frac{0.25}{\left[\log_{10} \left(\frac{\epsilon}{3.7 d} + \frac{5.74}{Re^{0.9}} \right) \right]^2}$		$Nu = 0.027 Re^{0.8} Pr^{\frac{1}{3}} \left(\frac{\mu_B}{\mu_W} \right)^{0.14}$	
Analogy	$\frac{Sh}{Re Sc} Sc^{\frac{2}{3}} = \frac{f}{2}$			$\frac{f}{2} = \frac{Nu}{Re Pr} Pr^{\frac{2}{3}}$		
	$\frac{Sh}{Nu} = \left(\frac{Sc}{Pr} \right)^{\frac{1}{3}} = Le^{\frac{1}{3}}$					

1.8.3.1 Reynolds analogy

The Reynolds analogy relates the parameters of velocity, thermal and concentration boundary layers. If the velocity is known the analogy can be used to determine the other parameters. Nevertheless there are some restrictions associated to the use of this analogy, like the pressure gradients (dp/dx) should be close to 0, which is applicable to open channel flows and not flows in pipes.

$$\frac{dp}{dx} \approx 0 \quad (1.112)$$

and the Prandtl and Schmidt numbers should be close to unity.

$$Pr = Sc \approx 1 \quad (1.113)$$

If applicable, the analogy can be written as:

$$f \frac{Re}{2} = Nu = Sh \quad (1.114)$$

Replacing the Nusselt and the Sherwood number by the Stanton number (St) and the mass Stanton number (St_m) respectively:

$$St = \frac{h}{\rho u c_p} = \frac{Nu}{Re Pr} \quad (1.115)$$

$$St_m = \frac{k_m}{u} = \frac{Sh}{Re Sc} \quad (1.116)$$

equation (1.114) becomes:

$$\frac{f}{2} = St = St_m \quad (1.117)$$

This relation is known as the Reynolds analogy, and it enables to determine the seemingly unrelated friction, heat transfer, and mass transfer coefficients when only one of them is known or measured. However, it should always be remembered that the analogy is restricted to situations for which equation (1.113) is fulfilled. Evidently, in this particular case of flow in a tube the analogy cannot be used.

1.8.3.2 Chilton-Colburn analogy

Due to the restrictions of the Reynolds analogy (Equations (1.112) and (1.113)), the Chilton-Colburn analogy adds a Prandtl number correction or Schmidt number correction depending, whether it concerns heat or mass transfer. This analogy has the following form:

$$\frac{f}{2} = St Pr^{\frac{2}{3}} \quad 0.6 < Pr < 60 \quad (1.118)$$

$$\frac{f}{2} = St_m Sc^{\frac{2}{3}} \quad 0.6 < Sc < 3000 \quad (1.119)$$

The Chilton–Colburn analogy ($Pr \neq Sc \neq 1$) has been observed to hold quite well in laminar or turbulent flow over plane surfaces. But this is not always the case for internal flow and flow over irregular geometries, and in such cases specific relations developed should be used. The previous equations are valid for turbulent flow, because they are less sensitive to

pressure gradient. On the other hand for laminar flow, the condition of equation (1.112) must still be fulfilled.

The main problem of these two analogies is that for internal pipe flow, they can only be used in the turbulent regime even if there are pressure gradients (i.e. pressure drop along the tube). In the particular case studied in this work the flow is in the laminar and transition regime. Therefore, they are not applicable. Nevertheless, the Lewis number can be used independent of the flow regime.

1.9 Numerical modelling

A large amount of research has been carried out during the last decade to understand the hydrodynamic behaviour in MBRs. A number of advantages of using CFD modelling for MBR applications should be emphasised. Conventionally, the way to approach these type of systems are threefold: 1) experimentally, which can only be done in a lab- and pilot-scale environment under specific conditions to produce specific results; however, scale-up is not completely reliable and measurement techniques that are currently available and that are expensive, as is setting up a pilot reactor, 2) theoretically, based on equations and correlation from experimental work and 3) computationally, using CFD which links to the theoretical approach and allows to solve numerically a set of partial differential equations that describes the system. Therefore, a link between these approaches can be used to improve modelling and simulation results based on experimental data. Therefore, the most important added value of modelling and simulation is the virtual prototyping which has a considerably lower cost compared to lab- and pilot-scale studies. Consequently, the benefits of this type of models are: 1) these models have become more precise and, hence, reliable due to the quality in the measurement techniques and the comparison with experimental data, 2) the models allow to obtain local (e.g. velocity profile, bubble frequency, etc) and global (e.g. dead zones, mixing, etc) prediction of important variables, 3) it is possible to mimic the hydrodynamics of MBR systems, taking into account different sizes (scale-up), operating conditions and membrane types, and 4) these models can be coupled with state-of-the-art models (biological models, filtration models, population balance models, etc) and process understanding, where it is possible to develop a core expertise in the design and optimization of MBR systems.

1.9.1 Multiphase flow modelling

Numerical models are introduced to simulate the flow field in two-phase flow. Navier-Stokes equations are used in the calculation of this flow field. In spite of this, solving these models requires the construction of complicated discretization grids and involves a large amount of calculations (computational power). The configuration of the interface between liquid and gas is unknown in advance and needs to be determined during the calculation. There are two CFD modelling approaches for two-phase flow system, which depend on the flow regime

that best represents the multiphase system: 1) the Euler-Lagrange approach and 2) the Euler-Euler approach.

- *Euler-Lagrange approach*: the liquid phase is described within an Eulerian approach, that is to say the average equations of Navier-Stokes are solved for the liquid phase, whereas each individual bubble is tracked and its motion described by Newton's law (Lagrangian approach). This approach presents the advantage of simple implementation of forces acting on the bubbles and the result gives a more physical representation of the dispersed phase. However Euler/Lagrange simulations are confronted with severe drawbacks. Because of the necessity to track each bubble individually, these simulations will in case of high gas hold up require high performance computers with large amounts of computer memory. Therefore, this approach is limited to gas holdup up to 10-12 % (Sokolichin et al., 1997). Since in most applications of bubble columns the gas volume fraction is generally not small, the use of Euler/Euler approach in this situation is much more suitable and practical (FLUENT, 2006).
- *Euler-Euler approach*: in this approach the dispersed phase is also considered as a fluid phase characterized by its volume fraction. This approach solves the Navier-Stokes equations for each phase and coupling terms are associated to take into account the interaction between the phases. Simulations differing mainly in the use of the inter-phase forces and the treatment of the turbulence were carried out by various authors (Kulkarni et al., 2007; Ranade, 1997; Ranade and Tayalia, 2001). This approach is more suitable to describe any poly-phase system as soon as the dispersed phase volume fraction is less than 15 %. Basically, these models solve the Navier-Stokes equation in an Eulerian manner for the continuous phase, and the difference between the different models lies in the treatment of the dispersed phase. Unfortunately, this approach does not converge very easily for gas-liquid flow because the sensitivity of the gas region to pressure changes is generally much greater than that in the liquid region. Moreover, the interface moves with an average velocity instead of different velocities for each phase. If the velocities of different phases have large difference, this often leads to unrealistic movement of the interfaces (FLUENT, 2006).

These two approaches have been widely used for the modelling of two-phase flow in bubble columns and airlift reactors. However, for MBR modelling, the Euler-Euler approach is commonly used. In this approach, there are three different multiphase models and they are presented in Table 1.7.

Table 1.7. Summary of three multiphase models

Modelling approach	Principle	Application
Mixture model	Close to the Eulerian-Eulerian approach Solving equations for the mixture + equation for the volume fraction of the dispersed phase	Two phase flow non miscible Dispersed phase holdup > 10-15 % E.g. Bubbly flow
Eulerian model	Dispersed phase = fluid phase Continuity equation solved for both phases Coupling between the phases to consider their interaction Several models associated to turbulence modelling	Approach the most used for the description of multi-phase systems for gas hold up < 15% E.g. Bubbly flow
Volume of Fluid (VOF)	Dispersed phase = deformable Solving the Navier-Stokes equation for each phase Gas-liquid interface reconstruction	Interface tracking E.g. Slug flow

A brief explanation as well as the mathematical equations are introduced below.

1.9.1.1 Mixture model

The mixture model, also known as the Algebraic Slip Mixture model (ASM) is a simplified multiphase model that allows the phases to move at different velocities. It assumes the phases to be interpenetrating continua (non miscible). It models two phases by solving the momentum and the continuity equation for the mixture, the volume fraction equation for the secondary phase, and an algebraic expression for the relative velocity. It does not assume that there is an interface between the two immiscible phases and mass transfer is not allowed (Vedantam, 2005).

The continuity equation for the mixture is:

$$\frac{\partial \rho_m}{\partial t} + \frac{\partial \rho_m \mathbf{u}_m}{\partial x_i} = 0 \quad (1.120)$$

The volume fraction equation for the secondary phase is:

$$\frac{\partial}{\partial t}(\rho_G \epsilon_G) + \nabla \cdot (\rho_G \epsilon_G \mathbf{u}_G) = -\nabla \cdot (\epsilon_G \rho_G \mathbf{u}_{DG}) \quad (1.121)$$

where ∇ is the gradient operator. The momentum equation for the mixture is:

$$\frac{\partial(\rho_m \mathbf{u}_m)}{\partial t} + \nabla \cdot (\rho_m \mathbf{u}_m \mathbf{u}_m) = \nabla \cdot \boldsymbol{\tau} - \nabla p + \rho_m \mathbf{g} + F_K + \frac{\partial}{\partial x_i} \sum_{K=1}^n \epsilon_K \rho_m \mathbf{u}_{DK} \mathbf{u}_{DK} \quad (1.122)$$

where, $\boldsymbol{\tau}$ is the stress tensor, ρ_m is the mixture density ($\rho_m = \sum_{K=1}^n \epsilon_K \rho_K$), μ_m is the

viscosity of the mixture ($\mu_m = \sum_{K=1}^n \epsilon_K \mu_K$), u_m is the mass averaged velocity

($u_m = \sum_{K=1}^n \frac{\epsilon_K \rho_K \mathbf{u}_K}{\rho_m}$) and u_{DK} is the drift velocity ($u_{DK} = u_K - u_m$).

The main assumption of this model is that a local equilibrium between the phases should be reached over a short spatial length scale. It is a simple model and might not be applicable when a wide distribution of the particulate phase occurs or when the interface laws are not well known. This model is commonly used for bubbly flows (e.g. bubble column and airlift reactors).

1.9.1.2 Eulerian model

The Eulerian model solves a set of momentum, enthalpy, continuity and species equations for each phase. Coupling of phases is achieved through the pressure and interface exchange coefficient. The laws of conservation of mass, momentum and energy are satisfied by each phase individually. A single pressure is assumed to be shared by all the phases in proportion to their volume fractions. The mass transfer between the phases is allowed in this model unlike in the mixture model (Vedantam, 2005)

The continuity equation for each phase is given by:

$$\frac{\partial}{\partial t}(\rho_K \epsilon_K) + \nabla \cdot (\rho_K \epsilon_K \mathbf{u}_K) = \sum_{K=1}^n \dot{m}_K \quad (1.123)$$

The generalized momentum balance of each phase is written as

$$\frac{\partial(\rho_K u_K)}{\partial t} + \nabla \cdot (\rho_K \epsilon_K u_K u_K) = -\epsilon_K \nabla p + \nabla \cdot \mu (\nabla \epsilon_K u_K + \nabla \epsilon_K u_K^T)_K + \rho_K g + F_K \quad (1.124)$$

Where ϵ_K is the volume fraction of the K-fluid in the flow. In addition, interfacial forces are considered and represent the interaction forces between the continuous and the dispersed phase. The forces acting on a bubble in a still liquid are pressure and gravity. Relative motion between bubble and liquid leads to local variations in pressure and shear stress in the liquid flow around individual bubbles. The resultant of these forces from the liquid phase on the bubble affecting its motion is referred to drag. If the motion is non-uniform, the concept of drag needs to include the various non drag forces such as the so-called virtual mass force and lateral lift force. These forces are in general described with analytical models, which contain empirical constants (Joshi, 2001).

The drag force is the most important force and accounts for the interaction force between liquid and bubbles in a uniform flow field under non-accelerating conditions. The drag force for a bubble swarm is complicated to formulate and authors have used different models (Clift et al., 2005).

When the bubbles accelerate relative to the liquid, part of the surrounding liquid has to be accelerated as well. This additional force contribution is called the “added mass force” (or virtual mass force). The acceleration induces a resisting force on the sphere equal to one-half of the mass of the displaced fluid times the acceleration of the sphere.

The lift force is a radial force which depends upon the bubble rotation around its own axis in a flow field; relative gas-liquid velocity and liquid velocity gradient, viscous and turbulent shear gradient, radial pressure gradients, bubble shape changes, wake phenomena and the coalescence tendency. The mathematical formulae of these forces are not presented here. This model is commonly used for bubbly flows.

1.9.1.3 Volume of Fluid (VOF)

The volume of fluid (VOF) model is a fixed grid technique designed for two or more immiscible fluids where the position of the interface between the fluids is of interest. This model solves the time dependent motion of the two phases, and of the interface separating the two phases. The main aspect of this model is the tracking of interface embedded in the overall motion of the flow field. The VOF formulation relies on the fact that two or more fluids (or phases) are non-interpenetrating. In this model, the fluids share a single set of momentum equations, and the volume fraction of each of the fluids in each computational cell is tracked throughout the domain. To track the interface between the phases, the VOF

model employs the fractional volume (ϵ_K) which specifies the fraction of the computational cell filled with liquid (Vedantam, 2005). Therefore, the following three conditions are possible.

$\epsilon_K = 0$ the cell is empty (of the K-fluid)

$0 < \epsilon_K < 1$ the cell contains the interface

$\epsilon_K = 1$ the cell is full (of the K-fluid)

The fields for all the variables and properties are shared by the phases and represent volume averaged values, as long as the volume fraction of each of the phases is known at each location. Thus, the variables and properties in any given cell are either purely representative of one of the phases, or are representative of a mixture of the phases, depending upon the volume fraction values.

The motion of the liquid and thus that of the interface can be tracked through the solution of the continuity equation for the volume fraction of one (or more) of the phases. For the K^{th} phase, the equation has the following form:

$$\frac{\partial \epsilon_K}{\partial t} + \nabla \cdot (\mathbf{u}_K \epsilon_K) = 0 \quad (1.125)$$

The volume fraction obeys the following constraint:

$$\sum_{K=1}^n \epsilon_K = 1 \quad (1.126)$$

A single momentum equation is solved throughout the domain and the resulting velocity field is shared amongst the phases. The momentum equation, given below, is dependent on the volume fractions of all the phases through the properties, ρ_m and μ_m .

$$\nabla \cdot \mathbf{u} = 0 \quad (1.127)$$

$$\frac{\partial \rho_m \mathbf{u}_m}{\partial t} + \nabla \cdot (\rho_m \mathbf{u}_m \mathbf{u}_m) = -\nabla p + \nabla \cdot \mu_m (\nabla \mathbf{u} + \nabla \mathbf{u}_m^T) + \rho_m \mathbf{g} \quad (1.128)$$

where the density and viscosity in equation (1.128) are defined by:

$$\rho_m = \epsilon_K(x, t)\rho_L + (1 - \epsilon_K(x, t))\rho_G \quad (1.129)$$

$$\mu_m = \epsilon_K(x, t)\mu_L + (1 - \epsilon_K(x, t))\mu_G \quad (1.130)$$

This model is commonly used to track the motion of large bubbles in a liquid (e.g. slug flow) and will be excessively used in this work.

1.9.2 Turbulence modelling of two-phase flow

In addition to the selection of the multiphase flow model, it is also required to model the turbulence of the two phase flow. Turbulent flows are characterized by fluctuations of velocity, pressure and concentration field. To simulate turbulent flow, two methods can be used (among others): Reynolds Averaging of the Navier-Stokes (RANS) and Large Eddy Simulation (LES). Both methods introduce additional terms in the governing equations that need to be modelled in order to achieve a “closure” for the unknowns.

The RANS equations govern the transport of the averaged flow quantities, with the whole range of the scales of turbulence being modelled. This approach reduces the required computational effort and resources, and is widely adopted for practical engineering applications. In Reynolds averaging, the solution variables in the instantaneous (exact) Navier-Stokes equations are decomposed into the mean (ensemble-averaged or time-averaged) and fluctuating components.

The LES provides an alternative approach in which large eddies are explicitly solved whereas the small eddies are modelled. However, LES requires finer meshes than those typically used for RANS calculations and has to be run for a sufficiently long flow time to obtain stable statistics of the flow being modelled. As a result, the computational cost involved with LES is normally higher than that for RANS calculations in terms of memory and CPU time. Therefore, high-performance computing (e.g. parallel computing) is a necessity for LES.

Most of the studies of two-phase flow have used the ReNormalized Group (RNG) k - ϵ model developed for single-phase flow, which assumes that the flow is fully turbulent, and the effect of the molecular viscosity is negligible which can be considered acceptable for describing the hydrodynamics of the system (Ndinisa et al., 2005; Ndinisa et al., 2006).

1.9.3 MBR-CFD modelling

It has been widely demonstrated that the filtration performances in a MBR can be highly improved by using gas bubbles (two-phase flow). This aeration used to limit fouling of the membrane surface, or clogging, is a key point for fouling control and energy considerations. The air introduced below the membrane is supposed to be “ideally” distributed but this assumption is in practice seldom verified (Kulkarni et al., 2007; Ranade and Tayalia, 2001). However, the distribution of the air bubbles is still not well controlled. The diagnostic of the distribution of the air inside the membrane modules and the optimization of the aeration systems is thus an important aspect of MBR development. The investigation can be undertaken using modern tools such as CFD to diagnose and understand the two-phase flow in a MBR. This study illustrates the possibility of using CFD to assist the further development of MBR technology.

In the previous section, three models were shown and they can be used to model MBR systems. However, the use of each model depends exclusively on the MBR configuration:

- Immersed MBR: In this type of system, there is bubbly flow in which the phases (gas and liquid) are dispersed and the volume fractions exceed 10 %. For this type of system two multiphase models are suitable: the mixture and the Eulerian models. However, for small systems, the VOF can also be used to model Taylor and cap bubbles (Ndinisa et al., 2005)
- Side-stream MBR: In this type of system, there is slug flow pattern and the multiphase model recommended to use is the VOF.

It is expected that CFD can be used to determine how the aeration systems influence self cleaning of the membrane (scouring aeration). As a first step to optimization and control, the aim of this study is to develop a two-phase CFD model which includes bubble-induced turbulence and shear conditions. Moreover, the models are validated with experimental data.

1.10 Experimental techniques for CFD model validation

The flow field generated by the two-phase flow is turbulent. This means that the velocities are randomly fluctuating in time and space. Often, it is desirable to compute these velocity vectors using CFD models. This latter rely on a number of more or less empirical models (i.e. turbulence, mixing, convection, etc). Nevertheless, all CFD models rely on the ability to obtain a correct flow field. The random character of a turbulent flow field calls for statistic measures (i.e. mean velocities, root mean square of fluctuations, etc). Currently, to measure and characterize a flow field, some techniques are available such as:

1.10.1 Local shear measurement using electrochemical shear probes

This technique measures the velocity gradient near the wall based on an electrochemical reaction in a single point. It is suited for applications in liquid and gas flows. The compact size of the probes allows mounting where other sensors simply will not fit. The technique requires a detailed calibration in single phase flow to extrapolate to two-phase flow. A single probe can measure wall shear stress magnitude, but not flow direction (unless two-probes are used). It can be used to study mass transfer boundary layer (Cognet et al., 1978; Geshev, 1996; Pallares and Grau, 2008a; Rode et al., 1994; Zhuoxiong and Hanratty, 1991).

1.10.2 Flow field velocity by Particle Image Velocimetry (PIV)

PIV is a non-intrusive, optical technique which provides instantaneous velocity vector measurements in a cross-section of a flow. It measures two velocity components, but when using a stereoscopic approach, it permits to measure all three velocity components, resulting in instantaneous 3D velocity vectors for the measured area. The technique requires the addition of light scattering particles or droplets (seeding). The seeding is used for particle tracking to obtain the velocity vector (Kurada et al., 1993; Nogueira et al., 2003; Sousa et al., 2005).

1.11 Objectives of this work

The main goal of this work is to improve understanding of the hydrodynamics in MBR systems using a model-based approach. The main objectives of this work can be summarized as follows:

- Experimental verification of the behaviour of developed gas slugs in a slug flow of a tubular membrane
- Quantification of the local shear stress at the membrane surface and gas slugs rising velocity
- Development of an empirical model for shear stress based on liquid and gas flow rates
- Quantification of the pressure drop and energy consumption of a tubular membrane system as a function of liquid and gas flow rates
- Development of a CFD model for shear stress and gas slugs rising velocity for a single tube in a membrane module
- Development and experimental validation of a CFD model of a full-scale Norit Airlift module (multi-tube), including both the membrane module and the air diffuser
- Development and experimental validation of a CFD model of a pilot GE ZeeWeed Hollow Fiber MBR module.
- Development of an on site measurement technique of activated sludge viscosity and determination of a suitable mathematical model for activated sludge viscosity.

- Development of an empirical model based on heat-and-mass transfer analogy for shear stress prediction in two-phase flow.

1.12 Outline

An outline of this work shows the links between the 8 chapters and is presented in Figure 1.14. This work aims to improve the understanding of hydrodynamics in MBR systems.

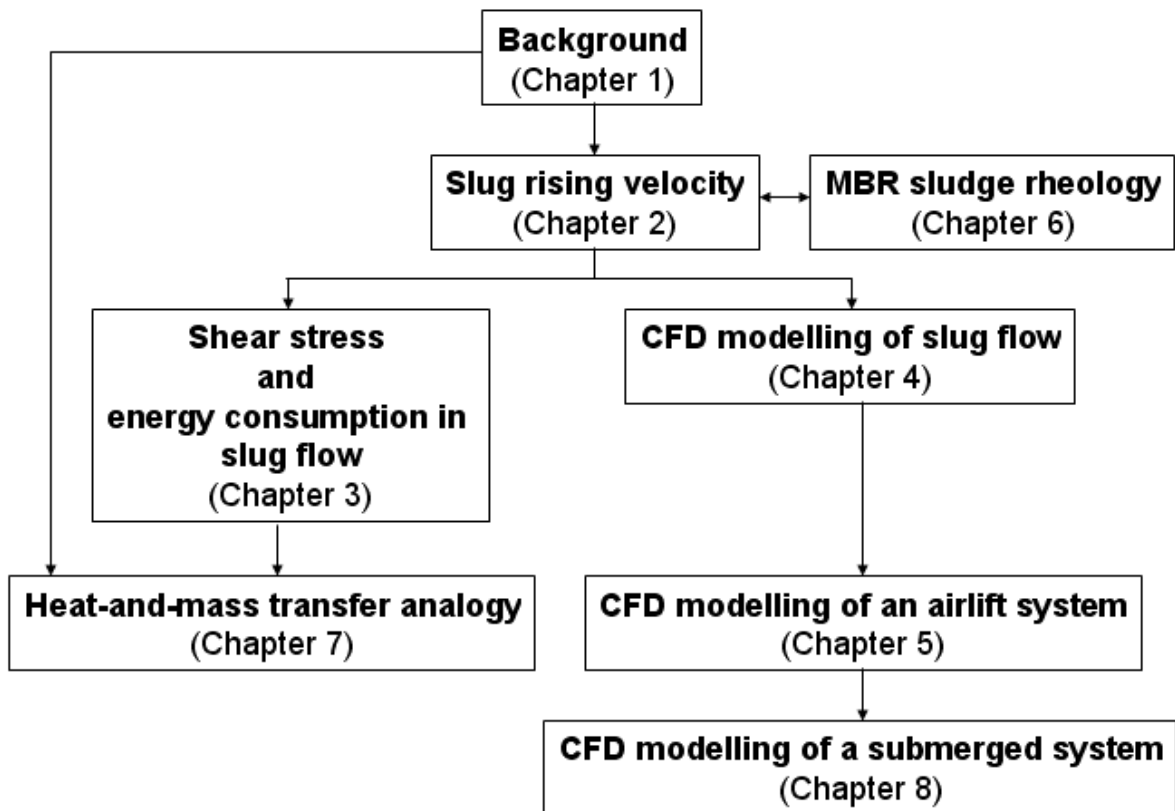


Figure 1.14 Outline of the work showing the links between the different chapters

Chapter 1 provides a write-up of the current state-of-the-art and background principles that will be used throughout the work.

Chapter 2 focuses on the slug flow rising velocity. The latter is measured for both Newtonian (water) and non-Newtonian (CMC and activated sludge) liquids at different liquid and gas flow rate combinations by means of a high speed camera. A correlation is looked for is compared with a theoretical equation from literature (chapter 1). A qualitative comparison of the behaviour of gas slugs rising in tubular Newtonian and non-Newtonian systems is given and a hypothesis is formulated regarding how viscosity affects the coalescence of the bubbles.

Chapter 3 presents wall shear stress time series for different gas and liquid flow rates. The latter are elegantly summarised in shear stress histograms (SSH) which allow compact representation, interpretation and comparison of the wall shear stresses in a slug flow. The SSH are obtained from electrochemical shear probes. Subsequently, they are modelled

using an empirical model and are used to determine the pressure drop and the energy consumption of the system based on theoretical equations. Finally, an empirical model to optimize the system for fouling control is presented.

Chapter 4 develops a CFD model of slug flow and validates it using the experimental data of shear stress (chapter 3) and slug rising velocity (chapter 2). As the empirical model presented in chapter 3 is only valid for specific operational conditions of the experiment, it cannot be extrapolated to other systems. The developed CFD model does not suffer from such a limitation and can be extrapolated to other systems (i.e. different tube diameters, flow rates)

Chapter 5 provides an attempt to extrapolate the CFD model of chapter 4 (micro-scale) to a model for a full-scale airlift MBR (macro-scale), considering a membrane module which consists of a multitude of tubes. Moreover, the air diffuser, which plays an important role in the air distribution within the system and can significantly reduce the fouling, is considered as well.

Chapter 6 presents a novel in-site measurement technique to determine activated sludge viscosity based on a tubular rheometer similarity observed in a filtration characterisation unit. Differences with traditional ex-situ rheometer measurements are observed and discussed. Furthermore, a literature model expressing activated sludge viscosity as a function of the suspended solids is calibrated using the obtained measurements.

Chapter 7 derives an empirical correlation, based on dimensionless quantities, in order to determine the shear stress from the heat transfer coefficient (chapter 1) instead of the mass transfer coefficient, which is difficult to measure experimentally. The new correlation is validated against the mass transfer coefficient presented in chapter 3.

Chapter 8 develops a CFD model of a submerged hollow fiber MBR. The model is validated with dedicated shear stress measurements using the same electrochemical method as presented in chapter 3.

Finally, **Chapter 9** provides a discussion and the main conclusions that can be drawn from the work.

Chapter 2. Gas slug rising velocity in vertical tubes

Abstract*

The behaviour of three different liquid-gas slug flows (water, carboxymethyl cellulose and activated sludge) in a vertical tube was studied using a High Speed Camera (HSC). Experiments were performed using different nitrogen gas and liquid flow rates and two tube diameters (6.3 and 9.9 mm). The observed difference in behaviour of the ascending gas slugs can be explained by the difference in viscosity of the fluids (Newtonian and non-Newtonian). Moreover, it was observed that the degree of coalescence of gas slugs is lower for non-Newtonian liquids and they behave like a succession of slugs without actually coalescing into a single larger gas slug. Finally, gas slug rising velocities were extracted, but no subsequent difference in the rising velocities of the different fluids was found.

* **Redrafted after:**

Ratkovich, N., Chan, C.C.V., Berube, P., Nopens, I. Investigation of the effect of viscosity on slug flow in airlift tubular membranes in search for a sludge surrogate. *Water Science and Technology* (in press)

Introduction

To date, the majority of the studies that have investigated the behaviour of slug flow used water as liquid phase (chapter 1). However, activated sludge is different from water in that it behaves as a non-Newtonian liquid (see section 1.3.3). The novelty of the presented work is, hence, to investigate the effect of the non-Newtonian rheological behaviour of activated sludge on the two-phase flow properties. The objective of the work is to provide better insight in the hydrodynamic behaviour of MBR systems, which can eventually lead to improved design and operation of this particular system.

This chapter is roughly broken down in 1) investigating and comparing the behaviour of gas slugs rising in tubular systems containing either a Newtonian (e.g. water) or a non-Newtonian liquid (e.g. carboxymethyl cellulose and activated sludge); 2) Analyzing the role of the tube geometry (two tube diameters of 6.3 and 9.9 mm were used) with respect to the gas slug rising velocity; and 3) Verifying if the degree of coalescence varies depending on the liquid properties (see section 1.3). Herein, the quantitative measure that is used for comparison is based on slug rising velocities determined using a high speed camera.

2.1 Setup description

A schematic of the experimental setup is presented in Figure 2.1. A Plexiglas tube, with dimensions similar to those of a tubular membrane in commercial X-Flow modules (Norit, The Netherlands), were used to collect the measurements (i.e. length of 2 m, inner diameter of 6.3 and 9.9 mm). A measurement cell was located half way along the length of the tube (at a height of 1 m). Surface shear stresses and rising velocities were measured as gas slugs flowed through the measurement cell. A MasterFlex pump and rotameter were used to control the flow of liquid (i.e. electrolyte solution), and a nitrogen gas cylinder and gas flow meter were used to control the flow of gas (i.e. nitrogen) through the system. Nitrogen gas was used instead of air to avoid the oxidation of the ferri- and ferrocyanide in the electrolyte solution. The mixture of nitrogen gas and the electrolyte solution flowed from the Plexiglas tube to a solution storage tank where nitrogen gas was released to the atmosphere. The solution storage tank was submerged in a temperature controlled water bath to maintain the temperature at 20°C for all experiments. The entire experimental set-up was placed inside an electrically grounded metal wire mesh cage to minimize electromagnetic interferences that can affect the measurements taken using electrochemical shear probes (Nakoryakov et al., 1986; Nakoryakov et al., 1989; Zheng and Che, 2006). A high speed camera (HSC) (Kodak Ektapro 1000 Imager) was placed in front of the flow cell. These conditions correspond to typical expected operating ranges in full scale side-stream MBRs.

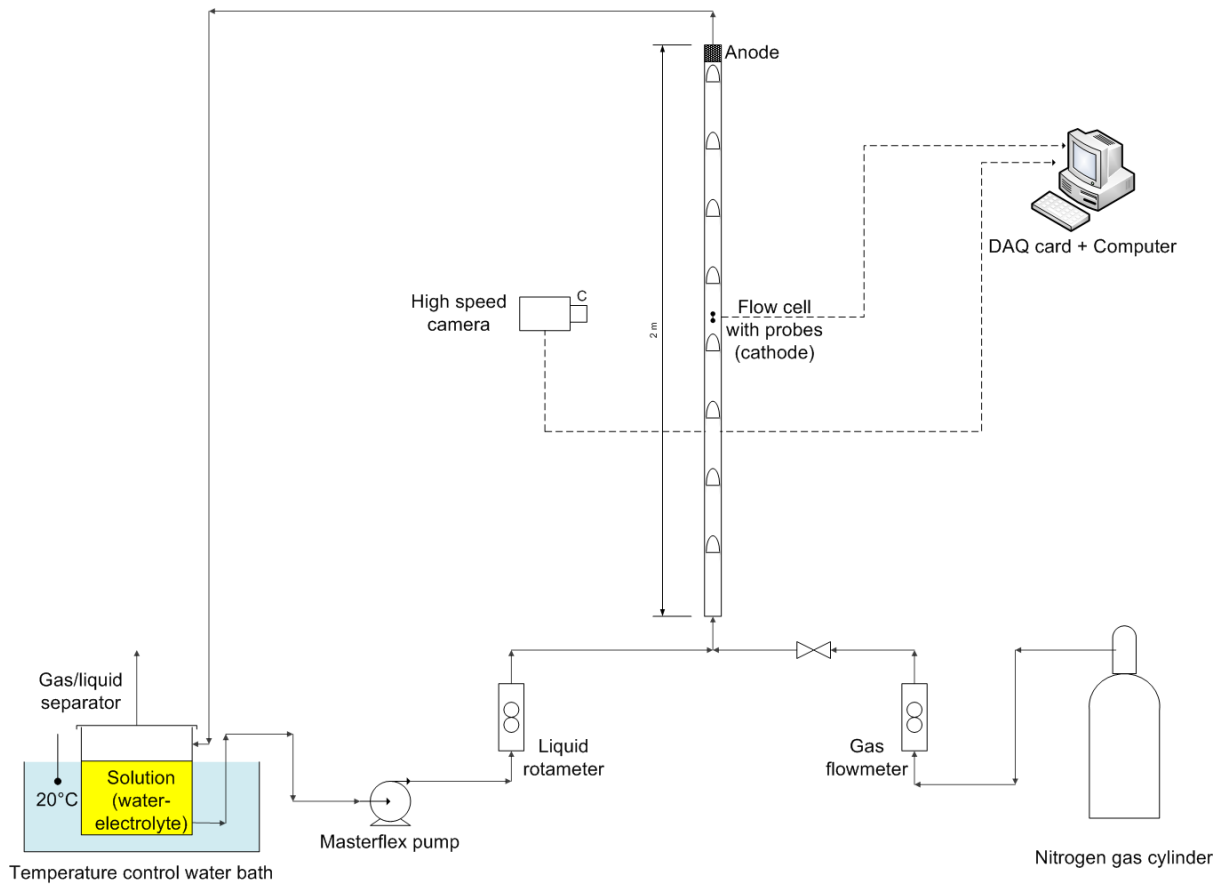


Figure 2.1 Experimental setup

A total of 15 experimental conditions, corresponding to flow rates of 0.1, 0.2, 0.3, 0.4 and 0.5 $\text{L}\cdot\text{min}^{-1}$, for the electrolyte solution, and flow rates 0.1, 0.2 and 0.3 $\text{L}\cdot\text{min}^{-1}$, for the nitrogen gas, were investigated. Gas slugs were fully developed before reaching the flow cell (Lakehal et al., 2008). For each experimental condition, data was collected for a period of 10 seconds; and each experimental condition was repeated six times, to verify the reproducibility of data.

The HSC (Figure 2.2) recorded digital images at a rate of 500 frames per second during a period of approximately 3.25 sec for each experimental condition (i.e. liquid-gas mixture). From the digital images the rising velocity of the gas slugs ($u_{TB,exp}$) was determined using the time required to travel between reference lines (l_{ref}) placed 5 cm apart (Figure 2.2b).

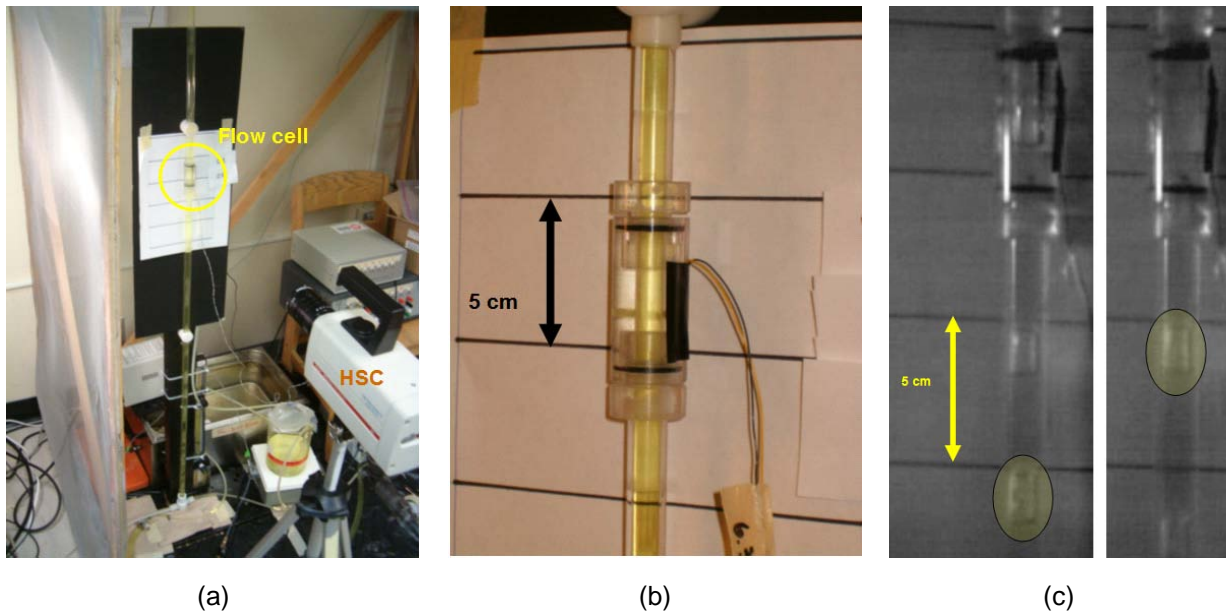


Figure 2.2. (a) Flow cell and HSC, (b) Close-up of the flow cell and reference lines to measure velocity and (c) HSC images of gas slugs rising by reference lines for a water-N₂ mixture of 0.1-0.1 L·min⁻¹

Since the time (t) taken for the gas slug (nose) to travel between the reference lines (5 cm) is known (obtained from the HSC videos), as illustrated in Figure 4c, it is possible to determine the velocity of the rising gas slug using equation (2.1).

$$u_{TB,exp} = \frac{l_{ref}}{t} \quad (2.1)$$

2.2 Properties of the fluids

The experiments were made using nitrogen gas instead of air to avoid electrolyte oxidation. The density and viscosity of nitrogen gas are 1.17 kg·m⁻³ and 1.755·10⁻⁵ Pa·s, respectively, at 20°C.

The surface tension for the water-air, CMC-air and sludge-air were measured resulting in 0.072, 0.075 and 0.069 N·m⁻¹, respectively (Fisher Scientific Surface Tensiometer 20). Note that the surface tension of the liquid-nitrogen was assumed to be similar to that of liquid-air, as it was not practically possible to measure the surface tension with nitrogen gas. To determine the impact of the surface tension on the slug flow (i.e. shape and size of the bubbles), the Weber number (We) for the gas can be used:

$$We = \frac{\rho_g u_{TB} d}{\sigma} \quad (2.2)$$

When We is smaller than 1, the surface tension dominates the regime, and when it is larger than 1 the inertial forces dominate the flow regime. For this study, the slug rising velocities were found to be between 0.6 and 0.9 m·s⁻¹, which results in Weber numbers between 0.03 and 0.12. Therefore, in the present study, surface tension significantly affects the behaviour of the slug flow. Changes in surface tension of the liquid phase (e.g. adding surfactants) were not explored but they will likely affect the shape of the bubble (inter-phase liquid-gas) and may affect the shear profile near the wall (Clarke and Issa, 1997; Zheng and Che, 2007). The other properties were already discussed in section 1.3.

Recently, Tzotzi et al., (2009) performed a study on the impact of thermo-physical properties on flow patterns in horizontal tubes using different liquids (water and n-butanol-water solution) and gas (air, CO₂ and He) mixtures. They found that the surface tension does not affect the slug flow boundaries in the horizontal flow pattern map but it does affect the boundaries of the other flow patterns (bubble, stratified and annular). It is important to highlight, though, that the slug flow in the mentioned study was developed in horizontal tubes, unlike the one used in this study, which used a vertical configuration.

2.3 Gas slug rising velocity

The regime of the two-phase flow was determined based on the mixture Reynolds number (equation 1.33) (Figure 2.3).

From Figure 2.3, it is possible to observe the following: 1) for the water-gas mixtures, in 6.3 mm diameter tube the flow is either laminar ($Re_m < 2000$) or in the transition regime ($2000 < Re_m < 4000$), depending on the mixture velocity. For the 9.9 mm diameter tube, the flow is exclusively in the laminar regime; 2) for CMC- and sludge-gas mixtures, the flow is exclusively in the laminar regime.

The mixture velocities versus the slug rising velocities (obtained from the HSC), for the two tube diameters and the three different mixtures investigated are presented in Figure 2.4.

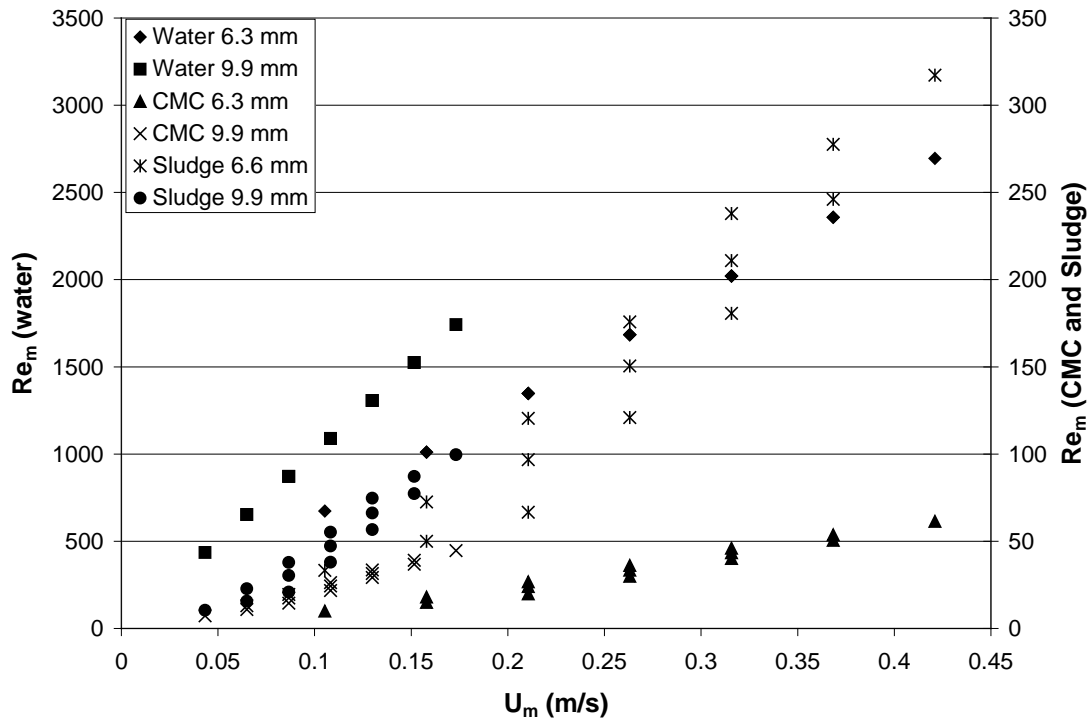


Figure 2.3. Mixture velocity vs. mixture Reynolds number for two tube diameters (6.3 and 9.9 mm) and three different solutions considered (water, CMC and sludge)

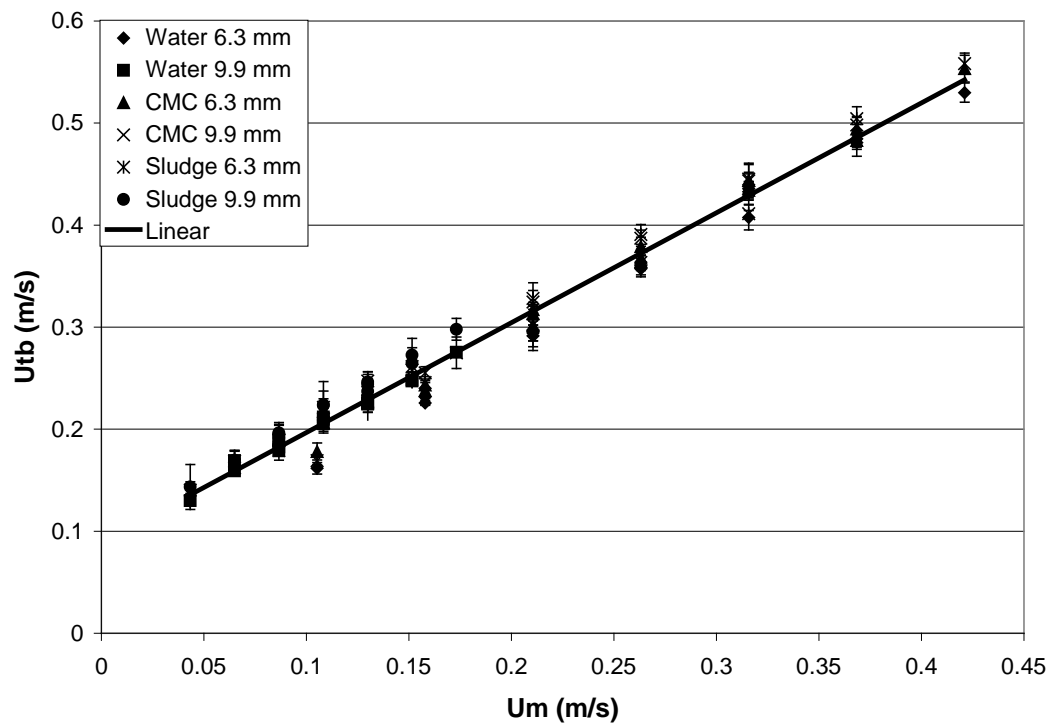


Figure 2.4. Mixture velocity vs. slug rising velocity for two tube diameters (6.3 and 9.9 mm) and three different liquids (water, CMC and sludge)

As expected based on equation (1.31) and (1.34), for all conditions investigated, a linear relationship (equation (2.3)) was obtained between the mixture velocity and the rising slug velocity.

$$u_{TB} = C u_m + k_{TB} \left(g d \frac{(\rho_L - \rho_G)}{\rho_G} \right)^{0.5} \quad (2.3)$$

It is possible to develop three correlations: one for each tube diameter (case 1 and 2) and one for the combination of the two tube diameters (case 3), the result is summarized in Table 2.1.

Table 2.1. Parameters of equation (2.3) for the three cases

	6.3 mm (Case 1)	9.9 mm (Case 2)	6.3 & 9.9 mm* (Case 3)
C	1.192 ± 0.021	1.088 ± 0.033	1.140 ± 0.010
k_{TB}	0.216 ± 0.024	0.301 ± 0.012	0.279 ± 0.007
R^2	0.996	0.962	0.990

* Figure 2.4

From Table 2.1, comparing the data obtained experimentally with the theory (section 1.5.2.1). It is possible to observe the following:

Literature values of C are reported between 1.2 and 2. For case 1, C is ~1.2, which has been reported for C under turbulent conditions (Frechou, 1986). For case 2, C is ~1.1, a discrepancy that could be due to a larger tube diameter. Mercier-Bonin et al. (2000) reported a C value of 1.02 for a 15 mm diameter tube, showing the same tendency. For case 3, C ~ 1.15 which is an average between case 1 and 2. This confirms that C depends on the tube diameter and it should be accounted for.

The value of k_{TB} is reported in literature to be 0.35. For case 1, k_{TB} is ~0.2, which is smaller compared to the empirical value. The discrepancy between the experimental and the theoretical relationship can be due to an increase in the gas slug rising velocity brought about by bubble coalescence (Pinto et al., 1998; Pinto et al., 2001). For case 2, k_{TB} is ~0.3, which is closer to the empirical value. Hence, the hypothesised coalescence phenomenon is less profound in this case, which is confirmed later as coalescence is typically delayed in

larger diameter tubes. Possibly, this difference is due to different viscosity effects, which are not included in the theoretical equation. Hence, these theoretical literature models are not entirely valid for non-Newtonian liquids and for different diameter tubes.

In this work, this value of k_{TB} was calculated as one part of the intercept in the linear correlation from equation (2.3). However, this value can be calculated experimentally, based on the rising velocities of gas slug in stagnant liquid and is related to the Froude number (Bugg et al., 1998; Bugg and Saad, 2002). However, measurements with stagnant liquid were not performed to determine whether the physical properties (density, viscosity and surface tension) have any effect on the rising velocity.

Also, it is important to consider that C and k_{TB} might be influenced by the multiple flow regimes that occur in slug flow, i.e. the falling film and wake zones being highly turbulent and the liquid zone being laminar. This could also impact the value of this parameter (Mayor et al., 2007; Mayor et al., 2008).

It is possible to conclude that C and k_{TB} depend on physical properties (density, viscosity and surface tension) as well as geometry (diameter of the tube) and operational conditions (superficial velocities) for Reynolds numbers in laminar regime. However, it is important to highlight that experiments were not performed under a turbulent regime, where these properties may not have as much of an impact as in laminar regime. Also, it is important to note that the range of flow rates used in this study are limited to the range applied in real vertical tubular side-stream MBRs (Futselaar et al., 2007).

Using equations (1.31) to (1.44), allows quantification of the falling film velocity, the void fraction and the thickness of the falling film of liquid as a function of both the mixture velocity and tube diameter (Figure 2.5). The recovered linear relationships are summarized in table 2.2.

Table 2.2. The falling film velocity, the void fraction and the thickness of the falling film of liquid as a function of the mixture velocity for 6.3 and 9.9 mm

	6.3 mm	9.9 mm
Falling film velocity ($\text{m}\cdot\text{s}^{-1}$)	$u_{ff} = -0.0950u_m + 0.6202$	$u_{ff} = -0.0773u_m + 0.7285$
Void fraction (-)	$\alpha_{TB} = -0.0352u_m + 0.8775$	$\alpha_{TB} = -0.0305u_m + 0.8915$
Thickness falling film (m)	$\delta_L = -5.89 \cdot 10^{-5} u_m + 1.99 \cdot 10^{-4}$	$\delta_L = -7.98 \cdot 10^{-5} u_m + 2.76 \cdot 10^{-4}$

From Figure 2.5a, it is possible to say that the thickness of the falling film zone for the tube of 9.9 mm is 50 % larger compared to the 6.3 mm tube at the same mixture velocity. This

thickness decreases as the mixture velocity increases which could be expected since at high mixture velocities the space between the bubble and the tube decreases. In Figure 2.5b, the void fraction increases only marginally with the tube diameter, which indicates that the void fraction of the gas slug does not depend on the tube diameter. Moreover, the increase in void fraction at elevated mixture velocity is marginal. Figure 2.5c reveals that the falling film velocity for the 9.9 mm tube is 20 % higher compared to the 6.3 mm tube at the same mixture velocity.

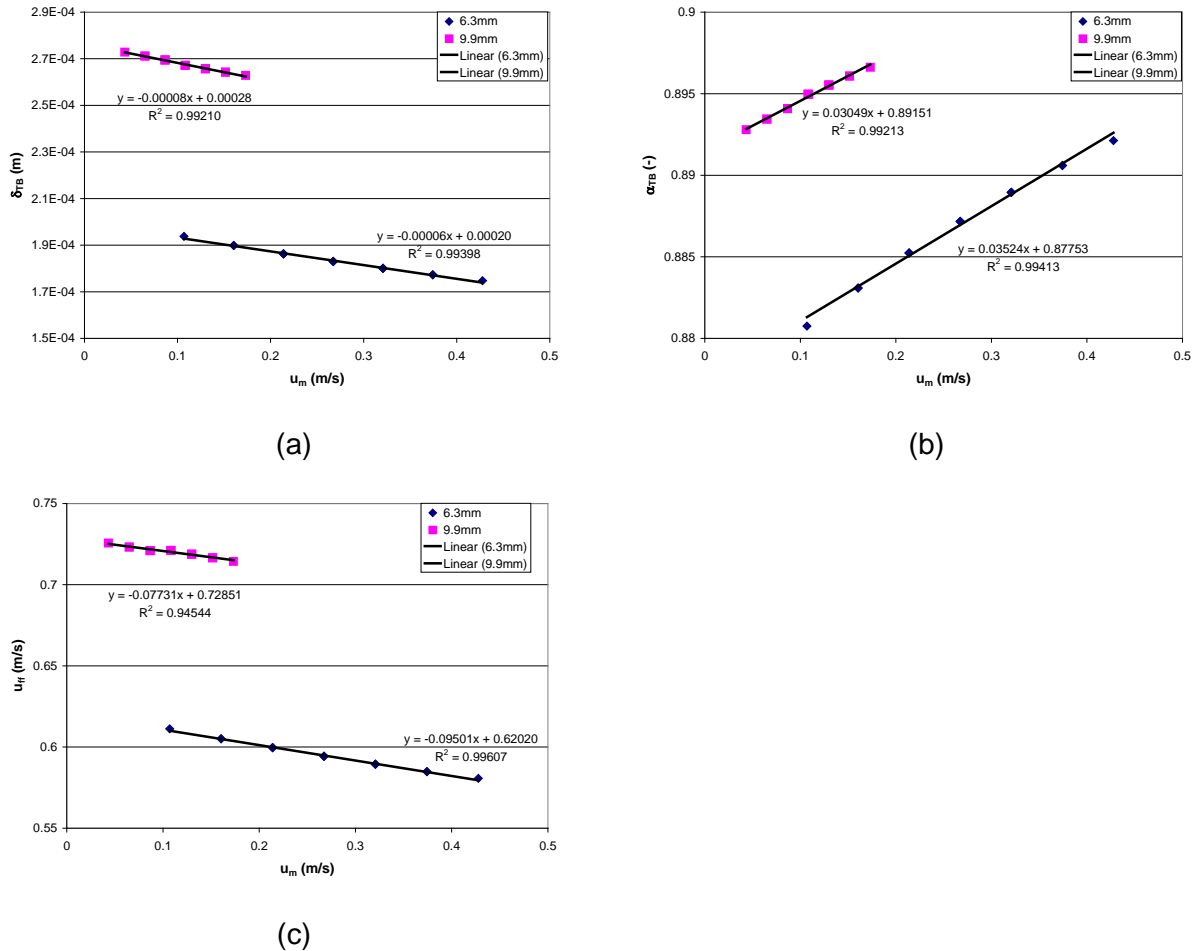


Figure 2.5. Mixture velocity vs (a) thickness of the falling film zone, (b) void fraction of the gas and (c) falling film velocity.

It is necessary to highlight that the relationships presented in table 2.2 were derived from equations from section 1.5.2.1, where none of the equations has a parameter as a function of viscosity. However, solely based on this it is impossible to conclude that they are independent of the viscosity. Nevertheless, it is important to emphasize that the void fraction is defined as the fraction of the total tube cross-sectional area occupied by the gas phase. Therefore, this void fraction can be correlated to the film thickness. Literature provides evidence that void fraction correlations for Newtonian fluids can be used for non-Newtonian fluids, given the non-Newtonian Reynolds number is used. The latter accounts for the non-Newtonian viscosity, from which it is possible to derive that the film thickness will be similar

(Farooqi and Ricardson, 1982; Heywood and Charles, 1979; Rosehart et al., 1975). However, detailed experiments, i.e. measurements of the thickness and velocity of the falling film zone, are required to further confirm this, which is a tedious task and was outside the scope of this work.

2.4 Qualitative behaviour of gas slugs

Besides extracting the gas slug rising velocity, it was possible to observe the coalescence behaviour of the slugs in vertical tubular systems from the recorded HSC images. For different mixture velocities, tube diameters and solutions considered, diverse behaviour was observed (Figure 2.6).

From Figure 2.6, it is possible to observe the coalescence phenomena at 1 m height (i.e. location of flow cell). This coalescence happens due to the fact that the space between two successive rising gas slugs is not constant, promoting slugs to join when they are ascending. Two slugs join together when the space between them gets smaller and the trailing slug reaches the wake of the leading slug, which makes the trailing slug accelerate and finally coalesce with the leading slug (Polonsky et al., 1999). It was observed that the slugs at the bottom of the tube (entry of gas and liquid) are small (they were not recorded by the HSC) and when they ascend, steadily grow due to coalescence.

For the water-gas mixture, the coalescence between two slugs occurs immediately when they join. On the other hand, for the non-Newtonian mixtures (CMC and sludge) that were investigated in the present study, it was found that despite the fact that rising slugs come into contact with each other, they do not immediately combine to form one larger slug (e.g. CMC and sludge at $0.2-0.3 \text{ L}\cdot\text{min}^{-1}$) and they need more time (longer distance) to coalesce and turn into a single, longer slug. Sousa et al. (2007) mentioned that in non-Newtonian liquids a “negative wake” exists behind the slug bubbles, which is an inhibitor of coalescence. That may explain the train of bubbles and delay the coalescence (Sousa et al., 2007). Another hypothesis could be the higher viscosity of the liquid, requiring a larger force to push out the remaining liquid between the slugs. Indeed, a fluid that exhibits a higher viscosity will resist more to the “pushing out” of the remaining liquid between two gas slugs that are about to coalesce. Therefore, it could take longer for a high viscosity liquid to allow coalescence which significantly impacts the slug flow pattern and all properties related to it like local shear stress near the membrane surface. The higher viscosity would in this case be brought about by the Non-Newtonian rheological behaviour of activated sludge. This hypothesis could also be valid for Newtonian liquids that have a higher viscosity (i.e. glycerol). However, no experiment was performed to confirm this. Moreover, the surface tension was found to be relatively similar for all the three mixtures. Dedicated surface tension measurements are required to be conclusive on its effect on coalescence of slugs.



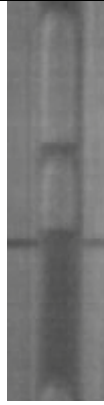
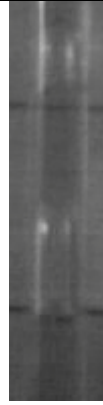














	6.3 mm			9.9 mm		
Flow rate (L·min ⁻¹) liquid-gas	Water	CMC	Sludge	Water	CMC	Sludge
0.1 – 0.1						
0.2 – 0.3						
0.3 – 0.5						

Figure 2.6. Different gas slug coalescence at different flow rates and tube diameters (taken at 1 m height).

Another observation is that the aforementioned phenomenon actually does not occur at smaller tube diameters. It is not clear why this is the case. Hence, it seems that the qualitative behaviour of a slug flow is significantly affected by both viscosity and tube diameter.

2.5 Conclusions

The behaviour of three substances were studied in a slug flow pattern: one was a Newtonian liquid (water) and the other two were non-Newtonian liquids (CMC and activated sludge). A quantitative study was performed based on the gas slug rising velocity, which resulted in a similar equation as reported in literature. However, the recovered relationship predicted smaller values compared to the theoretical literature equation. The following reasons were hypothesised: 1) the slope of the theoretical equation does not account for the diameter of the tube, which clearly influenced the TB rising velocity prediction, 2) the intercept of the theoretical equation includes the diameter of the tube but it does not include the viscosity of the substance which may affect the rising velocity and 3) the experimental measurements were made in laminar-transition regime and the theoretical equation was developed for turbulent regime. This, indeed, could influence the final expression, as it may make the expression more sensitive to the geometry (tube diameter) and thermo-physical properties of the fluids (viscosity).

From a qualitative point of view, it was possible to see the following: 1) for a Newtonian liquid (water), the coalescence occurs immediately after a gas slug encounter; 2) for non-Newtonian liquids (CMC and sludge), the coalescence of two bubbles does not occur instantaneously, and forms a “train of bubbles” which was more evident in the tube of 9.9 mm. This was hypothesised to be caused by increased viscosity which opposes more to the coalescence. Therefore, viscosity deserves more attention and will be investigated further in chapter 6.

Chapter 3. Shear stress quantification and relationship with energy consumption in a slug flow

Abstract*

Application of a two-phase slug flow in side-stream MBRs has proven to increase the permeate flux and decrease fouling through a better control of the cake layer. Literature has shown that the hydrodynamics near the membrane surface have an impact on the degree of fouling by imposing high shear stress near the surface of the membrane. An experimental setup was developed to investigate the shear stress imposed on the surface of a membrane under different two-phase flow conditions (gas and liquid), by varying the flow of each phase. Due to the random behaviour of the shear stress values, caused by the continuous passing of slugs and their difference in size (coalescence), the results were analysed using shear stress histograms (SSH). A bimodal SSH was observed, with one peak corresponding to the shear induced by the liquid slug, and the other induced by the gas slug. This distribution was modelled using simple empirical relationships. Literature suggests that fouling control is expected to be optimal when the frequency of shear stress induced by the liquid slug is approximately equal to that induced by the gas slug. Therefore, the simple empirical relationships could be used to identify the two-phase flow conditions that optimize fouling control. For these conditions, the total energy consumption of the system was estimated based on the two-phase pressure drop. It was found that a combination of low liquid flow rates and relatively high gas flow rates (around 4 times higher than liquid flow rate) balances the peaks in the SSH and minimizes the energy consumption.

* Redrafted after:

Ratkovich, N., Chan, C.C.V., Berube, P., Nopens, I., Analysis of shear stress and energy consumption in a tubular airlift membrane system. *Journal of Membrane Science* (submitted).

Introduction

It has been documented that for a given bulk flow velocity, the shear stresses induced by two phase flow are substantially larger than those induced by single phase (Laborie and Cabassud, 2005). However, the mechanism governing the mass transfer of foulants under two-phase flow conditions are poorly understood, and therefore, a trial-and-error experimental approach is typically used to optimize the hydrodynamics of two-phase flow near membrane surfaces. This two-phase approach results in an increase in energy consumption (Laborie et al., 1998), because compressed air is introduced into the system, without fully understanding the two-phase slug flow hydrodynamics and how the shear affects the processes taking place near the membrane surface. It is well documented that slug flow is considered to be the best flow pattern in terms of foulant removal (Cui et al., 2003) compared to other flow patterns (section 1.5.1). Nevertheless, to optimize airlift tubular membrane systems, it is necessary to have proper understanding of magnitude and dynamics of surface shear stresses in these systems. For slug flow, three different zones can be distinguished (section 1.5.2.1). Each of these zones generates different magnitude and directions of shear stresses near the membrane surface. Zone 1 generates a “negative” shear stress because the flow moves in the opposite direction of the gas slugs. Zone 2 generates an oscillating shear due to the mixture between liquid and gas and zone 3 generates a “positive” shear because the liquid moves in the same direction as the gas slugs.

A number of studies have suggested that changes in the direction of surface shear stresses are more important than the magnitude of the actual forces themselves (Ducom et al., 2003; Ochoa et al., 2007; Rochex et al., 2008). Ochoa et al. (2007) developed a setup to study the behaviour of a biofilm subjected to an erosion test in which a non-uniform distribution of local shear stresses was applied in a modified Couette-Taylor reactor. The biofilm was developed homogeneously on plastic sheets under low shear stress conditions and once at steady state, shear stresses were imposed to the biofilm. The local hydrodynamics in the setup was analysed experimentally and numerically (CFD). The distribution of the shear stress was determined and two zones with different hydrodynamic characteristics were found. A first one, where the shear stress was constant (and always pointed in the same direction) and a second one, exhibiting a sudden contraction allowing detachment of stream lines (backflow), inducing the formation of a recirculating loop. In the first zone, the biofilm was not removed, whereas in the second zone biofilm removal was observed. This strongly indicates that conditions promoting evenly distributed positive and negative peaks, are likely to promote better fouling control in membranes. However, this is a hypothesis and needs further confirmation.

This chapter focuses on characterizing the shear stress profiles in an airlift tubular system using electrochemical shear probes. These shear probes have been used experimentally to study the hydrodynamics of slug flow in tubular systems. This method uses an electrolyte solution with a well known stoichiometry reaction which allows estimation of surface shear stresses from a difference in electrical potential (Gaucher et al., 2002). Subsequently, a simple numerical approach to correlate the experimentally determined surface shear stress

to the energy consumed in airlift tubular systems is developed. This allows determination of the optimal multicriteria operating conditions in terms of fouling control and minimal energy consumption. (Pal et al., 1980; Spedding et al., 1998; Tchobanoglous et al., 2003; Tengesdal et al., 1999).

3.1 Surface shear stress measurements

The setup description was introduced in section 2.1. The measurement cell contained two electrochemical shear probes (cathodes) aligned vertically (i.e. in the direction of flow) and separated by a distance of approximately 0.3 mm (Figure 3.1).



Figure 3.1. Shear probe

This configuration enabled to measure both the magnitude and direction of the shear stresses (i.e. the magnitude of the signal from the probe that is upstream provides the true reading and is higher than the magnitude of the signal from the probe that is downstream) (Cognet et al., 1978). Each probe was constructed using platinum wires (0.5 mm diameter), machined to be flush with the inside of the tube surface (Berube et al., 2006). Because of the machining process the shear probes were observed (digital microscope with Motic Images v2.0 software) to be slightly oval with an average diameter slightly larger than 0.5 mm (i.e. 0.54 mm). The surface of the machined probe was also observed to be uneven, further increasing the actual surface area of the probe. A stainless steel fitting (anode) was located downstream of the shear probes (i.e. measurement cell). A potential of 300 mV was applied between the anode and shear probes (cathode) (Chan et al., 2007). The electrolyte solution contained ferri- and ferrocyanide as described by Chan et al., 2007.

Each probe had its own independent measurement circuit. The shear probe signals were obtained via the voltage drop across the 100 Ω resistor. This signal was then conditioned through an amplifier and a low pass filter. A data acquisition box with two different channels acquired the signals from the probes at a frequency of 1000 Hz, and real time data was recorded using a custom Labview (National Instruments, USA) application. Currents (in the range of μA) flowing through the electrolytic circuit are converted to a voltage drop value via a resistor (100 Ω) and a subsequent amplifier ($G = 1000$). As a result, shear signals recorded in LabView (National Instruments, USA) are in units of Voltage. For the set up, an intrinsic instrument bias exists (there is a background signal from the signal processing unit even when probes are not plugged into the circuit). To correlate the voltage readings back to shear measurements, the following procedure described in literature was used (Rosant, 1994).

The current (I_L) through the system can be calculated based on the corrected signal (V), resistor value and known amplifier gain:

$$I_L = \frac{V}{RG} \quad (3.1)$$

where V is the voltage signal (V), R is the resistance (= 100 Ω), G is the amplifier gain (= 1000). Knowing the current, it is possible to determine the mass transfer coefficient (k_m) of the electrolyte:

$$k_m = \frac{4I_L}{v_e F \pi d_e^2 C_o} \quad (3.2)$$

where v_e is the number of electrons involved in the reaction (= 1), F is the Faraday constant (= 96 500 $\text{C}\cdot\text{mol}^{-1}$), d_e is the diameter of the probe (m), C_o is the bulk concentration of ferricyanide (= 3 $\text{mol}\cdot\text{m}^{-3}$). The mean wall velocity gradient (or shear rate \bar{S}) is then defined by:

$$\bar{S} = \frac{d_e}{D_f^2} \left(\frac{k}{0.862} \right)^3 \quad (3.3)$$

where D_f is the diffusion coefficient of ferricyanide ($7.14 \cdot 10^{-10} \text{ m}^2 \cdot \text{s}^{-1}$ at 20°C (Rosant, 1994)) and μ_L is the dynamic viscosity of the solution ($= 0.001 \text{ Pa} \cdot \text{s}$). Since the electrolyte is a Newtonian liquid, the shear stress is defined by:

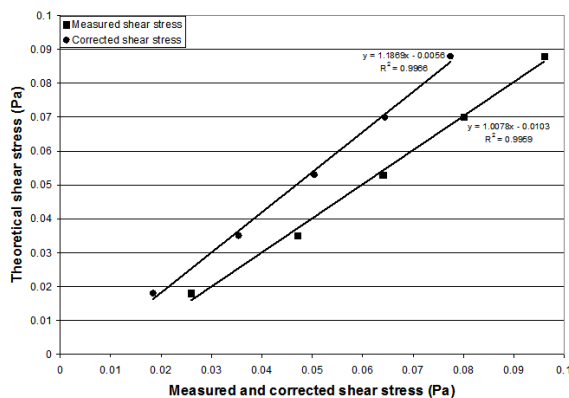
$$\tau = \mu_L \bar{S} \quad (3.4)$$

Combining equations (3.1) to (3.4) yields a direct relation between the voltage and the shear stress:

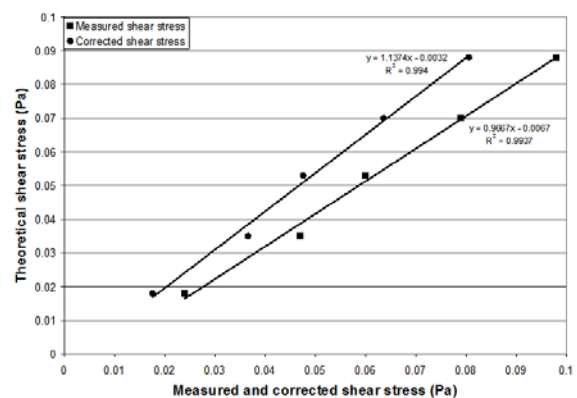
$$\tau = \mu_L \left[\frac{4.64 \text{ V}}{\left(v_e F \pi d_e^{\frac{5}{3}} C_o D_f^{\frac{2}{3}} R G \right)} \right]^3 \quad (3.5)$$

It is important to note that the following assumptions were made in deriving equation (3.5): 1) the axial diffusion is negligible, 2) the velocity gradient normal to THE surface is negligible relative to that parallel to the surface, 3) a linear velocity gradient exists in the region of the probe surface, and 4) a quasi-steady-state condition exists near THE probe surface.

The surface shear stresses, measured with the shear probes, were compared to those calculated theoretically using equation (1.13) and (1.14), for single-phase flow conditions (Figure 3.2). If perfect, this would give rise to a linear curve with slope 1.



(a)



(b)

Figure 3.2. Measured and corrected shear stress vs theoretical shear for (a) probe 1 and (b) probe 2.

The small discrepancies between the measured and calculated surface shear stresses were attributed to the fact that the surface of the shear probes was not perfectly round and flat. To correct for this, the measured probe diameter (d_e) was multiplied by a geometric calibration factor that resulted in the measured surface shear stresses being similar to the calculated surface shear stresses. The geometric correction factors for the two shear probes used in the present study were 1.034 and 1.035. For the experimental conditions investigated, the Reynolds number ranged from 218 to 1090, which is in the laminar flow range ($Re < 2000$).

The shear probes used in the present study are expected to be able to capture rapid changes in surface shear stresses caused by the passage of gas slugs (Gradeck and Lebouché, 1998; Pallares and Grau, 2008b). For the experimental conditions investigated, the fastest changes in shear measurements were observed to occur over a period of approximately 100 ms (i.e. frequency of 10 Hz) and the magnitude of the peak surface shear measurements ranged from 1 to 2 Pa. To obtain consistently accurate surface shear stress measurements, the surface of the shear probes was cleaned with cotton buds, between each experiment.

A typical shear event, induced by a gas slug passing by the shear probes, is illustrated in Figure 3.3a and 3.3b in terms of the measured raw voltage signals and surface shear stresses, respectively.

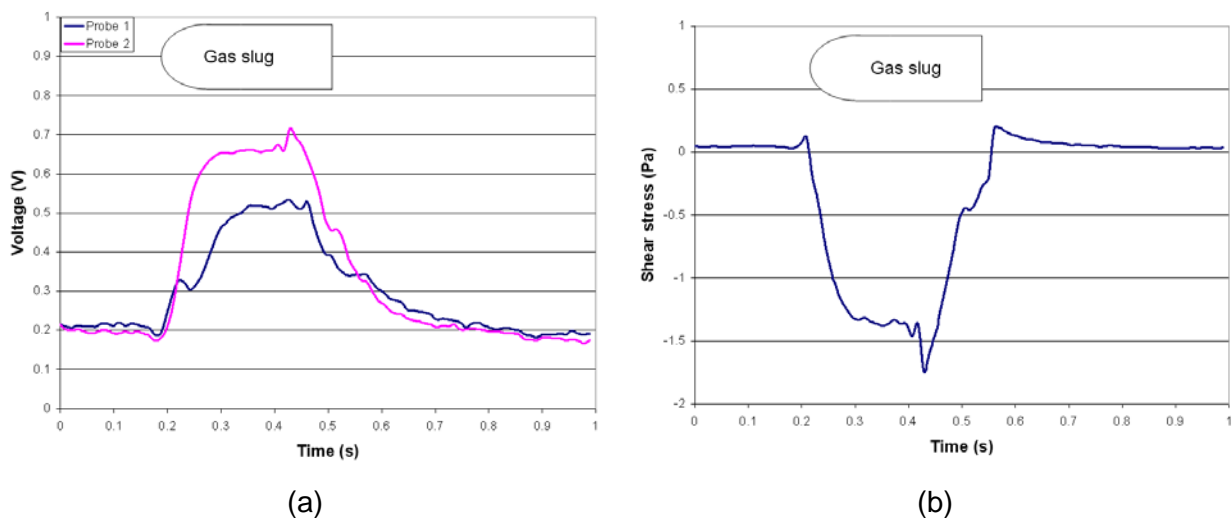


Figure 3.3. (a) Raw voltage signal for the two probes and (b) conversion to shear stress for a water-N₂ combination of 0.1-0.1 L·min⁻¹ during a period of 1 sec.

As presented, upstream and downstream of a gas slug, the magnitude of the surface shear stress was relatively low (i.e. 0.1 to 0.3 Pa) and positive (i.e. in the direction of liquid flow). However, in the presence of a gas slug, the magnitude of the surface shear was relatively high (i.e. 1 to 2 Pa) and negative (in the opposite direction of the overall liquid flow). Positive surface shear stresses of relatively high magnitude (i.e. 0.5 Pa) were also periodically

measured for a short duration in the wake section of a gas slug. These results are consistent with those from previous studies that investigated the surface shear stresses induced by rising gas slugs (Nakoryakov et al., 1989; Zheng and Che, 2006). Taha and Cui (2002a) used a tube diameter of 12.7 mm, with a liquid and gas superficial velocity of 0.2 and 0.08 $\text{m}\cdot\text{s}^{-1}$. They obtained shear stress values between -2 and 1 Pa, which is in the same order of magnitude as those observed in the present study. The length of the gas slugs, and therefore the duration of a shear event, was observed to vary substantially due to the coalescence of gas slugs as they travelled up the Plexiglas tube (Figure 3.4). However, the magnitude of the peak surface shear stress during a shear event was not observed to vary significantly. The experimental conditions significantly affected the extent to which the gas slugs coalesced. More coalescing between gas slugs was typically observed for the experiments performed with higher gas flow rates and lower liquid flow rates. Therefore, the results imply that the frequency of alternating shear events decreases at higher gas flow rates and lower liquid flow rates.

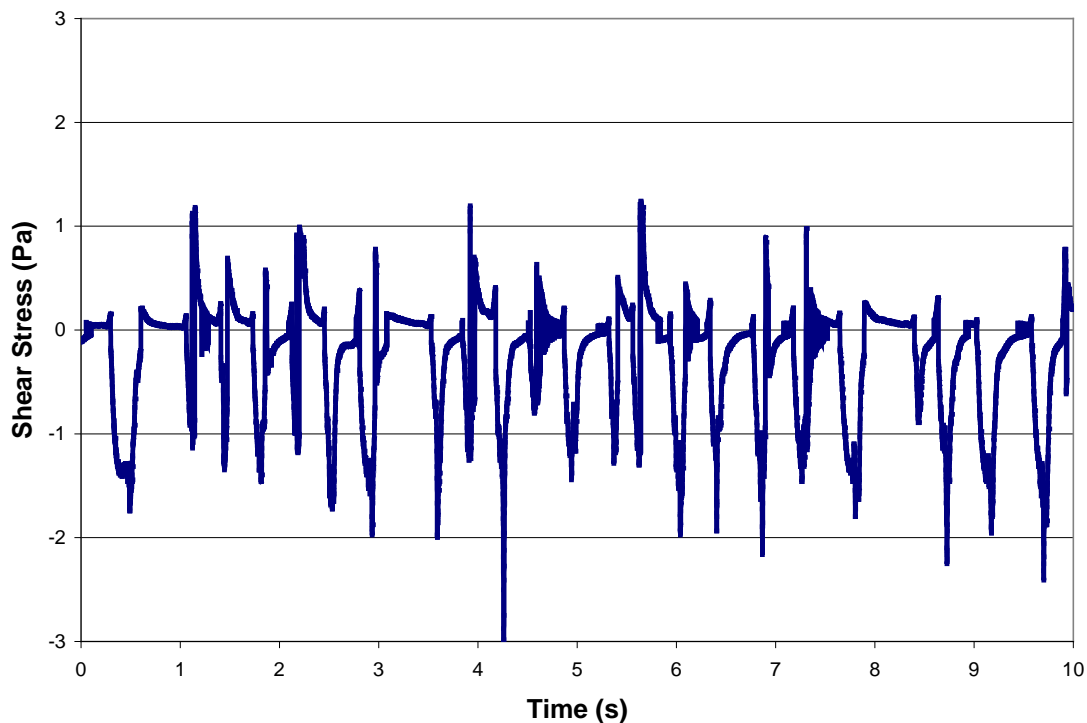


Figure 3.4 Shear stress vs time for water-N₂ 0.1-0.1 $\text{L}\cdot\text{min}^{-1}$.

3.2 Shear stress histograms

This coalescence behaviour makes different experimental conditions hard to compare (Figure 3.4). To overcome the latter, shear stress histograms (SSH) were introduced to explore the effect of the different experimental conditions with respect to the resulting shear stresses. The histograms show the relative frequency at which surface shear stresses of a given magnitude and direction (i.e. sign) occur. The histogram bin size was chosen to be 0.5

Pa, and the considered surface shear range was chosen from -3 Pa to 3 Pa based on the measurements. Smaller bin sizes were considered, but these resulted in highly variable SSHs and made peak identification difficult. The SSHs summarize two important features: 1) the range of shear stresses that the membrane surface experiences and 2) the relative frequency of this exposure. SSH for the different experimental conditions investigated are shown in Figure 3.5.

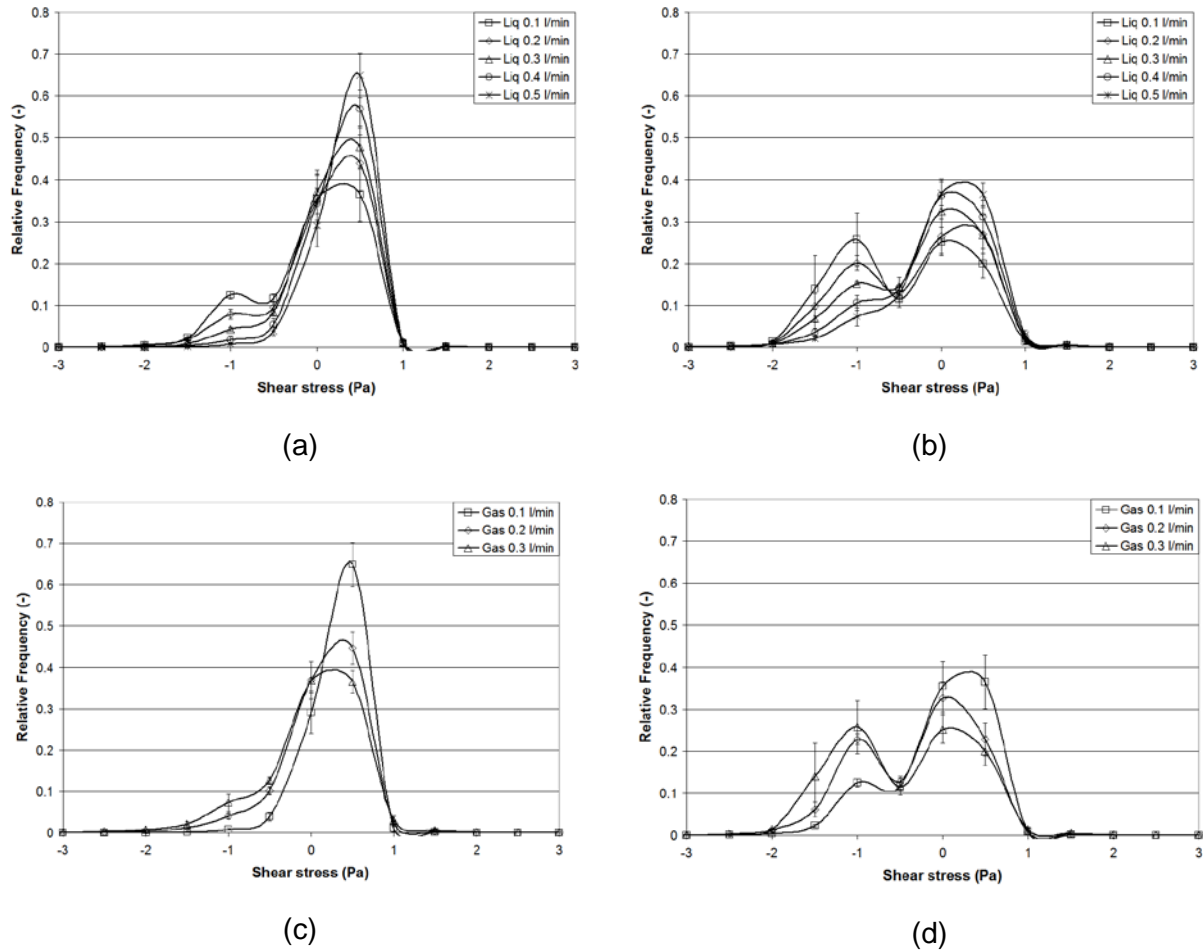


Figure 3.5. Shear stress histogram for two different gas flow rates (a) 0.1 and (b) 0.3 $\text{L}\cdot\text{min}^{-1}$ with five liquid flow rate combinations and for two different liquid flow rates (c) 0.5 and (d) 0.1 $\text{L}\cdot\text{min}^{-1}$ with three gas flow rate combinations.

For all cases, it is possible to clearly distinguish two peaks in the SSH (bi-modal distribution): a first peak occurs at a marginally positive shear value and is caused by the passage of liquid slugs and a second peak occurs at a negative shear value and is caused by the passage of gas slugs (see also Figure 3.3).

The bi-modal distributions observed shape change depending on the gas and liquid flow rate. At lower gas flow rates, the frequency of shear stresses in the positive peak (liquid slug) is larger than that in the negative peak (Figure 3.5a and c) and further increased with

increasing liquid flow rates, also resulting in decrease in frequency in negative shear stresses (gas slug). However, at higher gas flow rates, the frequency of the shear stresses in both the negative and positive peaks are more evenly distributed (Figure 3.5b and d). The best balance is found at lower liquid flow rates, the frequency of the shear stresses in both the negative and positive peaks was more evenly distributed (Figure 3.5d). However, at higher liquid flow rates, the frequency of shear stresses in the positive peak was larger than that in the negative peak (Figure 3.5c) and increased with decreasing gas flow rates. For all cases, increasing the liquid flow rate and decreasing the gas flow rate tends to result in a predominant positive peak. Opposite actions tend to balance the peaks. It is important to highlight that changing gas-liquid flow rates do not impact shear magnitude significantly, at least for these operational conditions investigated. Also, in figure 3.5c and d it is possible to observe an inflection point (~ -0.5 Pa) which is related to the wake and, hence, the shift between the liquid and gas slug. The height of this inflection point can actually be regarded as an indication of the frequency of shift between positive and negative shear, which is thought to be of importance with respect to fouling control rather than shear magnitude. Indeed, a number of studies have suggested that changes in the direction of surface shear stresses are more important than the magnitude of the forces themselves (Ducom et al., 2003; Ochoa et al., 2007; Rochex et al., 2008). Therefore, conditions that promote evenly distributed positive and negative peaks and a high frequency near the inflection point, are likely to promote better fouling control of membrane surface. Although this hypothesis needs further confirmation, it can for now be used to find optimal gas-liquid flow rate combinations that promote these conditions. A model will be developed to find these, given one of the flow rates is chosen or fixed.

3.3 Development of a bi-modal model for shear stress histograms (SSH)

A number of studies have suggested that fouling control can be correlated to the variability (i.e. the frequency of changing shear stress sign) in the magnitude of surface shear stresses (Ducom et al., 2002; Ducom et al., 2003). Therefore, conditions that maximize the occurrence of both positive (liquid slug) and negative (gas slug) shear conditions are likely to promote better fouling control (Ochoa et al., 2007). In order to identify the conditions (gas-liquid flow rates) that equilibrate the occurrence of positive and negative shear conditions (given one of them is fixed or known), an empirical relationship is developed based on Gaussian distributions to model the bi-modal SSH for the different experimental conditions investigated:

$$f(\tau) = \underbrace{\frac{A_1}{w_1 \sqrt{0.5 \pi}} \exp\left[-\frac{2(\tau - \tau_1)^2}{w_1^2}\right]}_{\text{Gas slug}} + \underbrace{\frac{A_2}{w_2 \sqrt{0.5 \pi}} \exp\left[-\frac{2(\tau - \tau_2)^2}{w_2^2}\right]}_{\text{Liquid slug}} \quad (3.6)$$

The first term on the right hand side describes the first peak in the SSH (negative shear stress), which is due to the gas slug, whereas the second term describes the second peak in

the SSH (positive shear stress), which is due to the liquid slug. The factor $A_i/w_i\sqrt{0.5\pi}$ corresponds to the height of each peak, τ_i corresponds to the position of the centre of each peak (average shear), and w_i corresponds to the width of each peak. Equation (3.6) contains six parameters (A_1 , A_2 , w_1 , w_2 , τ_1 and τ_2) that need to be identified from the experimental data.

Equation (3.6) was fitted to the SSHs using SPSS v16 (IBM, USA) to each of the 15 experimental conditions and repetitions investigated. The estimated values of the Gaussian distribution parameters for each experimental condition investigated are presented in Table 3.1. The standard error of each of the estimated values was around 5 %. The R^2 was relatively high ($R^2 > 0.999$) for all experimental conditions indicating that equation (3.6) could be used to model the SSH.

Table 3.1: Gaussian distribution for the bimodal distributions for each experimental condition investigated

Liquid flow rate l·min ⁻¹	Gas flow rate l·min ⁻¹	u_{SL} m·s ⁻¹	u_{SG} m·s ⁻¹	A_1	A_2	w_1	w_2	τ_1	τ_2	R^2
0.100	0.100	0.022	0.022	0.135	0.363	0.727	0.501	-0.781	0.259	0.99993
0.200	0.100	0.043	0.022	0.111	0.389	0.888	0.472	-0.686	0.286	0.99994
0.300	0.100	0.065	0.022	0.098	0.405	0.980	0.495	-0.453	0.296	0.99994
0.400	0.100	0.087	0.022	0.094	0.734	1.092	0.269	-0.112	0.274	0.99998
0.500	0.100	0.108	0.022	0.086	0.824	0.983	0.255	0.034	0.283	0.99994
0.100	0.200	0.022	0.043	0.204	0.281	0.705	0.530	-0.920	0.203	0.99951
0.200	0.200	0.043	0.043	0.163	0.321	0.712	0.571	-0.869	0.210	0.99964
0.300	0.200	0.065	0.043	0.259	0.577	1.378	0.247	-0.387	0.245	0.99951
0.400	0.200	0.087	0.043	0.208	0.295	1.219	0.474	-0.195	0.252	0.99998
0.500	0.200	0.108	0.043	0.170	0.332	1.160	0.460	-0.155	0.293	0.99991
0.100	0.300	0.022	0.065	0.253	0.240	0.777	0.625	-1.065	0.209	0.99980
0.200	0.300	0.043	0.065	0.222	0.271	0.880	0.583	-0.962	0.264	0.99975
0.300	0.300	0.065	0.065	0.189	0.303	0.958	0.637	-0.868	0.229	0.99990
0.400	0.300	0.087	0.065	0.262	0.533	1.435	0.252	-0.365	0.252	0.99934
0.500	0.300	0.108	0.065	0.228	0.275	1.353	0.459	-0.233	0.269	0.99925

Next, simple linear relationships (equations (3.7) to (3.11)) are used to correlate the Gaussian distribution parameters (as dependent variables) with the different operating conditions, i.e. bulk liquid (u_{SL}) and gas (u_{SG}) velocities (as independent variables).

$$A_1 = m_{1,L} u_{SL} + m_{1,G} u_{SG} + b_1 \quad (3.7) \quad A_2 = m_{2,L} u_{SL} + m_{2,G} u_{SG} + b_2 \quad (3.8)$$

$$w_1 = m_{3,L} u_{SL} + m_{3,G} u_{SG} + b_3 \quad (3.9) \quad w_2 = m_{4,L} u_{SL} + m_{4,G} u_{SG} + b_4 \quad (3.10)$$

$$\tau_1 = m_{5,L} u_{SL} + m_{5,G} u_{SG} + b_5 \quad (3.11) \quad \tau_2 = m_{6,L} u_{SL} + m_{6,G} u_{SG} + b_6 \quad (3.11)$$

where $m_{i,L}$, $m_{i,G}$ and b_i are empirical constants. A multivariate linear regression analysis was performed using SPSS v16, in order to estimate the empirical constants for the different Gaussian distribution parameters. The estimate for each empirical constant in equations (3.7) to (3.11), their standard deviation and p value for each experimental condition are presented in Table 3.2.

Table 3.2: Estimate and standard error of empirical constants for Gaussian distribution parameters

	$m_{i,L}$	Std. Error	$m_{i,G}$	Std. Error	b_i	Std. Error	R ²	P value**
A_1	-0.289	0.126	1.212	0.219	0.124	0.013	0.749	0.000
A_2	0.488	0.155	-1.923	0.268	0.395	0.016	0.837	0.000
w_1	4.830	0.396	-1.047	0.686	0.686	0.041	0.926	0.000
w_2	-0.183	0.359	2.695	0.623	0.426	0.037	0.613	0.003
τ_1	6.956	0.786	-6.886	1.362	-0.790	0.082	0.896	0.000
τ_2	0.225	0.096	-0.442	0.166	0.260	0.010	0.512	0.014

** ANOVA test

The R² for the different Gaussian distribution parameters are relatively low ranging from 0.512 to 0.926. To gain further insight into the ability of the simple linear relationship to model the different Gaussian distribution parameters, the SSH predictions using the simple relationships presented in equations (3.6) to (3.11) are compared to those obtained experimentally (Figure 3.6). At high gas flow rates, the frequencies are similar, deviating by less than approximately 5 %. However, at low gas flow rates, the differences between the frequencies obtained numerically and experimentally are slightly higher, exceeding 10 %. These results indicated that although the R² values for simple linear relationships (equation

(4) to (9)), are low (Table 3.2), they could nonetheless be used to model the Gaussian distribution parameters relatively well.

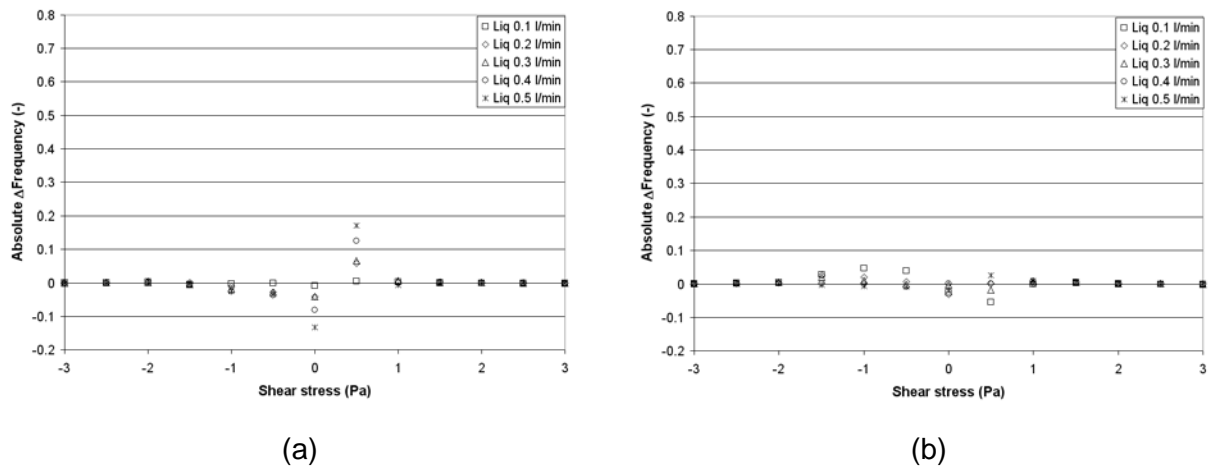


Figure 3.6. Difference in absolute frequency from SSH obtained numerically and experimentally for two different gas flow rates (a) 0.1 and (b) 0.3 l·min⁻¹ with five liquid flow rate combinations.

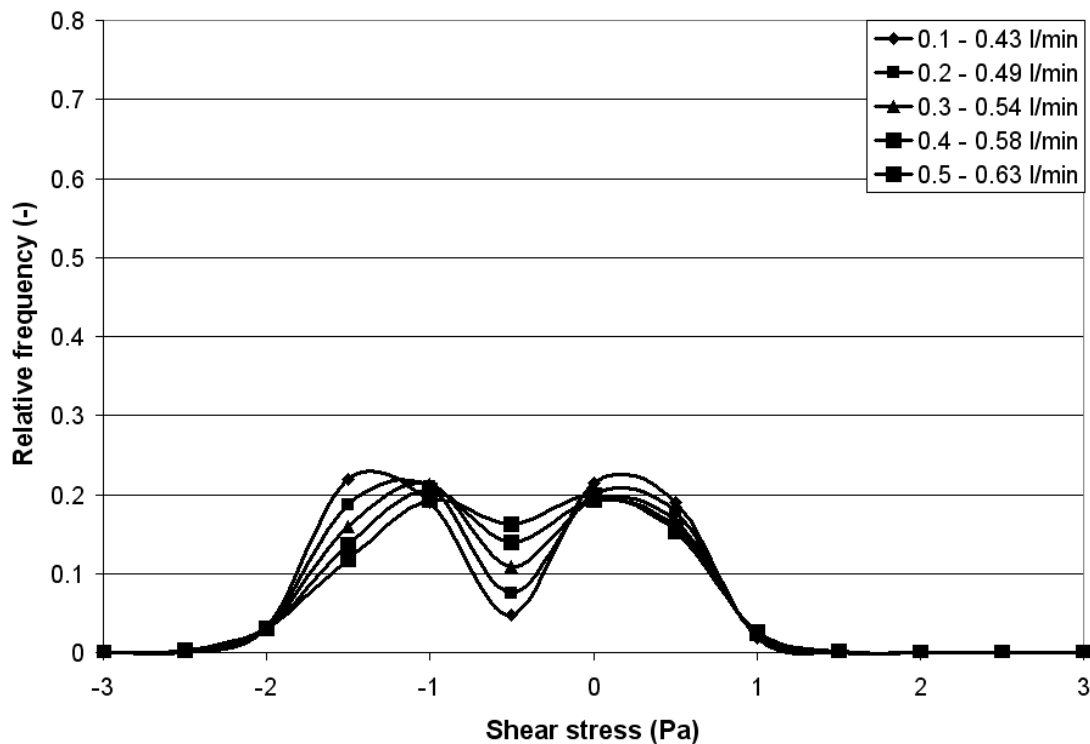


Figure 3.7. SSH for a liquid-gas flow rate that equilibrates the frequency of positive to negative shear conditions

Using the simple linear relationships (equation (3.7) to (3.11)) and the Gaussian distribution (equation 3.6)) validated against measurements, it is now possible to identify conditions (i.e.

liquid and gas flow rate combinations) that equilibrate the frequency of the positive and negative shear peaks in the SSH. Therefore, either the gas or liquid flow rates need to be fixed. Hence, for each liquid flow rate, a gas flow rate that equilibrated the positive to negative shear conditions could be identified by an iterative process. For the liquid flow rates investigated, the corresponding gas flow rates are illustrated in Figure 3.7.

The results indicate that to equilibrate the positive and negative peaks in the bimodal SSH, different gas-liquid ratios than the ones used in the experiments are required. E.g. for a liquid flow rate of $0.1 \text{ L}\cdot\text{min}^{-1}$, a gas flow of $0.43 \text{ L}\cdot\text{min}^{-1}$ is needed to balance the two peaks, which results in a gas-liquid ratio of approximately four times. On the other hand, to balance the two peaks for a liquid flow rate of $0.5 \text{ L}\cdot\text{min}^{-1}$, a gas flow rate of $0.62 \text{ L}\cdot\text{min}^{-1}$ is needed, yielding an approximate gas-liquid ratio of only 1.2. A linear relationship (equation (3.12)) is obtained between the bulk liquid and bulk gas velocities that equilibrate the peaks in the bimodal SSH ($R^2=0.999$):

$$u_{SG} = 0.4849u_{SL} + 0.0841 \quad (3.12)$$

From Figure 3.7, comparing the two bimodal distributions (e.g. $0.1 - 0.43$ and $0.5 - 0.63 \text{ L}\cdot\text{min}^{-1}$), it is possible to observe that for the former case, the two peaks are well established, which means that there is a similar occurrence of positive and negative shears. In the latter case, the two peaks are not as well established. This is caused by high frequency shifts between positive and negative shear stresses. It causes more overlap of both peaks (i.e. both peak maxima are moving towards the origin). Also, the inflection point increases at high gas and liquid low rates and decreases at low gas flow rates. It should be noted, however, that maximising the frequency near the inflection point results in shifts of the peaks to smaller shear magnitudes which is also not wanted. Hence, the optimisation should also account for this phenomenon.

The above analysis indicates that relatively simple models can be used to describe the SSH and identify conditions that equilibrate the two peaks. Note that since the relationships presented in equation (3.6) to (3.11) are empirical, it is recommended not to use the relationship presented in equation (3.12) outside of the range of experimental conditions investigated in this work. Nevertheless, a minor extrapolation is needed for the gas flow rate. The range in which the experimental measurements are performed is based exclusively on the operational range of a real airlift MBR (Futselaar et al., 2007).

3.4 Optimizing energy consumption

Next to fouling control, another factor to consider is energy consumption. The latter can be expressed in terms of the relationships presented in section 1.5.1.2 and 1.5.3. A summary of the calculated total pressure drop and energy consumption for the different experimental conditions investigated is presented in Figure 3.8. For comparison purposes, the calculated pressure drop and energy consumption for single phase liquid flow is also shown.

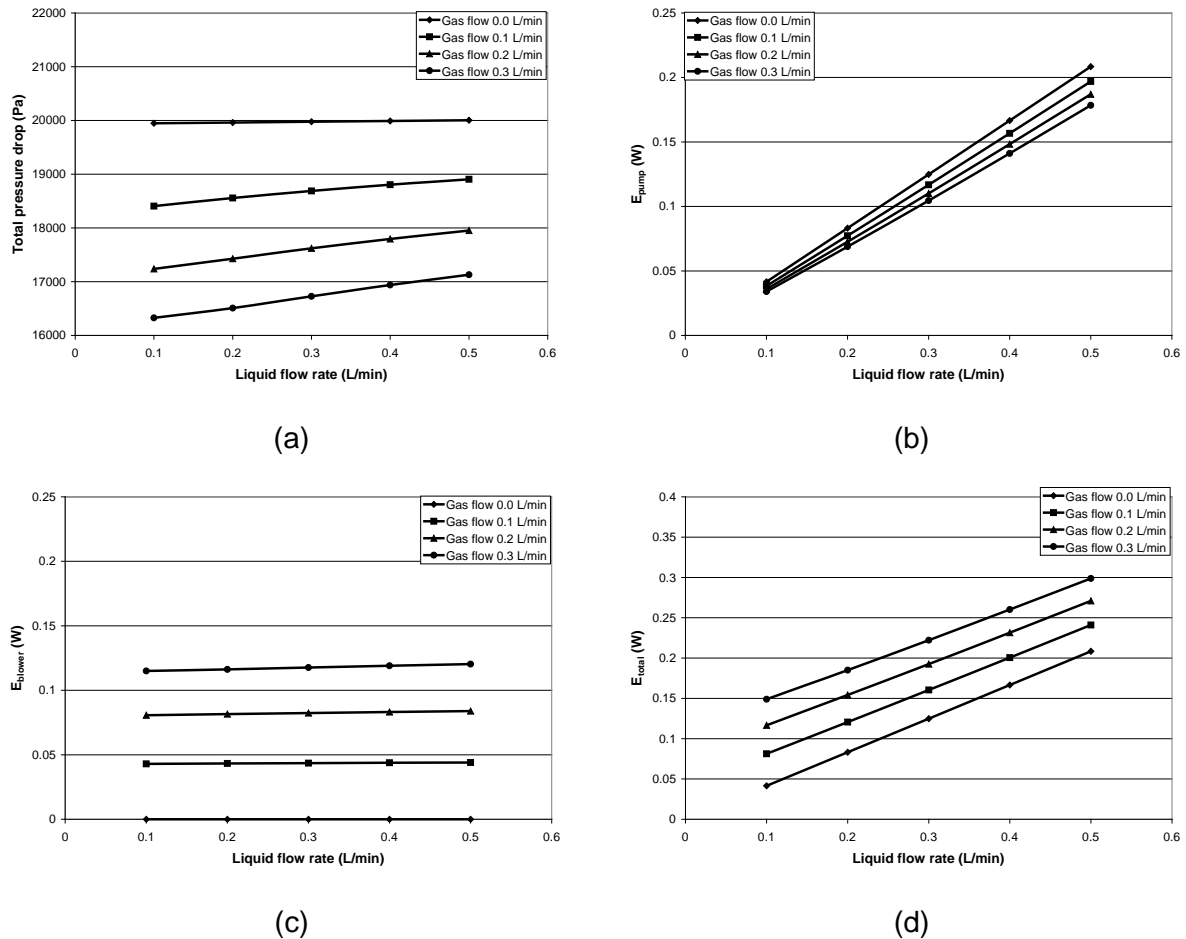


Figure 3.8. Pressure drop and energy consumption for different liquid and gas flow rates combinations investigated (a) total pressure drop (Pa), (b) pump energy consumption (W), (c) blower energy consumption (W) and (d) total energy consumption (W).

Figure 3.8a illustrates that when there is no gas flow (i.e. single phase flow), the pressure drop increases as the liquid flow rate increases. However, a pressure drop decrease occurs when gas is introduced to the system, even when the liquid flow is increased. The reason for this is that the static and friction pressure drop behave differently in two-phase flows compared to single phase flow. Moreover, when the gas flow rate increases by $0.1 \text{ L}\cdot\text{min}^{-1}$, (from 0.1 to 0.2 and from 0.2 to $0.3 \text{ L}\cdot\text{min}^{-1}$) the total pressure drop along the tube decreases by approximately 6%. As a result, a gas flow rate increase of $0.1 \text{ L}\cdot\text{min}^{-1}$ decreases the liquid pumping power consumption by approximately 7% (Figure 3.8b). However, a similar gas flow rate increase of $0.1 \text{ L}\cdot\text{min}^{-1}$ leads to a significant increase in power consumption of

the blower (70 %) (Figure 3.8c). The overall total energy consumption of the system increases by approximately 40 %, for a gas flow rate increase of 0.1 L·min⁻¹ (Figure 3.8d).

It was observed that the pressure drop and energy consumption relationships could also be estimated using simple linear relationships as presented in equations (3.13) to (3.16) ($R^2 > 0.922$).

$$\Delta P_{total} = m_{7,L} u_{SL} + m_{7,G} u_{SG} + b_7 \quad (3.13) \quad E_{blower} = m_{9,L} u_{SL} + m_{9,G} u_{SG} + b_9 \quad (3.14)$$

$$E_{pump} = m_{8,L} u_{SL} + m_{8,G} u_{SG} + b_8 \quad (3.15) \quad E_{total} = m_{10,L} u_{SL} + m_{10,G} u_{SG} + b_{10} \quad (3.16)$$

where $m_{i,L}$, $m_{i,G}$ and b_i are empirical constants (Table 3.3). By combining equations (3.13) to (3.16) and equation (3.12) respectively, the total pressure drop and energy consumption for the different liquid flow rates investigated that equilibrate the peaks in SSH can be determined as shown in Figure 3.9.

Table 3. Estimate and standard error of empirical constants for pressure drop and energy relationships.

	$m_{i,L}$	Std. Error	$m_{i,G}$	Std. Error	b_i	Std. Error	R^2	P value**
ΔP_{total}	7810.067	612.396	-44942.751	1060.701	19107.403	63.589	0.922	0.000
E_{pump}	1.748	0.020	-0.273	0.035	0.009	0.002	0.998	0.000
E_{blower}	0.037	0.010	1.712	0.017	0.005	0.001	0.998	0.000
E_{total}	1.786	0.015	1.439	0.027	0.014	0.002	0.998	0.000

From Figure 3.9, it is possible to observe that the pressure drop decreases as more liquid and gas is pushed into the system using equation (3.12). Exploring the energy consumption for liquid pumping, each 0.1 L·min⁻¹ increase of liquid flow, results in an increase of 0.035 W (around 38 % increase). Similar reasoning for the blower, results in an increase of 0.018 W (around 8 % increase). Eventually, the total energy consumption for each 0.1 L·min⁻¹ of increase in liquid flow, increases by 0.053 W, i.e. 17 %. These results show that even if the gas flow rate has to increase, the total power required to balance the two peaks only increases by 17 %. Therefore, adding more gas to reduce the extent of fouling in a way that the two peaks are balanced does not result in a large increase in energy consumption. In summary, based on the results from the SSH, in order to have more balanced peaks and minimize the energy consumption, it is recommended to use low liquid flow rate and high

gas flow rate (four times the liquid flow rate) to decrease the fouling and the energy requirements.

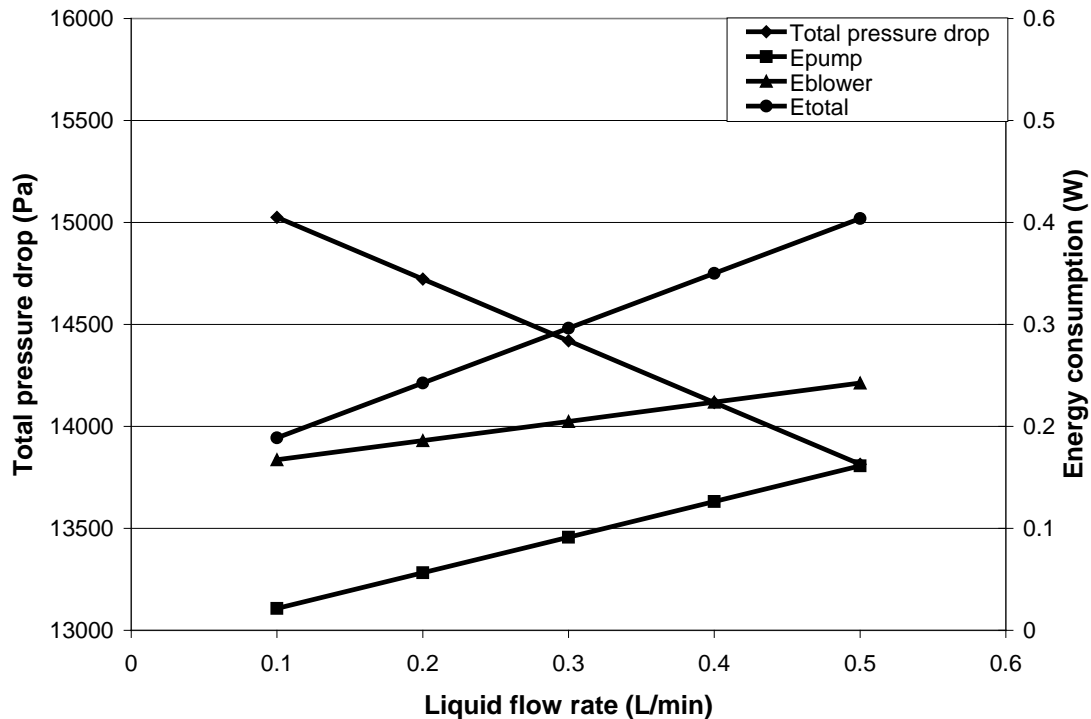


Figure 3.9. Pressure drop and energy consumption calculated for different liquid flows rates that equilibrate the peaks in the SSH.

3.5 Conclusions

An experimental setup was designed to measure local shear stress near the membrane surface using an electrolyte solution. Due to coalescence of bubbles different sized bubbles occur. Hence, to analyze the data SSH were used. A bimodal SSH was observed, with two peaks: one corresponding to the shear induced by the liquid flow, and one corresponding to the gas flow. This SSH was modelled using simple empirical linear relationships. It was assumed that the best condition to reduce/control the fouling is to have a balanced SSH. This means that the frequency of shear stress induced by the liquid slug flow should be approximately equal to the gas slug flow. Therefore, it was possible to identify the two-phase flow conditions that optimize fouling control.

Also, it was possible to quantify the pressure drop for two-phase flow in vertical tubes and energy consumption (blower and pump) based on theoretical equations and link them to the SSH. It could be concluded that at low liquid flow rates in combination with high gas flow rates (around 4 times higher than liquid flow rate) the SSH is balanced and the energy consumption is minimized.

It is important to highlight that the model that was developed in this chapter is an empirical model. However, extrapolation to other systems and operational conditions is dangerous and not recommended. For this reason, a CFD model will be developed in chapter 4 that can provide more mechanistic insight in the behaviour of a slug flow.

Chapter 4. CFD modelling of a slug flow

Abstract*

A CFD model to study the effect of slug flow on the surface shear stress in a vertical tubular membrane has been developed. The model was validated using: (1) surface shear stresses, measured using an electrochemical shear probe and (2) gas slug rising velocities, measured using a High Speed Camera (HSC). The Shear Stress Histograms (SSHs) introduced in chapter 3 are used to validate the CFD model. At high liquid and low gas flow rates, the frequencies obtained numerically and experimentally were found to be similar, deviating by less than approximately 10%. However, at high gas and low liquid flow rates, the differences were slightly higher, exceeding 20%. Under these conditions, the CFD model simulations over predicted the shear stresses induced by gas slugs. In terms of the gas slug rising velocity, it was found to be 10 % over predicted compared to the experimental data. Nonetheless, the results indicate that the CFD model was able to accurately simulate shear stresses induced by gas slugs for conditions of high liquid and low gas flow rates. The novelty of this CFD slug flow model compared to the models in literature, is that the models in literature only model one fixed single bubble in a small tube section. Instead, in this work multiple bubbles are modelled as a train of bubbles in a 2 m long tube and the interaction between bubbles can be accounted for.

* Redrafted after

Ratkovich, N., Chan, C.C.V., Berube, P.R., Nopens, I. Experimental study and CFD modelling of a two-phase slug flow for an airlift tubular membrane. *Chemical Engineering Science* 64 (2009) 3576-3584.

Introduction

Fouling control in vertical tubular membranes has been linked to the hydrodynamic conditions near the membrane surface, which in this case are induced by a slug flow, (Ghosh and Cui, 1999). A number of studies have suggested that the change of liquid flow direction and the corresponding change in the direction of the induced surface shear stresses promotes fouling control (Ochoa et al., 2007; Rochex et al., 2008). The aim of the present study was to develop a CFD model to study the effect of slug flow on the surface shear stress in a commercial-scale vertical tubular membrane. Fluent® (Ansys Inc., USA) was used as the modelling platform, and the model was validated using surface shear stresses, measured using two electrochemical shear probes and gas slug rising velocities, measured using a high speed camera. It should be noted that in literature a number of CFD models have been developed to study the effect of slug flow on the surface shear stress in vertical tubular membranes (Ndinisa et al., 2005; Ndinisa et al., 2006; Taha and Cui, 2002; Taha and Cui, 2006a; Zheng et al., 2007). However, these models only considered the effect (i.e. gas volume, bubble shape) of distinct gas slugs of constant size. In contrast, the present study considers the effect of gas slugs of variable size, which is typical of commercial-scale vertical air-sparged tubular membrane module where slugs tend to be of a different size and coalesce as they rise through the tubes. To the author's knowledge, this is the first attempt in literature to accomplish this. In chapter 3, an empirical model was developed based on experimental data. However as was discussed before, experimental data-based models have their own drawbacks, that they only work for specific conditions of the experiment and extrapolation of these models to other cases should be avoided. Therefore, a CFD model was built which, with proper validation, can be extrapolated to other cases as is not the case for empirical models. Moreover, mechanistic models based on physical laws help to better understand the system behaviour and important degrees of freedom.

4.1 Description of the CFD model

The CFD package used (Fluent v6.3) contains the volume of fluid (VOF) approach for modelling two-phase flows to track the motion of a single bubble in vertical tubes (slug flow) both in stagnant and flowing liquids (section 1.7.1.3). This VOF model is used for immiscible fluids where the position of the interface between the fluids is important. It has a single set of momentum equations for both fluids and a volume fraction for each phase (Taha and Cui, 2006a). A two-dimensional axisymmetric geometry was built in Gambit v2.3 (Ansys Inc., USA) with a height of 2 m and a radius of 0.00495 m. In order to properly capture the shape of the bubble it was necessary to have a relatively fine grid close to the wall, where the shear stress acts on the membrane. A growth function was used to build the grid with these properties. The cell closest to the tube wall has a width of 1×10^{-5} m (0.01 mm). The falling film (high downward liquid velocity) and wake (mixture of liquid and gas) zones of the slug flow are slightly turbulent (~3000) and, therefore, the k- ϵ RNG (ReNormalized Group) was used for CFD modelling of slug flow (Taha and Cui, 2002a; Taha and Cui, 2002b). To initialize the bubbles at the inlet boundary of the tube a volume fraction of gas was defined based on the flow rates of the liquid and gas.

The solver was set up to use the explicit interpolation scheme with geometric reconstruct discretization for VOF which is recommended for transient simulations (Taha and Cui, 2006a; Taha and Cui, 2006b). Due to the unsteady behaviour of the slug flow (different bubble size, shape and coalescence), LES (Large Eddy Simulation) is the best approach. However, this technique requires a very fine mesh and would be very computationally intensive (even in 2D) especially when modelling a train of bubbles in a 2 m long tube. Therefore, unsteady RANS (Reynolds-averaged Navier–Stokes) was used (section 1.10). The turbulent eddies are expected to be much smaller than the typical size of the grids, and, hence, a turbulence model was essential to capture their impact in the system. The time scales of the eddies are also expected to be much shorter than the typical time steps used in the simulation. The “geometry reconstruct” scheme for surface tracking (bubble interface) assumes that the boundary between air and water has a linear slope for each cell. To achieve this, it uses the quantity of fluid of each cell to determine the interface. To solve the momentum transport equation the QUICK (Quadratic Upwind Interpolation) scheme was used, which increases stability of the solution, provides a faster convergence and has 4th order accuracy. To solve the pressure equation, the PRESTO! (PREssure STaggering Option) scheme was used as it increases stability in the solution. For the pressure-velocity coupling the SIMPLE (Semi-Implicit Method for Pressure-Linked Equations) scheme for faster convergence was used (Taha and Cui, 2002; Taha and Cui, 2006a). A time step of 0.0001 s was adopted. The grid dependency was investigated using three different mesh resolutions (20x6250, 17x5000 and 15x4000) with a total run time of 20 s and using the highest flow rates (water-N₂ 0.5-0.1 L·min⁻¹). Three surface monitors (a kind of virtual sensor function in Fluent) were located at a height of 1 m: one located near the wall of the tube at the height of the shear probes monitoring the wall shear stress and another two in the middle of the tube. Of the latter, one monitors the phase shifts (liquid to gas and vice versa) and the other monitors the gas slug rising velocity. The reason to use the highest flow rates is to decrease the simulation time as the bubble will reach the surface monitor much faster in order to compare the different meshes.

4.2 Grid dependency and surface monitors

Three meshes (20x6250, 17x5000 and 15x4000) with different coarseness were developed in Gambit v2.3 using squared cells to capture the bubble shape as accurately as possible (Figure 4.1). These meshes are to be used with the VOF model in Fluent. The drawback of a fine mesh compared to a coarse one is the simulation time as this can increase from days to weeks as is indicated in Table 4.1:

Table 4.1. mesh resolution and simulation time

Mesh	a (mm)	Time (for 20 sec of simulation)
20x6250	0.32	20 days
17x5000	0.40	12 days
15x4000	0.50	5 days

* "a" is the side of the square in figure 4.1

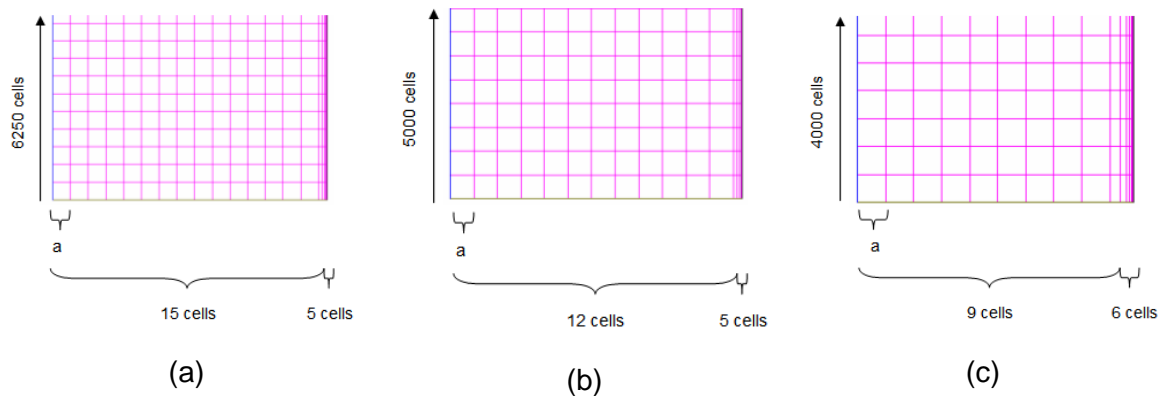


Figure 4.1. Mesh resolutions: (a) 20x6250, (b) 17x5000 and (c) 15x4000. The closest cell near the wall is at 1×10^{-5} m (0.01 mm)

Figure 4.2 shows illustrations of the three different simulation outputs from the user-defined surface monitors in Fluent using the mesh of 20x6250 in the middle of the tube (from 0.9 to 1.1 m). It is possible to appreciate the gas slugs, the first plot is at a point located in the center of the tube cross-section to determine the volume fraction of gas to know the location of the bubble (= 1) or the liquid (= 0). The second plot shows the mixture velocity, and based on the first figure it is possible to determine an average gas slug rising velocity (average between the velocity at the nose and at the tail of the bubble) and the liquid velocity. The final figure shows the shear profile near the membrane surface. Table 4.2 shows the gas slug rising velocity from the simulation.

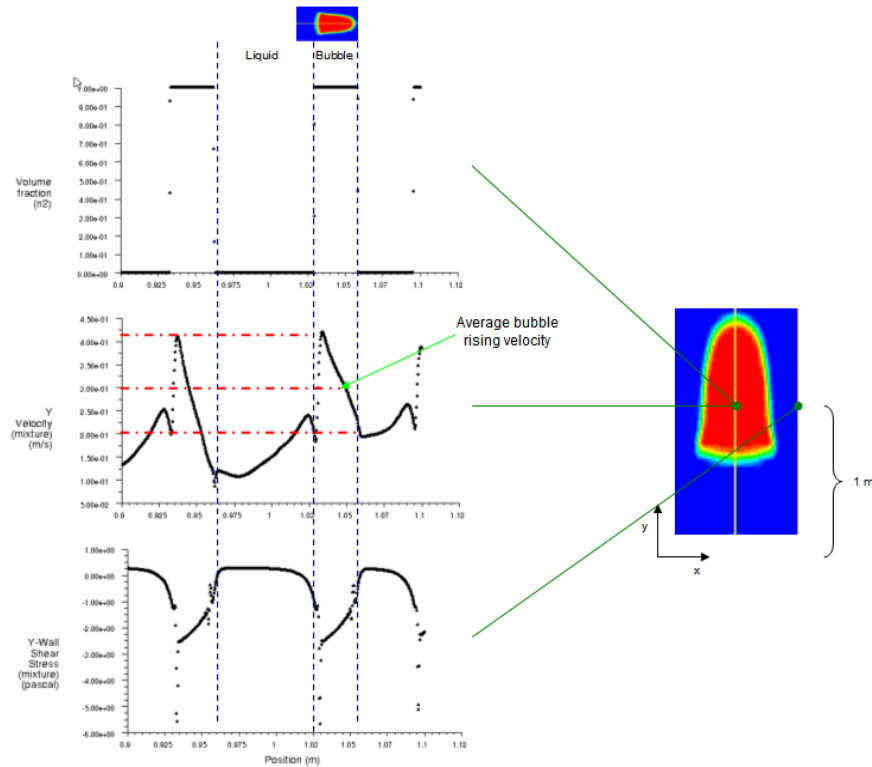


Figure 4.2. Volume fraction, velocity and shear stress time series for the mesh 20x6250

Table 4.2 Average gas slug velocities:

	Average gas slug velocities (m s^{-1})
Equation 1.31 (theoretical)	0.32
Table 2.1 (experimental)	0.27
Mesh 20x6250	0.305
Mesh 17x5000	0.310
Mesh 15x4000	0.265

When comparing the outcome of Equation (1.31) with that of the experimental data, a difference of 20 % can be noticed. The latter is probably due to the use of a correlation for turbulent regime whereas the experiments were performed in the laminar-transition regime. Moreover, experiments of gas slug rising velocity in stagnant water were not performed, which could also affect the slug rising velocity due to buoyancy forces.

Comparing the results of the gas slug rising velocity (Table 4.2), it can be concluded that meshes 20x6250 and 17x5000 yield similar velocities that are, moreover, close to the theoretical equation (1.31). For the mesh 15x4000 the value is close to the one obtained from the experimental data (HSC) correlation (Table 2.1). Herein, the simulation slightly over predicts the experimental values by 15 %. However, it is important to mention that the

velocity was determined from the movement of the interface between the gas and liquid (bubble) at the axis of the tube, so its value is subject to some uncertainty. Therefore, it was concluded that a 15 % deviation is acceptable. From the results of Table 4.2 using the gas slug rising velocity it is possible to determine whether the flow is laminar or turbulent using the slug flow Reynolds number (equation 1.44), it was found to be 2600 justifying the turbulent regime and the selection of the turbulent model.

Regarding the shear stress, Figure 4.3 shows a typical time series of simulated shear stress at the point where the shear probes were located (1 m) for both the shear measurements and simulations using different meshes.

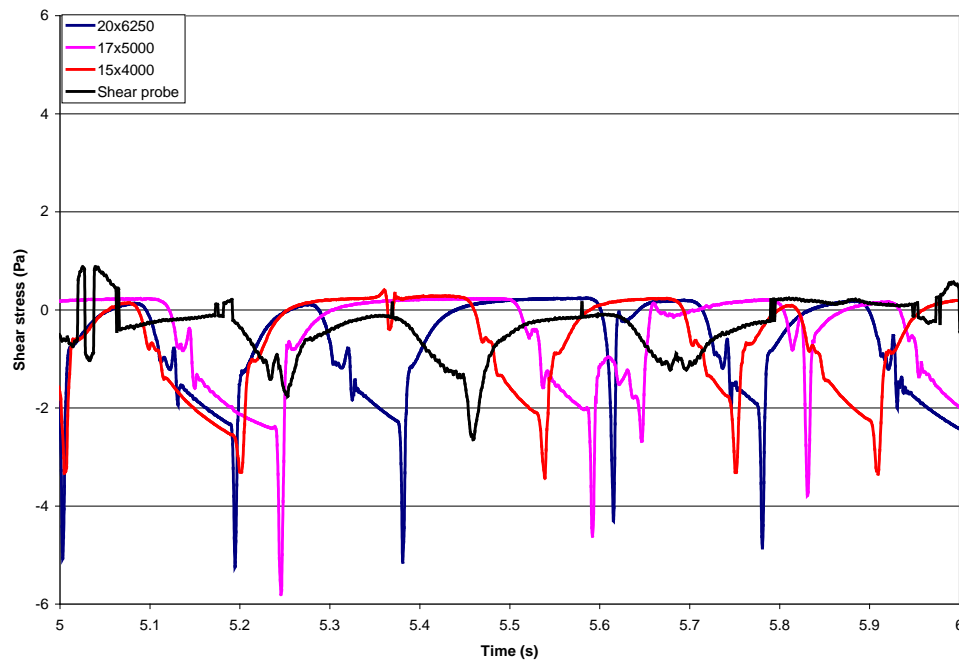


Figure 4.3. Simulated shear stress for three different mesh resolution and the shear probes for (water-N₂ 0.5-0.1 L·min⁻¹).

In Figure 4.3, for the liquid slug the shear is positive because the liquid near the tube is moving upward. In the falling film zone and the wake there is a reverse of flow (liquid moving downwards) and the shear stress becomes negative. Also it is possible to observe that the shear stress in the liquid is not always positive which can be attributed to the space between the bubbles that is too short to allow the liquid slug to develop completely in the boundary layer. Also, it is possible to observe that there is no unique pattern (the bubbles are longer or shorter) due to coalescence although a general shape can be observed. Sometimes spikes occur, which is probably due to a sudden change in the direction of the flow. Also, it is possible to observe that all three meshes have the same upper boundary (around 0.25 Pa). Meshes 20x6250 and 17x500 share similar lower boundaries which over predict the results from the experimental measurements (Figure 4.3). The result from mesh 15x4000 looks more similar to the shear probe. To analyze in a better way Figure 4.3, SSH will be used as is presented in Figure 4.4.

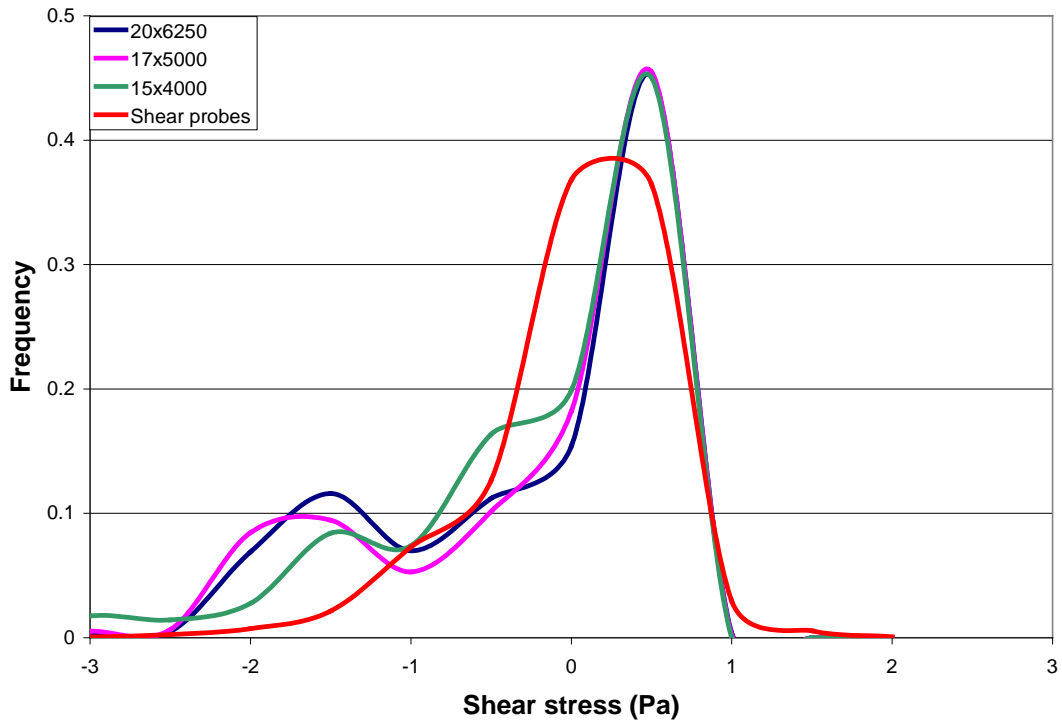


Figure 4.4. SSH during 10 sec for the experimental measurements and three different mesh resolutions (water-N₂ 0.5-0.1 L·min⁻¹) with a bin of 0.5 Pa.

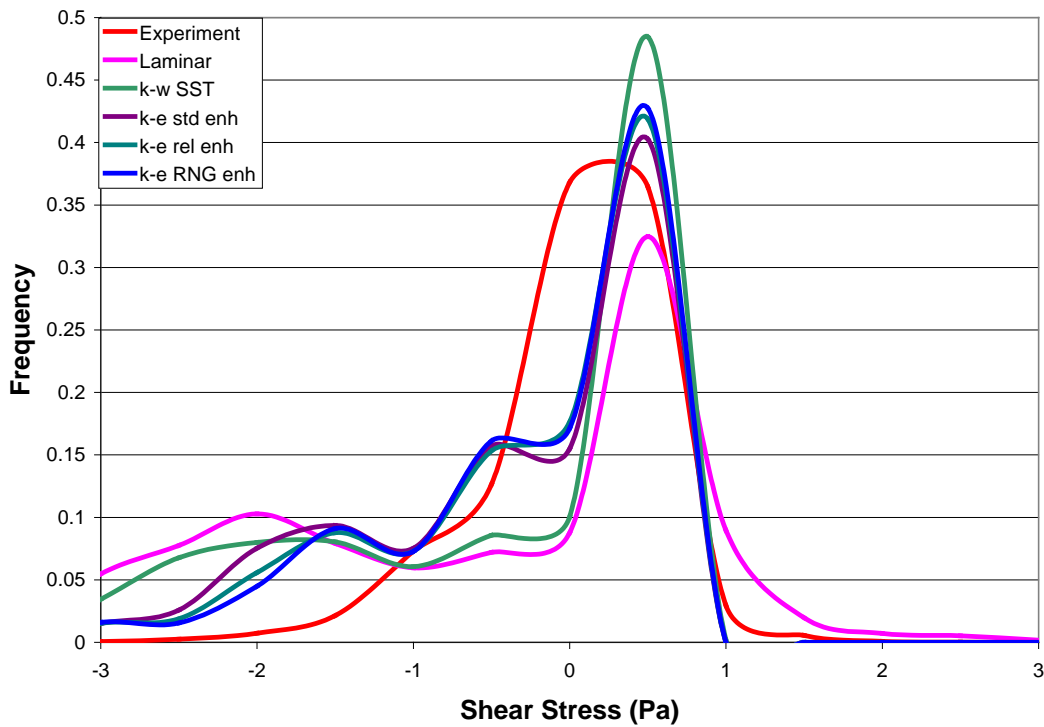


Figure 4.5. SSH for different turbulence models compared with the experimental data for the mesh of 15x4000 (water-N₂ 0.5-0.1 L·min⁻¹) with a bin of 0.5 Pa. Std: standard, enh: enhanced wall treatment, rel: realizable

From the SSH (Figure 4.4), it is possible to have a clear picture of the shear stress values and their frequency of occurrence. It is possible to observe that for the three meshes the results are quite similar in the liquid slug (positive peak) region and comparable in the gas slug (negative peak) and they are also close to a certain extent to the experimental data. Therefore, based on these observations, it was assumed that grid independency occurred. Hence, in the remainder of this chapter, the coarser mesh (15x4000) will be used considering the computational time (Table 4.1).

Another factor to consider is the overall slug flow Reynolds number, which ranged from 1300 to 2800 and, therefore, the turbulent CFD model used for the simulations (k- ϵ RNG) may not have been able to accurately simulate shear stresses in the transitional regime. Therefore, other turbulence models were tested and the result of this investigation is shown in Figure 4.5.

As for the laminar model, it could not accurately describe the negative peak as is smeared out over the negative range of shear stress and the frequency of the positive peak is underpredicted. The k- ω SST (Shear Stress Transport) has a similar result as the laminar model for the negative peak but the frequency in the positive peak is better predicted. The k- ϵ standard and realizable over predicted the positive peak compared to the RNG. The RNG represents the height of the peak better than the other two (standard and realizable k- ϵ models) compared to the experimental data. For the negative peak the three k- ϵ models yield similar results and the negative peak is shifted to the left. Another important factor to highlight is that for the k- ϵ standard, realizable and k- ω SST, the time of simulation is much larger than the RNG as the time step needs to be smaller to avoid divergence in the simulation, which is an important reason on selecting the RNG to perform the remaining simulations. In conclusion, the other turbulence models investigated (e.g. k- ϵ Realizable and k- ω SST) produced results that were similar to those obtained with the k- ϵ RNG model used for the numerical CFD simulations presented in Figure 4.5. Nonetheless, for further simulation the RNG k- ϵ model will be used as it is commonly used for slug flow simulations.

4.3 Slug flow rising velocity

The slug rising velocity was obtained from the CFD simulation and is compared to the experimental data of the HSC (Table 2.1) (see section 2.3), the results are presented in Table 4.2 and Figure 4.6 from the CFD simulation.

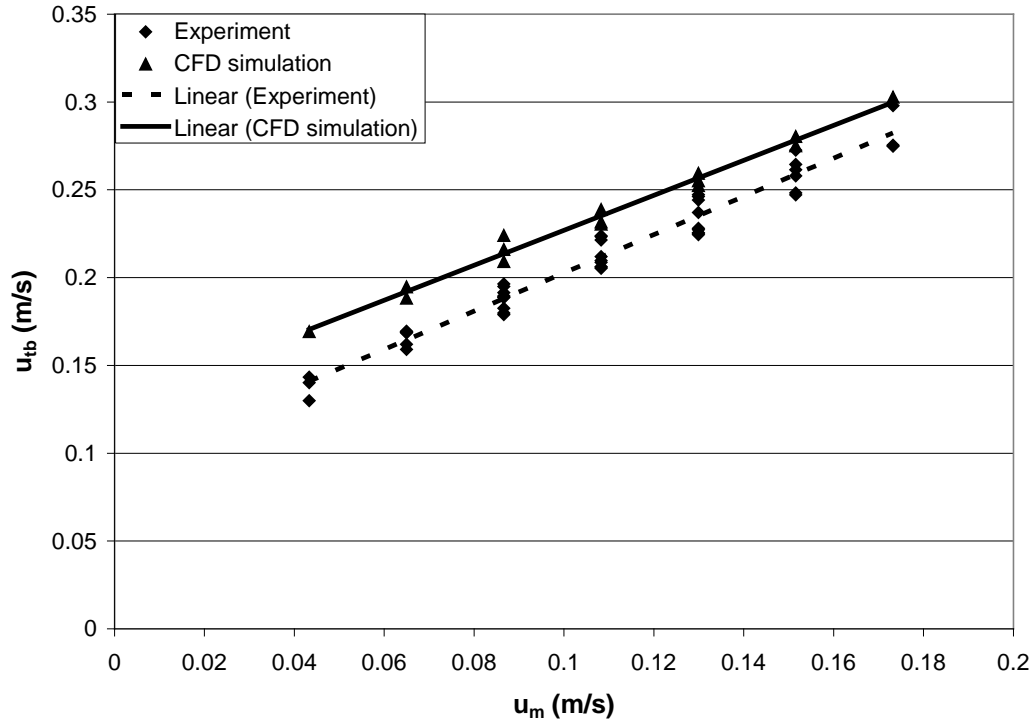


Figure 4.6. Gas slug rising velocity versus mixture velocity for the experimental measurements and the numerical simulations.

Table 4.2

	Experimental*	CFD simulation
C	1.088 ± 0.033	0.996 ± 0.032
k_{TB}	0.301 ± 0.012	0.409 ± 0.012
R^2	0.962	0.986

*Table 2.1 case 2

Using the experimentally collected bubble rising velocities, the empirical parameters C and k_{TB} were estimated to be 1.088 and 0.301 respectively, with a 95 % confidence interval (Table 4.2). The value of C was significantly lower than the range proposed by section 1.5.2.1. This discrepancy was attributed to the diameter of the tube used in the present study, which was smaller than those reported in literature (25 mm) (Frechou, 1986). Furthermore, if the diameter decreases, bubbles are slimmer and their velocity will increase, which means that the empirical parameters are likely to be function of the diameter as well. Similar values to those observed in the present study for C (i.e. 1.02) have been reported by others when using smaller tube diameters (15 mm) (Mercier-Bonin et al., 2000). These results suggest that the tube diameter can significantly affect the flow regime and that simple empirical relationships (like in section 1.5.2.1) should be used with caution. The value of k_{TB}

was also slightly smaller. This discrepancy could also be due to the geometry of the experimental setup. Unfortunately, no other studies were found which report similarly low values for k_{TB} .

For the CFD model simulations, the empirical parameters C and k_{TB} were estimated to be 0.996 and 0.409 respectively (Table 4.2). Differences in the values for parameters C and k_{TB} between the experimental measurements and the simulation are likely due to the turbulent model that was selected and the fact that the simulation is in the transition regime range (1300 - 2800) based on the slug flow Reynolds number, which is slightly different from the mixture Reynolds number, in that the gas slug rising velocity is used instead of the mixture velocity. It can be observed that the simulations overpredict the gas slug rising velocity but that a similar trend was observed. The simulation results yielded a C value of 1.00 which is in good agreement with the results obtained using the HSC. However, k_{TB} was over predicted (0.41) compared to 0.30 obtained from the HSC. This can be attributed to an overprediction in the buoyancy forces over the bubbles in the simulation introduced by the turbulence model. However, the predictions are within 15 % of the experimental values which is considered to be acceptable considering the complexity of simulating a train of gas slugs. Other studies that focused on one single gas slug report an error of 10 % when comparing the gas slug rising velocities obtained using experiments and the simulations (Ndinisa et al., 2005).

4.4 Modelled shear stresses near the membrane wall

In this section the CFD simulations are compared with the experimental results obtained from the shear stresses. Simulation results suggested that rising gas slugs have a spherical nose, a cylindrical body and a fluctuating tail.

15 different CFD simulations were performed for all experimental conditions investigated. The simulations were performed using a 15x4000 mesh, changing only gas and liquid flow rates and gas volume fractions. It is important to highlight, as it was discussed in section 2.3, that some of the Reynolds number values are below 2100, therefore the turbulent model should not be applied for all the velocity combinations. However, due to the fact that the wake region is highly turbulent, it is possible to assume that there is an early transition from laminar to turbulent. Therefore, the k- ϵ RNG with enhanced wall treatment was used in the simulations. Figure 4.7 shows the results for the different combinations.

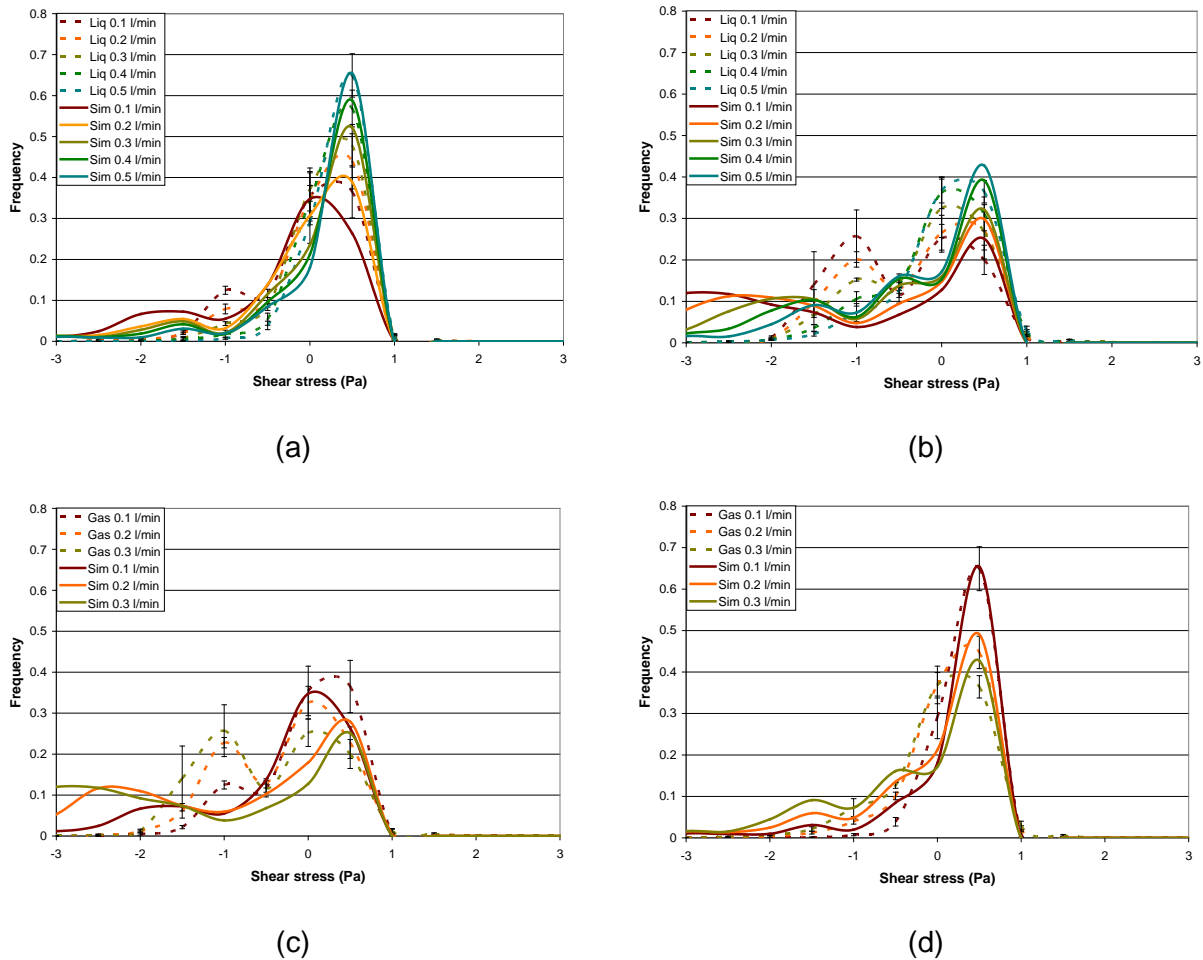


Figure 4.7. SSH for experimental data and numerical simulations for two different gas flow rates (a) 0.1 and (b) 0.3 L·min⁻¹ with five liquid flow rate combinations and for two different liquid flow rates (c) 0.1 and (b) 0.5 L·min⁻¹ with three gas flow rate combinations.

From Figure 4.7a and b, two aspects are clearly observed. First, the numerical simulations are capable of predicting the magnitude of the frequency for the first peak. However, when the velocity of the gas increases, the prediction of the peak by the model shifts slightly to the right. Secondly, the second peak is not well predicted as it is shifted to the left. At high liquid velocities the simulations are closer to the experimental values. The latter can be due to the use of the turbulent model (at high liquid velocities the Reynolds number increases). In conclusion, this model has proven to accurately describe the first peak which is related to the liquid slug and to a reasonable extent the second peak given the model assumptions made.

The shear stress values obtained numerically using CFD simulations were compared to those obtained experimentally using shear probes. The comparison was based on the absolute differences between the relative frequencies from the SSH for both the CFD simulations and the experimental measurements (Figure 4.8).

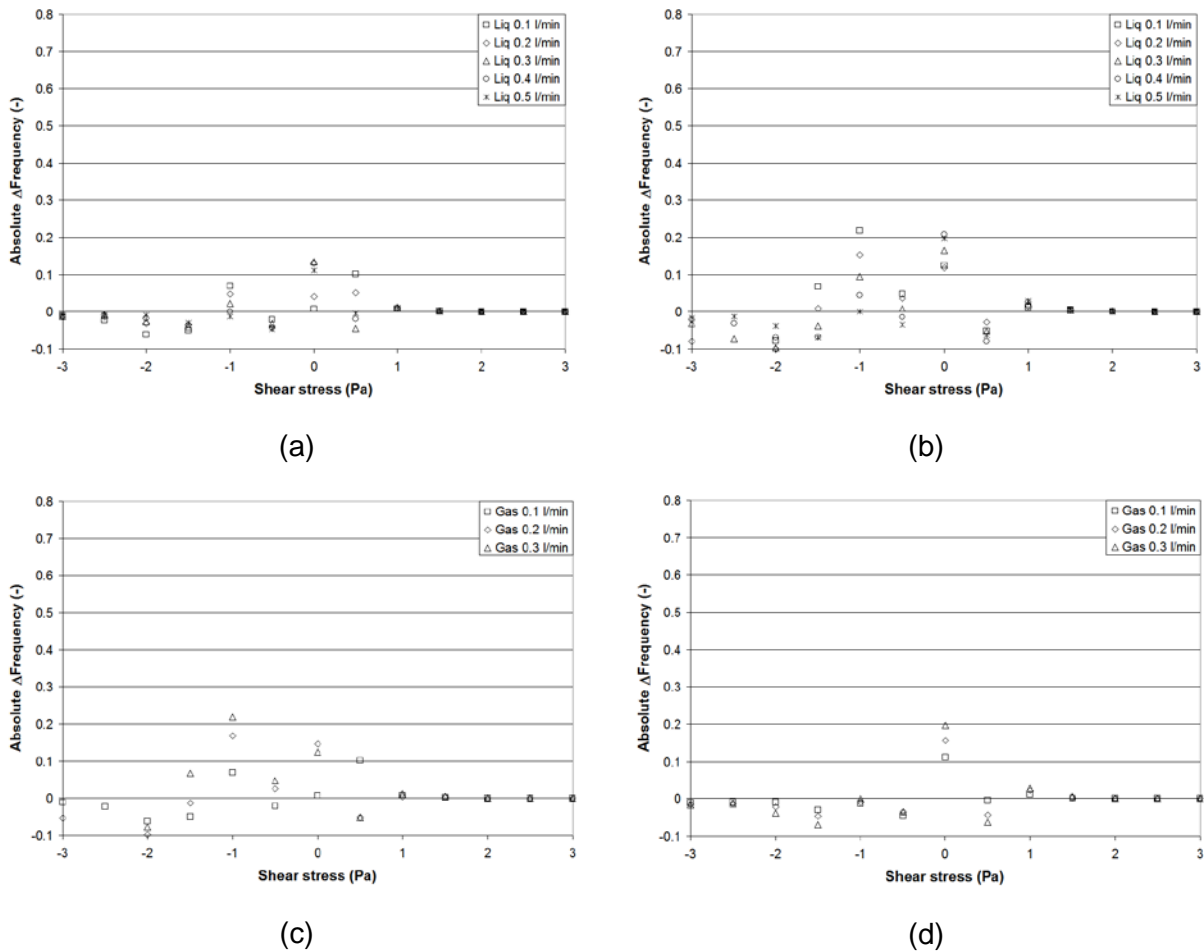


Figure 4.8. Absolute difference in frequency from shear stress histograms between experimental data and numerical simulations for two different gas flow rates (a) 0.1 and (b) 0.3 L·min⁻¹ with five liquid flow rate combinations and for two different liquid flow rates (c) 0.1 and (b) 0.5 L·min⁻¹ with three gas flow rate combinations.

The relative frequencies were determined in exactly the same way for the CFD simulation as for the experimental data (see section 3.2). These differences between the relative frequencies of both the experimental and CFD simulation result in the absolute error. E.g. in the case of Figure 4.8a, for a liquid flow rate of 0.1 L·min⁻¹ and a shear stress of -1 Pa, the relative frequency in the experiment was found to be 0.12, whereas for the CFD simulation a value of 0.06 was observed (Figure 4.7a). The absolute frequency is the difference between the two previous values, which is 0.06 (Figure 4.8a), this means that the absolute error is 6 % as these numbers are expressed as %.

At high liquid and low gas flow rates, the absolute frequencies obtained numerically and experimentally were found to be similar, deviating by less than approximately 10 %. However, at high gas and low liquid flow rates, the differences were slightly higher, exceeding 20 %. Under these conditions, the CFD model simulations over predicted the shear stresses induced by gas slugs.

4.5 Conclusions

A CFD model was developed to study the effect of slug flow on the surface shear stress in a vertical tubular membrane. A grid dependency test was performed based on shear stress and slug rising velocity to find the most adequate grid and turbulence model. The model was validated using the SSH developed in chapter 3 and the gas slug rising velocity from chapter 2.

Regarding the SSH, two peaks were found as for chapter 3. The positive peak (liquid slug) was well described by the CFD model. However, the prediction of the second peak (gas slug) was shifted to the left. This shift to the left was assumed to be related to the turbulence model selected. As discussed, the Reynolds numbers are in laminar-transition regime and the turbulence model ($k-\varepsilon$ RNG) is designed for high turbulent flows. However, other turbulence models were tested and similar results in the second peak were found.

Regarding the slug rising velocity, an over prediction of 10 % compared to the experimental data was found. This over prediction can be attributed as well to the turbulence model.

Chapter 5. CFD modelling of an airlift MBR module

Abstract*

A CFD model of an entire airlift membrane bioreactor (MBR) module was built to determine the air dispersion within a membrane module. The model development was divided in three parts: 1) membrane module: A single membrane module was modelled and a value for the membrane resistance (filtration process) was derived. Next, this single membrane tube was extrapolated to a full-scale membrane module (700 tubes), necessitating the definition of two zones: one zone for the bundle of tubes and another zone for the membrane resistance. These two zones were introduced to mimic the operation of a real airlift MBR module. 2) Two types of air diffusers were tested (ring and disk aerator) to observe the air distribution within the membrane module. 3) Both models (membrane module + air diffuser) are integrated. The disk aerator was found to provide a better air distribution to the module which implies better mixing and decrease in fouling at the membrane wall due to a better two-phase cross flow. However, the latter is still a hypothesis based on the modelling exercise that was conducted and should be further backed up with experimental evidence.

* Redrafted after:

Ratkovich, N., Hunze, M., Futselaar, H., Nopens, I. Use of CFD to model and optimize the hydrodynamics of an airlift MBR side-stream module. 2009. Proceedings of WEFTEC (Water Environment Federation's Annual Technical Exhibition and Conference) 2009 on October 10-14, 2009 in Orlando, FL, USA.

Introduction

The hydrodynamics near the membrane surface play an important role in controlling the fouling (Cabassud et al., 2001; Laborie et al., 1998; Tardieu et al., 1998; Tardieu et al., 1999; Vera et al., 2000). To reduce the fouling on the membrane often air is introduced in order to create a two-phase gas-liquid cross-flow. This is done to increase the surface shear stress to remove foulants already attached and results in an increase in permeate flux. However, the actual whereabouts of this gas-liquid flow are not well understood. Hence, in practice the system is operated in a trial and error approach which is costly in terms of energy consumption.

Gas sparging in tubular membranes has proven to be a powerful tool for fouling control. Therefore, an appropriate air sparging device that allows adequate distribution of the gas phase to the entire cross-section of a multi-channel module plays an important role. The design of the aerator is based on different hydraulic conditions (e.g. type of air injection, distance between the diffuser and the module entrance, use of turbulence promoters, etc). The performance of the air diffuser is based on the distribution of air over the module cross-section, the size and distance of the air bubbles. It was found that aeration systems with multiple orifices injecting air homogeneously in the feed flow performed better (Mayer et al., 2006).

The modelling of air diffusers is based on experience from bubble column reactors. The understanding of the complexity of the fluid dynamics in the latter is very important due to its many applications in process engineering (Sanchez Perez et al., 2006). In an attempt to enhance the performance of bubble columns, an accurate predictive model of the flow regime is required (Joshi, 2001). There has been considerable development in the modelling of multiphase flows in bubble columns over the past decade. Models of air bubbles flowing through a stagnant liquid column were validated against experimental data (Svendsen et al., 2009). Other authors investigated the effect of the bubble wake models on the overall structure of bubble column flow in both two and three dimensions for steady flows (Ranade, 1997; Ranade and Utikar, 1999). Air diffusers are important in the design of bubble columns. More detailed designs are required to better control the air-diffuser systems according to varying field conditions and in what way the bubble plume is affected (Dhotre and Smith, 2007).

CFD has already proven to be a powerful tool for improving design and operation of wastewater treatment systems (Brannock et al., 2010a; Brannock et al., 2010b). In chapter 4, a two-phase slug flow CFD model was developed for a single tube. However, in industrial applications, membranes have several hundreds of tubes, for which an extrapolation of the previous model is required. A CFD model of an entire airlift MBR module was developed to determine the air dispersion and distribution within the membrane module. The model was extrapolated from a single membrane tube model where the resistance due to the bundle of tubes and the membrane respectively were included to mimic the operation of a real airlift MBR module. In a second stage, two types of commercially used air diffusers were tested

(ring and disk aerator) to observe the air distribution within the membrane module. The final stage was to merge the membrane module and the air diffuser system in one single model.

5.1 Airlift MBR

The AirLift MBR system under study (X-Flow, Norit, The Netherlands) consists of membrane modules located outside the bioreactor tank (Figure 5.1).

The membrane modules are connected to the bioreactor in series (Figure 5.1a). The sludge is pumped to the membrane module, which is arranged vertically (Figure 5.1b) and is aerated continuously from the bottom to create an airlift system (Figure 5.1c). The feed pump is only used to overcome hydraulic losses (i.e. pipe roughness and bends) and the permeation is controlled by a suction pump (Futselaar et al., 2007). A module is 3 m high and contains 700 tubes (Figure 5.1c). Each tube has an internal and external diameter of 5.2 and 6 mm respectively and the membrane is made of PVDF with a nominal pore size of 30 nm. It is important to highlight that the shear stress measurements (chapter 3 and 4) were performed for a tube with an internal diameter of 9.9 mm. The operational parameters of the airlift system are summarized in Table 5.1.

Table 5.1. Operational parameters of Norit Airlift MBR module

Parameter	
Liquid flow rates ($\cdot 10^{-3} \text{ m}^3 \cdot \text{s}^{-1}$)	3.3 – 5.6
Air flow rates ($\cdot 10^{-3} \text{ Nm}^3 \cdot \text{s}^{-1}$)	1.4 – 2.8
Flux ($\cdot 10^{-5} \text{ m}^3 \cdot \text{m}^{-2} \cdot \text{s}^{-1}$)	1.3 – 1.7
TMP (kPa)	5 – 30
TSS ($\text{g} \cdot \text{l}^{-1}$)	8 – 12
Membrane area (m^2)	34

5.2 CFD modelling of the bundle of tubes

The main problem of building a CFD model for a membrane module is that even if the geometry could be constructed with 700 tubes (although it would be a tedious task), the major concern is meshing and running the simulation in an acceptable time frame. Therefore, the following approach and assumptions were made: 1) Simulate a single UF tube (as explained in chapter 4) and determine the filtration resistance according to the operational parameters and 2) extrapolate this finding to the whole bundle of tubes (700 tubes) regarding the module as a “single tube” and approximating it to a porous medium in

which the properties of the membrane (permeability) can be added and validated as a function of the operational parameters. The latter can, in this particular case, be based on the permeate flow.

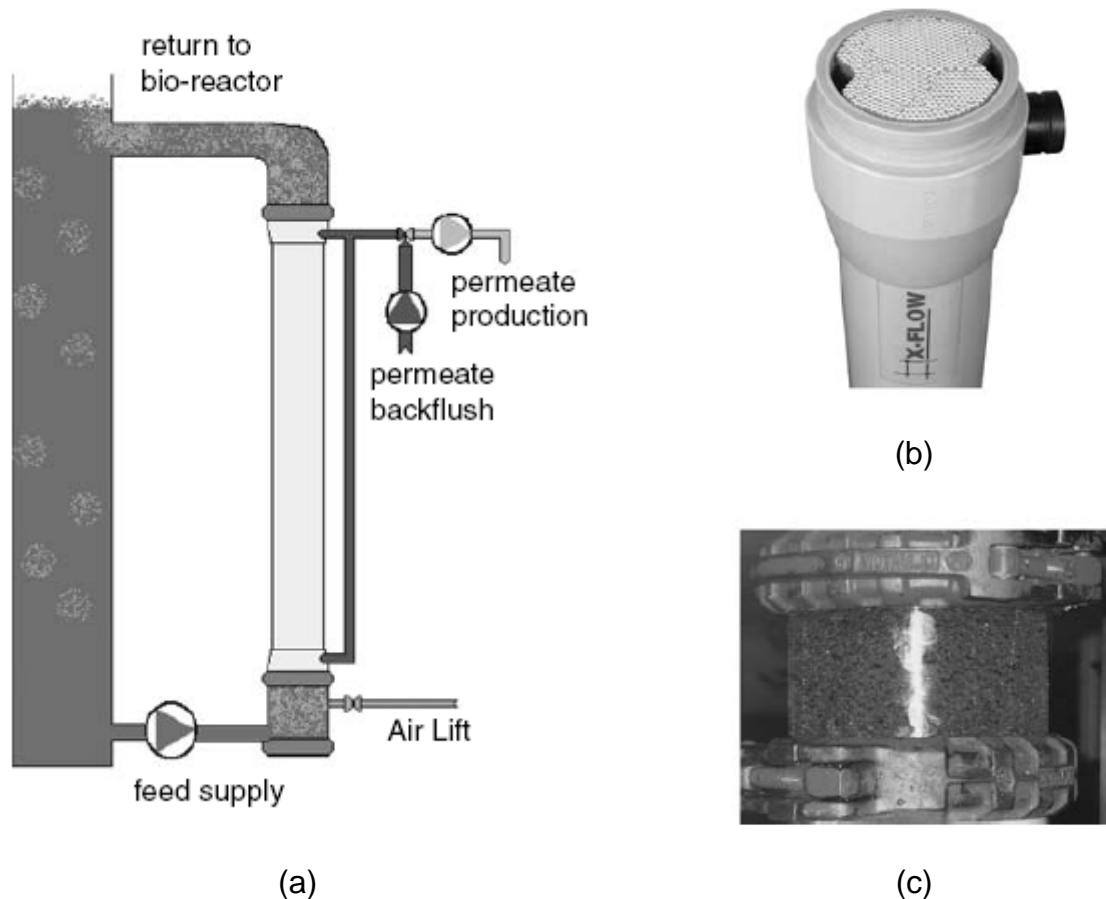


Figure 5.1 (a) Basic principle of the NORIT AirLift MBR with (b) 22 cm X-Flow COMPACT membrane module and (c) air diffuser (Futselaar et al., 2007)

Initial 2D CFD simulations of a single membrane tube were made using the VOF model (chapter 4) with the CFD software package Fluent v6.3 (Ansys, USA). The VOF model is commonly used to model slug flow. However, the VOF model is CPU expensive and it requires a very fine grid to capture the interphase between the liquid and gas and can, therefore, not be used to model the entire membrane module. This is especially true considering the fact that the module consists of 700 tubes and in each of them a slug flow pattern occurs. Hence, it was decided to first model a single membrane tube in 3D (Figure 5.2) starting out with a single phase flow, but including the filtration process and subsequently extrapolate it to 700 tubes. It is important to highlight that in chapter 4 the filtration (permeation through the membrane) was not included, whereas the filtration process is considered in the model developed on this chapter. Also, the module porosity is included in this model.

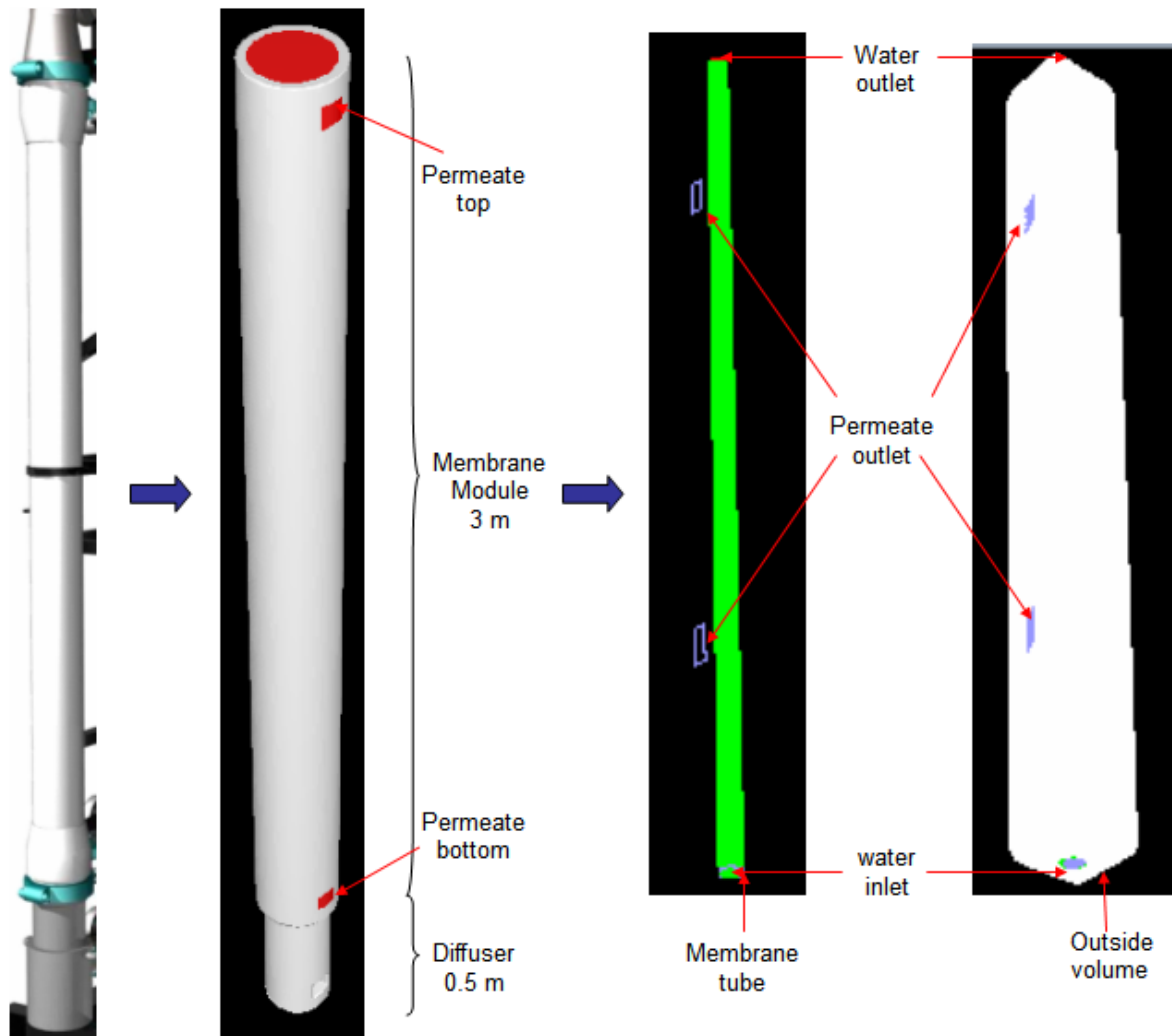


Figure 5.2. Side-stream module and single tube model

5.2.1 Modelling of the porous zone (membrane)

Two meshes (220 000 and 125 000 elements) were developed to model the single membrane tube in 3D and to check grid dependency (Figure 5.3).

Assuming average operating conditions (liquid flow rate of $16 \text{ m}^3 \cdot \text{hr}^{-1}$ and flux of 53 lmh), it is possible to determine the inlet velocity for one single tube of $0.3 \text{ m} \cdot \text{s}^{-1}$. The two permeate outlets (bottom and top of the membrane) had an area (the area of the permeate outlets was scaled down to keep the same permeate flow rates) of 0.02 cm^2 each, based on the operational parameters supplied by Norit. The simulation is conducted with water (single phase flow), due to the fact that a two-phase flow would be too CPU demanding and the purpose of this simulation is to check the behaviour of the filtration model and mesh resolutions, hence, two other meshes were constructed consisting of 220 000 and 125 000 elements respectively (Figure 5.3). This CFD model uses the $k-\epsilon$ RNG turbulence model for single phase flow.

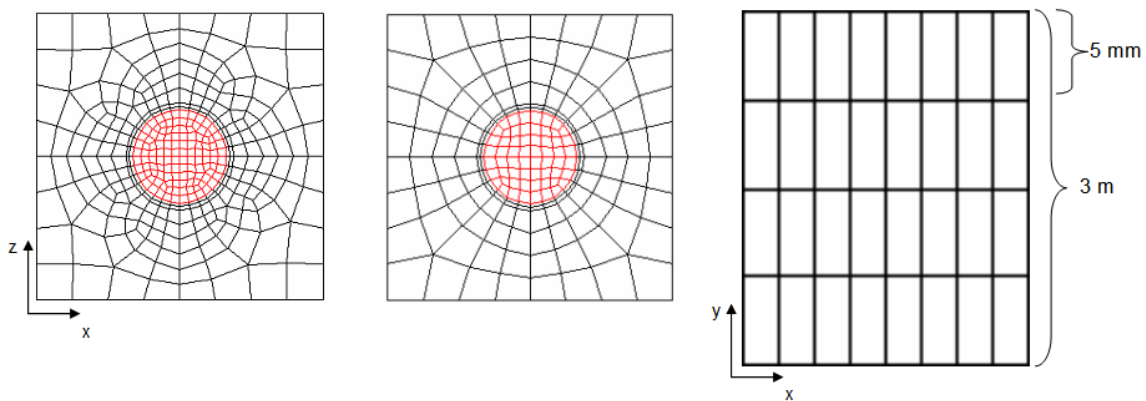


Figure 5.3. Mesh discretization for a single UF membrane tube: Mesh of 220 000 (left), 125 000 (center) and mesh along y direction (right)

The determination of the resistance value was made using the viscous (Darcy's law) (equation (1.63)) and inertial resistance model. The latter is an extra resistance of a porous medium to fluid flow, beyond that predicted by Darcy's law, and which is caused by local accelerations within the tortuous pore volume. This resistance is proportional to the fluid density times the flow rate and is calculated using equation (5.1):

$$TMP = \frac{1}{2} R_T t_x \rho_L J^2 \quad (5.1)$$

where t_x is the thickness of the membrane (m), R_T is the membrane resistance for (m^{-1}). Based on the operational conditions ($TMP = 0.2$ bar) an initial guess was made to determine the resistance value ($= 1.44 \cdot 10^{12} \text{ m}^{-1}$) using equation (1.63). The comparison of the two meshes with the previous resistance value is presented in Table 5.2.

Table 5.2. Comparison made with resistance of $1.44 \cdot 10^{12} \text{ m}^{-1}$

Mass flow rate ($\text{kg} \cdot \text{s}^{-1}$)	Norit	218 000	125 000
Inlet	0.00633	0.00630	0.00627
Outlet	0.00566	0.00536	0.00526
Permeate	0.00068	0.00093	0.00101
% Error (outlet)	-	5.23175	7.12710
% Error (permeate)	-	37.70498	49.20418

Table 5.2 shows the errors that are calculated using the reference provided by Norit. The permeate outflow error was from 38 and 50% for the finer and coarser mesh respectively. Therefore, a new resistance value was tested. This new resistance value was obtained by a trial-and-error approach to determine the correct permeate flow rate. The new resistance value was found to be $8.3 \cdot 10^{14} \text{ m}^{-1}$ resulting in error less than 5% in the permeate values (Table 5.3).

Table 5.3. Comparison made with resistance of $8.3 \cdot 10^{14} \text{ m}^{-1}$

Mass flow rate (kg·s ⁻¹)	Norit	218 000	125 000
Inlet	0.00633	0.00630	0.00627
Outlet	0.00566	0.00567	0.00559
Permeate	0.00068	0.00063	0.00068
% Error (outlet)	-	0.19495	1.32692
% Error (permeate)	-	7.55792	0.32328

Another factor, which is necessary to consider is the time for each simulation. The finest mesh takes 12 h whereas the coarser one only needs 3 h. Therefore, the best option is to use the coarser mesh. Once the resistance value is fixed, the next step was to simulate 7 tubes in the module having 700.000 elements (Figure 5.4) and to compare the results with the theoretical values.

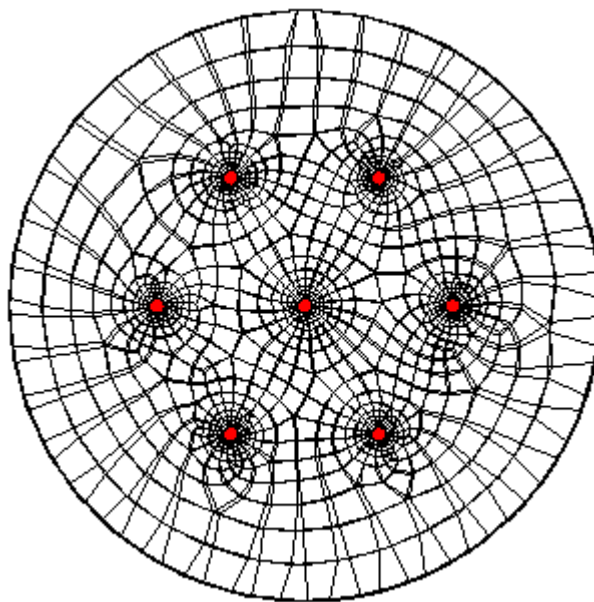


Figure 5.4. Seven tubes located in a side-stream module

Comparing only the permeate flow rates (in- and outlet flow rates have an error less than 1% so will not be discussed in further analysis) in the same way the theoretical values of 7 tubes with the simulation of seven tubes was found an error of less than 3.8 % compared to operational parameters from Norit which is acceptable for this purpose. 7 tubes required an additional 100 000 elements per tube. In order to make a complete mesh of the membrane module containing 700 tubes will need roughly $7 \cdot 10^7$ elements, which is currently impossible to simulate. Instead, the idea is to extrapolate these seven tubes to a single tube with the same cross section area (Figure 5.5)

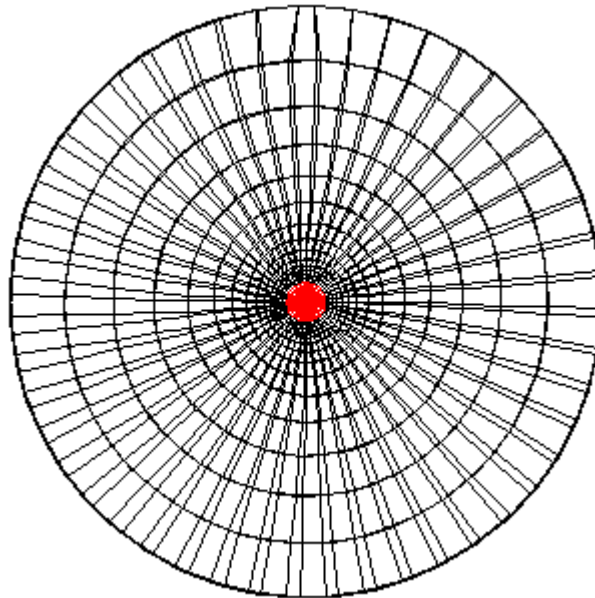


Figure 5.5. One tube with the same cross-sectional area of 7 tubes placed in a module

The results from the two simulations are compared in Table 5.4.

Table 5.4. Comparison of the simulation with seven tubes and 1 tube (with the cross-section area of seven tubes)

	7 tubes	1 tube
Cross-section area (cm ²)	1.49	1.49
Inlet (kg·s ⁻¹)	0.04386	0.04386
Permeate (kg·s ⁻¹)	0.00469	0.00134
Area membrane (m ²)	0.34	0.12

From Table 5.4, it is possible to observe that the inlet mass flow rate is the same. However, the permeate for one tube is 1/3 less than for 7 tubes which can be explained by the difference in surface area of the membrane. Due to the fact that the area of 7 tubes is 3

times larger than in the case of one tube with the same cross-sectional area of 7 tubes. Therefore, it is necessary to reduce the resistance value inside the tube to compensate for the decrease in the membrane area. Once again it is necessary to perform a calibration for this inside resistance value. It was found that in order to match the 7 tubes permeate mass flow rate of $0.00469 \text{ kg}\cdot\text{s}^{-1}$ it is necessary to use a resistance of $7\cdot 10^3 \text{ m}^{-1}$.

The module with 7 tubes has already 700 000 elements and for simulation purposes the mesh cannot have more than 1 000 000 elements. Therefore, it was only possible to simulate a single tube with the cross-sectional area of several tubes. Therefore, geometries of a cross-sectional area of 700 tubes were made and the resistance inside was extrapolated to match the permeate outlet and was found to be $6.1\cdot 10^5 \text{ m}^{-1}$ (Figure 5.6).

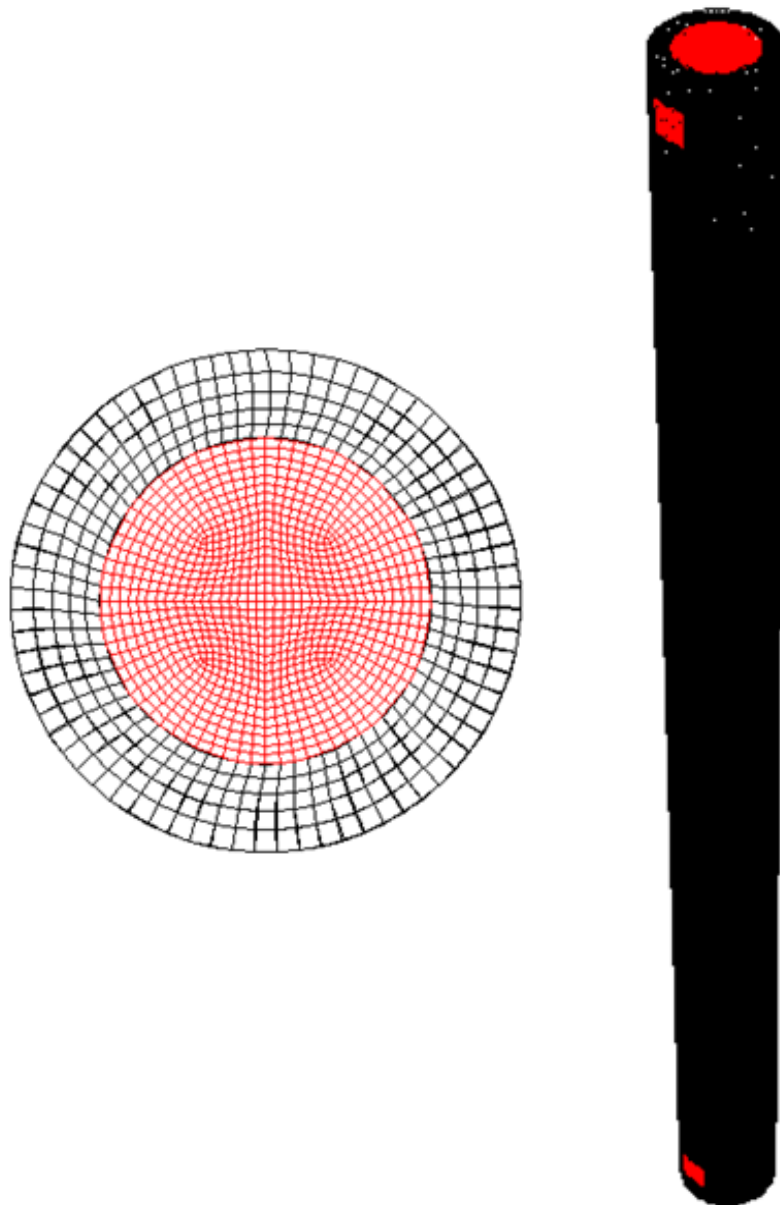


Figure 5.6. 1 tube with the same cross sectional area of 700 tubes

5.2.2 Extrapolation to a membrane module

The transversal cut of a membrane module can be seen in Figure 5.7.

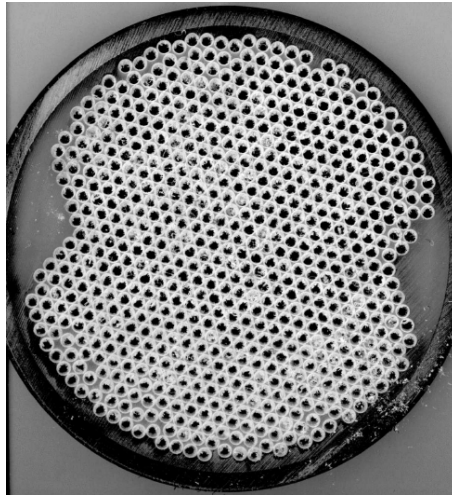


Figure 5.7. Transversal cut of a 22 cm X-Flow COMPACT membrane module

Comparing Figure 5.6 with Figure 5.7 it can be observed that one single tube with the cross-sectional area of 700 tubes located in the middle of the membrane module will not be realistic because it will give rise to an unrealistic and virtual contraction at the boundary between the air diffuser and the membrane module because the streamlines coming from the air diffuser to the membrane module cannot abruptly change direction (vena contracta). Therefore, a modification of the previous approach was adopted. A single tube with the cross sectional area of the membrane module and with an internal resistance was used to mimic the filtration and flow rate velocities for 700 tubes (~500 000 elements) (Figure 5.8). Also for the complete module the resistance value could be determined.

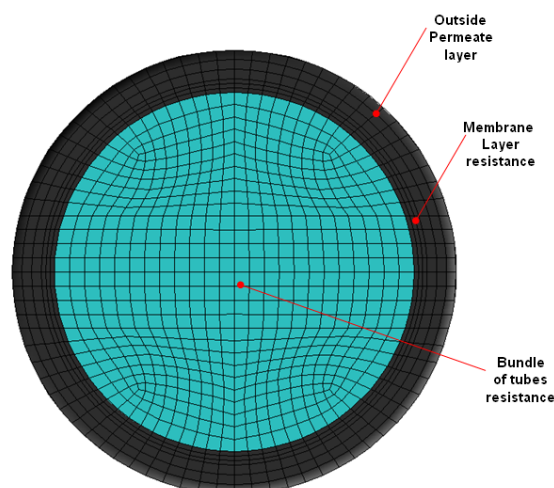


Figure 5.8. Discretization of the membrane module in three layers: bundle of tubes, membrane and permeate layer.

In Figure 5.8, three layers can be distinguished. An internal layer (bundle of tubes) with the diameter of the module (0.22 m) with a specific resistance to account for the array of 700 tubes. A second layer (membrane) with the resistance value discussed in section 5.2.1 and a third layer (permeate) with no resistance. To determine the resistance due to the bundle of tubes a similar trial-and-error approach was used as the one performed to determine the membrane resistance (see section 5.2.1). The exact resistance value cannot be disclosed as it is protected IP of FlowConcept. Moreover, it is possible to determine the velocity profile within the bundle of tubes for a single phase flow (Figure 5.9).

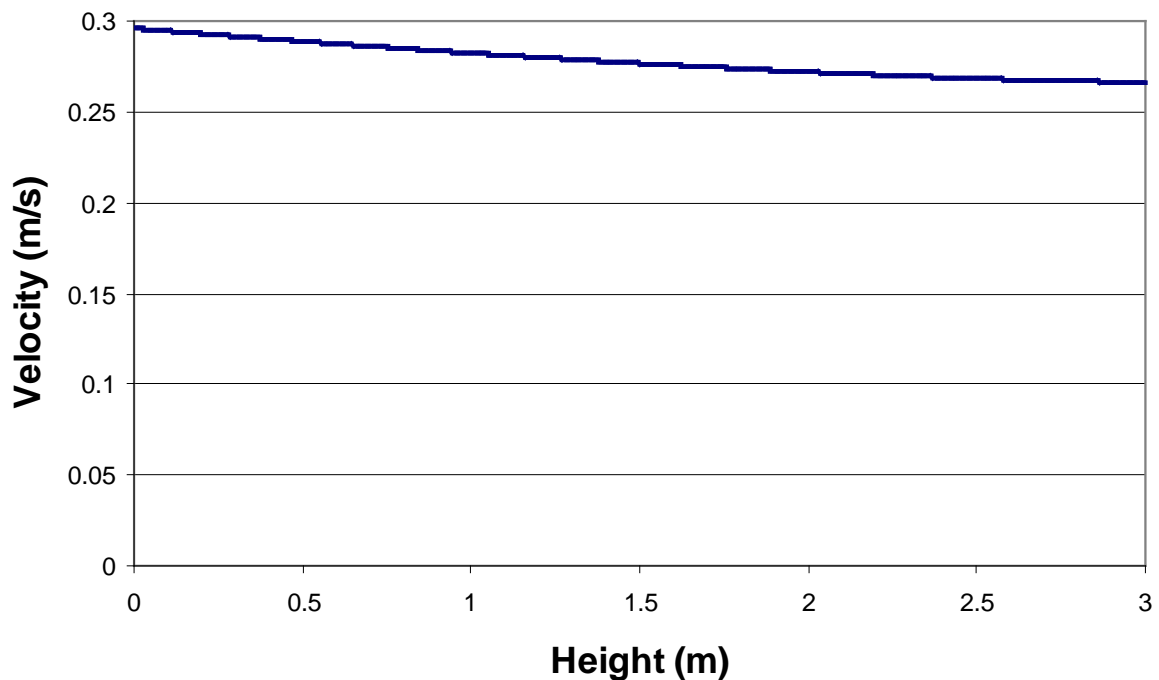


Figure 5.9. Velocity profile along the y-axis of the module

Figure 5.9 shows the velocity profile along the membrane tube axis and shows a reduction of 10 % comparing the in- and outlet velocity due to the loss of mass flow rate caused by the permeation along the membrane module and the filtration resistance. The permeate outlet is within 5% error compared to measured values proving the validity of the CFD model (Table 5.5).

Table 5.5 comparison between the theoretical operation and the CFD model

Mass flow rate ($\text{kg}\cdot\text{s}^{-1}$)	Norit	500 000
Inlet	4.43556	4.43556
Outlet	3.96428	3.94571
Permeate	0.47128	0.48985
% Error (permeate)	-	3.94063

5.3 CFD modelling of the air diffusers

Conventionally, side-stream MBRs are operated in single phase flow. In this case, in order to remove fouling, high cross-flow velocities are needed which leads to more energy consumption of the pumping process. To overcome this, air can be injected to create a two-phase flow and use the buoyancy effect to move the liquid in the upward direction (airlift) requiring less energy compared to having a single phase flow (Figure 3.8). The added value is also that this approach allows to better control the fouling. Nevertheless, it is important to have a good mixing (better air distribution in the cross-sectional surface of the membrane) and to avoid dead zones which will promote fouling. The objective is to model two different air diffusers and to determine which one performs better in terms of distribution of air to the bundle of membrane tubes above it. The scheme of where the air comes into the system is shown in Figure 5.10 for the disk and ring aerator.

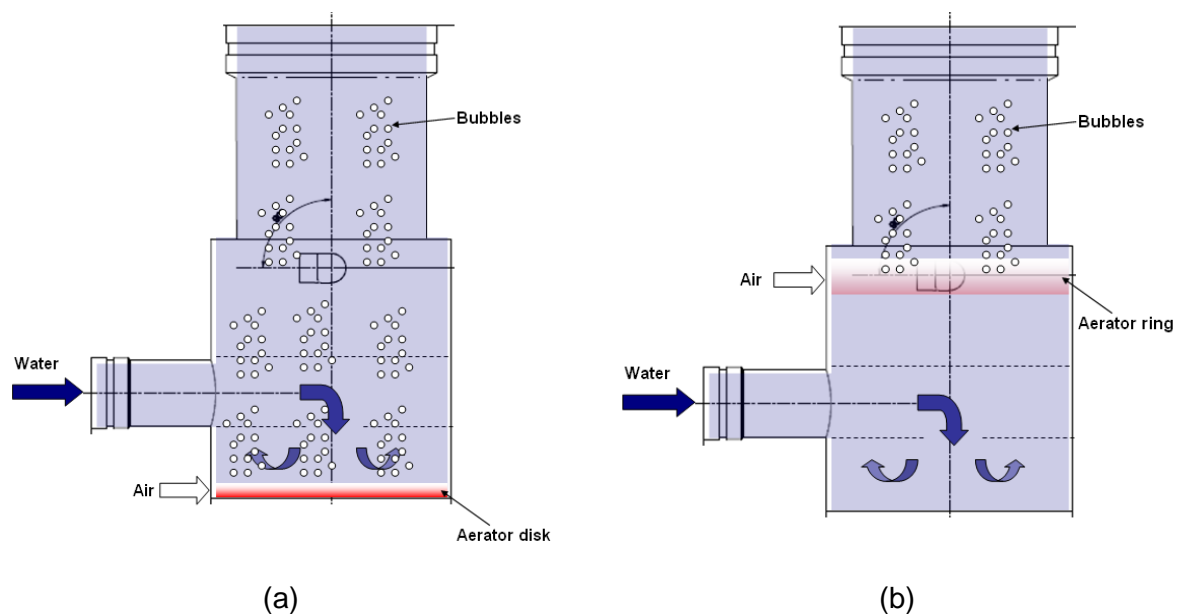


Figure 5.10. scheme of the aerator (a) disk and (b) ring

From Figure 5.10 and 5.11 it is possible to see how the water enters the air diffuser system. The inlet is a tube that crosses the entire air diffuser and has a hole close to the center of the membrane module. This hole can be either positioned face down or face up. Normally, it is facing in the downward direction to promote the mixing. Figure 5.11a and 5.11b show the disk and ring aerators respectively. The ring aerator has 35 holes in the wall.

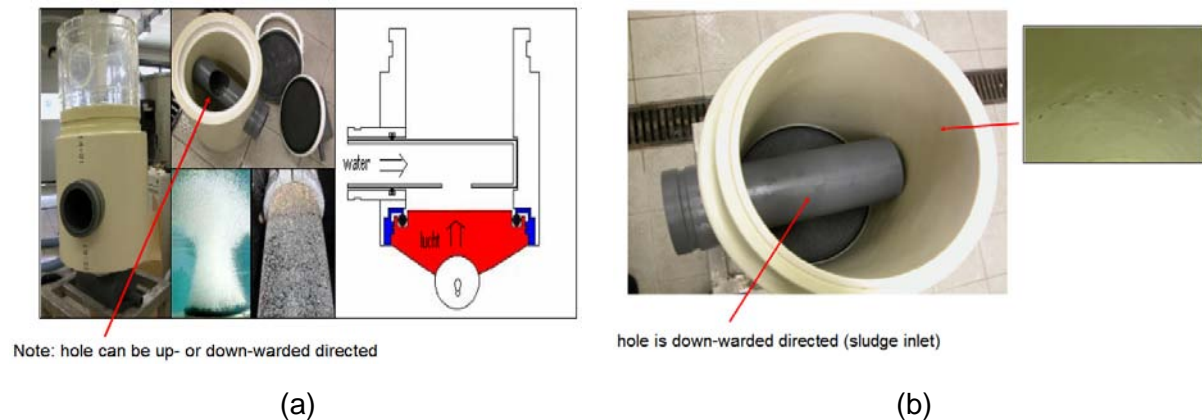


Figure 5.11. Aerator (a) disk and (b) ring

The geometry of the air diffuser system was built in Gambit v6.3 (Figure 5.12). The mesh has ~1 000 000 elements, a height of 0.5 m and a diameter of 0.22 m. The tube, where the water comes into the system which in reality is a tube (Figure 5.11) was modelled as a square duct for simplicity in the mesh generation, keeping the same area as the tube.

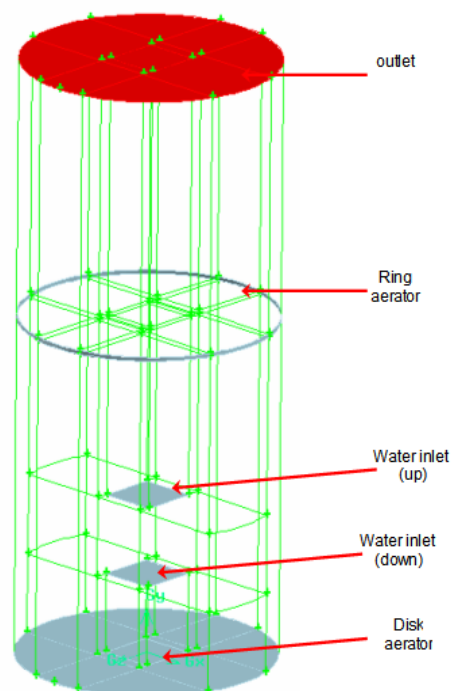


Figure 5.12. Air diffuser grid

In Figure 5.12, two air inlets (disk and ring aerator) and two water inlets (down and up) were implemented. Depending on which aeration system is to be simulated the different boundary conditions can be switched to “wall”. E.g. if it is necessary to analyze the ring aerator with the water inlet coming down, the disk aerator and the water inlet up are modelled as a wall. This only requires setting up one grid and mesh, which saves time.

Two other important aspects regarding the geometry are worthwhile mentioning. First, the circular tube where the water comes in (Figure 5.11) was drawn as a square tube for simplicity in the mesh generation. Similarly the water inlet being a circular inlet was drawn as a square inlet maintaining the same surface area yielding the same velocity and flow rate in the system. Second, the ring aerator, which in reality consists of 35 holes with a diameter of 3 mm located around the module, was modelled as a surface of 3 mm (same diameter of the hole) thick around the aerator and the flow rates are conserved to simulate the aeration. It is important to highlight that this changes in shape (from circular to square) could generate velocity gradients within the system, but as this was a modelling exercise, it was acceptable. The inlet flow rates, areas and velocities are summarized in Table 5.6.

Table 5.6. Operational conditions of the air diffusers

		Parameter	
Air		Flow rate ($\text{m}^3 \cdot \text{h}^{-1}$)	8.8000
		Flow rate ($\text{m}^3 \cdot \text{s}^{-1}$)	0.0024
	Ring	Diameter (m)	0.2020
		Height (m)	0.0030
		Area (m^2)	0.0019
		Velocity inlet ($\text{m} \cdot \text{s}^{-1}$)	1.2815
	Disk	Diameter disk (m)	0.2020
		Area (m^2)	0.0322
		Velocity inlet ($\text{m} \cdot \text{s}^{-1}$)	0.0760

		Parameter	
Water		Flow rate ($\text{m}^3 \cdot \text{h}^{-1}$)	16.0000
		Flow rate ($\text{m}^3 \cdot \text{s}^{-1}$)	0.0044
		Diameter (m)	0.0500
		Area (m^2)	0.0020
		L (m)	0.0443
		W (m)	0.0443
		Area (m^2)	0.0020
		Velocity inlet ($\text{m} \cdot \text{s}^{-1}$)	2.2637

When starting the simulation, it is necessary to first run the simulation to steady state using a single phase (only water) until the solution converges in order to retrieve the velocity profile in the system. The turbulent model that was used is the k- ϵ RNG model. To model the two phase flow, the mixture model with a bubble diameter of 5 mm is used (Nguyen Cong Duc et al., 2008a). This profile is presented in Figure 5.13, where the water is coming from the bottom inlet.

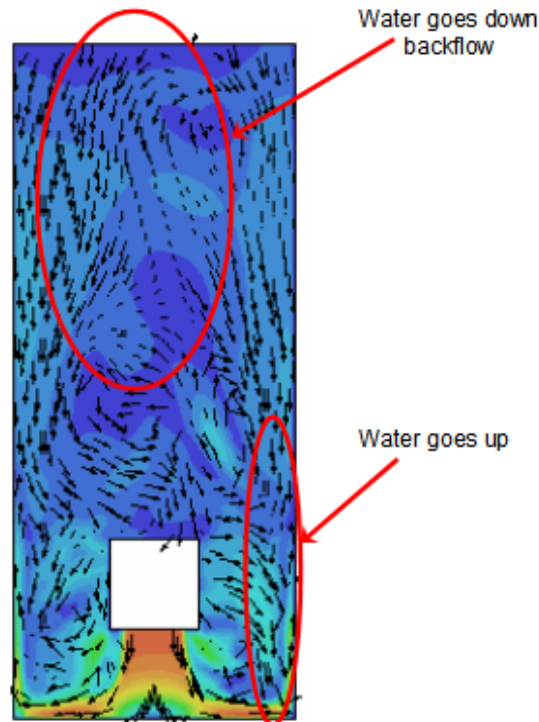


Figure 5.13. Velocity contours and vectors (scale: red 2.5 and blue $0 \text{ m}\cdot\text{s}^{-1}$)

From Figure 5.13 it is possible to observe how the water goes to the bottom and then ascends near the walls. However, where the square duct is located, above there is backflow of water and the water starts coming down there. In the section below air is added for the aerators.

5.3.1 Simulation of the disk aerator

During this simulation, the ring aerator boundary condition is set to wall (no air coming from the ring aerator). The water is coming from the bottom with a velocity of $2.3 \text{ m}\cdot\text{s}^{-1}$ and the air with a velocity of $0.076 \text{ m}\cdot\text{s}^{-1}$ (Table 5.1). The results of the air distribution after 10 s are presented in Figure 5.14 along with the velocity profile.

From Figure 5.14, it can be seen how air is well distributed along the air diffuser (apart from near the tube). Also, at the top, which is the inlet of the membrane module, it is possible to see how the air is well distributed, which, indeed, will help to control the fouling. From the velocity vector plot, it is possible to see, that there is still a backflow above the inlet tube compared to single phase flow (Figure 5.13). Figure 5.15 shows the distribution of the air in 3D, proving a well mixed system, except above the square duct, which resembles a dead zone. This may be different when modelling it as a tube. Nevertheless, a dead zone in that location is not important because the membrane is located high above the square duct, which allows that the mixing takes place. On the contrary, if the membrane module would be located closer to the inlet, it could affect drastically the performance of the air diffuser. It is possible to see that the water inlet is located just above the air diffuser and, therefore, the air

diffuser will not work properly. So it is recommended to have a sort of torus ring shaped instead of a disk.

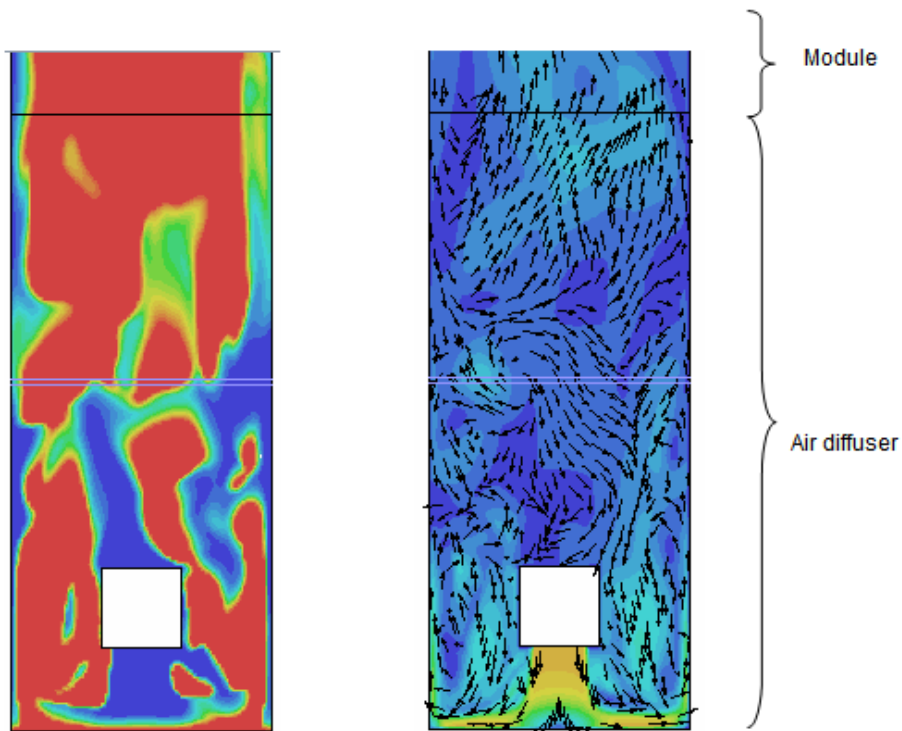


Figure 5.14. Contours of volume fraction of air (left) from 0.05 red to 0 blue and velocity vectors (right) red 3 to blue 0 $\text{m}\cdot\text{s}^{-1}$

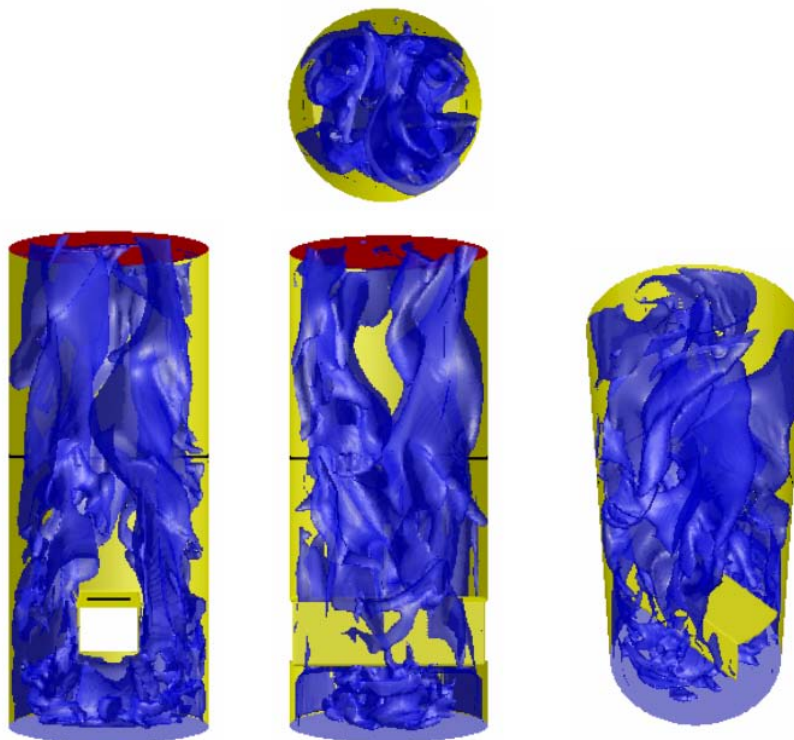


Figure 5.15. Air distribution in the diffuser for a volume fraction of air above 5%.

5.3.2 Simulation of the ring aerator

For this case, the disk aerator boundary condition is set to wall. The water is coming from the bottom with a velocity of $2.3 \text{ m}\cdot\text{s}^{-1}$ and the air with a velocity of $1.3 \text{ m}\cdot\text{s}^{-1}$. Initial conditions were those obtained after convergence of the single-phase steady state simulation. The results of the air distribution after 10 s are presented in Figure 5.16 along with the velocity profile.

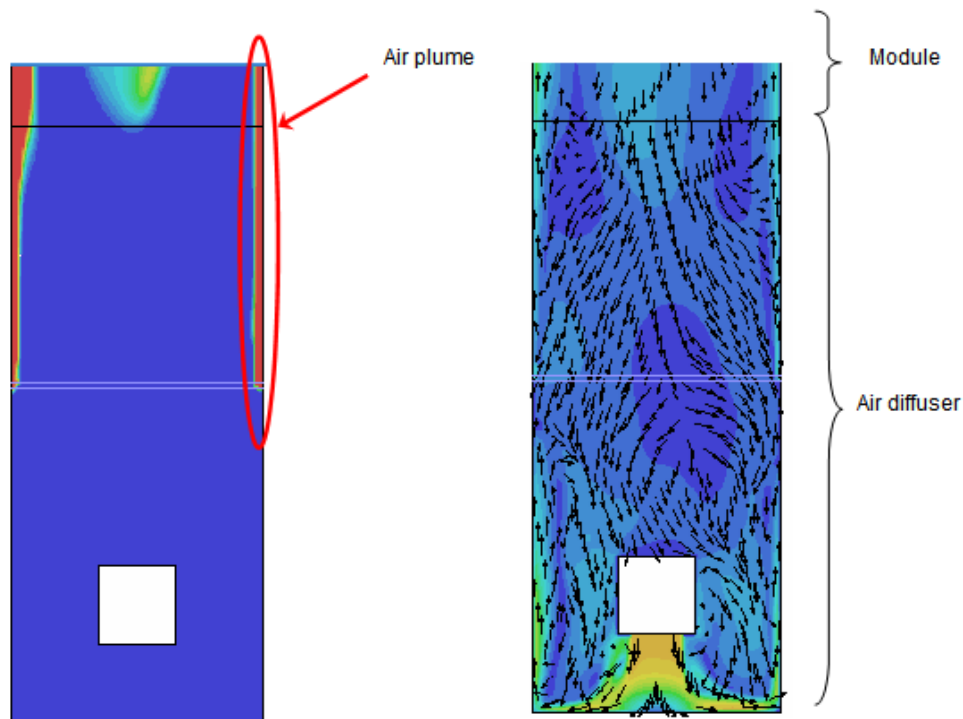


Figure 5.16. Contours of volume fraction of air (left) from 0.05 red to 0 blue and velocity vector (right) from $3 \text{ m}\cdot\text{s}^{-1}$ red to $0 \text{ m}\cdot\text{s}^{-1}$ blue

From Figure 5.16, it is possible to see that the plume of air is developing close to the wall and does not mix with the bulk of the diffuser. In Figure 5.17 the air distribution in 3D of the whole air diffuser is presented.

From Figure 5.17 it is possible to observe that there is no good mixing of water-air in the diffuser system. The air ascends close to the wall and does not diffuse into the bulk zone. Therefore, membrane tubes that are located in the middle of the module will not receive much air making them more prone to fouling. This model-based analysis shows its power to improve the design of the diffuser system.

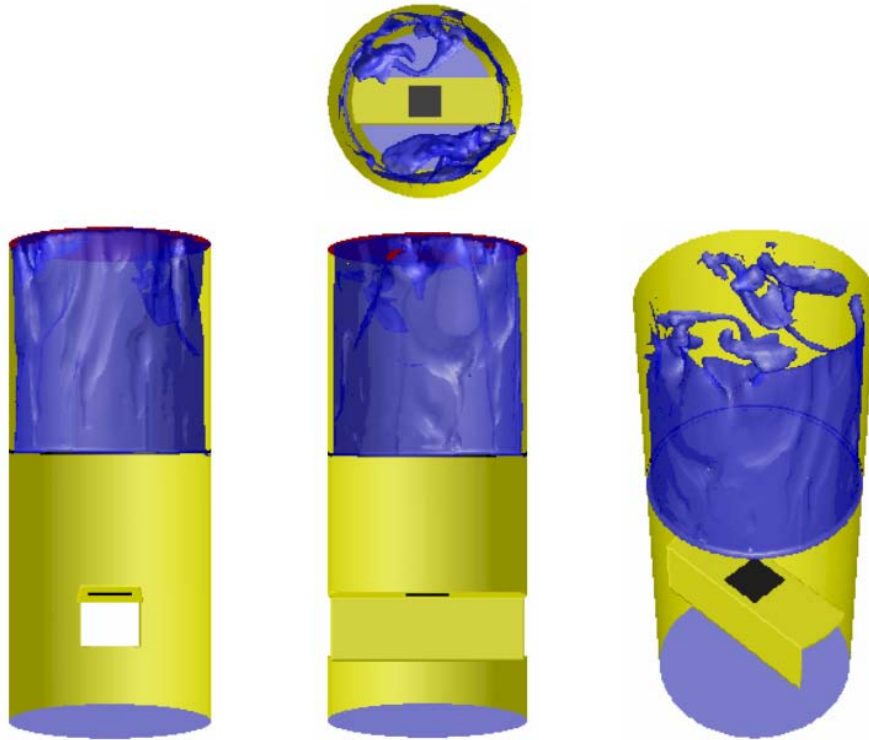


Figure 5.17. Air distribution in the diffuser for volume fraction of air above 5%

5.3.3 Comparison of the air diffusers

Comparing the air distribution at the inlet of the membrane module (Figure 5.18) being the top of the diffuser, it is possible to observe that in the case of the ring aerator most of the air is directed to the tubes located at the outside of the module. On the other hand, for the disk aerator, homogeneous air distribution to the bundle of tubes was found.

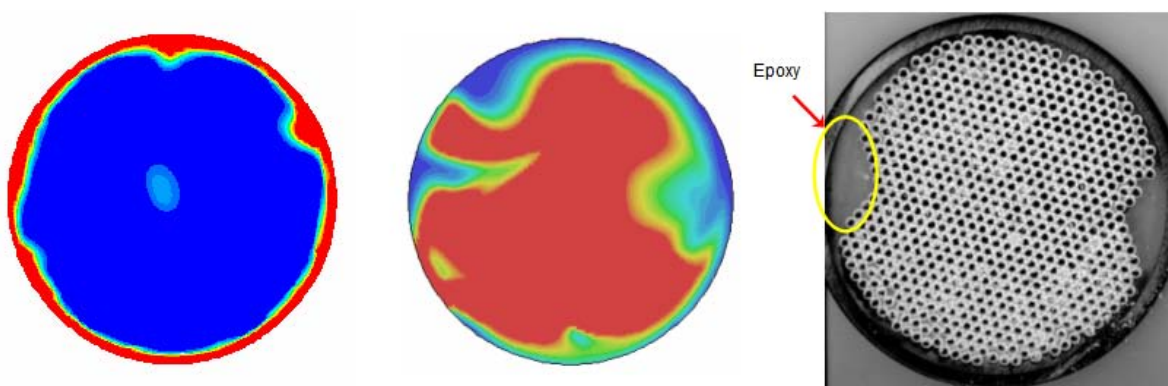


Figure 5.18. Contour of volume fraction of air from 0.05 red to 0 blue at the inlet of the membrane module for the ring (left), disk (center) and real module inlet (right)

Based on Figure 5.18 (right), it can be observed that the model did not include the big section of epoxy which will clearly increase the velocity of the two-phase flow at the inlet of

the bundle of membrane tubes. Therefore, in order to capture this phenomenon, it would be necessary to add a resistance for the epoxy to make the simulation more realistic. However, this was outside the scope of this work.

Bearing these results in mind and assuming that the model predictions can be validated, it could be suggested to, in future, design systems that combine the two aerator systems to produce a more homogeneous distribution of air at the entrance of the module. The disk aerator with a torus ring shaped will ensure air going to the bulk region of the entrance, whereas the ring aerator will take care of the wall region. Moreover, different flow rates could also be used. This will also provide more control authority at no real additional cost.

5.4 CFD modelling of the membrane module + air diffusers

In sections 5.2 and 5.3, a CFD model was developed for the membrane module and the air diffusers respectively. However, the airlift MBR system works as a whole, for which the integration of these two CFD simulations needs to be made to see the overall behaviour of the systems as they clearly interact. Also, having a 3 m high structure above the air diffuser affects the pressure drop along the membrane module. In addition, in section 5.2, where the membrane module model was built, it was based on single phase, but once the air diffuser is added to the system a two-phase flow exists. Therefore, a geometry including the membrane module (bundle of tubes) and air diffuser was set up (Figure 5.19).

The new mesh has a total of ~ 500 000 elements and takes 1 week for 60 s of simulation. It used the same parameters as the air diffuser model (section 5.3) with the membrane resistance values (section 5.2). The distribution of air, in volume fraction of air is presented in Figure 5.20 for both aerators, where the same air flow rate is pushed into the system.

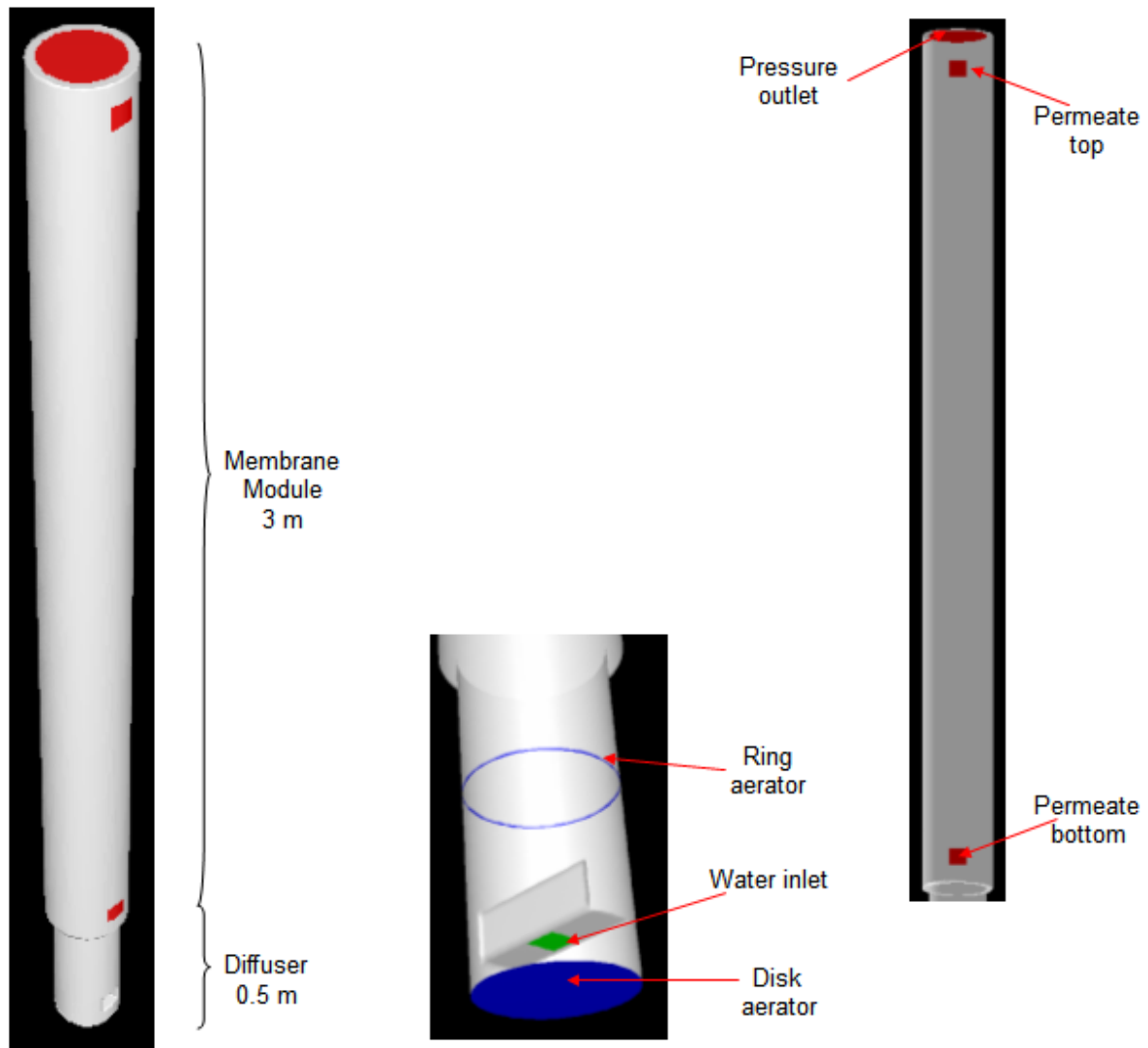


Figure 5.19. Discretization of the membrane module and the air diffuser.

From Figure 5.20, it is possible to observe that the case of the ring aerator, the air concentrates towards the outside wall of the membrane module and less in the bulk region due to buoyancy. On the other hand the disk aerator provided a better diffusion of air within the bundle of tubes. Hence, it is likely that in case of a ring aerator, the tubes that are located in the center of the module shall be more prone to fouling due to less scouring of particles attached to the membrane surface.

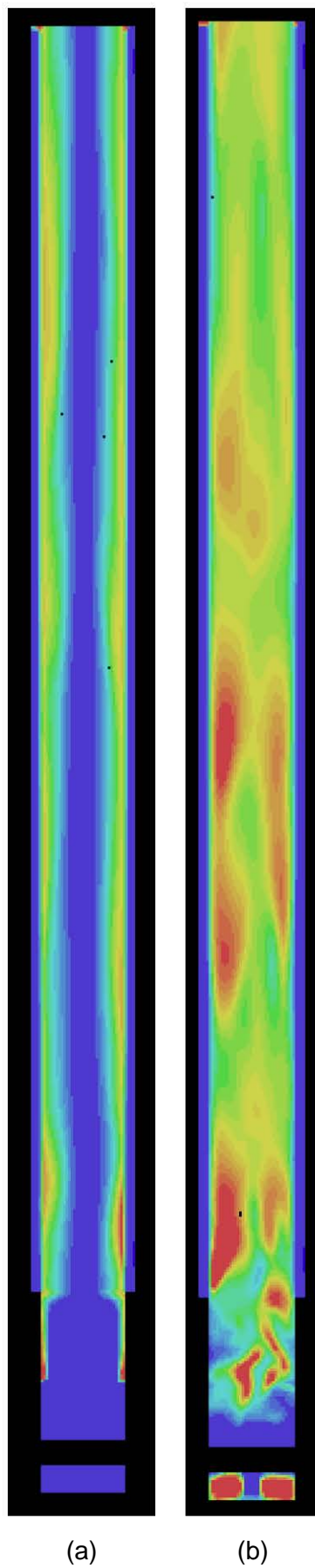


Figure 5.20. Volume fraction of air (blue 0.0 – red 0.2) for (a) ring and (b) disk aerator.

Detailed simulated SSHs were not computed for these simulations as there is no data to validate with. Nevertheless, a qualitative representation of expected SSH can be given at different locations of the inlet of the membrane module and is shown in Figure 5.21.

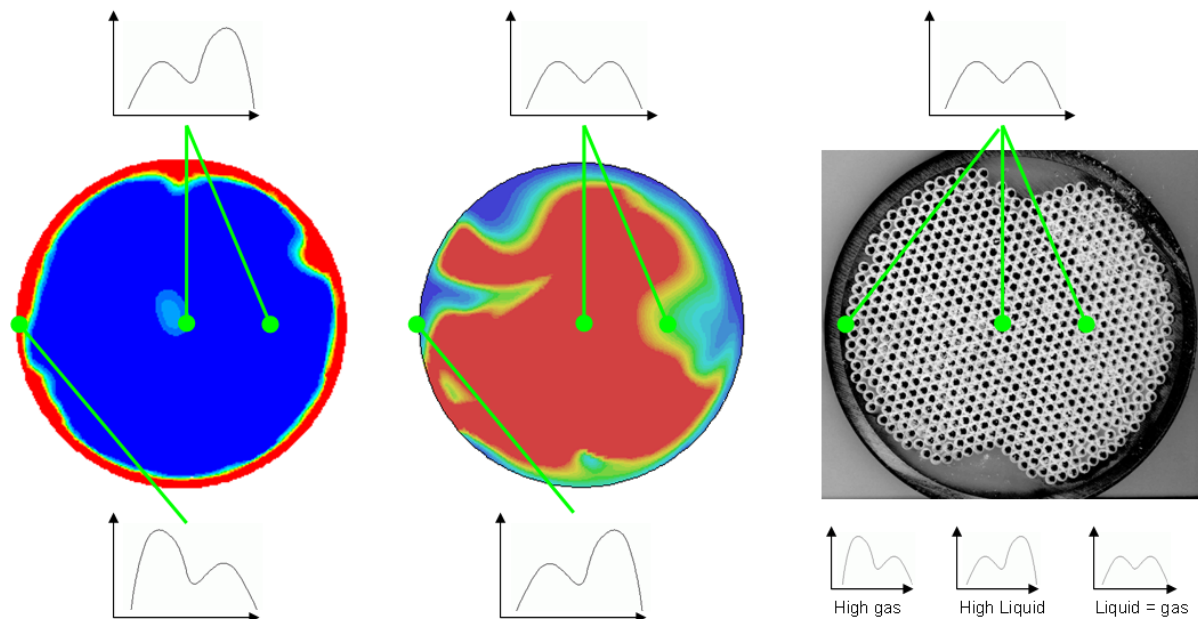


Figure 5.21. Qualitative representation of SSH at the inlet of the membrane module for the ring (left), disk (center) and ideal module inlet (right)

From Figure 5.21, it is possible to observe the following:

- *Ring aerator*: in the bulk region there will be more liquid going through the membrane (liquid slug peak) whereas near the wall the opposite is true, more gas going into the membrane (gas slug peak) and there will not be a balance between the bulk and the wall region. Optimal fouling control as assumed to be represented by a well-balanced SSH is not the case.
- *Disk aerator*: the bulk region will have a better balance of liquid and gas (liquid and gas slug peaks), whereas, on the other hand the wall will have more liquid going to the membrane (liquid peak). The ideal case will be that liquid and gas will flow evenly distributed along the cross-section of the membrane module which will improve the fouling rejection characteristics based on hydrodynamics.

This type of CFD model can be used to determine the dispersion of air within the membrane module and locate dead zones, or in this case, where the air is not well dispersed within the membrane module. This CFD model needs to be validated, for instance, for the cases presented here; because it was a modelling exercise and cannot be used as such for design and optimization of this system and second, using physical properties of activated sludge (density and viscosity) due that it has a non-Newtonian behaviour, which will affect the air diffusion within the system as well as the resistance of the porous zone. However, the model

output is promising and after validation can be a powerful tool for improved design of air diffusers.

5.5 Conclusions

To study the filtration and the air diffusion in a full-scale side-stream MBR (Norit X-Flow) three CFD models were built. The CFD modelling was restricted to model predictions as the results obtained from these CFD models were not validated due to lack of proper experimental data. Hence, results should not as such be used for design and optimization of real systems. However, a combination of a disc (torus ring shaped) and ring aerator system could be a good option to design for a more homogenous air distribution near the inlet of the module.

The first CFD model was related to the membrane module. This model was built stepwise from a single UF membrane tube (micro-scale), where the membrane resistance was determined by calibration based on operational parameters for single phase flow. Subsequently, the model was extrapolated to the entire membrane module (700 tubes – macro-scale). This conceptual model contains two zones, one zone related to the membrane, defined based on the simulation of one single membrane tube, and a second zone related to the effect of the resistance caused by the 700 tubes (bundle of tubes). Also the latter was determined based on calibration.

The second CFD model was related to two types of air diffusers (ring and disk aerator) and aimed at predicting the air distribution within the membrane module. The disk aerator was found to provide a better air distribution in the module which implies better mixing and decrease of fouling in the membrane wall due to the two-phase cross flow.

Finally, a third CFD model integrated the two previous models, maintaining the same parameters as for the two individual CFD models. The simulation was made in two-phase flow. The disk aerator provides a better air distribution compared to the ring aerator where the air accumulates towards the outside wall of the membrane modules and not in the bulk region.

Chapter 6. MBR Sludge Rheology

Abstract*

Viscosity measurements play an important role in activated sludge characterization, especially with respect to MBR operation where high shear rates occur near the membrane surface. Chapter 2 revealed the possible impact of viscosity on slug flow patterns. Moreover, viscosity plays a major role in terms of oxygen transfer efficiency and energy consumption (e.g. pumping). Therefore, an accurate viscosity relationship as a function of *TSS* and temperature is important in order to model the behaviour of the activated sludge. Ten pilot and full-scale municipal membrane bioreactor plants throughout Europe were investigated during the period 2007-2008 using the Delft Filtration Characterisation method (DFCm). Unlike all literature work, sludge rheology was measured on site exploiting the resemblance of the DFCm to a tubular rheometer. A new rheological model for the viscosity of activated sludge was developed maintaining the same mathematical structure as previous rheological models made for MBRs. This model was also compared with the former models and it was found to yield higher predictions by a factor of two. The reason for this discrepancy may be attributed to other sludge properties not included in the model, the usage of different rheometers (geometry) and limitations of the model. Finally, the effect of temperature was found statistically insignificant.

* Redrafted after:

Moreau, A.A., **Ratkovich, N.**, Nopens, I., van der Graaf, J.H.J.M. The (in)significance of apparent viscosity in full-scale municipal membrane bioreactors. *Journal of Membrane Science* 340 (2009) 249–256.

Introduction

MBRs are typically operated at elevated Total Suspended Solids (*TSS*) content to decrease the waste sludge and the plant footprint. However, these elevated *TSS* result in higher viscosity values compared to conventional systems. This high viscosity remains a challenge in terms of oxygen transfer and energy consumption optimization of MBRs (Judd, 2006).

Activated sludge is considered a non-Newtonian fluid behaving as a pseudo-plastic fluid (Seyssiecq et al., 2003) as was previously discussed briefly in section 1.3.2. It is composed of flocs which tend to get disrupted under high shear rate conditions, resulting in an apparent viscosity decrease. Rheological characterization was investigated (Le-Clech et al., 2003) to describe activated sludge flow behaviour in terms of activated sludge apparent viscosity and dependency on applied shear rate and suspended solids concentration. Sludge rheology was also found to depend on sludge age (40 to 80 days) (Laera et al., 2007). Apparent viscosity for a large number of small scale MBR plants, with a range in *TSS* content (5 to 40 g·L⁻¹) was also reported (Rosenberger et al., 2006). Typically, municipal full-scale MBR systems are operated around 10 - 12 g·L⁻¹ and SRT of around 20 days. However, there is not a uniform model of apparent viscosity that can be used for design and optimization of equipment (pumps, mixers, diffusers, etc) because the models developed in literature (e.g. Rosenberger et al. (2006)) do not seem valid for different sludges mixtures (high heterogeneity among different sludge) and they are not representative.

In this work, ten large-scale MBR plants were investigated during and data needed to calculate the apparent viscosity of activated sludge on site for each plant was gathered. The aim of this chapter is to quantify variations in activated sludge apparent viscosity in municipal full scale MBR applications, which was, to our knowledge, never done before. In a second part, a popular rheological model of activated sludge was calibrated on the obtained data.

6.1 Plant description

Specifications of each MBR plant are presented in Table 6.1. Six full-scale and four pilot MBRs were investigated during this study. MBRs were operated with a sludge age ranging from 13 to 30 days. Seven of the investigated MBRs followed hollow fiber (HF) membrane configuration, four flat sheet (FS) membrane configuration and two multi tube (MT) membrane configuration.

Table 6.1 Characteristics of the MBR plants (Moreau et al., 2009)

	Location A	Location B	Location C	Location D	Location E	Location F	Location G	Location H	Location I	Location J
Scale	Pilot	Full	Full	Pilot	Pilot	Full	Full	Full	Full	Pilot
Membrane type	HF/FS/MT	Hollow fibre	Hollow fibre	HF/FS	Flat sheet	Flat sheet	Hollow fibre	Multi tube	Hollow fibre	Hollow fibre
SRT (d)	20	21	24	13	13	25	20	30	24	20-25
Pore size (mm)	0.08/0.1	0.04	0.04	0.04/0.1	0.2	0.2	0.04	0.03	0.04	0.04
SADm ($\text{m} \cdot \text{h}^{-1}$)	0.7-1.5	0.38		0.5-1.25	0.86	0.33	0.4			0.3-0.6
SADp ($\text{m}^3 \cdot \text{m}^{-3}$)	35-90	16		25-70	52	20.6	17			
TSS ($\text{g} \cdot \text{L}^{-1}$)	5.5-11.5	6.9-13.9	9-9.5	3.5-13.6	5.6-10.4	6.4-16.4	14-14.9	9-9.3	9.8-11	8-8.5
T (°C)	9.7-14.1	12.7-17.8	9.7-12.4	16-19.6	17-27.4	11.9-24.7	17.9-21	17.6-18.9	21.1-22.2	21.9-25

*SRT: Solid Retention Time; SADm: Specific Aeration Demand to membrane area and SDAp: Specific Aeration Demand to permeate volume

6.2 Delft Filtration Characterization method (DFCm)

Delft University of Technology has developed a small scale filtration characterisation installation combined with a measuring protocol to investigate sludge reversible fouling potential. The DFCm stands for Delft Filtration Characterization method. It is a short term experiment, which has a single side stream ultrafiltration membrane tube (X-flow, diameter = 8 mm, nominal pore size = $0.03 \mu\text{m}$) forming the basic filtration system of the unit. A peristaltic pump is used for the activated sludge recirculation with a cross-flow velocity (CFV) of 1 m s^{-1} (single-phase flow). The permeate is extracted at a constant flux (80 l/h). Activated sludge samples collected from different MBRs can be filtered under identical operational conditions. In this way, differences in filterability can be related exclusively to the properties of the MBR activated sludge sample. The main step of the measurement protocol is the activated sludge filtration step. During the filtration step, several parameters (TMP, flux, temperature, pH) are monitored and stored in a computer file using the software application called Testpoint (National Instruments, USA).

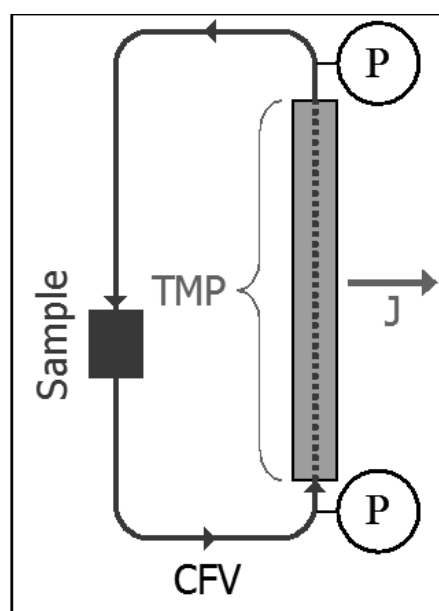


Figure 6.1 Schematic of the Delft Filtration Characterization method (DFCm) unit

6.3 Description of different rheometer principles

Two types of classical rheometers have typically been used in literature to measure ex-situ apparent viscosity of MBR activated sludge: rotational and tubular rheometers.

The rotational rheometers consist of an inner cylinder (bob) and an outer cylinder (cup), with the sample fluid placed in the gap in between the two cylinders (Figure 6.2a). In this case, the bob rotates and the resistance to flow by the sample fluid to the movement of the rotating cylinder is measured as torque. The annular flow, which is formed in the gap between the two cylinders, is similar to the Couette flow, where one cylinder moves relative to the other leading to a centrifugal instability. The rotation of the bob generates a velocity gradient across the gap. This gradient is defined as the change in linear velocity between two fluid elements divided by their distance. As a result, the shear rates are expressed as a reciprocal of seconds (s^{-1}). While the rotation of the bob causes the fluid to flow, this resistance to deformation creates a shear stress on the cup, measured in pressure units (Pa). The shear stress depends on the torque and the dimensions of the geometry. This type of rheometer was used by Rosenberger et al. (2006) and Pollice et al. (2007) to measure the apparent viscosity of activated sludge samples up to shear rates of $2000 s^{-1}$. The main drawback of this system is that at higher shear rates, Taylor vortices start to form (Figure 6.2b) disrupting the liquid velocity field and forming eddies, which gives a wrong reading of viscosity due to the onset of turbulent viscosity (a flow property and not a fluid property). Therefore, extreme care needs to be taken when interpreting results. The formation of eddies can be avoided by decreasing the gap between the rotational (bob) and the static (cup) cylinder and reducing the rotational speed of the bob. However, the gap should remain larger than the largest particle in the suspension to prevent that the fluid moves at the bob velocity (Mori et al., 2006; Seyssiecq et al., 2003). A second drawback is that at high shear rates during the experiment, significant floc breakage may occur, which affects the viscosity measurements (De Clercq, 2003)

Capillary (tubular) rheometers (Figure 6.2b) induce the sample to flow in a laminar regime (depending on the cross-flow velocity (CFV)) in response to a pressure drop along the tube that is measured at both ends. It is possible to quantify the viscosity knowing the diameter and the length of the tube. Therefore, tubular rheometers are considered more suitable than their rotational counterparts (Seyssiecq et al., 2003) to study the rheology of activated sludge under real operating conditions (e.g. pumping process). Detailed information about the advantages and disadvantages of these types of rheometers can be found in Seyssiecq et al. (2003) and Rosenberger et al. (2006).

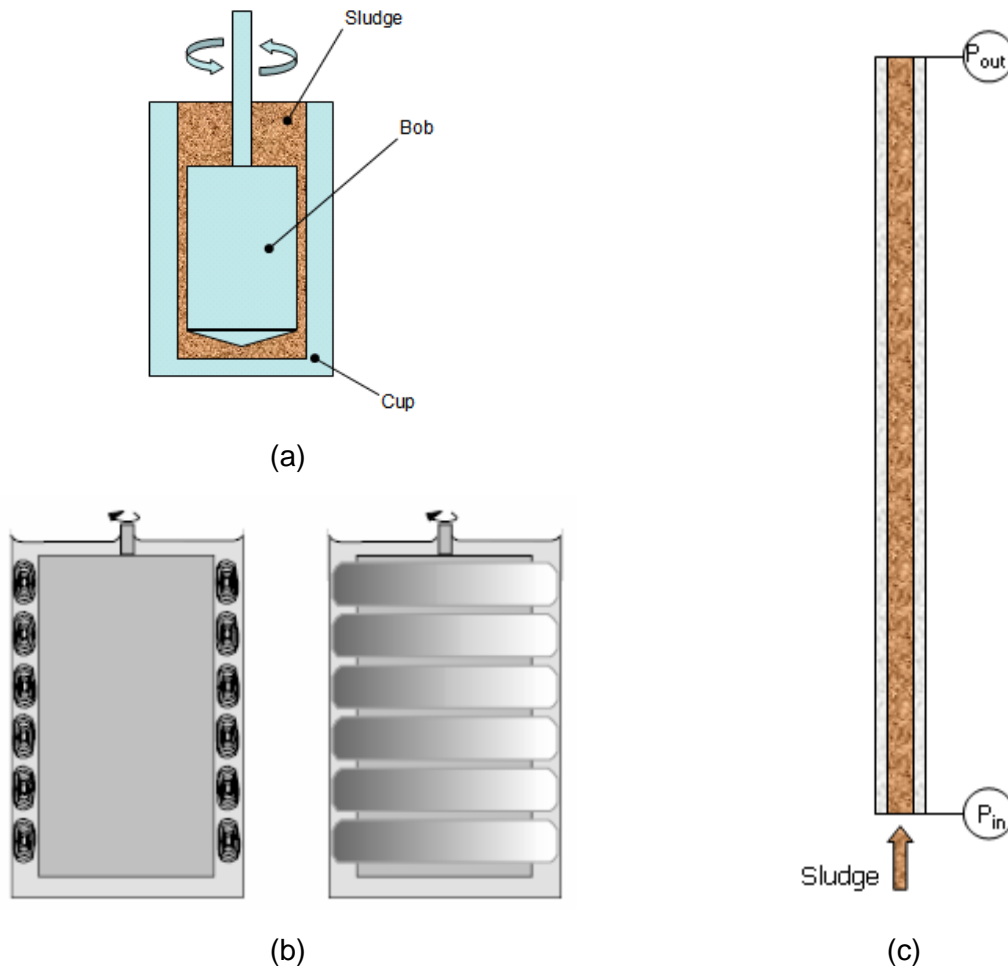


Figure 6.2 (a) Rotational rheometer, (b) formation of eddies and (c) capillary rheometer

The DFCm was originally built to measure sludge filterability characteristics. However, the way the DFCm unit is operated, it can actually be used as a tubular rheometer (Figure 6.1). Nevertheless, it is important to highlight that a capillary rheometer typically has a diameter of 1 mm, whereas the DFCm unit has a diameter of 8 mm. However, the same principle can be used, although attention should be paid to the occurrence of concentration gradients, which will give rise to a viscosity gradient between the wall and the bulk region. The applicability of the DFCm to serve as a tubular rheometer will be investigated in this chapter. It is important to highlight that when a sludge sample is under continuous shear stress (rotational or tubular rheometer), it is expected that de-flocculation (floc breakage) may occur. Nevertheless this was not studied in this work.

6.4 Apparent viscosity calculation

For each experiment conducted with the DFCm, the pressure loss along the membrane tube is monitored with two pressure sensors (Figure 6.1). The DFCm does not include air sparging (i.e. single-phase flow) and, hence, exhibits well-defined hydrodynamic conditions.

Therefore, pressure drop values and shear stresses occurring in the membrane tube can be theoretically derived.

The pressure drop along the membrane (ΔP_{mem}) can be determined from the reading of the pressure sensors (ΔP_{mea}):

$$\Delta P_{mem} = \Delta P_{mea} - \rho g L_{mem} \quad (6.1)$$

where L_{mem} is the membrane length (= 1 m). Subsequently, the shear stress can be calculated using equation (1.13) and the calculated pressure drop:

$$\tau_w = \frac{1}{4} \frac{d_{mem}}{L_{mem}} \Delta P_{mem} \quad (6.2)$$

where d_{mem} is the membrane diameter (= 0.008 m). Alternatively, shear stress can be defined as (equation 1.13):

$$\tau_w = \frac{1}{8} f_{mem} \rho u_{mem}^2 \quad (6.3)$$

where u_{mem} is the liquid cross-flow velocity in the membrane ($1 \text{ m}\cdot\text{s}^{-1}$). Hence, the Fanning friction factor (f_{mem}) can be determined combining equations (6.2) and (6.3):

$$f_{mem} = \frac{1}{2} \frac{d_{mem}}{L_{mem}} \frac{\Delta P_{mem}}{\rho u_{mem}^2} \quad (6.4)$$

This friction factor allows the calculation of the Reynolds number depending on the flow regime using equations (1.14) and (1.15). However, the flow regime (laminar or turbulent) needs to be known a priori in order to select the right equation. Therefore, the model proposed by Rosenberger et al. (2006) is used to make a first estimate of the Reynolds number and the critical Reynolds number (equation (1.23)). This model can account for *TSS* dependency by combining equations (1.19) and (1.20). It is important to highlight that to warranty the use of the previous equations; the permeation through the membrane should not affect the pressure drop. This was verified by performing experiments with- and without filtration. No difference in pressure drop along the tube was observed. Figure 6.3 shows two

curves, one with the Reynolds number as a function of TSS and a second curve function of the critical Reynolds number. When the first curve is below the second curve ($TSS > 7 \text{ g}\cdot\text{L}^{-1}$) the flow is in laminar regime, otherwise a turbulent regime prevails.

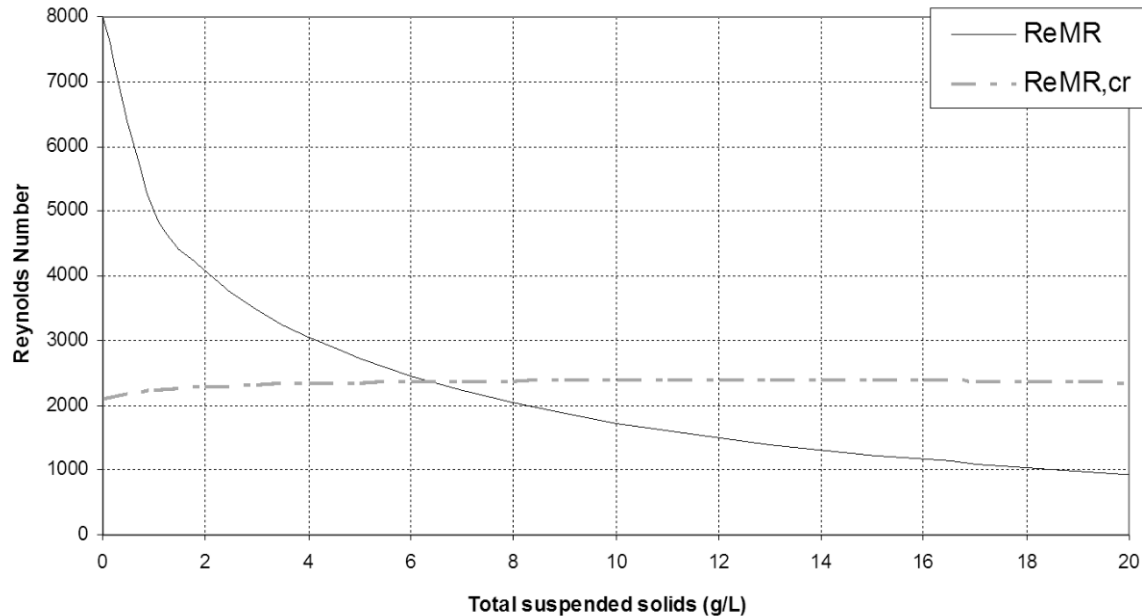


Figure 6.3. Reynolds number and critical Reynolds number vs TSS based on the Rosenberger et al. (2006) for the DFCm conditions. (Moreau et al., 2009)

Full-scale MBRs are usually operated at a TSS content between 8 and $12 \text{ g}\cdot\text{L}^{-1}$. Based on this, it is possible to assume a laminar regime (Figure 6.3). Equation (1.14) can now be used to calculate the Reynolds number and equation (1.19) to calculate the apparent viscosity of the activated sludge from the experimental data.

Apparent viscosities calculated based on the experimental full-scale MBR data are plotted versus the apparent viscosities calculated using the model of Rosenberger et al. (2006) in Figure 6.4 (mind the difference in scale). It seems that the model of Rosenberger et al. (2006) is under estimating practical apparent viscosities by a factor of two. This difference might be due to the difference between the DFCm and the rheological device used by Rosenberger. In the DFCm, apparent viscosity is calculated from the pressure drop along the tubular membrane. Due to the diameter of the membrane, a gradient of the TSS concentration can be expected between the membrane wall and the activated sludge bulk. The activated sludge near the membrane wall will have higher TSS concentration compared to the bulk. This is not the case in a rotational rheometer because the gap between the two cylinders is small and the TSS concentration gradient is negligible. Because of traditional rheometer design and characteristics, only the viscosity of the bulk is measured. Therefore, the higher apparent viscosity value obtained experimentally could result from the non-homogeneity of the apparent viscosity in a tubular membrane tube.

Although the DFCm was designed in order to quantify activated sludge filterability, it can also be used efficiently as a rheometer. Keeping in mind the shear rate applied in the DFCm (1000 s^{-1}), apparent viscosities calculated from the DFCm data can therefore be considered more representative of MBR applications than traditional ex-situ rheological measurements.

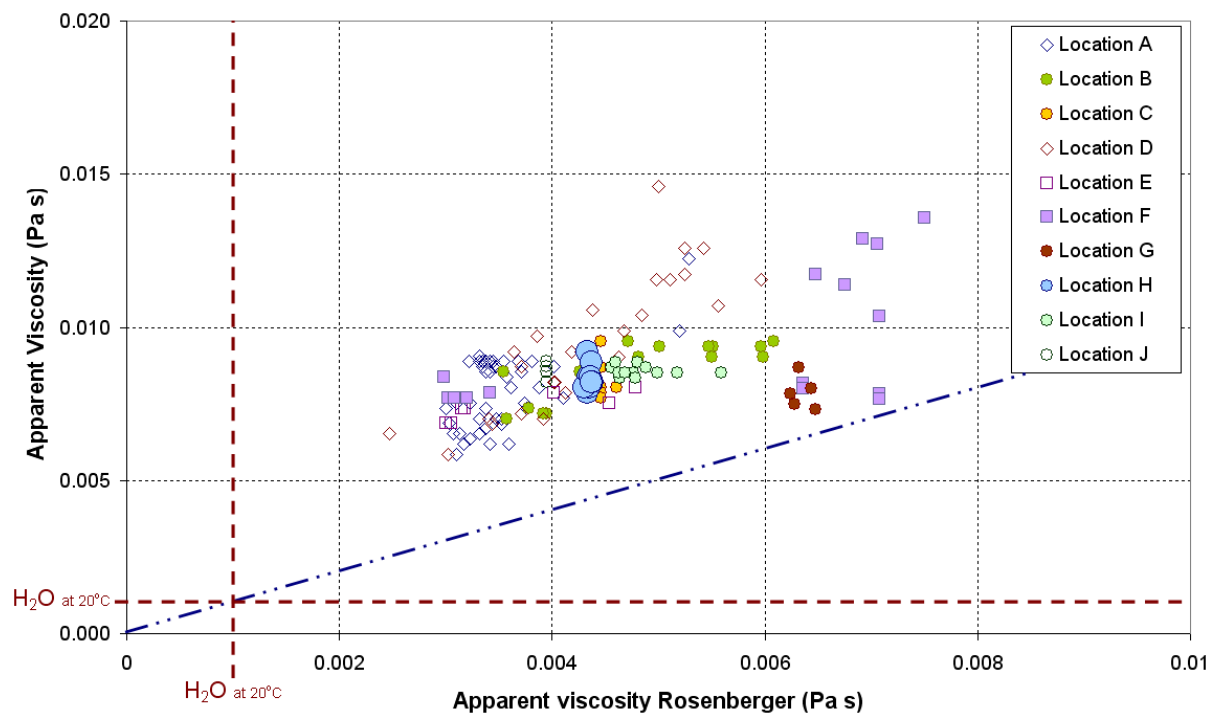


Figure 6.4. DFCm vs to Rosenberger et al. (2006) apparent viscosity (Moreau et al., 2009)

The full-scale measurements were, in contrast to Rosenberger et al. (2006), performed at different temperatures. However, Moreau et al. (2009) did not find a clear correlation between the apparent viscosity and temperature, no matter what rheological method or model was used. The apparent viscosity is plotted versus temperature in Figure 6.5. There is no clear correlation between apparent viscosity values and temperature in the range of investigated large scale MBR plants (from 9 to 27.4°C). Temperature does not seem to have a direct impact on apparent viscosity within this range of temperature in contrast with other findings, where temperature affects the flow behaviour of sludge (Yang et al., 2009). However, the temperature might have an indirect impact on apparent viscosity through the sludge growth and hence the total suspended solids content. But this is an effect on a much larger time-scale.

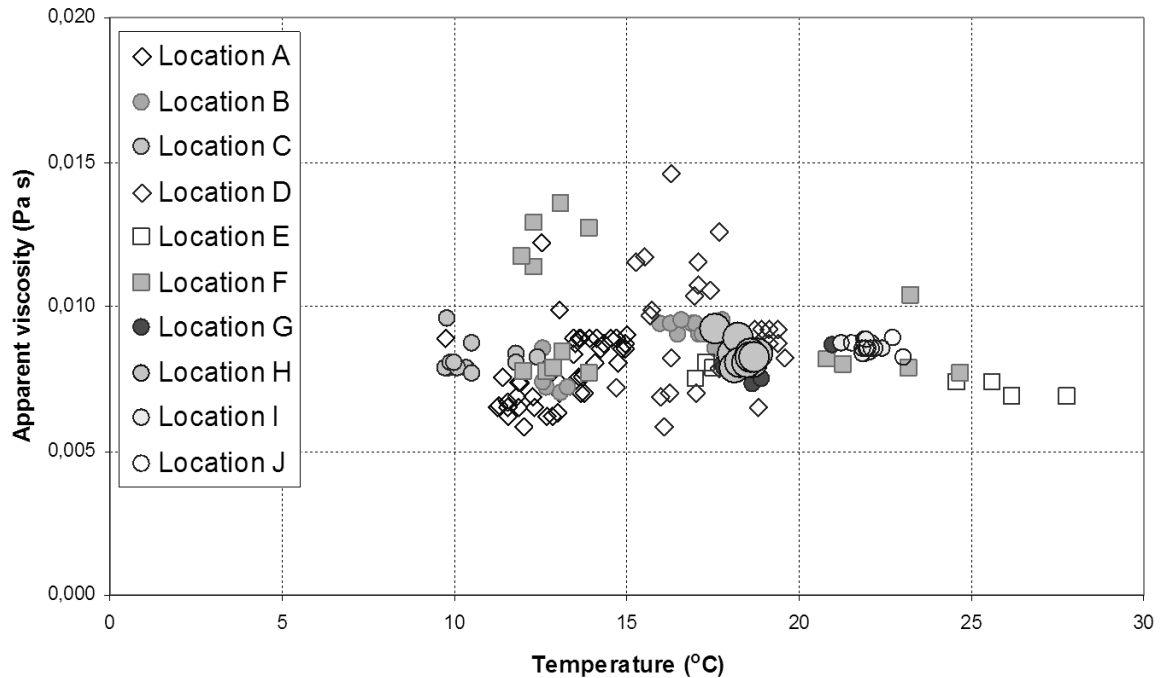


Figure 6.5 Apparent viscosity vs temperature (Moreau et al., 2009)

Temperature can be accounted for in rheological models according to an exponential Arrhenius type relation (Yang et al., 2009) as follows:

$$\mu_{app} = k \left(\frac{3n+1}{4n} \right)^{n-1} \left(\frac{8u_{mem}}{d_{mem}} \right)^{n-1} \exp \left(\frac{E_a}{R_{gas} T} \right) \quad (6.5)$$

When considering this model extension, where E_a is the activation energy and it becomes an additional fitting parameter. Rosenberger *et al.* (2006) and Pollice *et al.* (2007) did not include a correction for temperature as their experiments were conducted at a constant temperature. However, in this study, the temperature in each measurement was different. Therefore, the exponential Arrhenius parameter is included in this analysis.

To determine the six parameters (a_1 , a_2 , a_3 , a_4 , a_5 and E_a) of equations (1.8), (1.9), (1.19) and (6.5), the statistical analysis software SPSS v16 (SPSS Corporation) was used. This software is capable of performing non-linear regression using the Levenberg-Marquardt algorithm to solve least squares curve fitting problems for non-linear equations which is clearly the case here.

Two non-linear regressions were performed, one without considering the temperature (equation (1.19)) and the other including temperature (Equation (6.5)). Table 6.2, summarizes the parameters for equations (1.19) and (6.5).

Table 6.2. Parameters for equations (1.19) and (6.5) compared to the parameters from Rosenberger *et al.* (2006) and Pollice *et al.* (2007)

Parameters	Rosenberger <i>et al.</i> (2006)	Pollice <i>et al.</i> (2007)	Equation (1.19)	Equation (6.5)
a_1 (Pa s)	0.001	0.001	0.0011 ± 0.0005	0.0002 ± 0.0002
a_2 (-)	2.000	0.882	1.5724 ± 39.5161	1.3679 ± 11.0217
a_3 (-)	0.410	0.494	0.2981 ± 10.9649	0.2886 ± 3.4265
a_4 (-)	0.230	0.050	0.0384 ± 85.8810	0.0158 ± 1.7355
a_5 (-)	0.370	0.631	0.5928 ± 12.6003	0.7313 ± 16.5669
E_a (J·mol ⁻¹)	-	-	-	4232.3191 ± 2058.2162
R^2			0.659	0.669
SSE			0.0002176	0.0002116
DF			148	147

From Table 6.2 there is not a significant difference between the two R^2 with or without including the Arrhenius correction factor in the model. However, having a look to the sum of squared errors (SSE) it is possible to see that the more complex model (equation (6.5)) (the one with more parameters) fits slightly better (i.e. has a smaller SSE) than the simple equation (1.19). Therefore, an F-test can be used to determine whether the difference between the two models (equations (1.19) and (6.5)) is significant. The F-test is defined by:

$$F - test = \frac{\frac{SSE_{eq.1.19} - SSE_{eq.6.5}}{DF_{eq.1.19} - DF_{eq.6.5}}}{\frac{SSE_{eq.6.5}}{DF_{eq.6.5}}} \quad (6.6)$$

where DF are the degrees of freedom (153 data points minus the number of variables). Evaluating equation (6.6) with the values from Table 6.2, the value of the F-statistic is 4.2. Comparing this value to the tabulated F-value, for example with a 95 % confidence limit, being 6.8, it can be concluded that there is no statistical significant improvement of adding an additional parameter (temperature correction) to improve the correlation performance.

This is in agreement with the results presented by Moreau *et al.* (2009), where the temperature is found not to be significant for the variations in sludge viscosity under normal operating ranges. Figure 6.6 shows the comparison between the experimental data with equations (1.19) and (6.5).

Another observation from Table 6.2 is that the confidence intervals of the parameter estimates are massive for all the parameters, which illustrates that the model is severely overparameterised and the five parameters cannot be uniquely identified based on the available data due to significant correlation. However, this was not further investigated, but should be in further research.

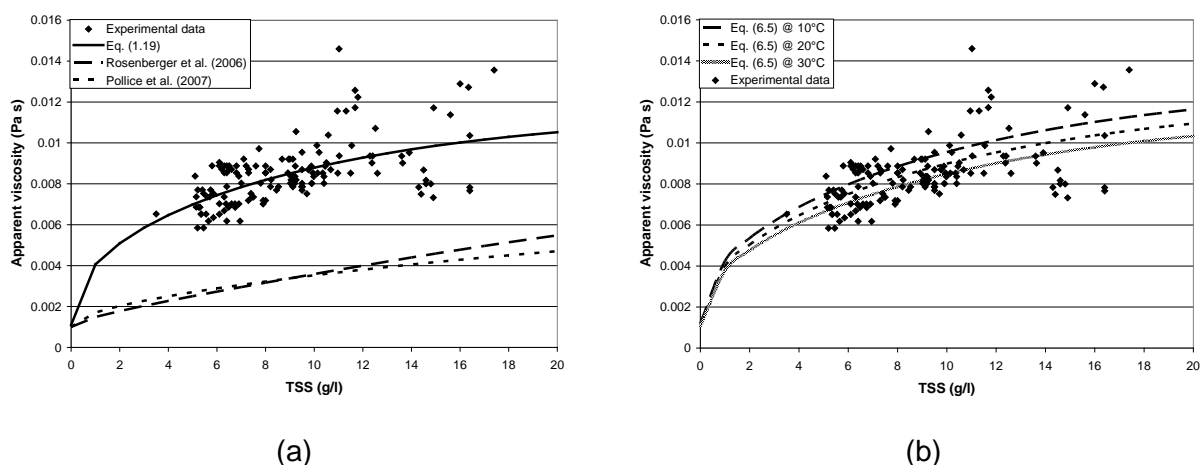


Figure 6.6. TSS vs apparent viscosity comparing the experimental data with 1) equation (1.19) and b) equation (6.5) with three fixed temperatures

From Figure 6.6, one can observe that when the TSS is equal to $0 \text{ g}\cdot\text{l}^{-1}$ the viscosity of the sludge is the same as water ($0.001 \text{ Pa}\cdot\text{s}$). Moreover, the model predictions by Rosenberg et al. (2006) and Pollice et al. (2007) at the same shear rate (1000 s^{-1}) are shown. When comparing these model predictions with the one from this study, based on the experimental data obtained with the DFCm unit, they under predict the data by a factor of two. Hence, the methods used to measure viscosity clearly have a severe impact on the results. Moreover, one should be careful when using calibrated models based on a certain type of data. Adding the Arrhenius factor (Figure 6.5b) does not affect the overall behaviour of the activated sludge viscosity. Therefore, equation (1.19) is currently the best equation around for design purposes. However, it is important to note the significant spread in the apparent viscosity data at fixed TSS , which indicates that other important factors and/or processes are missing in the model. Possible candidates are floc structure and floc size distributions (Fu and Dempsey, 1998; Huisman et al., 1999; Jamal Khan et al., 2008; Wakeman, 2007). Hydrodynamics can impact the particle size distribution (PSD) through the appearance of shear. Population balance models (PBM) (Ramkrishna, 2000) are commonly used to model dynamics of particles or droplet size distributions (e.g. aggregation, flocculation,

crystallization, coalescence, etc) which could shed some light into the viscosity modelling. However, this was beyond the purpose of this work and is suggested for further research.

Ignoring the latter, a further comparison between the calibrated model derived in this work and those proposed by Rosenberger et al. (2006) and Pollice et al. (2007), at different fixed TSS concentrations (8, 10 and 12 g·L⁻¹) is presented in Figure 6.7. It is important to highlight that the model proposed in this work was set up at 1000 s⁻¹ but the values of k and n (equations (1.8) and (1.9)) are independent of the shear rate, which allows to extrapolate the model to other shear rates.

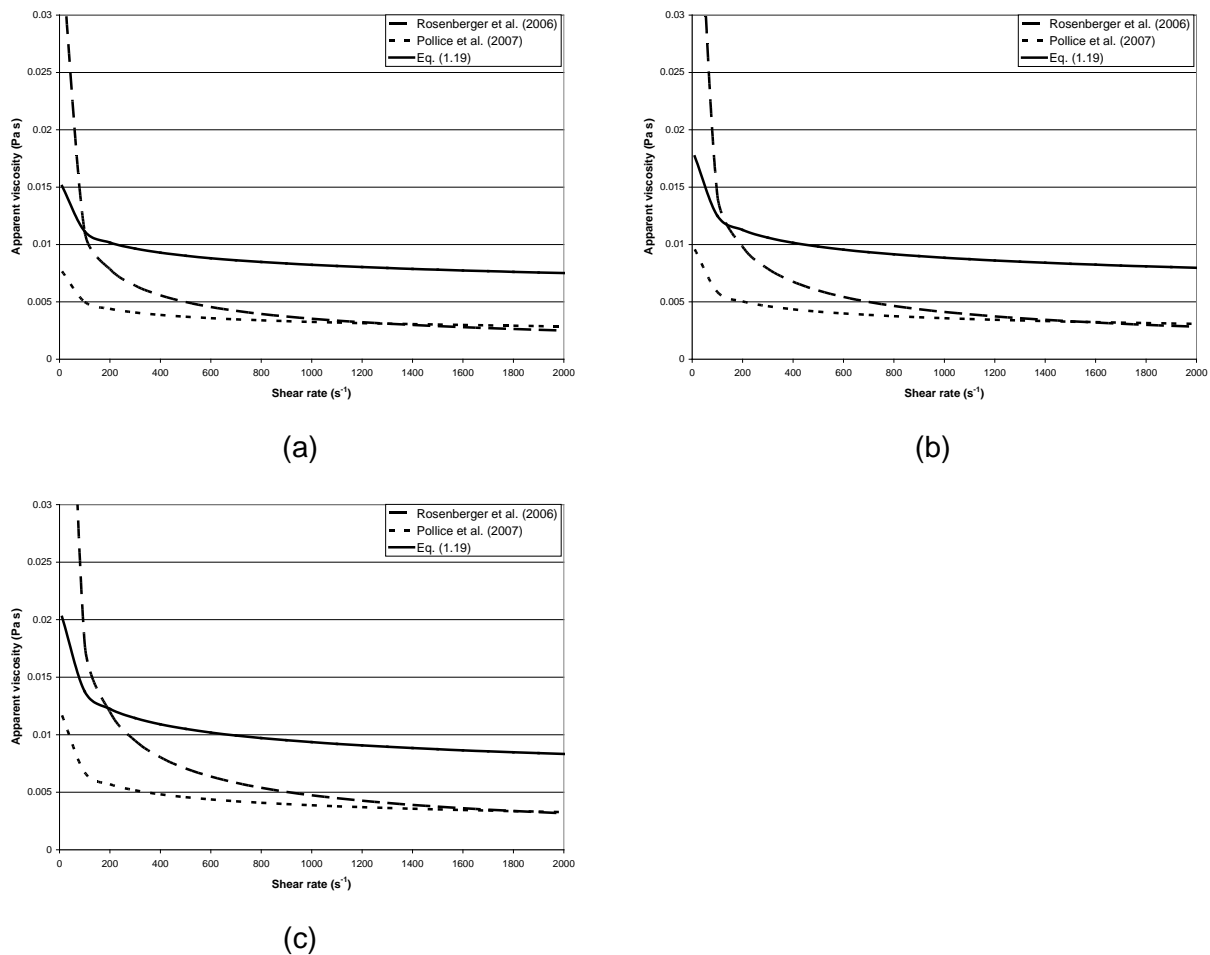


Figure 6.7. Shear rate vs apparent viscosity for MBR sludge with TSS of (a) 8, (b) 10 and (c) 12 g·L⁻¹ for the models proposed by Rosenberger et al. (2006), Pollice et al. (2007) and this work (equation (1.19)).

From Figure 6.7, it is possible to observe clearly that the three models although using the same structure behave differently, as could be expected from the parameter values. The model derived in this work roughly predicts double the apparent viscosity of the other two models. At low shear rates the model of Pollice et al. (2007) and this work have similar slope. However, the model of the Rosenberger has a sharper slope. It is hypothesised that

this behaviour is related to differences in floc strength and resistance to breakage (deflocculation) of the different sludges used. At high shear rates, it is possible to observe that the apparent viscosity from this work and the one of Rosenberger et al. (2006) decreases whereas, on the other hand, the model proposed by Pollice et al. (2007) quickly reaches a plateau which could indicate that sludge is already completely broken (deflocculated) at low shear values. Also, the impact of sludge concentration can be observed. Indeed, the levelling off of the viscosity occurs at higher shear values for larger sludge concentration. This can be explained by the fact that reflocculation happens at a higher rate and the same level of breakage requires higher shear. Finally, it should be noted that when using an ex-situ rheometer, the measured values are depending on the history of the measurement which is not desirable. In that respect, the DFCm unit is a closer representation of a real system under real operating conditions (e.g. pumping process) and independent of sludge history.

6.5 Impact of apparent viscosity on pumping

Comparing the viscosity of the calibrated model of this study with the other two (Rosenberger et al., 2006 and Pollice et al., 2007), it is possible to observe that the apparent viscosity is roughly doubled. This will considerably affect the energy consumption (calculations) in a full-scale MBR (e.g. aeration, pumping) for which an adequate rheological model is required.

The energy consumption of a pump can be estimated using equation (1.61). For example, assuming a horizontal pipe of 100 m length, with an internal diameter of 0.6 m and a liquid velocity of $1 \text{ m}\cdot\text{s}^{-1}$, the pumping power for the different rheological models (Rosenberger et al. (2006), Pollice et al. (2007) and this work) as a function of TSS is presented in Figure 6.8.

Figure 6.8, shows that if the sludge has the same viscosity as water (i.e. $TSS = 0 \text{ g}\cdot\text{L}^{-1}$), the pumping power will be 330 W for all models. Therefore, using the viscosity of water to calculate energy requirements will significantly underestimate the total energy required for the process no matter which model is used. The models by Rosenberger et al. (2006) and Pollice et al. (2007) behave in a similar fashion. One can observe a first steep linear increase which then levels off. The model of Rosenberger et al. (2006) exhibits a decreasing trend beyond a TSS of $14 \text{ g}\cdot\text{L}^{-1}$ which is questionable. The model proposed by Pollice et al. (2007) and this work show a similar trend. Nevertheless, the model calibrated in this study based on DFCm results in 20 % higher pumping costs compared to the other models. To be conclusive, the rheological model needs further validation to confirm these findings

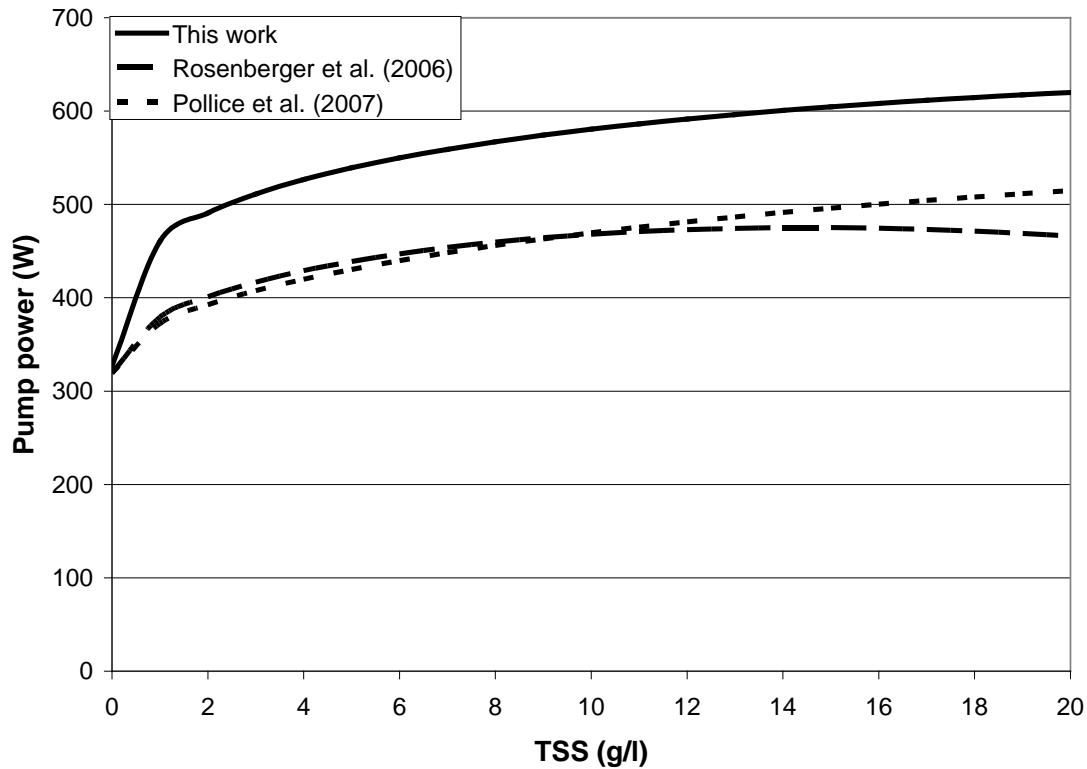


Figure 6.8. Pumping power vs TSS for the models proposed by Rosenberger et al. (2006), Pollice et al. (2007) and this work.

A recent study used a tracer test (residence time distributions - RTD) to validate a CFD model including rheological properties of activated sludge (Brannock et al., 2010b). It was found that, although the viscosity difference between sludge and water is large (at least 5 times that of water), it has minimal impact on RTD due to the high energy input into the system and the resultant high turbulent viscosity ratio. The latter means that the diffusive momentum transport due to turbulence is much greater than diffusive momentum transport due to mixture viscosity (Brannock et al., 2010b). This indicates that the energy requirement to operate a MBR plant with sludge is greater than with water.

6.6 Conclusions

The DFCm unit was used as an on site rheometer and the activated sludge apparent viscosity was calculated experimentally for ten pilot and full-scale municipal MBR plants. A new rheological model for MBR activated sludge is presented based on the data collected. The new model was compared with two previous models which have the same mathematical structure. The main factor influencing activated sludge apparent viscosities was TSS content confirming the findings in the literature. Temperature was found to not significantly affect activated sludge apparent viscosity. Also, it was found that the previous models underestimate the data collected from different MBR plants. The reasons for this could

reside in: 1) difference in sludge composition, 2) the difference in the apparatus used to perform the rheological measurements, 3) the DFCm unit measures in situ, which is not the case for the other methods and 4) the mathematical structure of the model may not represent properly the rheological behaviour of sludge. Upon further validation, this new model can be used to design and optimize systems (e.g. design of pumps, aeration system and energy consumption).

Chapter 7. Heat-and-mass transfer analogy

Abstract*

The mass transfer coefficient plays an important role in predicting shear stresses in tubular systems as it is directly proportional to the shear stress. However, measuring the mass transfer coefficient is complex and difficult in heterogeneous mixtures (like activated sludge). Currently, there are electrochemical methods to measure the shear stress, but they are only applicable when the chemical reaction is well defined. In wastewater treatment, this is not the case, as sludge is a heterogeneous mixture. Therefore, a multidisciplinary approach is followed by applying commonly used techniques in chemical and mechanical engineering to the system under study, MBR. This approach is based on dimensionless analysis and similarities between heat-and-mass transfer mechanisms (using the Lewis number), an empirical model is proposed to predict mass transfer coefficients (thus shear stress) for two-phase slug flow in vertical pipes based on the heat transfer coefficient. The model is evaluated by using water-N₂ mass transfer experimental data obtained from the experimental setup described in chapter 3 and the heat transfer is evaluated based on a robust correlation found in literature which was evaluated against extensive data sets. This empirical correlation can be used to determine the average shear stress due to the liquid and gas slug.

* Redrafted after:

Ratkovich, N., Chan, C.C.V., Berube, P., Nopens, I., A heat-and-mass transfer correlation to optimize shear stress in tubular airlift membrane systems for wastewater treatment. *International Journal of Heat and Mass Transfer* (in preparation).

Introduction

Chapters 2 and 3 indicate that alternating shear stresses (i.e. change in shear direction) help to control and/or reduce fouling. Moreover, it has been proven in literature that the slug flow pattern has a higher scouring effect to remove particulates due to the high shear rates and high mass transfer coefficient between the membrane surface and the bulk region (Ghosh and Cui, 1999). In the field of petroleum engineering, numerous research works have focused on multiphase flow because it is the predominant flow in this type of industry. It is possible to extrapolate the outcome of these studies and apply it to wastewater treatment.

In the oil and gas industry, multiphase flow transport generates several problems: i.e. the corrosion and the wear (attrition) of the tubes, which are the pipe damage generated by chemical reaction and physical interaction respectively. These systems are operating under two or three-phase flow conditions (multiphase flow). Different flow patterns can be found (i.e. stratified, slug and annular flow) which lead to corrosion of the pipelines due to a very high fluctuating mass transfer rates (particularly in slug flow). Associated with the slug flow pattern are the even larger fluctuations of the surface shear stress (chapter 3) which can lead to attrition of tube material. Corrosion-multiphase flow models have been developed to predict the flow pattern and how the hydrodynamic properties (i.e. velocities of gas and liquid, film thickness, void fraction, etc.) affect the corrosion rate.

Mass transfer coefficients are commonly measured using electrochemical techniques which are applied to study corrosion in pipelines carrying oil and gas (Adsani et al., 2006; Neic, 2007; Zheng and Che, 2006). Electrochemical probes are mounted flush to an inert wall in presence of an electrolyte liquid flow to determine the wall shear stress by the measurement of limiting diffusion current delivered by such probes. In this technique, the oxidizing-reduction at the probe surface must be rapid to ensure that the mass transfer is dependent only to the convection-diffusion equation (Section 3.1). This technique is a non-intrusive method permitting to measure local, instantaneous mass transfer or wall shear stress (Rehimi et al., 2008). This technique of wall shear stress measurements presents some limitations on both steady and unsteady cases (i.e. it does not take into account the axial and transverse mass transfer) which may induce error in the measurements. Besides, this technique can only be used with a specific electrolyte to carryout the electrochemical reaction. Therefore, extrapolation to other systems is limited.

Another option to measure the shear stress is using hot-film anemometry (HFA) (Farrar and Bruun, 1996; Lewis et al., 2002). This technique uses an electrically heated element exposed to a fluid medium for the purpose of measuring a property of that medium. Normally, the property being measured is the velocity. Since these elements are sensitive to heat transfer between the element and its environment, temperature and composition changes can also be monitored. The obtained voltage signal from the probes carries information of the liquid and the gas phase, and it can be converted into velocity. However, in two-phase flow the difficulty arises from the large variability of the gas signal and the increasing complexity of the fluid signal for increasing void fraction.

The problem of the previous two techniques is that they cannot be used with activated sludge. The electrochemical method will not work because activated sludge has an electrical charge which interferes with the electrolyte. The hot-film anemometry will not work because activated sludge has solid particles which will damage the probe.

Because of various complexities involved in mass transfer measurements in multiphase flow, most previous studies of mass transfer rely on heat transfer data to develop correlations for mass transfer coefficients (Adsani et al., 2006; Shirazi et al., 2004). These studies exploit the heat-and mass transfer analogy (as discussed in section 1.8.3). It is well known that there are certain similarities among the transport of momentum, mass, and energy. The transport of momentum, mass, and energy all depend on turbulent diffusion which is caused by turbulent eddies and transport coefficients (heat-and-mass transfer coefficients). The main motivation of using the transport analogy is that experimental measurements or correlations obtained in one system can be applied to another. For example, heat transfer data can be applied to solve a mass transfer problem where direct experimentation to reveal mass transfer may be difficult. The governing equations for mass and heat transfer are similar when compared in dimensionless form. It can be shown that the Sherwood and the Schmidt numbers in mass transfer are analogous respectively to the Nusselt and the Prandtl number in heat transfer when dimensionless forms of the governing equations are considered (see sections 1.8 and 1.9).

This study tries to present an alternative approach for mass transfer measurements in activated sludge using empirical correlations based on dimensionless numbers. These dimensionless numbers can be used to extrapolate the mass transfer coefficient of the electrochemical probe (chapter 2 and 3) to that of the entire tube. Dimensionless numbers are frequently encountered in engineering studies of complicated processes and are used as similarity criteria in model studies. Among the advantages are: 1) A reduction in the number of variables to be investigated; that is, because each dimensionless number contains several physical variables that can be treated as a single compound variable, thereby, reducing the number of experiments needed as well as the time required to correlate and interpret the experimental data. 2) It predicts the effect of changing one of the individual variables in a process (which may be impossible to vary in an experiment) by determining the effect of varying the dimensionless group containing this parameter. 3) Making the results independent of the scale of the system which ease the scaling-up (or -down) of results obtained with models of systems by generalizing the conditions which must exist for similarity between a system and its model, and 4) deducing variation in importance of mechanisms in a process from the numerical values of the dimensionless groups involved (White, 2002).

The goal is to use already existing heat transfer correlations for two-phase flow (Nusselt number) and link them through a dimensionless number to the mass transfer coefficient (Sherwood number) to obtain an empirical correlation which can be used to determine the

shear stress for the different zones in the slug flow. The objective of the work presented here focuses on a better understanding of the mass transfer coefficient near the membrane surface, thereby making an empirical correlation with shear stress and the Nusselt number.

7.1 Shear profiles in single phase flow

Measurements were performed initially in single-phase flow to calibrate the wall shear stress with theoretical equations using the friction factor as it was described in detail in chapters 2 and 3. The friction factor is defined by equation (1.13). For all experimental conditions that were investigated, the voltage was obtained from the experimental setup, and by using equation (3.5) the voltage was converted to shear stress. It was found that the flow was in the laminar regime (Figure 7.1a). An intermediate step to reach equation (3.5) is substituting equation (3.1) into (3.2) yielding the mass transfer coefficient ($k_{m,probe}$) for the probe:

$$k_{m,probe} = \frac{4V}{RG v_e F \pi d_e^2 C_o} \quad (7.1)$$

The mass transfer measurement value obtained with the small circular electrode corresponds to an incompletely developed mass transfer boundary layer. This necessitates its conversion into the actual mass transfer coefficient value, which corresponds to the fully developed mass transfer boundary layer for the entire tube diameter. The mass transfer of the probe should be equal to the mass transfer of the tube which can be expressed in terms of the Sherwood number means (based on dimensionless analysis):

$$Sh_{tube} = Sh_{probe} \quad (7.2)$$

Using equation (1.70) and solving for the mass transfer coefficient of the tube yields:

$$k_m = k_{m,probe} \frac{d_e}{d} \quad (7.3)$$

To check the validity to use a single phase approach to obtain the mass transfer coefficient, one can verify whether the Leveque equation (equation (1.71)) is obeyed (Figure 7.1b).

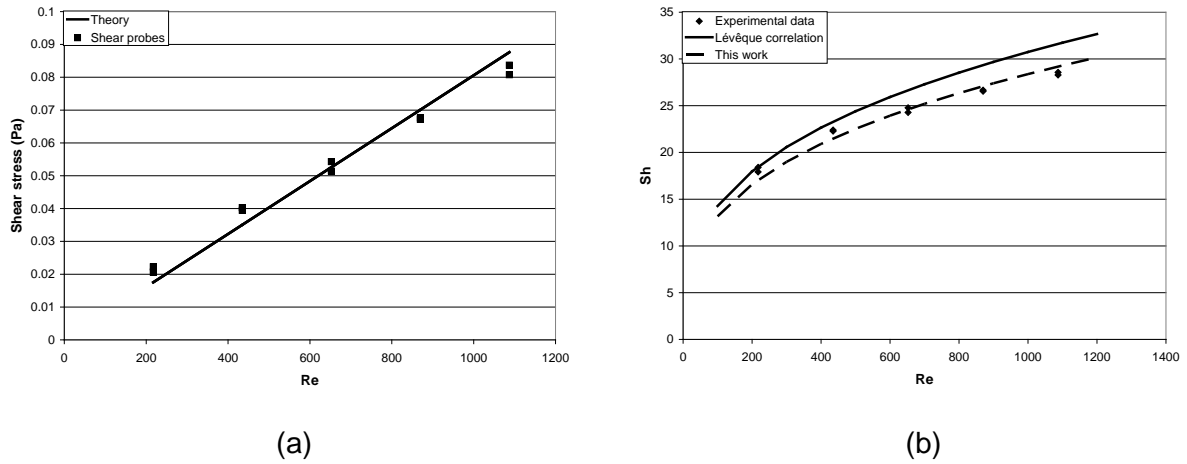


Figure 7.1. Reynolds number vs (a) shear stress and (b) Sherwood number; comparison between experimental data and theoretical equations.

Using software SPSS v16 to fit the coefficients, the proposed model becomes:

$$Sh = 1.495 \left(Re Sc \frac{d}{L} \right)^{\frac{1}{3}} \quad (7.4)$$

which is 8% lower compared to the theoretical model which is acceptable and can be used as a starting point for the analysis of the two-phase flow. Substituting equation (7.1) in (3.5) and solving for the mass transfer coefficient of the probe yields:

$$k_{m,probe} = 0.862 \left(\frac{\tau_w D_f^2}{\mu d_e} \right)^{\frac{1}{3}} \quad (7.5)$$

The mass transfer coefficient for the tube then becomes:

$$k_m = 0.862 \frac{d_e}{d} \left(\frac{\tau_w D_f^2}{\mu d_e} \right)^{\frac{1}{3}} \quad (7.6)$$

Using the Lewis number (Equation (1.110)) to determine the exponent n' , one obtains:

$$n' = \frac{\ln\left(\frac{Nu}{Sh}\right)}{\ln\left(\frac{Pr}{Sc}\right)} \quad (7.7)$$

The Nusselt number for a single-phase flow in the laminar regime is defined by equation (1.88). The Prandtl number is 7 and the Schmidt number is 1380 at 20°C for water with the electrolyte solution (the diffusion coefficient is equal to $7.14 \cdot 10^{-10} \text{ m}^2 \cdot \text{s}^{-1}$). Furthermore, it is assumed that the viscosities in the bulk and in the wall region are the same. This results in an exponent n' of 0.293 which is close to the theoretical value of 0.333. This analysis shows that the analogy between heat and mass transfer can be used.

Now the objective is to determine the wall shear stress from the heat transfer point of view (using the Nusselt number). It is possible to write the wall shear stress as a function of the Sherwood number as follows:

$$\tau_w = \frac{1.561 \mu D_f}{d_e^2} Sh^3 \quad (7.8)$$

The Sherwood number can be replaced by the Nusselt numbers using the Lewis number as the link between heat-and-mass transfer phenomena as follows:

$$Sh = Nu \left(\frac{Sc}{Pr} \right)^{\frac{1}{3}} \quad (7.9)$$

Combining equations (7.8) and (7.9) yields:

$$\tau_w = \frac{1.561 \mu D_f}{d_e^2} \left(\frac{Sc}{Pr} \right) Nu^3 \quad (7.10)$$

This is a general equation valid for single phase flow. Nevertheless, the behaviour of two-phase flow is different and, hence, some corrections are needed.

7.2 Shear profiles in two-phase flow

Typical voltage results obtained using the electrochemical shear probes, and the corresponding shear stresses, are presented in section 3.2. It is important to highlight, nevertheless, that gas slugs rising in vertical tubes were observed to periodically coalesce when trailing slugs reached the wake of the leading slugs, accelerating the trailing slugs to finally coalesce with the leading slug. For this reason, the shear stress profiles induced by successive slugs were not exactly the same. As a result, the profile of shear stresses in successive shear events, induced by rising gas slugs, varied considerably over time. To overcome this random behaviour, SSHs were used to explore the effect of the different experimental conditions investigated (Figure 3.4) on the resulting shear stresses (Ratkovich *et al.*, 2009).

As it was mentioned previously, it is possible to distinguish two peaks in the SSH. Therefore, equation (7.10) can be written for two zones, instead of 3 zones for simplicity (Figure 1.9): One zone for the liquid slug (ls) and one zone for the gas slug (gs) (this zone will include the falling film zone and the wake zone, since the wake zone cannot be clearly identified in the SSH):

$$\tau_{w,ls} = \frac{1.561 \mu D}{d_e^2} \left(\frac{Sc_L}{Pr_L} \right) Nu_L^3 \quad (7.11)$$

$$\tau_{w,gs} = \frac{1.561 \mu D}{d_e^2} \left(\frac{Sc_{tp}}{Pr_{tp}} \right) Nu_{tp}^3 \quad (7.12)$$

From the SSH, it is possible to get the average shear stress for the liquid and the gas slug peaks (equations (7.11) and (7.12) (Ratkovich *et al.*, 2010a). Due to the fact that the slug flow has a random behaviour, the length of the bubbles is different due to coalescence and the values obtained from the SSH distribution are just averages. Therefore, a correction factor needs to be added to equation (7.11) and (7.12).

This correction factor should consider the fact that the hydraulic diameter changes in the falling film zone (thickness of the boundary layer), and that the slug flow Reynolds number (~1800 - 3000) is either in the laminar or transition regime (Ratkovich *et al.*, 2010b). The correction factor is a function of the Reynolds number as follows:

$$\xi = a_1 Re_i^{a_2} \quad (7.13)$$

This correction factor considers several characteristics of the flow, such as: coalescence of bubbles, bubble length, hydraulic diameter and transition regime (as there is no definition for the transition regime). Therefore, equations (7.11) and (7.12) become:

$$\tau_{w,ls} = \frac{1.561 \mu D_f}{d_e^2} \left(\frac{Sc_L}{Pr_L} \right) \xi_{ls}^3 Nu_L^3 \quad (7.14)$$

$$\tau_{w,gs} = \frac{1.561 \mu D_f}{d_e^2} \left(\frac{Sc_{tp}}{Pr_{tp}} \right) \xi_{gs}^3 Nu_{tp}^3 \quad (7.15)$$

It is important to highlight that the power 3 in the correction factor of equation (7.14) and (7.15) is just to maintain the same exponent of the Nusselt number. For simplicity, the first term of the equation is grouped in a constant.

$$a_3 = \frac{1.561 \mu D_f}{d_e^2} \left(\frac{Sc_L}{Pr_L} \right) \approx \frac{1.561 \mu D_f}{d_e^2} \left(\frac{Sc_{tp}}{Pr_{tp}} \right) \quad (7.16)$$

The previous expression is valid because the ratio of the Schmidt to the Prandtl number of the liquid (= 200.7) is similar to the one in two-phase (= 215.7 ± 5.9) flow, because there is no change of temperature or phase (e.g. boiling) so these two dimensionless numbers are governed mainly by the liquid phase. Therefore a_3 is 0.00072 and 0.00077 ± 2.1 · 10⁻⁵ for the liquid and two-phase flow.

Re-writing equations (7.14) and (7.15) and combining with (7.13) and (7.16) yields:

$$\tau_{w,ls} = a_3 \left(a_{1,ls} Re_i^{a_{2,ls}} \right)^3 Nu_L^3 \quad (7.17)$$

$$\tau_{w,gs} = a_3 \left(a_{1,gs} Re_i^{a_{2,gs}} \right)^3 Nu_{tp}^3 \quad (7.18)$$

The correction factor can now be determined from fitting equation (7.17) and (7.18) to experimentally gathered data. This was done through a power-law regression with the software SPSS v16 using:

$$\xi_{ls} = a_{1,ls} Re_i^{a_{2,ls}} = \left(\frac{\tau_{w,ls}}{a_3 Nu_L^3} \right)^{\frac{1}{3}} \quad (7.19)$$

$$\xi_{gs} = a_{1,gs} Re_i^{a_{2,gs}} = \left(\frac{\tau_{w,gs}}{a_3 Nu_{tp}^3} \right)^{\frac{1}{3}} \quad (7.20)$$

The problem now arises as to which Reynolds number to use (liquid, superficial gas, mixture, falling film, mixture or slug flow Reynolds number). To determine which Reynolds number to use, the R^2 can be used as goodness of fit criterion. Tables 7.1 and 7.2 show the parameters of equations (7.19) and (7.20) and R^2 for the different Reynolds numbers tested.

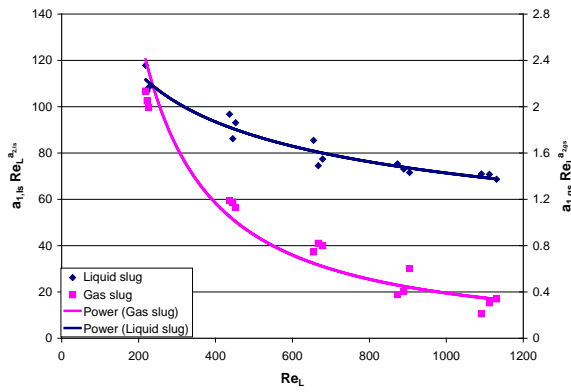
Table 7.1. Parameters of equation (7.19) and R^2 of the different Reynolds number.

	a_2	Std. error	a_1	Std. error	R^2
Re_L	-0.295	0.019	545.738	67.954	0.973
Re_{SG}	-0.062	0.104	102.476	34.933	0.163
Re_m	-0.425	0.057	1581.727	618.652	0.902
Re_{ff}	10.663	1.531	$3.642 \cdot 10^{-23}$	$2.935 \cdot 10^{-22}$	0.888
Re_{sf}	-0.810	0.109	39562.405	32845.651	0.899

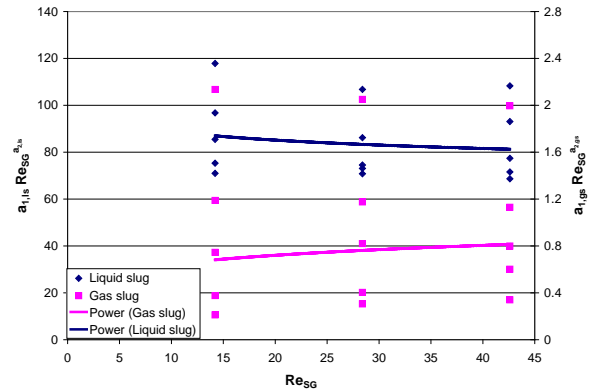
Table 7.2. Parameters of equation (7.20) and R^2 of the different Reynolds number.

	a_2	Std. error	a_1	Std. error	R^2
Re_L	-1.196	0.103	1508.757	997.177	0.955
Re_{SG}	0.161	0.433	0.445	0.633	0.102
Re_m	-1.551	0.327	34104.673	77308.205	0.796
Re_{ff}	39.688	8.285	$1.568 \cdot 10^{-91}$	$6.833 \cdot 10^{-90}$	0.799
Re_{sf}	-2.993	0.616	$5.668 \cdot 10^{09}$	$2.653 \cdot 10^{10}$	0.803

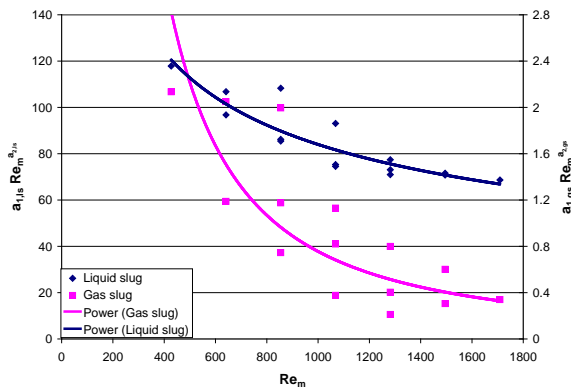
Plots of all the Reynolds numbers versus equations (7.19) and (7.20) the results is shown in Figure 7.2



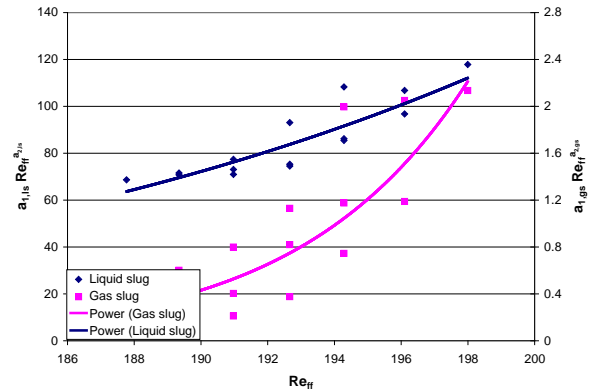
(a)



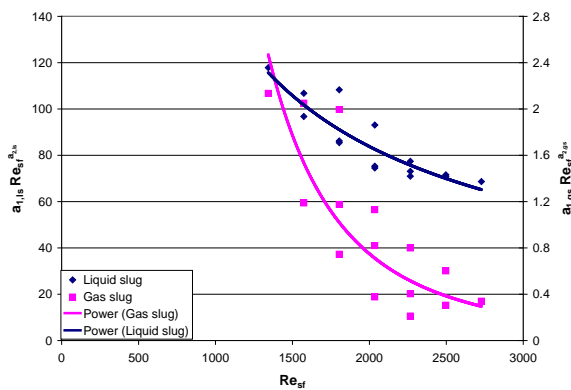
(b)



(c)



(d)



(e)

Figure 7.2. (a) liquid, (b) superficial gas, (c) mixture, (d) falling film and (e) slug flow Reynolds number vs the correction factor of equations (7.19) and (7.20) for the liquid and gas slug respectively.

From Tables 7.1 and 7.2, the values that are in bold provide the best fit to the experiment data. From Figure 7.2 it is possible to see all the Reynolds numbers function of the correction factors. In Figure 7.2a, it is possible to observe that the liquid Reynolds number is adequate to fit the empirical equations (7.19) and (7.20) to the experimental data. Also this

Reynolds number considers the mixture velocity and the void fraction of the gas slug which is clearly important to account for the liquid and gas slugs.

Figure 7.2b shows the superficial gas Reynolds number. It is expected that this correlation will provide the worst fit for the liquid slug (i.e. no liquid velocity is included in the Reynolds number). However, it was expected that it would provide a good correlation for the gas slug, which is not the case. The reason for that could be that it should include the combined liquid and gas velocities to account for the increase in gas velocity due to buoyancy effects.

Figure 7.2c shows the mixture Reynolds number. It is possible to see that it provides a good fit for the liquid and gas slug. However, for the liquid slug it is possible to see that the data is more scattered. This can be due to the fact that the velocity of the gas slug is larger than the mixture velocity (buoyancy).

Figure 7.2d shows the falling film velocity. It gives a good correlation for the liquid slug, due to the reason that the falling film velocity is function of the slug flow rising velocity and the mixture velocity. On the other hand, for the gas slug, it provides a good correlation too, for the same reasons as before, but the data is more scattered.

Figure 7.2e shows the slug flow Reynolds number, this Reynolds number is a function of the slug flow rising velocity and does not consider void fraction which is possibly the reason that the correlation is not so good for the liquid and slug zones.

Both the liquid and gas slug were found to be more dependent of the Re_L rather than any of the other Reynolds numbers. Therefore, Re_L was withheld in equations (7.19) and (7.20) and the final expressions of equations (7.17) and (7.18) have the form:

$$\tau_{w,ls} = \left(48.900 Re_L^{-0.295}\right)^3 Nu_L^3 \quad (7.21)$$

$$\tau_{w,gs} = \left(138.741 Re_L^{-1.196}\right)^3 Nu_p^3 \quad (7.22)$$

From Figure 7.2a, it is possible to observe that the results of the heat-and-mass transfer correlation is adequate to predict the shear stress for the liquid and gas slug and an empirical model is presented.

The above analysis indicates that relatively simple dimensionless models can be used to describe the shear stress in the slug flow. Note that since the relationships presented in

equation (7.21) and (7.22) are empirical, care must be taken when using them for design purposes.

7.3 Practical use of the heat-and-mass transfer analogy: an example

To start this analysis, it is necessary to know the diameter of the tube, the liquid and gas superficial velocities and the thermo-physical properties of the fluids (i.e. density, viscosity, thermal conductivity, surface tension and specific heat) or in other terms, the geometry and the operating conditions of the system to be analyzed.

Example: assume a two-phase flow of water and air with a superficial velocity of 0.1 and 0.05 m·s⁻¹ respectively in a vertical tube (0.01 m of diameter) and the thermo-physical properties for these two compounds as summarized in Table 7.3

Table 7.3 Thermo-physical properties of water and air at 20°C (Linstrom et al., 2009)

	Water	Air
ρ (kg·m ⁻³)	998.21	1.20
μ (Pa·s)	0.0010016	1.81·10 ⁻⁵
k_c (W·m ⁻¹ ·K ⁻¹)	0.59846	0.025546
c_p (J·kg ⁻¹ ·K ⁻¹)	4184.1	1000
σ (N·m ⁻¹)	0.0727	
D_f (m ² ·s ⁻¹)	7.14·10 ⁻¹⁰	

The procedure to calculate the shear stress and the order of equations is summarized in Table 7.4.

Table 7.4 Procedure to use to calculate the average shear stress from the heat-and-mass transfer analogy.

Parameter	Value	Equation
Pr_L (-)	7	1.91
Pr_G (-)	0.56	1.91
\dot{m}_L (kg·s ⁻¹)	$7.84 \cdot 10^{-3}$	1.24
\dot{m}_G (kg·s ⁻¹)	$4.71 \cdot 10^{-6}$	1.25
x (-)	$6.01 \cdot 10^{-4}$	1.49
u_{GM} (m·s ⁻¹)	0.474	1.99
C_o (-)	0.667	1.98
α_{tp} (-)	0.087	1.97
u_L (m·s ⁻¹)	0.110	1.101
u_G (m·s ⁻¹)	0.574	1.102
F_S (-)	0.017	1.100
F_P (-)	0.913	1.96
Eö (-)	13.417	1.104
I^* (-)	14.417	1.103
Re_L (-)	1043 (laminar)	1.107
h_L (m·s ⁻¹)	803	1.106*
h_{tp} (m·s ⁻¹)	945	1.95
k_{tp} (W·m ⁻¹ ·K ⁻¹)	0.549	1.95
Nu_{tp} (-)	17.225	1.93
Nu_L (-)	0.103	1.88**
$\tau_{w,ls}$ (Pa)	0.272	7.21
$\tau_{w,gs}$ (Pa)	-0.202***	7.22

* Even if the Re_L is in laminar regime it is recommended to use the turbulent correlation for h_L as the h_{tp} correlation was designed for laminar and turbulent regime (Ghajar and Tang, 2010)

** For the calculation of the Nu_L , the laminar correlation is used and not the turbulent one, as in the case before.

*** the (-) sign indicates the opposite direction of the flow.

It is important to highlight that the unknown mass diffusivity (mass transfer) of activated sludge cannot be determined to our knowledge, due to the complexity of the chemical and biological reactions that are occurring in the activated sludge. In this analogy, this unknown was replaced by the specific heat and the thermal conductivity (heat transfer), which can be obtained from calorimetric and hot-wire experiments respectively. Nevertheless, it is important to consider that these kinds of analogies are only applicable for Newtonian liquids, whereas, sludge exhibits non-Newtonian behaviour. However, it could be possible to use a correction for non-Newtonian behaviour for the Nusselt number (equation (1.92)). But more data is required to confirm this.

7.4 Conclusions

An empirical correlation was developed to determine the shear stress for gas and liquid slug. This correlation is function of the mass transfer coefficient obtained from the electrochemical setup introduced in chapters 2 and 3. This alternative approach was used based on a dimensionless analysis, more specifically the heat-and-mass transfer analogy. As heat transfer is widely studied in the petrochemical industry, mechanistic and empirical models exist to determine the heat transfer in multiphase flow. Therefore, this model incorporated the mass transfer coefficient using the Lewis number in order to determine the shear stress. Nevertheless, a correction factor was introduced to account for the two distinguished zones in slug flow (liquid and gas slug). However, this analogy needs to be further extended for activated sludge, but as was mentioned before (chapter 6), this requires a well defined viscosity model.

Chapter 8. Hydrodynamic CFD model of a hollow fiber MBR validated with experimental shear stress measurements

Abstract^{*}

The main drawback of MBR systems is the fouling of the membrane which is typically decreased and/or prevented by gas sparging. Nevertheless, in practice this gas sparging is applied based on existing rules of thumb or a trial-and-error approach which both are tedious and very time-consuming. Another important factor to consider is that the aeration used for fouling control is about 40 % of the total energy consumption of an MBR. Therefore, dedicated experiments are needed to fully understand the hydrodynamics of this two-phase flow and how it exactly “controls” fouling. This work focuses on the validation of a Computational Fluid Dynamics (CFD) model using extensive experiments collected with a pilot-scale Hollow Fiber GE-Zenon submerged MBR. It was found that the CFD model underpredicts the experimental data in terms of shear stress. This probably is attributed to the fact that the CFD model only considers the two-phase flow and not the movement and collision of fibers within the system, which is likely to impose high shear conditions, indirectly caused by aeration.

^{*} Redrafted after:

Ratkovich, N., Chan, C.C.V., Berube, P., Nopens, I., Experimental validation of a hydrodynamic CFD model of a HF MBR using shear stress measurements in the bundle. *Journal of Membrane Science* (in preparation).

Introduction

For a better control of fouling in MBR, research has focused mainly on the determination of the fouling constituents (i.e. colloidal particles). However, it has been shown that the hydrodynamics near the membrane surface play an important role in fouling control. That is why, to reduce the fouling, air is introduced to create a gas-liquid two-phase flow. This mixture of gas-liquid increases the surface shear stress which removes foulants that are already attached to the membrane surface (scouring effect) and prevent the formation of a cake layer. Nevertheless, the fouling mechanisms are not well understood, which results in mainly experimental trial and error approaches to find the best air sparging strategies. Although air sparging has proven to be successful in controlling fouling, the energy used for blowing air into the system is a significant contribution to the operating cost for MBR systems up to 40 % of the total energy consumption (Judd, 2006).

A hydrodynamic model of the submerged MBR system is needed to better understand the mechanisms that govern fouling control, and to identify optimal air sparging scenarios and membrane module configurations to better control the fouling phenomenon. This work focuses on developing a numerical model using computational fluid dynamics (CFD) and validate it with experimental data using electrochemical shear probes of a pilot submerged MBR. To optimally design air sparging scenarios and membrane module geometries, knowledge of the shear stress induced by air sparging on membrane surfaces is needed. The surface shear stress was mapped for a pilot-scale submerged MBR system (ZeeWeed® 500c, GE Water and Process Technologies, Canada) using electrochemical shear probes (Fulton, 2009). The mapping indicated that the air sparging scenario, the module spacing and the fiber tension significantly affected shear stress profiles in the system. The objective of this work is to validate and calibrate a CFD model based on experimental measurements. Once the model is validated it can be used for optimization (i.e. different aeration conditions, other module spacing, diffuser location, etc).

8.1 Description of the setup

A GE ZeeWeed® MBR pilot plant is located at the Department of Civil Engineering at the University of British Columbia (Vancouver, Canada). The pilot consists of one cassette which contains three hollow fiber (HF) ZeeWeed 500c (ZW500) membrane modules (GE - Water and Process Technologies, Oakville, Canada). Figure 1 shows the modules and the fibers. The performance of this pilot system, especially in terms of fouling, has been reported to be similar to full-scale MBR systems. Therefore, the outcome of this analysis in terms of shear forces can be considered representative for full-scale systems. It is important to highlight that experiments were carried out without suction for reasons of simplicity.

The cassette frame has pneumatic actuators that allow: 1) to change the tension of the fibers (Figure 8.1) and 2) to alter the spacing between the modules (Figure 8.2).

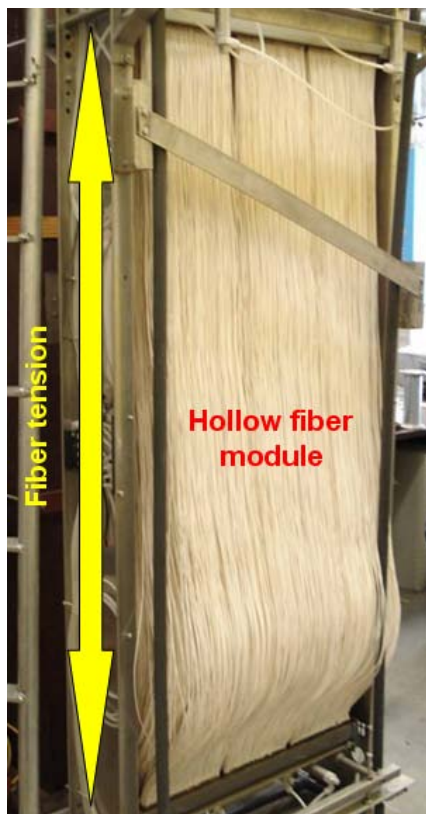


Figure 8.1. Cassette frame with three membrane modules and fiber tension.



Figure 8.2. Spacing between the three modules

Nitrogen (instead of air, as oxygen would oxidize the electrolyte solution) sparging was applied to the MBR tank via two coarse bubble diffusers. Each diffuser consists of a 0.025 m diameter tube with 11 holes, each having a diameter of 0.005 m. The two diffusers are fixed to the base of the cassette and 0.2 m below the membrane modules. The gas flow rate was monitored using a rotameter to control the different gas sparging conditions. The dimensions of the MBR tank are H: 2.18 m, W: 0.85 m and L: 0.47 m. The cassette was located in the center of the tank, with a spacing of only a few centimeters between the cassette and the tank wall. Due to system symmetry and, hence, similar expected behaviour in the system, the surface shear forces were only characterized for one quarter of the system, as presented in Figure 8.3. Within this quarter, the surface shear forces were characterized for five vertical planes (or sheets): sheet 1 (located in the middle of the inner module), sheet 2 (located in the outside edge of the inner module), sheet 3 (located in the inside edge of the outer module), sheet 4 (located in the middle of the outer module) and sheet 5 (located in the outside edge of the outer module) (see Figure 8.3a). For each of these sheets, surface shear forces were measured at 12 locations in the plane (Figure 8.3b). Hence a total of 60 locations within the MBR tank were sampled for shear dynamics.

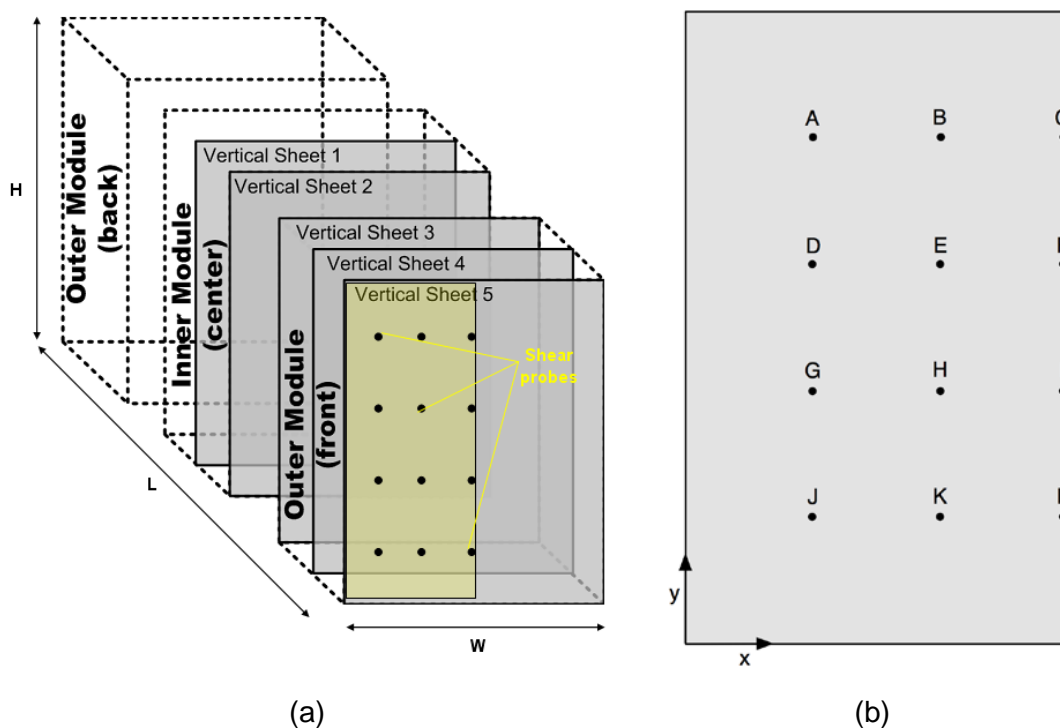


Figure 8.3. (a) Shaded vertical sheets within three modules and area of interest (yellow) and (b) location where shear forces were measured on each vertical sheet (rows ABC, DEF, GHI, and JKL at 'y' of 1.57, 1.08, 0.59, and 0.10 m, respectively, and columns ADGJ, BEHK and CFIJ at 'x' of 0, 0.18 and 0.36 m, respectively)

8.2 Operational conditions

To study the effect of different operational variables, fiber tension, module spacing and sparging flow rate are varied, each with three set-points (see Table 8.1). For each condition three repetitive measurements were performed, resulting in a total of 81 experiments (3x3x3x3) each lasting approximately 10 minutes. In addition, 10 experimental blanks were performed where no sparging was applied. These experiments were performed without interruption over a period of 42 h. A detailed analysis of the effect of the experimental variables on the surface shear is presented in Fulton and Bérubé (2010).

Table 8.1. Description of the operational condition of the GE ZeeWeed® MBR pilot plant.

Condition	Descriptor	Set-point	Letter code	Value
Fiber tension (vertical distance between the modules, Figure 1)	Loose ⁵	160 cm (95.4 %) ¹	X	L
	Medium ⁵	164 cm (97.8 %) ¹		M
	Tight	167 cm (99.6 %) ¹		T
Module spacing² (horizontal distance between the modules, Figure 2)	Wide	12.3 cm	Y	W
	Medium	8.26 cm		M
	Narrow ⁵	6.35 cm		N
Gas flow rate	High ⁵	15 m ³ ·h ⁻¹	Z	H
	Medium	10 m ³ ·h ⁻¹		M
	Low	5 m ³ ·h ⁻¹		L
Sparging settings	Fast alternating ³	3 s	PQ	FA
	Slow alternating ³	6 s		SA
	Fast pulse ⁴	3 s on / 3 s off		FP
	Slow pulse ⁴	6 s on / 6 s off		SP
	Continuous	On		CA

¹ Percent tension values were calculated as the distance between the top and bottom bulkheads of the cassette divided by the maximum fiber length (167.6 cm).

² The horizontal module spacing was measured between the center of the inner module and the center of one of the outer modules. The width of each module was approximately 5 cm.

³ Alternating flow between the two diffusers

⁴ Alternating flow on and off (both diffusers on, then both diffusers off)

⁵ Typical (manufacturer suggested) operating configurations for Zeeweed-500c systems: fiber slack of 1-5%, narrow spacing (6.0cm, center to center), high sparging rate (~15m³·h⁻¹).

A code of five letters (XYZ-PQ) will be used to explain the operational condition, where X will refer to the fiber tension (i.e. L: Loose, M: medium and T: tight), Y will refer to module spacing (i.e. W: wide, M: medium and N: narrow) and Z will indicate the flow rate (H: high, M: medium and L: low) and PQ will indicate the sparging setting (FA: fast alternating, SA: slow alternating, FP: fast pulse, SP: slow pulse and CA: continuous aeration). E.g. TMH-FP represents conditions of tight fiber tension, medium module spacing, high gas flow rate and fast pulse.

8.3 Electrochemical shear measurements

The shear forces were measured using an electrochemical method (Dumont et al., 2002; Dumont et al., 2000; Legrand et al., 2000). With this method, the shear forces at a surface can be estimated based on the diffusion limited current passing from a cathode (shear probe), embedded flush to the outer surface of Teflon® tubes (similar in diameter and flexibility to ZW500c hollow fibers) (Figure 8.4), to an anode, through a reversible ion couple solution in which the surface is submerged (electrolyte).

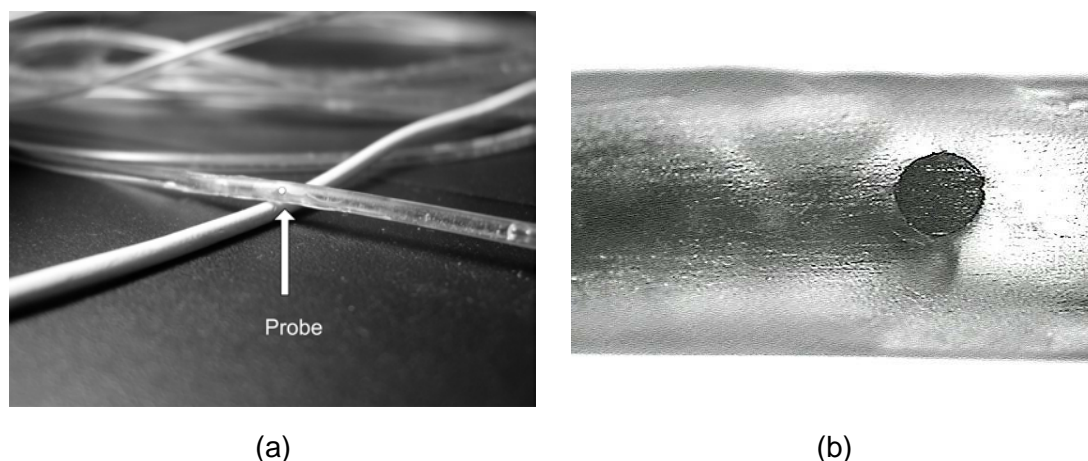


Figure 8.4. Shear probes on test fiber. (a) test fiber with probe, resting on ZW500c hollow fiber for comparison and (b) close-up of probe surface

To ensure that conditions of limiting current occurred only at probe surfaces, and not at the anode surface, an anode surface area 210 times larger than that of the active probe surface area was used. A total of 60 shear probes were constructed. The solution used for the electrochemical method was as described by Chan et al. (2007), and consisted of 0.003 M ferricyanide, 0.006 M ferrocyanide, and 0.3 M potassium chloride in deoxygenated, dechlorinated tap water. A potential of 0.310 ± 0.002 V was applied between the probes and the anode to generate conditions of limiting current. A detailed description of the procedure used to determine the limiting conditions is presented in Mitchell and Hanratty (1966) and Rajeshwar & Ibanez (1997). The relationship between the voltage and the surface shear forces is given by Equation (3.5). In this case, the diffusion coefficient of ferricyanide is $6.6 \cdot 10^{-10} \text{ m}^2 \cdot \text{s}^{-1}$ (Rosant, 1994) at 16.5 °C.

Voltage signals were collected at a frequency of 500 Hz using Signal Express software (National Instruments, USA), and saved in text files for subsequent analysis. Since only six signal conditioning circuits were available to collect the voltage signals from the 60 shear probes, six switches, each with 10 inputs, were used to collect the signals for the 60 shear probes (i.e. probes were operated six at a time). For each experimental condition, signals were collected for one minute for each shear probe; therefore, for each experimental condition investigated, it took 10 minutes to collect the signals from the 60 probes. Because switching was done manually over a period of approximately 5 seconds every minute, the first 10 and last 5 seconds of each one-minute signal was excluded from the analysis presented below.

8.4 CFD model specification

Given the experimental degrees of freedom, there are a total of 81 combinations. However, to setup and perform 81 numerical CFD simulations is extremely time consuming and CPU intensive. Therefore, only 15 combinations were selected and they are summarized in Table 8.2. For the fiber tension, the tight fiber tension (T) case was selected. The reason behind this choice is the practical difficulty in modelling fiber movement. Assuming to ignore this, it is valid for the tight fiber configuration. For the module spacing, the medium spacing (M) was selected assuming an average spacing between the narrow and wide module spacing. All the cases of air sparging were simulated.

Table 8.2. Summary of the CFD simulations

Simulation number	Operational condition	Simulation number	Operational condition
Sim01	TML-SA	Sim09	TMM-FP
Sim02	TML-SP	Sim10	TMM-CA
Sim03	TML-FA	Sim11	TMH-SA
Sim04	TML-FP	Sim12	TMH-SP
Sim05	TML-CA	Sim13	TMH-FA
Sim06	TMM-SA	Sim14	TMH-FP
Sim07	TMM-SP	Sim15	TMH-CA
Sim08	TMM-FA		

Each simulation (from Table 8.2) was run for a total of 60 s (~ 8 weeks of simulation per case). From which, the first 24 s were assumed to be needed to reach a quasi-steady state

for the velocity profiles in the system. The remaining 36 s were used for model prediction analysis.

8.4.1 System geometry

The complete geometry and dimensions of the GE ZeeWeed® MBR pilot plant are presented in Figure 8.5.

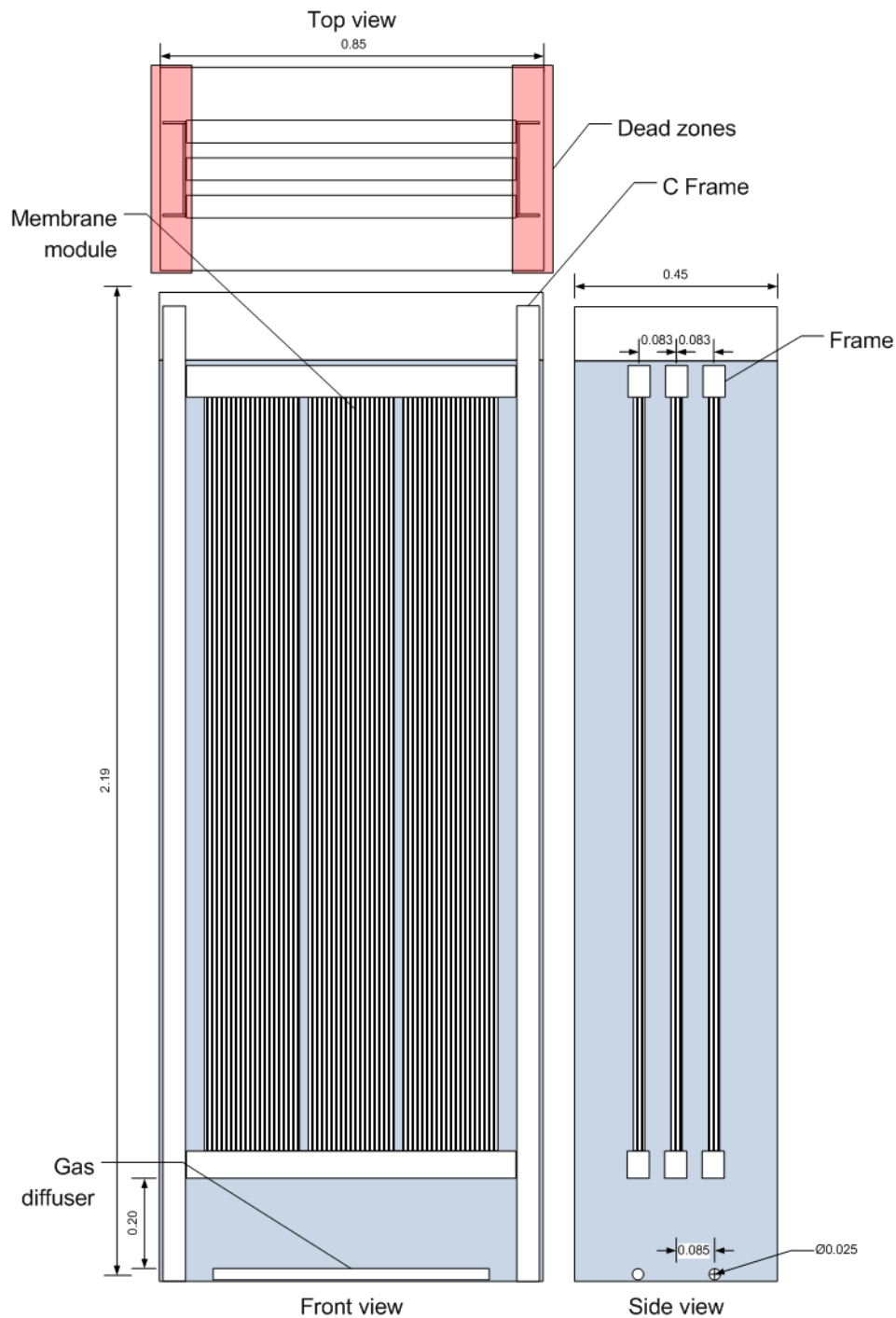


Figure 8.5. Dimension (in m) of the GE ZeeWeed® MBR pilot plant

As mentioned earlier, the probes are located in only one corner of the tank (see Figure 8.3a). By assuming perfect system symmetry, measurements from one corner of the membrane cassette are used to linearly interpolate the shear stress throughout the entire system which is assumed to be valid. The supports for the frames (C frame) were not modelled because it is considered that a liquid dead zone exists inside.

8.4.2 Boundary and operational conditions

The location of the membrane modules, frames (to support the modules) and the two diffusers as drawn in Gambit v6.3 (Ansys, USA) are shown in Figure 8.6.

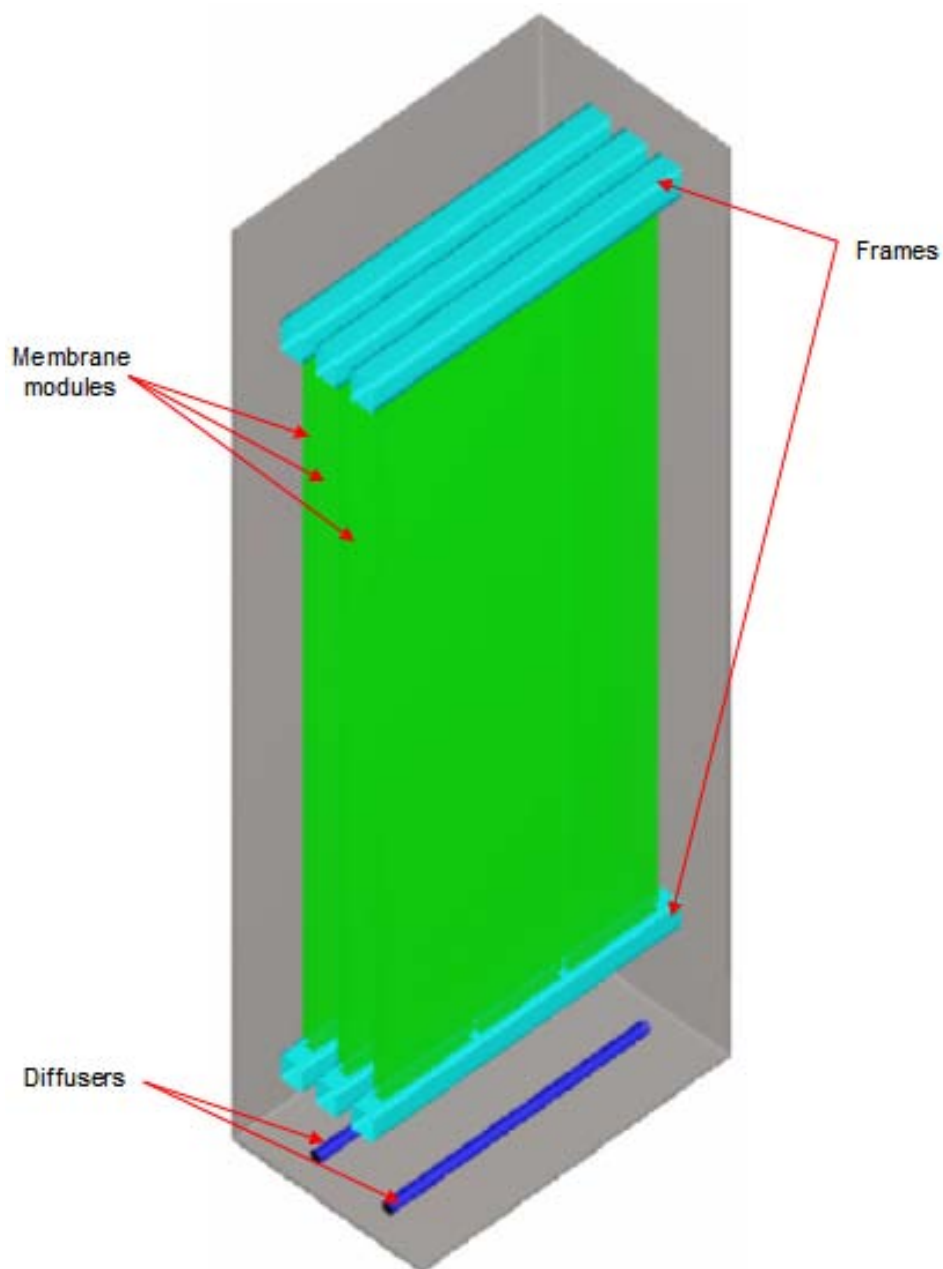


Figure 8.6. Schematic of the submerged MBR

The hollow fiber module was modelled as a rigid wall (e.g. flat sheet modules), which means, that water and nitrogen cannot penetrate the membrane modules and filtration was not considered. It is important to highlight that for the simulation case only vertical sheets 2, 3 and 5 can be considered. Indeed, vertical sheets 1 and 4 are within the HF bundle and cannot be simulated because of the rigid walls approach. Therefore, it is possible only to compare the data from 36 of the 60 shear probes (probes that are within the bundle were not considered as mentioned above).

Due to the complexity of drawing and meshing the 11 holes of 5 mm in each diffuser, it was assumed that the air originates only from the top part of the diffuser keeping the same flow rate for simplicity (Figure 8.7).

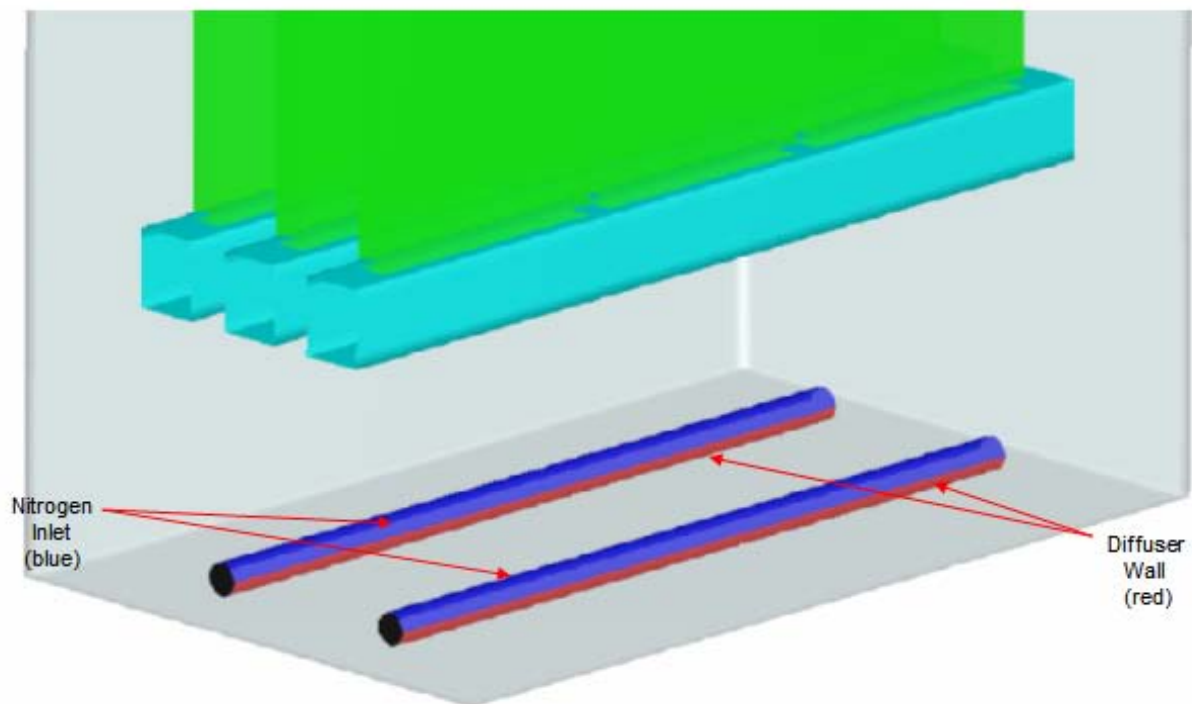


Figure 8.7. Detailed schematic of the diffusers in the CFD model setup

8.4.3 Numerical specifications of the CFD model

A CFD model was developed to simulate the pilot-scale submerged MBR system for which shear maps have been developed for different sparging conditions and membrane module geometries. The CFD package used (Fluent v6.3, Ansys) contains the mixture model (also known as the Algebraic Slip Mixture model (ASM) which is a simplified multiphase model that allows the phases to move at different velocities. It assumes the phases to be in interpenetrating continua (non miscible). It models two phases by solving the momentum and the continuity equation for the mixture, the volume fraction equation for the secondary phase, and an algebraic expression for the relative velocity. It does not assume that there is an interface between the two immiscible phases and mass transfer is not allowed. This

model is commonly used to model bubble columns. A three-dimensional geometry was built in Gambit v2.3 (Ansys) with the dimensions presented in section 8.1. To properly capture the shear value at the wall of the fibers, a fine grid was built, where the shear stress has an impact. The $k-\varepsilon$ RNG (ReNormalized Group) turbulence model with enhanced wall treatment was used to capture properly the shear stress at the membrane wall. This turbulence model is commonly used for modelling of bubble columns (Kulkarni et al., 2007). To initialize the simulation, the system starts without gas (still liquid) and after the specific flow rate of the gas is defined for each diffuser during a specific time (Table 8.1), there is no inlet of liquid and no permeation occurring. To solve the momentum transport equation the QUICK (quadratic upwind interpolation) scheme was used, which increases stability of the solution, provides a faster convergence and has 4th order accuracy. For pressure, the BFW (Body Force Weighted) scheme was used which capture buoyancy and increases stability in the solution. For the pressure-velocity coupling the PISO (Pressure Implicit solution by Split Operator method) scheme for faster convergence was used (Taha and Cui, 2002). A time step of 0.001 s was adopted.

36 surface monitors were implemented in the CFD model at exactly the same location as the shear probes (Figure 8.3b). They are located in the membrane modules for the sheets 2, 3 and 5. The surface monitors record the absolute wall shear stress value (no direction). The physical properties of the materials are summarized in Table 8.3.

Table 8.3. Material properties

Material	Density (kg m^{-3})	Viscosity (Pa s)
Water + electrolyte	1016	0.001
Nitrogen	1.1789	$1.7417 \cdot 10^{-5}$

8.5 Surface shear measurements

Surface shear forces were measured at different locations in the commercial-scale ZW500c modules (Figure 8.8). As it was mentioned earlier, the raw data obtained from the shear probes is in units of voltage. To convert it into shear stress, one can use (based on equation (3.5)):

$$\tau = 9.755V^3 \quad (8.1)$$

For all experimental conditions investigated, the shear forces varied over time. The baseline shear forces (i.e. minimum values) were likely to be induced by the bulk liquid movement within the system, while shear events (i.e. frequent peak values) were likely to be induced by the passage of gas bubbles (Chan et al., 2007). Although the range of average shear forces

(average of all probe measurements across the entire cassette) for the different experimental conditions investigated was relatively small (i.e. 0.3 to 1.75 Pa), the instantaneous shear forces ranged from approximately 0 to over 10 Pa. In addition, as presented in Figure 3, the surface shear forces were not homogeneously distributed within the system due to channelling of sparged bubbles towards the center of the system tank (Nguyen, 2008). The latter along with shielding of some areas within the module (Chan et al., 2007) are likely to be responsible for this distribution of surface shear forces. Detailed experimental analysis can be found in Fulton (2010) and is not reproduced here.

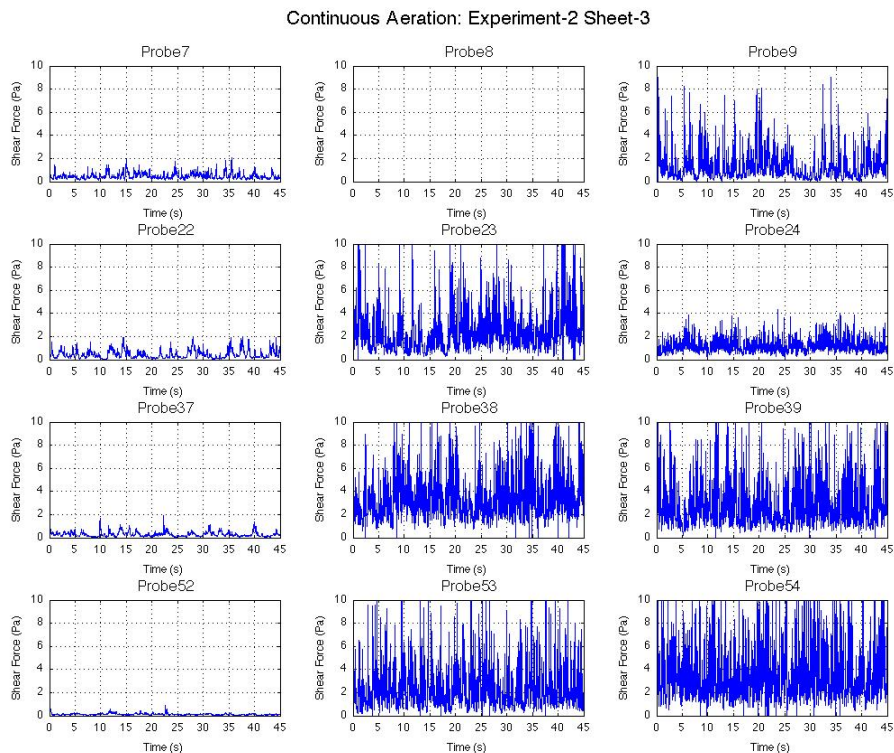


Figure 8.8. Typical surface shear forces measured on sheet 3 in a commercial-scale ZW500c membrane cassette. Probes 7, 8, 9, 22, 23, 24, 37, 38, 39, 52, 53, and 54, correspond to probe locations A to L (Figure 8.3b) on sheet 3 (Figures 8.3a). Note: of the 60 probes, 5 did not work properly during testing, including probe 8 in the figure.

From Figure 8.8, it is possible to observe highly variable shear profiles due to the passing of bubbles. E.g. the fibers located in the corner of the module (probes 7, 22, 37 and 52) are only slightly affected by the aeration, and it could be expected that these fibers will be more prone to fouling. On the other hand the probes that are close to the centre exhibit higher variations in shear forces. This suggests that the aeration system is not equally distributing air along the module.

Due to the high shear variation, it is necessary to interpret this data in a more efficient way, relative and/or cumulative frequencies can be used to determine which sparging condition is

more efficient. Figure 8.9 shows the relative frequency for loose fiber tension (L), the three module spacings and three different gas flow rates (Table 8.1).

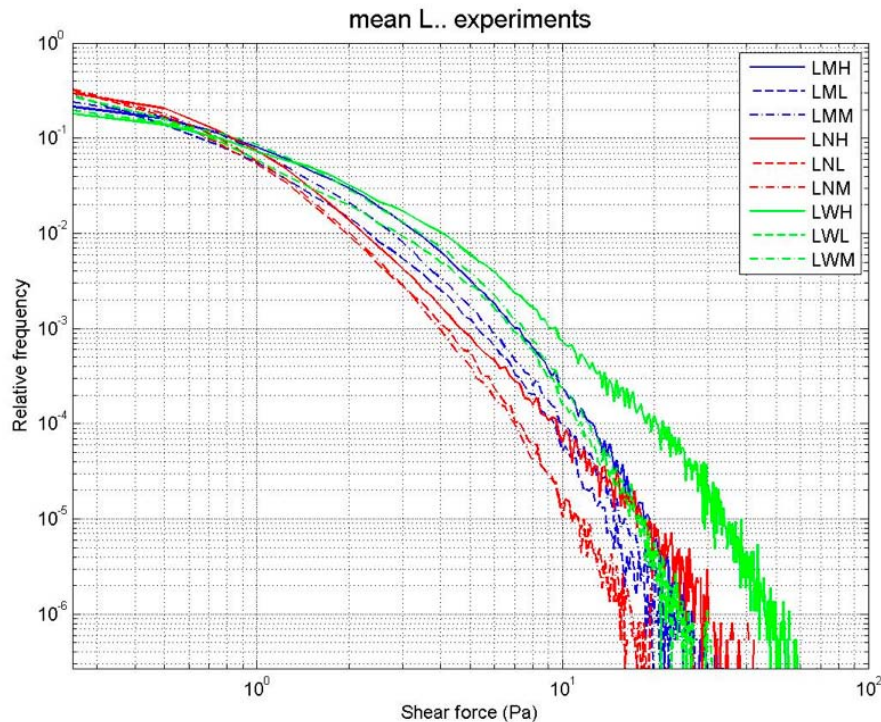


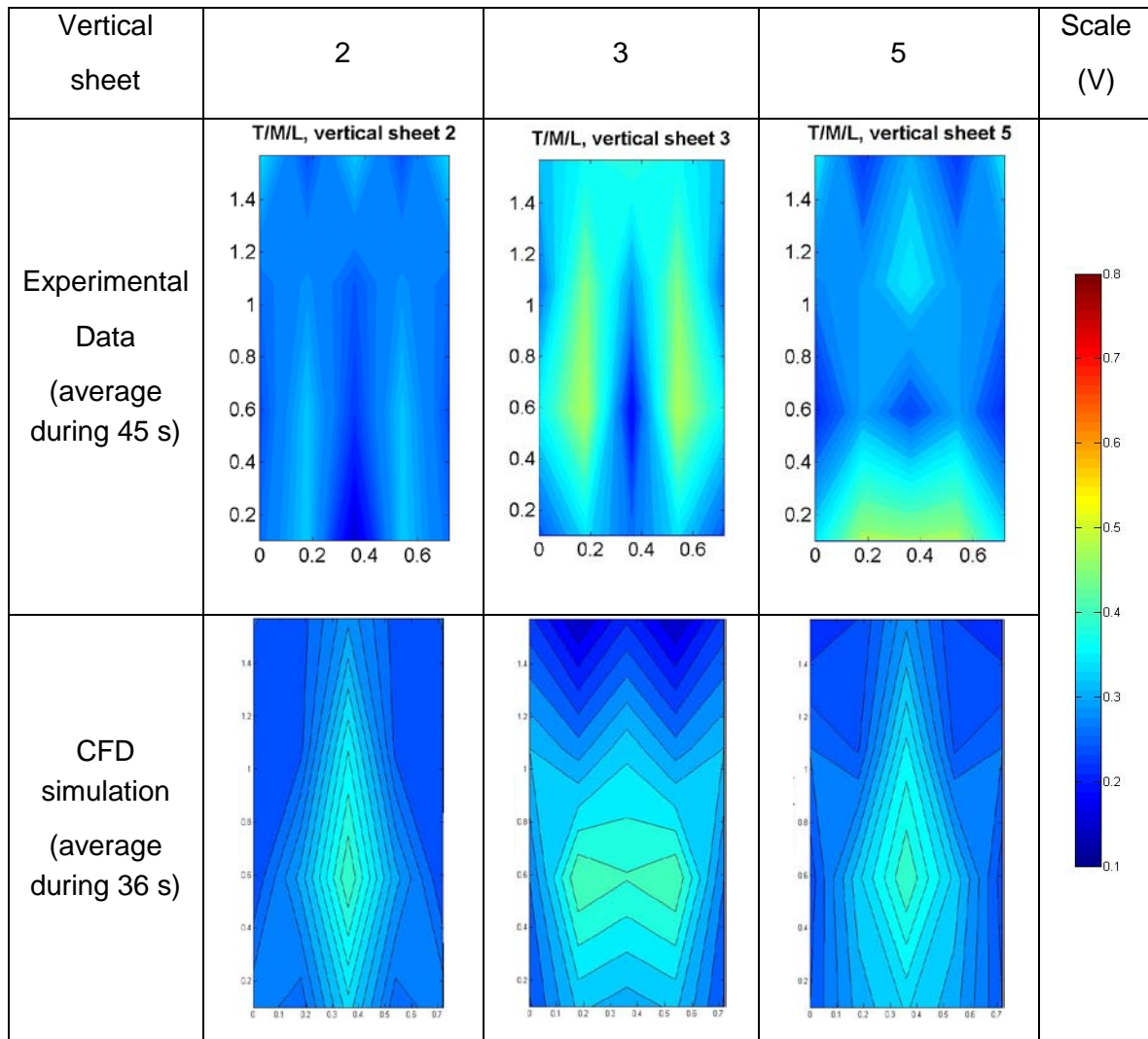
Figure 8.9. Relative frequency vs shear forces for loose fiber tension and different cases of model spacing and gas flow rate for continuous aeration

From Figure 8.9, it is possible to see the following based on the module spacing: the high shear forces are found with a wide module spacing and high gas flow rate (high relative frequency). On the other hand, the narrow module spacing provides the lowest relative frequency. The medium spacing provides medium shear compared to the narrow spacing. Comparing based on gas flow rate: the low and medium gas flow rates give relatively the same shear forces but the high gas flow rates provide much higher shears.

8.6 Numerical simulations

As was discussed in section 8.3, only the medium module spacing combined with the tight fiber tension case was modelled. One way to compare the experimental and numerical simulation can be by using contours of voltage (\sim wall shear) using equation (8.1) but solving for voltage, as the data obtained from Fluent is in shear, it needs to be converted into voltage (Table 8.4).

Table 8.4. Comparison of the voltage contours for the experimental measurements and CFD simulations (sim12)



From Table 8.4, it is possible to observe that the pattern of the contours of voltage are not similar to the experimental measurements; the order of magnitude is the same ($\sim 0.2 - 0.5 \text{ V} = 0.1 - 1.2 \text{ Pa}$). This indicates that the “average” of the simulation resembles the experimental data but it cannot capture local values as several assumptions were made while building the CFD model (i.e. hollow fiber mimicked by flat sheet implying there is no movement of fibers induced by bubbles and rigid module wall which means that gas and liquid cannot flow through the module). Hence, these contours mainly serve as a qualitative comparison.

It is important to highlight that other CFD work in flat sheet membranes (Khalili et al., 2009) reported average shear values of $\sim 1 \text{ Pa}$ for similar operating condition, which is similar to the ones obtained in this work. However, in the study performed by Khalili et al. (2009), shear stresses were not measured experimentally, but rather only the velocity profiles. The latter were in good agreement with the CFD model suggesting that shear stresses inferred from the CFD model should at least have similar orders of magnitude. Hence, this could be

regarded as a, say it weak, validation of the CFD model presented here. However, the assumptions made to use if for a hollow fiber are probably too rough at this point and further work is needed.

Besides using contours to compare model predictions by the experimental data, a more quantitative comparison is possible using surface monitors, which allow to produce similar graphs as in Figure 8.8. These are shown in Figure 8.10.

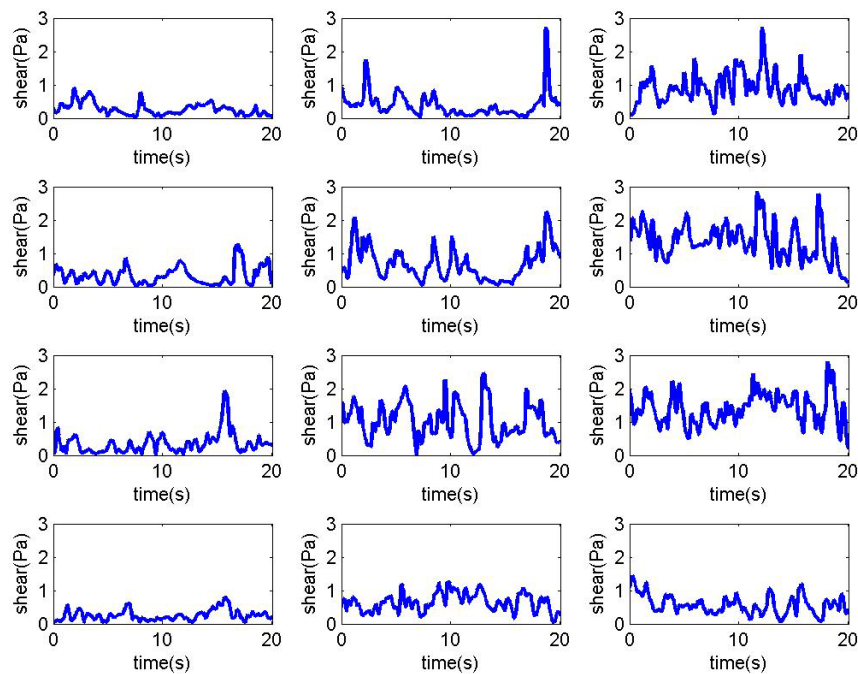


Figure 8.10. Typical surface shear forces simulated for the same sheet as in Figure 8.8.

Comparing Figure 8.10 to Figure 8.8 reveals a difference in shear scales. They go from 0 to 3 and from 0 to 10 Pa respectively. Having a closer look at the probes located in the corner, the same behaviour is observed, the shear forces are lower compared to the probes in the middle, which is similar as the experimental measurements (Figure 8.8). The simulations seem to under-predict the data, at least comparing the instantaneous shear forces. This allows to conclude that an important process is not captured by the CFD model (i.e. movement of fibers). Some reasoning as to where the model fails is given below:

- The hollow fiber module was approximated as a flat sheet module, which is not true in reality. That is why “tight” fibers were modelled instead of the “loose” fibers. However, this seems still to be a severe assumption, in the sense that the shear experienced by the fibers originates from both gas-liquid movement and fiber movement (Berube et al., 2006) which is not accounted for in the CFD model.

- The shear induced by the gas-liquid movement can be obtained from the simulations. Research characterizing velocity profiles in submerged MBR (Ghidossi et al., 2006; Ndinisa et al., 2006) has been made and the CFD models have proven to be accurate in terms of velocity profiles and air distribution (Khalili et al., 2009; Nguyen Cong Duc et al., 2008b).
- CFD modelling of hollow fibers has been reported earlier. (Dasilva et al., 2004) assume the hollow fibres as rigid cylinders in their CFD model. (Nguyen Cong Duc et al., 2008b) approximate the hollow fibres as flat sheets membranes for the sake of geometry simplicity. Therefore, the shear induced by the movement of the fibers is not straightforward to add to the model. Another important limitation to consider in the CFD model is that it does not consider the gas and liquid flows through the bundle (in the simulation the module is made by rigid walls).

8.6.1 Preliminary CFD comparison

An option to compare the data and model predictions is by using relative frequencies in a similar way as presented in Figure 8.9.

Each sheet contains 12 probes (shear monitors) which allows to obtain the relative frequencies distribution for each probe. That will produce 12 graphs per sheet which will be still too complicated to perform comparisons. Therefore, the data will be grouped per sheet as one single distribution (one curve for each sheet) (Figure 8.11).

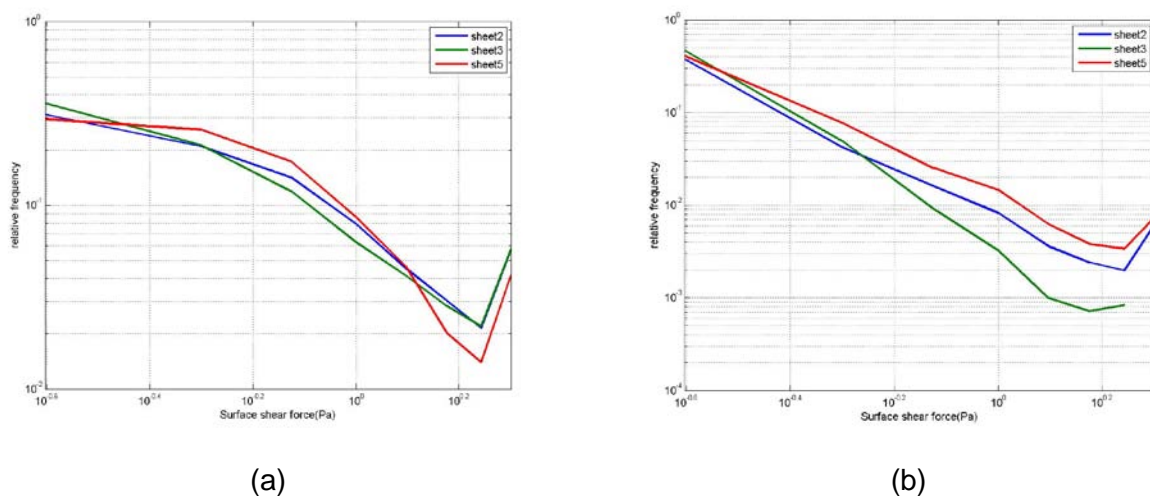


Figure 8.11. Comparison of the relative frequency for the different sheets in (a) sim13 and (b) sim03

From Figure 8.11a, it is possible to see that the wall forces in the three sheets are rather similar in terms of relative frequency. Therefore, it is not possible to identify which sheet is performing “better” (having a high relative frequency of shear). Looking at Figure 8.11b it is possible to see that sheet 5 performs best, followed by sheet 2 and sheet 3. This difference can be due to the location of the modules above the air diffuser and the air sparging conditions. Similar analysis can be made for the remaining 13 simulations but it will not be shown in this study.

Another option for comparison is to account for all probes in the entire system (considering all 36 probes at once) to have an overall performance of the whole system and compare the 15 cases at once.

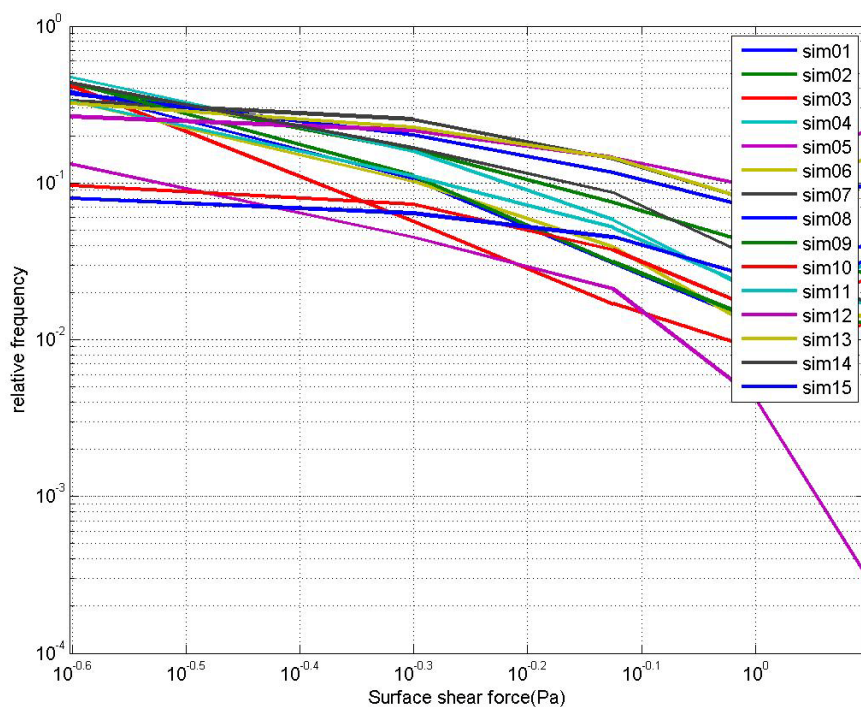


Figure 8.12 Comparison of the relative frequency for the 15 different operating conditions

From Figure 8.12, it is possible to observe that the best performing is sim12, with slow pulse and high gas flow rate. However, as this was mentioned before, the experimental analysis is ongoing. Therefore, this is just a preliminary analysis using relative frequencies and the work is still ongoing.

8.7 Conclusions

A CFD model was developed for a GE ZeeWeed® MBR pilot plant. This pilot plant was equipped with 60 shear probes in different locations to map the module surface in terms of shear forces. The CFD model was “equipped” as well with surface monitors in the same locations as the shear probes to record the shear forces and ease the comparison between the model and the experimental setup. Two main comparisons were made between the CFD model and the experimental data: 1) Contours of average voltage were plotted based on which it was found that the range of voltage (or shear forces) was similar. However, the contour pattern could not be accurately predicted. 2) The instantaneous shear force from the CFD model was under-predicted by an order of magnitude compared to experimental data. These differences are attributed to the main assumptions of the CFD model, which are: 1) Hollow fibers were modelled as rigid walls (like a flat sheet module); 2) movement of hollow fibers and collision among them are not considered, it is merely the liquid and gas movement; 3) it is assumed that the high shear fraction comes from the movement of fibers and not from the liquid-bubble-wall interaction, which is captured by the current model; 4) liquid and bubbles do not flow through the module.

Chapter 9. Conclusions

Introduction

A common problem encountered with MBR systems is fouling of the membrane resulting in frequent cleaning and replacement which makes the system less appealing for full-scale applications. This hampers its commercialization due to reduction of productivity and increased maintenance and operational cost. Literature has shown that the hydrodynamics near the membrane surface have an impact on decrease and control of fouling. However, the mechanism behind the hydrodynamics of two-phase flow is not fully understood. One factor that is commonly agreed on, is that a two-phase flow reduces the fouling due to increased shear forces, no matter which MBR configuration (hollow fibre, flat sheet or multi-tube) is used. The aim of this study was to provide more insight into this two-phase flow used in MBRs. This was done both from an experimental as well as from a model-based perspective. The major findings of the work are summarised here.

9.1 Slug flow

Application of a two-phase slug flow in side-stream MBRs has proven to increase the permeate flux and decrease fouling through a better control of the cake layer. Literature has shown that the hydrodynamics near the membrane surface have an impact on the degree of fouling by imposing high shear stress near the surface of the membrane. In this work, an experimental setup was used to investigate the shear stress imposed on the surface of a membrane under different two-phase flow conditions (gas and liquid). The latter was achieved by varying the flow rates of each phase. The experimental setup was equipped with electrochemical shear probes to measure the shear stress and a HSC to measure the gas slug rising velocity. This electrochemical technique stems from petrochemical research where it is used to identify two-phase flow patterns and measure corrosion rates. This technique can be applied as well for wastewater treatment, which is an added value to the field and makes optimal use of an interdisciplinary approach.

9.1.1 Gas slug rising velocity

The gas slug rising velocity obtained experimentally is found to be lower than that expected from theoretical analysis. This confirms expectations since the theoretical correlations do not take into account the different flow regimes (laminar, transition and turbulent) that occur in slug flow. It is found that the slug rising velocity can be correlated by means of a linear

correlation as a function of the mixture velocity. However, the slope and intercept of the linear regression depends on the mixture Reynolds number which is related to the thermo-physical properties of the liquids (density and viscosity) as well as the diameter of the tube.

9.1.2 Coalescence

From a qualitative point of view, it is highly likely that viscosity plays an important role in the coalescence of rising gas slugs. It is observed for water-gas mixtures that, when the distance between two slugs is short, they join immediately as they contact each other. On the contrary, CMC-gas and sludge-gas slug flows do not exhibit this behaviour. When the slugs are ascending they stick together, but do not immediately join to form a single larger slug. They need more time (longer travelling distance in the tube) to coalesce and become a single longer slug compared to the case of water-gas mixtures. It is hypothesised that increased viscous forces provide a larger resistance for the liquid to be pushed out from between the trailing, coalescing slugs. Hence, a larger force is required to achieve this.

9.1.3 Shear Stress Histograms (SSH)

Due to the scattered behaviour of the shear stress time series caused by the continuous passing of slugs and their difference in size (coalescence), the experimental conditions significantly affected the extent to which the gas slugs coalesced. More coalescing between gas slugs was typically observed for the experiments performed with higher gas flow rates and lower liquid flow rates. Therefore, the results imply that the frequency of shear events decreases at higher gas flow rates and lower liquid flow rates. Shear stress time series are converted to Shear Stress Histograms (SSH) for compact representation. A typical bimodal SSH is observed for all cases, with one peak corresponding to the shear induced by the liquid slug, and the other induced by the gas slug. This distribution is modelled using simple empirical relationships. Literature suggests that fouling control is expected to be optimal when the frequency of shear stress induced by the liquid flow is approximately equal to that induced by the gas flow. Corroborating these findings, the simple empirical relationships are used to identify those two-phase flow conditions that balance the peaks and, hence, should optimize fouling control, which was found to be a ratio of 4:1 gas-liquid flow rates. Currently, in practice is a ratio of 2:1 is applied. For these optimal conditions, the total energy consumption of the system is estimated based on the two-phase pressure drop. It is found that low liquid flow rates in combination with high gas flow rates (around 4 times higher than liquid flow rate), balance the SSH and minimize the energy consumption. Nevertheless, this empirical model was made for specific operational conditions. Therefore, to extrapolate this model to a real system is doubtful as empirical models are restricted to the same conditions, which clearly limit its applicability. As a real system does not contain one single tube but several hundreds of tubes, the scale-up should be made carefully. Nevertheless, this study shows a new way to analyze shear stress into SSH, and to correlate the shear stress with pressure drop and infer the energy consumption of the system for optimization purposes.

9.1.4 CFD model of slug flow

To overcome the limitations of the empirical model and through experimental investigation of slug flow, a CFD model is developed to study the effect of slug flow on the surface shear stress in a vertical tubular membrane. The model is validated using: (1) surface shear stresses, measured using an electrochemical shear probe and (2) gas slug rising velocities, measured using a HSC. The CFD simulations also predicted a bimodal SSH. In the SSH, two peaks were found, the first peak (positive) due to the liquid slug was well described by the CFD model. However, the second peak (negative) due to the gas slug was shifted to the left. This shifting was attributed to the turbulence model selected. As in literature, to model slug flow the $k-\epsilon$ turbulence model is used, which is developed for high Reynolds numbers. However, in this study the Reynolds number was in the laminar-transition regime, for which this model is not so accurate. Other models were tested as well, but the results did not improve. Therefore, this model was used in all the simulations.

At high liquid and low gas flow rates, the frequencies obtained numerically and experimentally were found to be similar, deviating by less than 10 %. However, at high gas and low liquid flow rates, the differences were slightly higher, exceeding by 20 %. Under these conditions, the CFD model simulations over predicted the shear stresses induced by gas slugs. Regarding the slug rising velocity, an over-prediction of 10 % was found. Nonetheless, the results indicate that the CFD model was able to accurately simulate shear stresses induced by gas slugs for conditions of high liquid and low gas flow rates.

9.2 Side-stream (airlift) MBR

Apart from studying slug flow at a micro-scale, also a macro-scale model was developed which, unlike the previous model, included the filtration and the air diffusion in a full-scale side-stream MBR (Norit X-Flow). For this purpose, three CFD models were built which needed to be downscaled in terms of complexity to allow reasonable simulation time. The study limits itself to CFD modelling as the results obtained could not be compared with experimental data. However, the orders of magnitude of retrieved predictions are believed to be realistic.

9.2.1 Membrane module

The development of a CFD model for an entire membrane module is achieved in a step-wise approach. In a first step a model for a single UF membrane tube is set up, where the membrane resistance is determined by calibration based on real operational parameters provided by the manufacturer. Subsequently, the model is step-wise extrapolated to 700 tubes, which is the number of tubes that exist in a membrane module. However, the main limitation is that it is not possible to simulate a geometry with 700 tubes plus the filtration process through the membrane. Eventually, the following considerations are proposed. Two types of resistances are adopted: one due to the membrane itself, where the resistance value was determined based on the single membrane tube and one due to the bundle of

tubes. These two resistance values are determined based on calibrations. This model is a numerical representation of a membrane module and can be used to understand the hydrodynamics of the flow in the tubes and the permeation through the membrane.

9.2.2 Air diffusers

Two types of air diffusers were modelled (ring and disk aerator) to observe the air distribution within the membrane module. The ring aerator was located near the wall of the diffuser unit, from which the air plume rises close to the wall and the air does not mix well with the liquid, generating a dead zone (in terms of air fraction) in the bulk region of the diffuser. This means that membrane tubes that are located near the wall, will receive a high amount of air for fouling control compared to the membrane tubes located in the bulk region, the latter being more prone to fouling. The disk aerator was located in the bottom of the air diffuser and provides a better mixing between gas and liquid with no dead zones. This diffuser provides a better air distribution in the cross-section of the membrane which is likely to control the fouling better as the air is well distributed in the bulk and in the wall regions. However, also this configuration could be further improved.

9.2.3 Combined CFD model

A single CFD model, including the membrane module and the air diffuser was built, maintaining the same parameters as for the two individual CFD models. A similar outcome was found: the disk aerator provides a better air distribution compared to the ring aerator where the air accumulates towards the outside wall of the membrane modules and not in the bulk region. This model was required as the membrane module was calibrated in single phase flow. Therefore it was required to verify that the resistance values were working properly. As well, having a 3 m high structure above the air diffuser affects the pressure drop along the membrane module.

9.3 MBR sludge rheology

Designs of equipment (pumps, mixers, diffusers, etc) are mostly based on thermo-physical properties of water. However, in waste water treatment, the rheological behaviour of water (Newtonian liquid) is far from being similar to the one of activated sludge (non-Newtonian liquid). For this reason, it is important to study in detail the rheology of activated sludge. Ten pilot and full-scale municipal MBR plants were investigated during this study. The DFCm was designed in order to quantify activated sludge filterability. However, this work shows that it can also be used as an on site tubular rheometer. Activated sludge apparent viscosity values for each experiment are calculated experimentally. Determined experimental apparent viscosity values are found to be twice as high as ex-situ determined values.

Within the representative range for full-scale applications (in terms of SRT, TSS and temperature), the apparent viscosity values are found to be in the range of 0.0058 - 0.0146

Pa.s. The main factor (of those inspected) influencing activated sludge apparent viscosities is TSS content confirming the findings in the literature. The scatter data that was found in the data can be explained by other factors, besides the TSS (e.g. floc structure and size) which was not further investigated. It was found that temperature had no significant influence on activated sludge apparent viscosity within the temperature range at pilot and full-scale municipal MBR plants. This was proven by a statistical F-test.

A widely used rheological model for MBR activated sludge is calibrated based on the data collected from different MBR plants using the DFCm unit. Comparing its prediction with two previous calibrations from literature significant differences are found. It was found that the model proposed in this work is over-predicted (by a factor of two) compared to the data collected. The differences in the models can be due to: 1) sludge composition, 2) difference in the apparatus used to perform the rheological measurements and 3) mathematical structure of the models.

9.4 Heat-and-mass transfer analogy

The mass transfer coefficient plays an important role in predicting shear stresses in tubular systems as it is proportional to the shear stress. However, to determine the mass transfer coefficient experimentally is an arduous task and requires a lot of time and experimental work. Besides, it can only be done for solutions where the mass diffusion coefficient and the chemical reactions are well-known. Therefore, applying it to activated sludge, which is a heterogeneous mixture and carries a negative charge, poses severe difficulties. Hence, a different approach was required.

The setup with shear probes and an electrolytic solution was used to measure the shear stress. From the shear probes readings, it is possible, besides obtaining the shear stress, to obtain the mass transfer coefficient as well. This mass transfer coefficient can be linked with the heat transfer coefficient through dimensionless analysis, more specifically, using the similarities of the heat-and-mass transfer mechanisms.

The heat transfer in two-phase flow is widely studied in literature and a robust correlation was used that was determined on several hundreds of data sets. This correlation is linked to mass transfer by the Lewis number. However, a correction factor was introduced to account for the two distinguished zones in slug flow (liquid and gas slug) that are presented in the SSH. The outcome of the mass transfer coefficient was validated and an empirical expression was developed as a function of the Nusselt number. However, this analogy could be extended for activated sludge, but a well defined viscosity model is required to use this analogy.

9.5 Submerged MBR

A GE ZeeWeed® MBR pilot plant equipped with 60 shear probes in different locations was used to map the module surface in terms of shear forces. A CFD model was developed to simulate these findings. The shear stresses obtained numerically (present study) and experimentally were relatively similar in magnitude, based on the voltage contours. However, some differences in the distribution and magnitude of shear stresses throughout the pilot-scale submerged MBR system could be observed. This was likely due to the approximations made in developing the CFD model (i.e. rigid membrane modules). Since modelling boundaries were met, the hollow fiber module was approximated as a flat sheet module. Hence, if a large fraction of the shear forces found its origin in the movement and collision of fibers and just a small fraction results from the liquid-gas movement, the CFD model was not able to capture this. Another important factor that was ignored in the CFD model was gas and liquid flows through the bundle (rigid walls) which might also increase the shear forces.

Although further improvements are needed to use the CFD model to accurately simulate shear stress distributions, the results from the present study are promising in that CFD modelling can be used to optimize the air sparging scenario and membrane module configuration to minimize the use of energy for fouling control.

9.6 Perspectives and future work

From this extensive study, it is evident that hydrodynamics play an important role in MBR operation. However, due to the exploratory nature of this work, further study is required on the matter in order to reach the eventual goal of optimizing the system and decreasing the energy consumption, in terms of air scouring, for removal of foulants. To achieve this, the following points should be addressed in more detail:

- Sludge rheology: as it was shown in this study, viscosity of activated sludge is extremely important for process design (pumping, mixing, etc). Therefore a model that includes TSS is not enough, because sludge besides having particles is a mixture of different substances, from which a more detailed characterization should be addressed in terms of floc structure, size, strength, etc. Also, it is important to look for a surrogate to do experiments that cannot be performed using real sludge. The latter presents a challenge due to the high heterogeneity of sludge.
- Surface tension: This property was not extensively investigated in this study. However, the interaction between activated sludge and gas should be studied in detail. The surface tension is an important parameter to study coalescence effects.
- Slug rising velocity: this aspect was partially investigated in this study. However, more research can be made using different tube diameters, a wider range of flow rates to account for the different flow regimes (laminar, transition and turbulent) and using more liquids to make a more general comparison. Also surfactants could be used to affect the surface tension to investigate if coalescence is affected.

- Shear stress for non-Newtonian liquids: an electrolyte solution mix with a non-Newtonian liquid (e.g. CMC) can be tested to quantify the shear stress in order to perform a stronger comparison of the effect between Newtonian and non-Newtonian liquids.
- Pressure drop: investigation of the pressure drop for single and two-phase flow with non-Newtonian liquids. This is currently not being researched although it is important to highlight that measuring pressure drop is one of the simpler and cheapest methods to validate mechanistic models of pipe flow.
- Air diffusers: currently, research in MBR is based on improving the air distribution within the MBR tank, but not on improving the air diffuser itself. Therefore, research should be made in this area and to study the air plume. Also this air plume behaves different for non-Newtonian fluids. Moreover, most designs are based on water, which is not representative for the real system.
- Filtration: currently, CFD models do not consider filtration as the extraction is $< 10\%$ and it is assumed that hydrodynamics are not affected. However, this is only true far from the membrane. Near the surface of the membrane, the hydrodynamics could be different, and especially the mass transfer coefficient would be affected by the suction.
- Multidisciplinary studies: in this work, cross-fertilisation between chemical and environmental engineering was illustrated. Research in different scientific fields should more frequently link to other disciplines (such as mechanical and chemical engineering) where other concepts are used which can be directly applicable.

Summary

Water scarcity is one of the biggest challenges our world is facing today. It is critical to utilize natural resources in a sustainable manner, which includes reusing and recycling the treated water. Membrane bioreactor (MBR) technology is proving to be a treatment technology having the potential to offer the previous demands. An MBR treatment plant is an activated sludge plant where the separation of the activated sludge and the treated effluent is accomplished through a membrane filter instead of a sedimentation tank as is the case in Conventional Activated Sludge (CAS) treatment plants. An MBR plant is characterised by an extremely low content of suspended solids in the effluent, as the membrane acts as an efficient barrier to particles larger than the membrane pore size including pathogens. This opens perspectives for water reuse and recycling.

However, the MBR technology is facing some challenges: membrane fouling and lower cost-effectiveness compared to CAS. For the former, the hydrodynamics are of great importance for reducing sludge deposition on the membrane surface and prolonging the operating period below the critical transmembrane pressure (TMP). Membrane performance measured in terms of membrane fouling has been observed to be enhanced by gas sparging. Several mechanisms were identified (i.e. bubble-induced secondary flow, physical displacement of the mass transfer boundary layer, pressure pulsing caused by bubbles). The purpose of this study was to develop tools to analyse and better understand the hydrodynamic conditions in MBR systems. This analysis consisted of both experimental investigation as well as a model-based approach to translate the observations into mechanistic models.

An experimental setup was developed to investigate the shear stress imposed on the surface of a tubular membrane under different two-phase flow conditions (gas and liquid), by varying the flow of each phase. The slug flow pattern behaviour of three different compounds (water, carboxymethyl cellulose and activated sludge) in two vertical tubes with different diameters was investigated using a high speed camera (HSC). The behaviour in terms of gas slug rising velocity was compared to theoretical equations from literature. Although these expressions seem valid, the tube diameter has and the fluid viscosity is likely to have an influence. Furthermore, it was observed that the degree of coalescence of gas slugs is lower and delayed for non-Newtonian liquids as successions of slugs without actual coalescence into a single larger gas slug were observed.

Due to the similar, though non-uniform, behaviour of shear profiles (long and short duration of shear events) caused by the difference in length of the gas slugs (due to the coalescing of gas slugs as they traversed up the tube), time series as such could not be used for analysis. Instead, for ease of interpretation and comparison of these shear profiles, Shear Stress Histograms (SSH) were introduced. For all cases, bimodal SSHs were observed, having one

peak corresponding to the shear induced by the liquid flow, and a second one induced by the gas flow. This distribution was modelled using a simple empirical relationship based on an overlapping combination of two normal distributions. As literature suggests that fouling control is expected to be optimal when the frequency of shear stress induced by the liquid flow is approximately equal to that induced by the gas flow, the simple empirical relationship could be used to identify those two-phase flow conditions that balance the peaks and, hence, optimize fouling control. It was concluded that for a combination of low liquid flow rates and relatively high gas flow rates, the peaks in the SSH are balanced and the energy consumption is minimized. However, the empirical model has its limitations that it cannot be extrapolated and that it does not learn us anything on the mechanisms that are occurring.

To overcome the limitations of the empirical model, a CFD model was developed to study the effect of slug flow on the surface shear stress in a vertical tubular membrane in more detail. The model was validated using: (1) surface shear stresses, measured using an electrochemical shear probe and (2) gas slug rising velocities, measured using a HSC. All simulated conditions resulted in bi-modal SSH (recovered from the simulation output), similar to the experimental measurements. It was found that the positive peak (liquid slug) was well described by the CFD model. However, the negative peak (gas slug) was shifted to the left due to the selection of the turbulence model for the entire flow. In reality, a slug flow changes flow pattern continuously when gas slugs are passing.

Next to this CFD model at micro-scale, a macro-scale CFD model was developed for an entire airlift membrane module present in full-scale MBRs. Due to computational limitations, a stepwise approach was followed to set up a more conceptual model. Moreover, filtration was included, which was not the case in the micro-scale model. First, a one-phase model including filtration (through a resistance representing the opposition to filtration) was developed and validated. This was then extrapolated to a bundle of tubes by defining a second resistance representing the resistance of the bundle to flow. Second, the air diffusion system was modelled for two types: ring aerator and disc aerator. The latter proved to give rise to a better air distribution. To account for influences of the membrane module on the behaviour of the air diffuser, both models were coupled and yielded comparable results. However, this verification was needed to check the values of the resistances.

Viscosity plays an important role in many aspects of activated sludge. Also here, it was found that the slug flow behaviour and, hence, the shear stress pattern that governs fouling control is affected by viscosity. An alternative, on site method is proposed. This viscosity was studied for 10 different pilot- and full-scale plants using the Delft Filtration Characterisation method (DFCm). The apparent viscosities determined were found having values twice as high as conventional rheological measurements performed with activated sludge. This can be caused by the difference in measurement technique. Here, both techniques exhibit flaws. The tube diameter of the presented method is significantly larger than that for which the rheological derivation is proposed. On the other hand, ex-site techniques suffer from floc breakage which is likely to influence the remainder of the measurement. A general

rheological model for the viscosity of activated sludge was developed as a function of Total Suspended Solids (TSS). First, it was observed that there is a large variation remaining in the data, suggesting that an important factor is missing in the model. Moreover, the model structure is overparameterised and needs further investigation as parameter estimations performed with it are highly unreliable.

The mass transfer coefficient plays an important role in predicting shear stresses in tubular systems. However, it is a quantity that is difficult to measure. Using similarities between heat-and-mass transfer mechanisms, an empirical model was proposed to predict heat and mass transfer coefficients for two-phase slug flow in vertical pipes. By using the same setup with shear probes and an electrolytic solution, it was possible to measure the mass transfer coefficient. An empirical model was developed as a function of the Nusselt number based on a robust two-phase heat transfer correlation.

Finally, to extend the study to a different type of MBR system, a CFD model of a submerged hollow fiber MBR was developed and validated using data obtained from 60 shear probes located in different sections of the MBR tank. It was found that the CFD model is under-predictive in terms of shear, caused by some assumptions made in the model to allow computation. One of those assumptions was to approximate the hollow fiber module as a flat sheet module. It is likely that a great fraction of the shear force comes from the movement and collision of fibers and only a small portion comes directly from the liquid-gas movement that can be obtained from the CFD simulation. Which effect has most impact on fouling control (shear magnitude or shear direction change) is to be further investigated. Although further improvements are needed to use the CFD model to accurately simulate shear stress distributions, the results from the present study look promising and suggest that CFD modelling could be used to effectively optimize the air sparging and membrane module configuration to minimize the use of energy for fouling control.

Samenvatting

Water schaarsheid vormt een van de grootste, huidige uitdagingen van onze planeet. Het is van primordiaal belang om de natuurlijke bronnen duurzaam te gebruiken wat onder meer het hergebruik en recyclage van water omhelst. Membraanbioreactor (MBR) technologie heeft reeds bewezen een technologie te zijn die het potentieel heeft om op voornoemde vragen een antwoord te bieden. Een MBR is een actief slib systeem waar de water-slib scheiding door middel van membraanfiltratie wordt bereikt in tegenstelling tot conventionele systemen (CAS), waar dit gravitair gebeurt. Een MBR wordt dan ook gekarakteriseerd door een extreem laag gehalte aan zwevende stoffen in het effluent, aangezien het membraan als een efficiënte barrière werkt die alle partikels groter dan de poriegrootte tegenhoudt, inclusief pathogenen.

Echter, zoals vaak heft ook de MBR technologie zijn problemen en uitdagingen: membraanvervuiling en een lagere kostenefficiëntie in vergelijking met CAS. Bij het eerste speelt de hydrodynamica een grote rol bij het reduceren van slibdepositie op het membraanoppervlak en het verlengen van de operationele periode onder de kritische transmembraandruk (TMP). Membraanperformantie, gemeten als membraanvervuiling, kan worden verhoogd door het inblazen van lucht. Verschillende mechanismen werden geïdentificeerd (o.a. luchtbel geïnduceerde secundaire stroming, fysische verplaatsing van de massatransfer grenslaag, drukpulsatie door de bellen). Het doel van deze studie was om tools te ontwikkelen voor het analyseren en beter begrijpen van hydrodynamica in MBR systemen. Deze analyse bestond uit zowel experimenteel werk als uit een modelgebaseerde aanpak om de observaties te vertalen in mechanistische modellen.

Een experimentele opstelling werd ontwikkeld om de afschuifkrachten die aan het membraanoppervlak van een tubulair membraan worden opgelegd te onderzoeken. Dit gebeurde bij verschillende twee-fase stromingscondities (gas en vloeistof) door de debieten van beide fluida te variëren. Het gedragspatroon van de slug flow voor drie verschillende fluida (water, carboxymethyl cellulose en actief slib) in twee verticale tubes met verschillende diameter werd onderzocht met behulp van een hoge snelheid camera (HSC). Het gedrag van de snelheid van opstijgende bellen werd vergeleken met theoretische vergelijkingen uit de literatuur. Hoewel deze uitdrukkingen geldig lijken, werd een invloed van tubediameter vastgesteld en werd gehypothetiseerd dat ook viscositeit hier een rol zou spelen. Verder werd ook vastgesteld dat de graad van coalescentie van gasbellen lager en bovendien trager gebeurt. Dit leidt tot de vorming van treinen van slugs die pas na verloop van tijd coalesceren.

Door gelijkaardig, doch niet-uniform, gedrag van afschuifkrachtprofielen (lang- en kortdurende afschuifkrachten) veroorzaakt door een verschil in lengte van de gas slugs

(door coalescentie van gas slugs bij het opstijgen in de tube) zijn tijdsreeksen op zich moeilijk bruikbaar voor analyse. In de plaats daarvan werden, voor het makkelijker interpreteren en onderling vergelijken van deze afschuifkrachtprofielen, afschuifkrachthistogrammen (SSH) geïntroduceerd. Voor alle onderzochte condities werden bimodale SSHs gevonden, waarbij een eerste piek overeenkomt met de afschuifkracht van de passerende vloeistofstroom en een tweede piek resultaat is van de passerende gas slug. Deze distributie werd gemodelleerd gebruik makende van een empirisch verband gebaseerd op een overlappende combinatie van twee normale verdelingen. Zoals gestipuleerd in de literatuur zou controle van vervuiling optimaal zijn wanneer de frequentie van beide pieken ongeveer gelijk zijn. De eenvoudige empirische vergelijking werd vervolgens gebruikt om die stromingscondities te identificeren die beide pieken balanceren en aldus vervuiling minimaliseren. Er kon worden besloten dat een combinatie van een laag vloeistofdebiet en relatief hoog gasdebiet aanleiding gaf tot gebalanceerde pieken in de SSH, waarbij de energieconsumptie bovendien wordt geminimaliseerd. Het dient echter vermeld dat een deregelijk empirisch model haar limitaties heeft in die zin dat het niet kan worden geëxtrapoleerd en het ons niks leert over de onderliggende mechanismen die plaatsvinden.

Om tegemoet te komen aan deze limitaties werd een CFD model ontwikkeld om het effect van de slug stroming op de afschuifkrachten ter hoogte van het membraanoppervlak van een vertikaal tubulair membraan in meer detail te onderzoeken. Het model werd gevalideerd met: (1) afschuifkrachten aan het membraanoppervlak gemeten met een electrochemische techniek en (2) opstijgsnelheden van de gas slug (Taylor bellen), gemeten door middel van een HSC. Alle gesimuleerde condities resulteerden in een bimodale SSH (geëxtraheerd uit de simulatie output), gelijkaardig als bij de experimentele observaties. De positieve piek (vloeistof slug) werd goed voorspeld door het model. De negatieve piek (gas slug) werd echter lichtjes overschat door het model, hoogstwaarschijnlijk te wijten aan het turbulentiemodel dat voor de gehele stroom diende worden te gebruikt. In werkelijkheid bestaat een slug stroming uit verschillende delen door de continue passage van luchtbellen.

Naast dit CFD model op microschaal werd ook een macroschaal CFD model ontwikkeld voor een volledige airlift membraanmodule zoals die wordt gebruikt op volle schaal. Door computationele limitaties werd een stapsgewijze aanpak gebruikt om een meer conceptueel model op te stellen. Bovendien werd filtratie meegemodelleerd, wat niet het geval was in het voorgaande microschaalmodel. Eerst werd een eenfase model ontwikkeld en gevalideerd, inclusief filtratie (door middel van een weerstand die de oppositie tegen filtratie voorstelt). Dit model werd vervolgens geëxtrapoleerd naar een bundel van tubes door het definiëren van een tweede weerstand, die de weerstand van de bundel tegen de stroming voorstelt. Vervolgens werd het luchtdiffusiesysteem gemodelleerd voor twee types beluchters: een ringvormige en een schijfbeluchter. De laatste leverde een betere verdeling van lucht op, wat echter niet experimenteel kon worden gevalideerd. Om de invloed van de membraanmodule op het gedrag van het luchtdiffusiesysteem te onderzoeken, werden beide modellen gekoppeld. Analoge resultaten werden gevonden, maar deze oefening was noodzakelijk om de geldigheid te verifiëren.

Viscositeit speelt een belangrijke rol bij vele aspecten van actief slib. Ook hier werd gevonden dat de slug stroming, en dus ook het afschuifkrachtpatroon dat de vervuiling controleert, wordt beïnvloed door viscositeit. Een alternatieve, on site methode voor de meting van viscositeit werd voorgesteld. De viscositeit werd onderzocht voor 10 verschillende piloot- en volle schaal installaties gebruik makende van de Delft Filtratie Karakterisatie methode (DFCm). De gevonden schijnbare viscositeit met de nieuwe methode bleken dubbel zo groot in vergelijking met metingen op basis van traditionele rheometers. De oorzaak hiervoor dient gezocht bij de meettechnieken zelf. Beide technieken hebben nadelen. De tubediameter van de voorgestelde methode is significant groter dan deze waarvoor de rheologische afleiding werd voorgesteld. Anderzijds lijden ex-situ technieken aan vlokopbreking en dus destructie of vervorming van het staal, wat een groot deel van de meting onbetrouwbaar maakt. Een algemeen aanvaard rheologisch model voor viscositeit van actief slib werd vervolgens gekalibreerd als functie van het zwevende stof gehalte (TSS). Er kon een grote resterende variatie worden waargenomen in de data, wat wijst op een belangrijke factor die ontbreekt in het model. Bovendien is het model hopeloos overparameteriseerd en dient dit verdere aandacht aangezien parameterschattingen die ermee worden uitgevoerd hoogst onbetrouwbaar zijn.

De massatransfercoëfficiënt speelt een belangrijke rol bij de voorspelling van afschuifkrachten in tubulaire systemen. Het is echter een waarde die moeilijk meetbaar is. Dit kan worden omzeild door gebruik te maken van similariteiten tussen warmte- en massa-overdracht. Op basis hiervan werd een empirisch model opgesteld om de warmte- en massatransfercoëfficiënten voor een tweefase slug stroming in verticale tubes te voorspellen. Door gebruik te maken van dezelfde opstelling met afschuifkrachtsensoren en een electrolytische oplossing, was het mogelijk de massatransfercoëfficiënt te bepalen. Een empirisch model werd ontwikkeld als functie van het Nusselt getal op basis van een robuuste tweefase warmtetransfercorrelatie.

Tenslotte werd, om de studie ook uit te breiden naar een ander type van MBR systeem, een CFD model ontwikkeld en gevalideerd voor een ondergedompeld holle vezel membraan. Validatie gebeurde op basis van 60 afschuifkrachtsensoren die op verschillende locaties en in verschillende secties van de MBR tank werden geïnstalleerd. Er werd gevonden dat het CFD model de afschuifkrachten onderschatte, hoogstwaarschijnlijk veroorzaakt door een aantal assumpties die nodig waren in het model om doorrekenen mogelijk te maken in een redelijk tijdsbestek. Een van deze assumpties was de holle vezel module te benaderen door een vlak membraan. Op basis van deze bevindingen kan worden gesteld dat een grote fractie van de afschuifkrachten in holle vezel systemen veroorzaakt wordt door beweging en botsing van de vezels en slecht een kleiner deel door rechtstreekse interactie met de tweefase stroming zoals voorspeld door het CFD model. Welk effect (magnitude of tekenwisseling van afschuifkracht) het meeste impact heeft op vervuilingcontrole kan op basis hiervan niet worden besloten en dient verder onderzocht. Hoewel verdere verbeteringen nodig zijn om het CFD model op een betrouwbare manier te gerbuiken, zijn de resultaten veelbelovend en kan worden besloten dat CFD modellen een krachtige tool

vormen bij de optimalisatie van membraanbeluchting en –configuratie om zo het energieverbruik en vervuilingsscontrole te verbeteren.

Bibliography

- Adsani, E., S. A. Shirazi, J. R. Shadley and E. F. Rybicki, Validation of mass transfer coefficient models used in predicting CO₂ corrosion in vertical two-phase flow in the oil and gas production, paper presented at NACE - International Corrosion Conference Series, Orlando, FL, United states, 2006.
- Baker, R. W., Membrane technology and applications, John Wiley & Sons Ltd, 2004.
- Barnea, D. and Y. Taitel, Model for slug length distribution in gas-liquid slug flow, *International Journal of Multiphase Flow*, 19(5), 829-838, 1993.
- Bellara, S. R., Z. F. Cui and D. S. Pepper, Gas sparging to enhance permeate flux in ultrafiltration using hollow fibre membranes, *Journal of Membrane Science*, 121(2), 175-184, 1996.
- Berube, P. R., G. Afonso, F. Taghipour and C. C. V. Chan, Quantifying the shear at the surface of submerged hollow fiber membranes, *Journal of Membrane Science*, 279(1-2), 495-505, 2006.
- Biswas, A. B. and S. K. Das, Two-phase frictional pressure drop of gas-non-Newtonian liquid flow through helical coils in vertical orientation, *Chemical Engineering and Processing: Process Intensification*, 47(5), 816-826, 2008.
- Brannock, M., G. Leslie, Y. Wang and S. Buetehorn, Optimising mixing and nutrient removal in membrane bioreactors: CFD modelling and experimental validation, *Desalination*, 250(2), 815-818, 2010a.
- Brannock, M., Y. Wang and G. Leslie, Mixing characterisation of full-scale membrane bioreactors: CFD modelling with experimental validation, *Water Research, In Press, Corrected Proof*, 2010b.
- Brepols, C., Economic aspects of large scale membrane bioreactors, 2009.
- Brepols, C., K. Drensla, A. Janot, M. Trimborn and N. Engelhardt, Strategies for chemical cleaning in large scale membrane bioreactors, *Water Science and Technology*, 57(3), 457-463, 2008.
- Broeckmann, A., J. Busch, T. Wintgens and W. Marquardt, Modeling of pore blocking and cake layer formation in membrane filtration for wastewater treatment, *Desalination*, 189(1-3 SPEC ISS), 97-109, 2006.
- Buetehorn, S., F. Carstensen, T. Wintgens, T. Melin, D. Volmering and K. Vossenkaul, Permeate flux decline in cross-flow microfiltration at constant pressure, *Desalination*, 250(3), 985-990, 2010.
- Bugg, J. D., K. Mack and K. S. Rezkallah, Numerical model of Taylor bubbles rising through stagnant liquids in vertical tubes, *International Journal of Multiphase Flow*, 24(2), 271-281, 1998.

- Bugg, J. D. and G. A. Saad, The velocity field around a Taylor bubble rising in a stagnant viscous fluid: Numerical and experimental results, *International Journal of Multiphase Flow*, 28(5), 791-803, 2002.
- Cabassud, C., S. Laborie, L. Durand-Bourlier and J. M. Laine, Air sparging in ultrafiltration hollow fibers: Relationship between flux enhancement, cake characteristics and hydrodynamic parameters, *Journal of Membrane Science*, 181(1), 57-69, 2001.
- Chan, C. C. V., P. R. Berube and E. R. Hall, Shear profiles inside gas sparged submerged hollow fiber membrane modules, *Journal of Membrane Science*, 297(1-2), 104-120, 2007.
- Chang, I. S., P. L. Clech, B. Jefferson and S. Judd, Membrane fouling in membrane bioreactors for wastewater treatment, *Journal of Environmental Engineering*, 128(11), 1018-1029, 2002.
- Chang, S. and A. G. Fane, Filtration of biomass with axial inter-fibre upward slug flow: Performance and mechanisms, *Journal of Membrane Science*, 180(1), 57-68, 2000.
- Cheng, L., G. Ribatski and J. R. Thome, Two-Phase Flow Patterns and Flow-Pattern Maps: Fundamentals and Applications, *Applied Mechanics Reviews*, 61(5), 2009.
- Cheng, N. S., Formulas for friction factor in transitional regimes, *Journal of Hydraulic Engineering*, 134(9), 1357-1362, 2008.
- Chhabra, R. P. and J. F. Richardson, Prediction of flow pattern for the co-current flow of gas and non-newtonian liquid in horizontal pipes, *Canadian Journal of Chemical Engineering*, 62(4), 449-454, 1984.
- Chhabra, R. P. and J. F. Richardson, Non-Newtonian Flow in the Process Industries: Fundamentals and Engineering Applications, Elsevier, 2001.
- Clift, R., J. R. Grace and M. E. Weber, Bubbles, Drops and Particles, Dover publications, 2005.
- Cognet, G., M. Lebouche and M. Souhar, Utilisation des techniques electrochimiques pour la mesure du frottement parietal dans les ecoulements diphasiques. Left bracket Electrochemical Methods for Measurement of Wall Shear Stress in Two-Phase Flow right bracket, *Houille Blanche*, 33(5), 319-322, 1978.
- Cote, P., S. Siverns and S. Monti, Comparison of membrane-based solutions for water reclamation and desalination, *Desalination*, 182(1-3), 251-257, 2005.
- Coulson, J. M. and J. F. Richardson, Chemical Engineering, Butterworth - Heinemann, 2002.
- Cui, Z. F., S. R. Bellara and P. Homewood, Airlift crossflow membrane filtration - a feasibility study with dextran ultrafiltration, *Journal of Membrane Science*, 128(1), 83-91, 1997.
- Cui, Z. F., S. Chang and A. G. Fane, The use of gas bubbling to enhance membrane processes, *Journal of Membrane Science*, 221(1-2), 1-35, 2003.
- Cui, Z. F. and K. I. T. Wright, Flux enhancements with gas sparging in downwards crossflow ultrafiltration: performance and mechanism, *Journal of Membrane Science*, 117(1-2), 109-116, 1996.

- Das, S. K. and M. N. Biswas, Pressure losses in two-phase gas-non-Newtonian liquid flow in a vertical tube, *Chemical Engineering Communications*, 135, 229-237, 1995.
- Dasilva, A., M. Heran, C. Sinfortz and A. Grasmick, Optimization of Flow Shear Stress Through a Network of Capillary Fibers With the Use of CFD, *International Journal of Chemical Reactor Engineering*, 2, 2004.
- De Clercq, B., Computational Fluid Dynamics of Settling Tanks: Development of Experiments and Rheological, Settling and Scraper Submodels, Ghent University, 2003.
- De, S. and P. K. Bhattacharya, Prediction of mass-transfer coefficient with suction in the applications of reverse osmosis and ultrafiltration, *Journal of Membrane Science*, 128(2), 119-131, 1997.
- De, S. and P. K. Bhattacharya, Mass transfer coefficient with suction including property variations in applications of cross-flow ultrafiltration, *Separation and Purification Technology*, 16(1), 61-73, 1999.
- Delgado, S., R. Villarroel and E. Gonzalez, Effect of the shear intensity on fouling in submerged membrane bioreactor for wastewater treatment, *Journal of Membrane Science*, 311(1-2), 173-181, 2008.
- Dhotre, M. T. and B. L. Smith, CFD simulation of large-scale bubble plumes: Comparisons against experiments, *Chemical Engineering Science*, 62(23), 6615-6630, 2007.
- Dieter, H. and K. Stephan, Heat and Mass Transfer, Springer, 2006.
- Ducom, G., F. P. Puech and C. Cabassud, Air sparging with flat sheet nanofiltration: A link between wall shear stresses and flux enhancement, *Desalination*, 145(1-3), 97-102, 2002.
- Ducom, G., F. P. Puech and C. Cabassud, Gas/liquid two-phase flow in a flat sheet filtration module: Measurement of local wall shear stresses, *Canadian Journal of Chemical Engineering*, 81(3-4), 771-775, 2003.
- Dumont, E., F. Fayolle, V. Sobolik and J. Legrand, Wall shear rate in the Taylor-Couette-Poiseuille flow at low axial Reynolds number, *International Journal of Heat and Mass Transfer*, 45(3), 679-689, 2002.
- Dumont, E., F. Fayolle and J. Legrand, Flow regimes and wall shear rates determination within a scraped surface heat exchanger, *Journal of Food Engineering*, 45(4), 195-207, 2000.
- Dziubinski, M., H. Fidos and M. Sosno, The flow pattern map of a two-phase non-Newtonian liquid-gas flow in the vertical pipe, *International Journal of Multiphase Flow*, 30(6), 551-563, 2004.
- Fabre, J. and A. Line, Modelling of two phase slug flow, *Ann. Rev. Fluid Mech.*, 24, 21-46, 1992.
- Farooqi, S. I. and J. F. Richardson, Horizontal flow of air and liquid (newtonian and non-newtonian) in a smooth pipe: part I. A correlation for average liquid holdup, *Transactions of the Institution of Chemical Engineers*, 60(5), 292-305, 1982.

- Fidos, H., J. Sowinski, M. Dziubinski and R. Krokos, Pressure drop in the slug flow of two-phase of gas-non Newtonian liquid mixtures, *Przemysl Chemiczny*, 83(2), 111-115, 2008.
- FLUENT, FLUENT 6.3 User Guide, 2006.
- Frechou, D., Etude experimentale de l'ecoulement gaz-liquide ascendant a deux et trois fluides en conduite verticale
Experimental Study of Upward Gas-Liquid Flow of Two and Three Fluids in a Vertical Pipe, *Revue de l'Institut Francais du Petrole*, 41(1), 115-129, 1986.
- Fu, L. F. and B. A. Dempsey, Modeling the effect of particle size and charge on the structure of the filter cake in ultrafiltration, *Journal of Membrane Science*, 149(2), 221-240, 1998.
- Futselaar, H., H. Schonewille, D. de Vente and L. Broens, NORIT AirLift MBR: side-stream system for municipal waste water treatment, *Desalination*, 204(1-3 SPEC. ISS.), 1-7, 2007.
- Garcia, F., J. M. Garcia, R. Garcia and D. D. Joseph, Friction factor improved correlations for laminar and turbulent gas-liquid flow in horizontal pipelines, *International Journal of Multiphase Flow*, 33(12), 1320-1336, 2007.
- Gaucher, C., P. Legentilhomme, P. Jaouen, J. Comiti and J. Pruvost, Hydrodynamics study in a plane ultrafiltration module using an electrochemical method and particle image velocimetry visualization, *Experiments in Fluids*, 32(3), 283-293, 2002.
- Germain, E., F. Nelles, A. Drews, P. Pearce, M. Kraume, E. Reid, S. J. Judd and T. Stephenson, Biomass effects on oxygen transfer in membrane bioreactors, *Water Research*, 41(5), 1038-1044, 2007.
- Geshev, P. I., The Green function method for calculating characteristics of a small strip-shaped shear stress probe, *Journal of Electroanalytical Chemistry*, 410(1), 1-8, 1996.
- Ghajar, A. J., Non-boiling heat transfer in gas-liquid flow in pipes - A tutorial, *Journal of the Brazilian Society of Mechanical Sciences and Engineering*, 27(1), 46-73, 2005.
- Ghajar, A. J. and C. C. Tang, Importance of Non-Boiling Two-Phase Flow Heat Transfer in Pipes for Industrial Applications, *Heat Transfer Engineering*, 31(9), 711-732, 2010.
- Ghidossi, R., J. V. Daurelle, D. Veyret and P. Moulin, Simplified CFD approach of a hollow fiber ultrafiltration system, *Chemical Engineering Journal*, 123(3), 117-125, 2006.
- Ghosh, R. and Z. F. Cui, Mass transfer in gas-sparged ultrafiltration: Upward slug flow in tubular membranes, *Journal of Membrane Science*, 162(1-2), 91-102, 1999.
- Gomez, L. E., O. Shoham, Z. Schmidt, R. N. Chokshi and T. Northug, Unified mechanistic model for steady-state two-phase flow: Horizontal to vertical upward flow, *SPE Journal*, 5(3), 339-350, 2000a.
- Gomez, L. E., O. Shoham and Y. Taitel, Prediction of slug liquid holdup: horizontal to upward vertical flow, *International Journal of Multiphase Flow*, 26(3), 517-521, 2000b.
- Gradeck, M. and M. Lebouché, Wall shear measurements inside corrugated channels using the electrochemical technique, *Experiments in Fluids*, Volume 24(1), 17-26, 1998.

- Hem, L. J., B. Rusten and H. +degaard, Nitrification in a moving bed biofilm reactor, *Water Research*, 28(6), 1425-1433, 1994.
- Heywood, N. I. and M. E. Charles, Stratified Flow of Gas and Non-Newtonian Liquid in Horizontal Pipes, *International Journal of Multiphase Flow*, 5(5), 341-352, 1979.
- Huisman, I. H. and G. Trägårdh, Particle transport in crossflow microfiltration - I. Effects of hydrodynamics and diffusion, *Chemical Engineering Science*, 54(2), 271-280, 1999.
- Huisman, I. H., G. Trägårdh and C. Tragardh, Particle transport in crossflow microfiltration - II. Effects of particle-particle interactions, *Chemical Engineering Science*, 54(2), 281-289, 1999.
- Jamal Khan, S., C. Visvanathan, V. Jegatheesan and R. BenAim, Influence of mechanical mixing rates on sludge characteristics and membrane fouling in MBRs, *Separation Science and Technology*, 43(7), 1826-1838, 2008.
- Joshi, J. B., Computational flow modelling and design of bubble column reactors, *Chemical Engineering Science*, 56(21-22), 5893-5933, 2001.
- Judd, S., The MBR book, Elsevier, 2006.
- Judd, S. J., A review of fouling of membrane bioreactors in sewage treatment, *Water Science and Technology*, 49(2), 229-235, 2004.
- Katsoufidou, K., S. G. Yiantsios and A. J. Karabelas, A study of ultrafiltration membrane fouling by humic acids and flux recovery by backwashing: Experiments and modeling, *Journal of Membrane Science*, 266(1-2), 40-50, 2005.
- Khalili, A., M. Mehrnia, N. Mostoufi and M. Sarrafzadeh, Flow Characteristics in an Airlift Membrane Bioreactor, *Chemical Product and Process Modeling*, 4(5), 2009.
- Kim, D., A. J. Ghajar and R. L. Dougherty, Robust heat transfer correlation for turbulent gas-liquid flow in vertical pipes, *Journal of Thermophysics and Heat Transfer*, 14(4), 574-578, 2000.
- Kim, D., A. J. Ghajar, R. L. Dougherty and V. K. Ryali, Comparison of 20 two-phase heat transfer correlations with seven sets of experimental data, including flow pattern and tube inclination effects, *Heat Transfer Engineering*, 20(1), 15-40, 1999.
- Kim, H. s., J. W. Gellner, J. P. Boltz, R. G. Freudenberg, C. K. Gunsch and A. J. Schuler, Effects of integrated fixed film activated sludge media on activated sludge settling in biological nutrient removal systems, *Water Research*, 44(5), 1553-1561, 2010.
- Krauth, K. and K. F. Staab, Pressurized bioreactor with membrane filtration for wastewater treatment, *Water Research*, 27(3), 405-411, 1993.
- Kulkarni, A. V., S. S. Roy and J. B. Joshi, Pressure and flow distribution in pipe and ring spargers: Experimental measurements and CFD simulation, *Chemical Engineering Journal*, 133(1-3), 173-186, 2007.
- Kurada, S., G. W. Rankin and K. Sridhar, Particle-imaging techniques for quantitative flow visualization: a review, *Optics & Laser Technology*, 25(4), 219-234, 1993.

- Laborie, S. and C. Cabassud, Modeling and measurement of shear stress for a slug flow inside a capillary, *AIChE Journal*, 51(4), 1104-1115, 2005.
- Laborie, S., C. Cabassud, L. Durand-Bourlier and J. M. Laine, Fouling control by air sparging inside hollow fibre membranes - effects on energy consumption, *Desalination*, 118(1-3), 189-196, 1998.
- Laera, G., C. Giordano, A. Pollice, D. Saturno and G. Mininni, Membrane bioreactor sludge rheology at different solid retention times, *Water Research*, 41(18), 4197-4203, 2007.
- Lakehal, D., G. Larrignon and C. Narayanan, Computational heat transfer and two-phase flow topology in miniature tubes, *Microfluidics and Nanofluidics*, 4(4), 261-271, 2008.
- Le-Clech, P., H. Alvarez-Vazquez, B. Jefferson and S. Judd, Fluid hydrodynamics in submerged and sidestream membrane bioreactors, *Water Science and Technology*, 48(3), 113-119, 2003.
- Lee, W. N., I. J. Kang and C. H. Lee, Factors affecting filtration characteristics in membrane-coupled moving bed biofilm reactor, *Water Research*, 40(9), 1827-1835, 2006.
- Legrand, J., E. Dumont, J. Comiti and F. Fayolle, Diffusion coefficients of ferricyanide ions in polymeric solutions - comparison of different experimental methods, *Electrochimica Acta*, 45(11), 1791-1803, 2000.
- Liao, B. Q., D. M. Bagley, H. E. Kraemer, G. G. Leppard and S. N. Liss, A review of biofouling and its control in membrane separation bioreactors, *Water Environment Research*, 76(5), 425-436, 2004.
- Linstrom, P.J, Mallard and w.g. NIST Chemistry WebBook, NIST Standard Reference Database Number 69. 2009. National Institute of Standards and Technology. Ref Type: Online Source
- Luostarinen, S., S. Luste, L. ValentEn and J. Rintala, Nitrogen removal from on-site treated anaerobic effluents using intermittently aerated moving bed biofilm reactors at low temperatures, *Water Research*, 40(8), 1607-1615, 2006.
- Marrot, B., A. Barrios-Martinez, P. Moulin and N. Roche, Experimental study of mass transfer phenomena in a cross flow membrane bioreactor: Aeration and membrane separation, *Engineering in Life Sciences*, 5(5), 409-414, 2005.
- Mayer, M., R. Braun and W. Fuchs, Comparison of various aeration devices for air sparging in crossflow membrane filtration, *Journal of Membrane Science*, 277(1-2), 258-269, 2006.
- Mayor, T. S., A. M. F. R. Pinto and J. B. L. M. Campos, Hydrodynamics of gas-liquid slug flow along vertical pipes in the laminar regime-experimental and simulation study, *Industrial and Engineering Chemistry Research*, 46(11), 3794-3809, 2007.
- Mayor, T. S., A. M. F. R. Pinto and J. B. L. M. Campos, Vertical slug flow in laminar regime in the liquid and turbulent regime in the bubble wake-Comparison with fully turbulent and fully laminar regimes, *Chemical Engineering Science*, 63(14), 3614-3631, 2008.

- Mercier-Bonin, M., C. Maranges, C. Lafforgue, C. Fonade and A. Line, Hydrodynamics of slug flow applied to cross-flow filtration in narrow tubes, *AIChE Journal*, 46(3), 476-488, 2000.
- Moreau, A. A., N. Ratkovich, I. Nopens and J. H. J. M. van der Graaf, The (in)significance of apparent viscosity in full-scale municipal membrane bioreactors, *Journal of Membrane Science*, 340(1-2), 249-256, 2009.
- Mori, M., I. Seyssiecq and N. Roche, Rheological measurements of sewage sludge for various solids concentrations and geometry, *Process Biochemistry*, 41(7), 1656-1662, 2006.
- Mulder, M., Basic Principles of Membrane Technology, Springer, 1998.
- Nakoryakov, V. E., O. N. Kashinsky, A. V. Petukhov and R. S. Gorelik, Study of local hydrodynamic characteristics of upward slug flow, *Experiments in Fluids*, 7(8), 560-566, 1989.
- Ndinisa, N. V., A. G. Fane, D. E. Wiley and D. F. Fletcher, Fouling control in a submerged flat sheet membrane system: Part II - Two-phase flow characterization and CFD simulations, *Separation Science and Technology*, 41(7), 1411-1445, 2006.
- Ndinisa, N. V., D. E. Wiley and D. F. Fletcher, Computational fluid dynamics simulations of Taylor bubbles in tubular membranes model validation and application to laminar flow systems, *Chemical Engineering Research and Design*, 83(1 A), 40-49, 2005.
- Nguyen Cong Duc, E., L. Fournier, C. Levecq, B. Lesjean, P. Grelier and A. Tazi-Pain, Local hydrodynamic investigation of the aeration in a submerged hollow fibre membranes cassette, *Journal of Membrane Science*, 321(2), 264-271, 2008a.
- Nguyen Cong Duc, E., C. Levecq, B. Lesjean and A. Tazi-Pain, Modelling the two phase flow in a pilot submerged Membrane Bioreactor, 2008b.
- Nogueira, S., R. G. Sousa, A. M. F. R. Pinto, M. L. Riethmuller and J. B. L. M. Campos, Simultaneous PIV and pulsed shadow technique in slug flow: A solution for optical problems, *Experiments in Fluids*, 35(6), 598-609, 2003.
- Ochoa, J. C., C. Coufort, R. Escudie, A. Line and E. Paul, Influence of non-uniform distribution of shear stress on aerobic biofilms, *Chemical Engineering Science*, 62(14), 3672-3684, 2007.
- Oliveira, T. A. C., U. Cocchini, J. T. Scarpello and A. G. Livingston, Pervaporation mass transfer with liquid flow in the transition regime, *Journal of Membrane Science*, 183(1), 119-133, 2001.
- Omebere-Iyari, N. K. and B. J. Azzopardi, A study of flow patterns for gas/liquid flow in small diameter tubes, *Chemical Engineering Research and Design*, 85(2 A), 180-192, 2007.
- Pal, S. S., A. K. Mitra and A. N. Roy, Pressure drop and holdup in vertical two-phase cocurrent flow with improved gas-liquid mixing, *Industrial & Engineering Chemistry, Process Design and Development*, 19(1), 67-75, 1980.

- Pallares, J. and F. X. Grau, Frequency response of an electrochemical probe to the wall shear stress fluctuations of a turbulent channel flow, *International Journal of Heat and Mass Transfer*, 51(19-20), 4753-4758, 2008a.
- Pallares, J. and F. X. Grau, Frequency response of an electrochemical probe to the wall shear stress fluctuations of a turbulent channel flow, *International Journal of Heat and Mass Transfer*, 51(19-20), 4753-4758, 2008b.
- Petersen, N., S. Stocks and K. V. Gernaey, Multivariate models for prediction of rheological characteristics of filamentous fermentation broth from the size distribution, *Biotechnology and Bioengineering*, 100(1), 61-71, 2008.
- Ramkrishna, D., Population Balances theory and applications to particulate systems in engineering, Academic Press, 2000.
- Ranade, V. V., Modelling of Turbulent Flow in a Bubble Column Reactor, *Chemical Engineering Research and Design*, 75(1), 14-23, 1997.
- Ranade, V. V. and Y. Tayalia, Modelling of fluid dynamics and mixing in shallow bubble column reactors: influence of sparger design, *Chemical Engineering Science*, 56(4), 1667-1675, 2001.
- Ranade, V. V. and R. P. Utikar, Dynamics of gas-liquid flows in bubble column reactors, *Chemical Engineering Science*, 54(21), 5237-5243, 1999.
- Randall, C. W. and D. Sen, Full-scale evaluation of an integrated fixed-film activated sludge (IFAS) process for enhanced nitrogen removal, *Water Science and Technology*, 33(12), 155-162, 1996.
- Ranjan, R., S. DasGupta and S. De, Mass transfer coefficient with suction for turbulent non-Newtonian flow in application to membrane separations, *Journal of Food Engineering*, 65(4), 533-541, 2004.
- Ratkovich, N., C. C. V. Chan, P. R. Berube and I. Nopens. Analysis of shear stress and energy consumption in a tubular airlift membrane system. *Journal of Membrane Science* . 2010a.
- Ref Type: In Press
- Ratkovich, N., C. C. V. Chan, P. R. Berube and I. Nopens. Investigation of the effect of viscosity on slug flow in airlift tubular membranes in search for a sludge surrogate. *Water Science and Technology* . 2010b.
- Ref Type: In Press
- Rehimi, F., J. Legrand and F. Aloui, Electrochemical method for precise determination of wall shear rate, *Russian Journal of Electrochemistry*, 44(4), 434-444, 2008.
- Rochex, A., J. J. Godon, N. Bernet and R. Escudiq, Role of shear stress on composition, diversity and dynamics of biofilm bacterial communities, *Water Research*, 42(20), 4915-4922, 2008.
- Rode, S., N. Midoux, M. A. Latifi, A. Storck and E. Saadjian, Hydrodynamics of liquid flow in packed beds : an experimental study using electrochemical shear rate sensors, *Chemical Engineering Science*, 49(6), 889-900, 1994.

- Rosant, J. M., Liquid-wall shear stress in stratified liquid/gas flow, *Journal of Applied Electrochemistry*, 24(7), 612-618, 1994.
- Rosehart, R. G., E. Rhodes and D. S. SCOTT, Studies of gas-liquid (non-Newtonian) slug flow: void fraction meter, void fraction and slug characteristics, *Chemical Engineering Journal and the Biochemical Engineering Journal*, 10(1), 57-64, 1975.
- Rosenberger, R., K. Kubin and M. Kraume, Rheology of Activated Sludge in Membrane Bioreactors, *Engineering in Life Sciences*, 2(9), 269-275, 2006.
- Rosenberger, S., A. Drews and M. Kraume, Comparison of Microfiltration Behaviour of Activated Sludge and Model Suspensions in a Novel Membrane Test Cell, *Chemie Ingenieur Technik*, 73(6), 2001.
- Salvetti, R., A. Azzellino, R. Canziani and L. Bonomo, Effects of temperature on tertiary nitrification in moving-bed biofilm reactors, *Water Research*, 40(15), 2981-2993, 2006.
- Sanchez Perez, J. A., E. M. Rodriguez Porcel, J. L. Casas Lopez, J. M. Fernandez Sevilla and Y. Chisti, Shear rate in stirred tank and bubble column bioreactors, *Chemical Engineering Journal*, 124(1-3), 1-5, 2006.
- Sethi, S. and M. R. Wiesner, Modeling of transient permeate flux in cross-flow membrane filtration incorporating multiple particle transport mechanisms, *Journal of Membrane Science*, 136(1-2), 191-205, 1997.
- Seyssiecq, I., J. H. Ferrasse and N. Roche, State-of-the-art: Rheological characterisation of wastewater treatment sludge, *Biochemical Engineering Journal*, 16(1), 41-56, 2003.
- Shannak, B. A., Frictional pressure drop of gas liquid two-phase flow in pipes, *Nuclear Engineering and Design*, 238(12), 3277-3284, 2008.
- Shirazi, S. A., E. Al-Adsani, J. R. Shadley and E. F. Rybicki, A mechanistic model for predicting heat and mass transfer in vertical two-phase flow, paper presented at Proceedings of the ASME Heat Transfer/Fluids Engineering Summer Conference 2004, HT/FED 2004, Charlotte, NC, United States, 2004.
- Sokolichin, A., G. Eigenberger, A. Lapin and A. Lubbert, Dynamic numerical simulation of gas-liquid two-phase flows - Euler/Euler versus Euler/Lagrange, *Chemical Engineering Science*, 52(4), 611-626, 1997.
- Sousa, R. G., A. M. F. R. Pinto and J. B. L. M. Campos, Interaction between Taylor bubbles rising in stagnant non-Newtonian fluids, *International Journal of Multiphase Flow*, 33(9), 970-986, 2007.
- Sousa, R. G., M. L. Riethmuller, A. M. F. R. Pinto and J. B. L. M. Campos, Flow around individual Taylor bubbles rising in stagnant CMC solutions: PIV measurements, *Chemical Engineering Science*, 60(7), 1859-1873, 2005.
- Spedding, P. L., G. S. Woods, R. S. Raghunathan and J. K. Watterson, Vertical two-phase flow. Part III: Pressure drop, *Chemical Engineering Research & Design, Transactions of the Institute of Chemical Engineers, Part A*, 76(A5), 628-634, 1998.

- Svendsen, H. F., H. A. Jakobsen and R. Torvik, Local flow structures in internal loop and bubble column reactors, *Chemical Engineering Science*, 47(13-14), 3297-3304, 2009.
- Taha, T. and Z. F. Cui, CFD modelling of gas-sparged ultrafiltration in tubular membranes, *Journal of Membrane Science*, 210(1), 13-27, 2002.
- Taha, T. and Z. F. Cui, CFD modelling of slug flow in vertical tubes, *Chemical Engineering Science*, 61(2), 676-687, 2006a.
- Taha, T. and Z. F. Cui, CFD modelling of slug flow inside square capillaries, *Chemical Engineering Science*, 61(2), 665-675, 2006b.
- Takehima, K., T. Fujii, N. Takenaka and H. Asano, The flow characteristics of an upward gas-liquid two-phase flow in a vertical tube with a wire coil: Part 1. Experimental results of flow pattern, void fraction, and pressure drop, *Heat Transfer - Asian Research*, 31(8), 639-651, 2002.
- Tang, C. C. and A. J. Ghajar, Validation of a general heat transfer correlation for non-boiling two-phase flow with different flow patterns and pipe inclination angles, paper presented at 2007 Proceedings of the ASME/JSME Thermal Engineering Summer Heat Transfer Conference - HT 2007, Vancouver, BC, Canada, 2007.
- Tardieu, E., A. Grasmick, V. Geaugey and J. Manem, Hydrodynamic control of bioparticle deposition in a MBR applied to wastewater treatment, *Journal of Membrane Science*, 147(1), 1-12, 1998.
- Tardieu, E., A. Grasmick, V. Geaugey and J. Manem, Influence of hydrodynamics on fouling velocity in a recirculated MBR for wastewater treatment, *Journal of Membrane Science*, 156(1), 131-140, 1999.
- Tchobanoglous, G., F. L. Burton and H. D. Stensel, Wastewater engineering: treatment and reuse, McGraw-Hill, Boston, 2003.
- Tengesdal, J. O., C. Sarica, Z. Schmidt and D. Doty, Mechanistic model for predicting pressure drop in vertical upward two-phase flow, *Journal of Energy Resources Technology, Transactions of the ASME*, 121(1), 1-8, 1999.
- Thome, J. R., Wolverine Heat Transfer Engineering Data book III, Wolverine Tube Inc, 2008.
- Travis, Q. B. and L. W. Mays, Relationship between Hazen-William and Colebrook-White roughness values, *Journal of Hydraulic Engineering*, 133(11), 1270-1273, 2007.
- Vedantam, S., Computational Flow Modelling and Flow Visualization of Multiphase Reactors., University of Mumbai, India, 2005.
- Vera, L., R. Villarroel, S. Delgado and S. Elmaleh, Enhancing microfiltration through an inorganic tubular membrane by gas sparging, *Journal of Membrane Science*, 165(1), 47-57, 2000.
- Verrecht, B., S. Judd, G. Guglielmi, C. Brepols and J. W. Mulder, An aeration energy model for an immersed membrane bioreactor, *Water Research*, 42(19), 4761-4770, 2008.

- Viana, F., R. Pardo, R. Yanez, J. L. Trallero and D. D. Joseph, Universal correlation for the rise velocity of long gas bubbles in round pipes, *Journal of Fluid Mechanics*, 494, 379-398, 2003.
- Wakeman, R., The influence of particle properties on filtration, *Separation and Purification Technology*, 58(2), 234-241, 2007.
- White, F., Fluid Mechanics, McGraw-Hill, 2002.
- Wicaksana, F., A. G. Fan and V. Chen, The relationship between critical flux and fibre movement induced by bubbling in a submerged hollow fibre system, *Water Science and Technology*, 51(6-7), 115-122, 2005.
- Wisniewski, C. and A. Grasmick, Floc size distribution in a membrane bioreactor and consequences for membrane fouling, *Colloids and Surfaces A: Physicochemical and Engineering Aspects*, 138(2-3), 403-411, 1998.
- Yang, F., A. Bick, S. Shandalov, A. Brenner and G. Oron, Yield stress and rheological characteristics of activated sludge in an airlift membrane bioreactor, *Journal of Membrane Science*, 334(1-2), 83-90, 2009.
- Yeo, A. P. S., A. W. K. Law and A. G. Fane, Factors affecting the performance of a submerged hollow fiber bundle, *Journal of Membrane Science*, 280(1-2), 969-982, 2006.
- Zheng, D. and D. Che, Experimental study on hydrodynamic characteristics of upward gas-liquid slug flow, *International Journal of Multiphase Flow*, 32(10-11), 1191-1218, 2006.
- Zheng, D. and D. Che, An investigation on near wall transport characteristics in an adiabatic upward gas-liquid two-phase slug flow, *Heat and Mass Transfer/Waerme- und Stoffuebertragung*, 43(10), 1019-1036, 2007.
- Zheng, D., D. Che and Y. Liu, Experimental investigation on gas-liquid two-phase slug flow enhanced carbon dioxide corrosion in vertical upward pipeline, *Corrosion Science*, 50(11), 3005-3020, 2008.
- Zheng, D., X. He and D. Che, CFD simulations of hydrodynamic characteristics in a gas-liquid vertical upward slug flow, *International Journal of Heat and Mass Transfer*, 50(21-22), 4151-4165, 2007.
- Zhuoxiong, M. and T. J. Hanratty, Analysis of wall shear stress probes in large amplitude unsteady flows, *International Journal of Heat and Mass Transfer*, 34(1), 281-290, 1991.

Curriculum Vitae

Personal information

Surname: Rios Ratkovich
Name: Nicolás
Date of birth: May 10th 1979
Place of birth: Bogotá, Colombia
Citizenships: Colombian and Croatian
Address: Coupure Rechts 164F
9000 Ghent
Belgium
Phone: +32 (0)9 225 39 43
E-mail: nriosrat@biomath.ugent.be

Education

2004 – 2006 Master of Science in Energy Technology and Sustainable Energy Systems –
Mälardalen University – Västerås, Sweden
Master thesis: *Modelling of the Heat Transfer in an Industrial Batch Furnace*
2003 – 2004 Master of Science and Technology in Process Engineering specialty in
Project Management for Environmental and Energy Engineering – Ecole des
Mines de Nantes – Nantes, France
Master thesis: *Modelling of Large-Scale Energy Storage in Electricity Supply
Networks Using Batteries*
1997 – 2002 B.Sc. in Chemical Engineering – University of Los Andes – Bogotá,
Colombia
1997 – 2002 B.Sc. in Mechanical Engineering – University of Los Andes – Bogotá,
Colombia
1985 – 1996 San Bartolome la Merced School – Bogotá, Colombia

Working experience

2010 Federal University of Santa Catarina (Florianópolis, Brazil)
Scholarship from the Euro Brazilian Windows II
Research stay on design and build a setup to monitor and measure two-
phase flow in horizontal pipes and U-bends for the oil industry
2009 – 2010 Ghent University (Ghent, Belgium)
Ambrein project (anaerobic MBR for industrial applications)
2006 – 2009 Ghent University (Ghent, Belgium)
MBR-TRAIN Marie Curie Early Stage Research Training Fellowship of the
European Community's 6th Framework Programme
PhD-research on Mathematical Modelling and Process Control of Membrane

- Bioreactors (MBR)
- 2005 – 2006 Mälardalen University (Västerås, Sweden)
Title project: Modelling of a Thermo-photovoltaic (TPV) energy concentrator
- 2005 Kanthal AB – Sandvik (Hallstahammar, Sweden)
Internship / M.Sc. Thesis project for Mälardalen University
- 2004 ABB AB Corporate Research (Västerås, Sweden)
Internship / M.Sc. Thesis project for Ecole des Mines de Nantes
- 2002 Land Fast S.A. (Bogotá, Colombia)
(Aeronautics sector – Ground operations)
Engineer - Apprentice Ramp Supervisor
- 2000 – 2001 University of Los Andes (Bogotá, Colombia)
Teaching Assistant in the following subjects:
Unitary Operations, Dept. of Chemical Engineering.
Agro industrial Processes, Dept. of Mechanical Engineering.
Fluid Mechanics, Dept. of Mechanical Engineering.

Professional training

- 16/07/2009 – 17/02/2009 **IRSA-CNR** (Bari, Italy)
Course on research founding
- 13/07/2009 – 15/02/2009 **IRSA-CNR** (Bari, Italy)
Course on biomass characterization for MBRs
- 11/02/2009 – 13/02/2009 **Cranfield University** (Cranfield, UK)
Course on desalination technologies
- 18/07/2008 – 18/07/2008 **Ghent University** (Ghent, Belgium)
Seminar on intellectual property rights
- 15/07/2008 – 17/07/2008 **Ghent University** (Ghent, Belgium)
Course on Modelling of MBR processes
- 30/05/2007 – 01/06/2007 **Veolia Wasser** (Berlin, Germany)
Course on Scientific presentation skills
- 19/03/2007 – 21/03/2007 **TU Delft** (Delft, The Netherlands)
Course on CFD of Dispersed Multiphase Flow
- 19/07/2006 – 20/07/2006 **Cranfield University** (Cranfield, UK)
Course on Research Ethics & PhD Writing
- 17/07/2006 – 19/07/2006 **Cranfield University** (Cranfield, UK)
Course on Membrane Bioreactors

Stays abroad

- 05/2009 – 06/2009 **FlowConcept** (Hannover, Germany)
Modeling a GE Zenon MBR module
Modeling on CFD a GE ZeeWeed MBR module with hollow fibers and validate the model with shear stress measurements.
- 11/2008 – 11/2008 **University of British Columbia** (Vancouver, Canada)
Experimental measurements of slug flow with CMC a non-Newtonian liquid
Experimental measurements of Taylor bubbles (bullet shape bubbles)

using a PIV system and shear probes to measure the bubble rising velocity and the shear stress using CMC-N₂ mixtures.

06/2008 – 07/2008 **FlowConcept** (Hannover, Germany)

Modeling an airlift MBR module and air diffuser

Modeling on CFD an airlift MBR module including the filtration process and the membrane porosity. Two types of air diffusers were modeled (ring and disk aerator) to determine the most efficient air distribution within the system.

10/2007 – 10/2007 **University of British Columbia** (Vancouver, Canada)

Experimental measurements of slug flow

Experimental measurements of Taylor bubbles using a PIV system and shear probes to measure the bubble rising velocity and the shear stress respectively for water-N₂ mixtures.

Scientific contributions

Peer reviewed publications

Ratkovich, N.; Chan, C.C.V.; Berube, P.R.; Nopens, I. Experimental study and CFD modelling of a two-phase slug flow for an airlift tubular membrane. *Chemical Engineering Science* 64 (2009) 3576-3584.

Moreau, A.A.; **Ratkovich, N.**; Nopens, I.; van der Graaf, J.H.J.M. The (in)significance of apparent viscosity in full-scale municipal membrane bioreactors. *Journal of Membrane Science* 340 (2009) 249–256.

Ratkovich, N., Chan, C.C.V., Berube, P., Nopens, I. Investigation of the effect of viscosity on slug flow in airlift tubular membranes in search for a sludge surrogate. *Water Science and Technology* (in press)

Ratkovich, N., Chan, C.C.V., Berube, P., Nopens, I., Analysis of shear stress and energy consumption in a tubular airlift membrane system. *Journal of Membrane Science* (submitted).

Ratkovich, N., Chan, C.C.V., Berube, P., Nopens, I., A heat-and-mass transfer correlation to optimize shear stress in tubular airlift membrane systems for wastewater treatment. *Journal of Heat and Mass Transfer* (in preparation).

Ratkovich, N., Chan, C.C.V., Berube, P., Nopens, I., Experimental validation of a hydrodynamic CFD model of a HF MBR using shear stress measurements in the bundle. *Journal of Membrane Science* (in preparation).

Conference proceedings

- Ratkovich, N.**, Hunze, M., Futselaar, H., Nopens, I. Use of CFD to model and optimize the hydrodynamics of an airlift MBR side-stream module. 2009. Proceedings of WEFTEC 2009 on October 10-14, 2009 in Orlando, FL, USA
- Ratkovich, N.**, Chan, C.C.V., Berube, P., Nopens, I., Analysis of shear stress and energy consumption in a tubular airlift membrane system. 2009. Proceedings of IWA-MTC 2009 on September 1-3, 2009 in Beijing, China.
- Ratkovich, N.**, Chan, C.C.V., Berube, P., Nopens, I. Investigation of the effect of viscosity on slug flow in airlift tubular membranes in search for a sludge surrogate. 2009. Proceedings of IWA-MTC 2009 on September 1-3, 2009 in Beijing, China
- Ratkovich, N.**, Chan, C.C.V., Berube, P., Nopens, I. Experimental measurements of shear stress in a tubular air lift membrane system. 2009. Proceedings of 7th World Conference on Experimental Heat Transfer, Fluid Mechanics and Thermodynamics on June 28 – July 3, 2008 in Krakow, Poland.
- Rios, N.**, Nopens, I., Brannock, M. and Essemiani, K. Modelling hydrodynamics in MBR systems using Computational Fluid Dynamics. 2008. Proceedings of 2008 IWA North American Membrane Research Conference on August 10-13, 2008. Amherst, Massachusetts, USA.
- Rios, N.**, Nopens, I. and Vanrolleghem, P.A. Mass transfer coefficient determination of a two-phase flow for an UF membrane in a side-stream MBR. 2008. Proceedings of 5th international conference on Transport Phenomena in Multiphase System on June 30 – July 3, 2008 in Bialystok, Poland.
- Rios, N.**, Nopens, I. and Vanrolleghem, P.A. Hydrodynamic CFD simulation of a two-phase flow in an ultrafiltration membrane tube for a side-stream membrane bioreactor. 2008. Proceedings of 5th international conference on Transport Phenomena in Multiphase System on June 30 – July 3, 2008 in Bialystok, Poland.
- Rios, N.**, Nopens, I. and Vanrolleghem, P.A. Using a two-phase hydrodynamic model to control fouling in an ultrafiltration side-stream MBR. 2008. Proceedings of Membrane Technology on January 27-30, 2008 in Atlanta, USA.
- Rios, N.**, Nopens, I. and Vanrolleghem, P.A. CFD simulation of an ultrafiltration membrane for wastewater treatment in a side-stream membrane bioreactor for reduction of fouling. 2007. Proceedings of the Particle Separation on July 9-12, 2007 in Toulouse, France
- Rios, N.**, Nopens, I. and Vanrolleghem, P.A. Hydrodynamic CFD simulation of a two-phase flow in a single tube of an ultrafiltration membrane for a side-stream membrane

bioreactor. 2007. Proceedings of the 2nd IWA National Young Water Professionals Conference on June 4-5, 2007 in Berlin, Germany

Rios, N., Nopens, I., De Schepper, V., Jiang, T., Verstraete, W. and Vanrolleghem, P.A. A Rheological Model for Activated Sludge in a Side-Stream MBR, 2007. Proceedings of the IWA membrane conference on May 15-17, 2007 in Harrogate, UK.

Conferences

- WEFTEC.09, 10-14 October, 2009, Orlando, FL, USA.
- 1st YWP BeNeLux, 30 September – 2 October, 2009, Eindhoven, The Netherlands.
- 3rd Workshop on CFD modelling for MBR applications, 11 September, 2009, Toulouse, France.
- Euromembrane, 6-10 September, 2009, Montpellier, France
- IWA Membrane Technology Conference, 1-3 September, 2009, Beijing, China
- 7th World Conference on Experimental Heat Transfer, Fluid Mechanics and Thermodynamics, 28 June – 3 July, 2009, Krakow, Poland.
- Final MBR-Network workshop, 31 March – 1 April 2009, Berlin, Germany.
- Symposium and Poster Day Membrane Technology, 26 November, 2008, Antwerp, Belgium.
- Network Young Membrains 10th edition conference, 18-19 September, 2008, Berlin, Germany.
- IWA World Water Congress and Exhibition, 7-12 September, 2008, Vienna, Austria.
- IWA North American Membrane Research Conference, 10-13 August, 2008, Amherst, MA, USA
- 2nd Workshop on CFD modelling for MBR applications, 14 July 2008, Ghent, Belgium.
- 5th international conference on Transport Phenomena in Multiphase System, 30 June – 3 July, 2008. Bialystok, Poland.
- Engineering with Membranes, 25-28 May, 2008, Vale de Lobo, Portugal.
- WEF Membrane Technology, 27-30 January, 2008, Atlanta, GA, USA.
- IWA International Conference on Particle Separation, 9-12 July, 2007, Toulouse, France
- 1st workshop on CFD modelling for MBR applications, 3 July, 2008, Berlin, Germany
- 2nd IWA National Young Water Professionals Conference, 4-5 June, 2007, Berlin, Germany.
- 4th International Membranes Conference, 15-17 May 2007, Harrogate, UK.

Conference organization:

- Summer School on Modelling Membrane Bioreactor Processes, July 15-17, 2008, Ghent, Belgium
- 2nd CFD/MBR workshop, July 14, 2008, Ghent, Belgium.
- 3rd International Conference on Population Balance Modelling, September 19–21, 2007, Québec city, Canada.